2018

Electrostatic Effects on Chemical Reactivity; Oriented Double Layer Effects on Chemical Bonding Kinetics and Thermodynamics

Long Zhang
University of Wollongong

UNIVERSITY OF WOLLONGONG AUSTRALIA

Australian Research Council Centre of Excellence for Electromaterials Science

The Intelligent Polymer Research Institute

The Australian Institute for Innovative Materials

Electrostatic Effects on Chemical Reactivity; Oriented Double Layer Effects on Chemical Bonding Kinetics and Thermodynamics

Long Zhang

under supervision of Dr. Simone Ciampi and Prof. Gordon G. Wallace

submitted this thesis in partial fulfilment of the requirements for the Award of the Degree of **Doctor of Philosophy** from University of Wollongong

The Intelligent Polymer Research Institute

The University of Wollongong

July 2018

This work is dedicated to my affectionate parents for their self-giving assistance and persistent encouragement and my deeply beloved wife Ai Tang for her endless support and love.

Thesis Certification

I, Long Zhang, declare that this thesis, submitted in fulfilment of the requirements for the award of Doctor of Philosophy, in the Department of Chemistry, University of Wollongong, is wholly my own work unless otherwise referenced or acknowledged. This document has not been submitted for qualification at any other academic institution.

Long Zhang

May 2018

Acknowledgements

This work has been enabled with the financial assistances from the Intelligent Polymer Research Institute (IPRI), University of Wollongong (UOW) and the Australian Institute of Nuclear Science and Engineering (AINSE) Ltd. as well as the technical helps from people who have been there in the past three years.

I would firstly like to express my sincere gratitude to my supervisors Prof. Gordon G. Wallace and Dr. Simone Ciampi. Their invaluable guidance has enabled me to perform this research smoothly. They have always been able to give instant responses and provide direct support during my entire PhD period. I was very lucky to be recruited by Simone as his first PhD student, as he is a very talented mentor with an endless array of practical solutions and constructive advices, and always devises at least two plans for each experiment, thus allowing me to perform my research efficiently. I can still recall several episodes with Simone while pursuing my degree. My English proficiency was less decent with limited scientific vocabulary and weak oral expression, but he is pretty patient to communicate with me and even sometimes wrote down what we talked of. On the other hand, he always initially has a discussion with me when my experiments did not proceed as expected. Although Simone moved to Curtin University for a new academic career in June of 2016, he kept in touch by skype/phone; communicating three times on a weekly basis. He has the incredible ability to help me in developing the abilities of independent thinking and addressing problems. Gordon provided most of the experimental instrumentations, especially the electrochemical measurements and synthesis works, and prompt support on chemical purchasing, ensuring my work can be done on time. His experience and diligence have been a very valuable resource to me, which means that I could avoid going in the wrong direction in my research.

Numerous data recorded in this thesis were from other reputed groups. I would specifically like to thank Prof. Justin Gooding (UNSW) for helping with the XRR characterizations, Prof. Michelle Coote (ANU) for assisting with the theoretical calculations, Prof. Joaquin Gonzalez (Universidad De Murcia) for providing digital

simulations, Dr. Nadim Darwish (Curtin Uni) for giving the STM-BJ measurements, and Dr. Anton Le Brun (ANSTO) for helping with the XRR measurements. All these works are essential components of my thesis, and my research would undoubtedly be hampered without their generous support.

The assistance of all members of the IPRI family is also greatly appreciated. In particular, I wish to express my acknowledgement of Dr. Pawel Wagner who shared his vast organic chemistry knowledge, and of Dr. Caiyun Wang who provided experimental platforms. Thanks are also due to my colleagues, all of whom helped me in the lab and/or made my stay in Australia a colorful experience.

Finally, my special appreciation goes to my family, to my parents who always kept me focused on my studies regardless of the long geographical distance; to my love in life, Ai Tang (Fiona). Fiona undertook much more family duties during my whole PhD study period, making me concentrate fully on my research, and supporting and comforting me mentally when I was stuck on some academic problems. Without her immediate help and encouragement, my work would not be completed with full colors.

Long Zhang

Abstract

The main goal of this thesis is to experimentally demonstrate that electric fields play a significant role in governing chemical reactivity. The electric forces are generated from either the electric double layer, electrostatic interactions between oxidized species and anions or electrons, or external electric field stimuli. These forces influence the catalysis/inhibitor effects on chemical changes through a detailed analysis of kinetic and thermodynamic data. These effects are also further corroborated with the assistance of digital simulations and quantum calculations.

An open-shell state of persistent nitroxide radical monolayers is successfully preserved on the semiconductor silicon surfaces upon grafting by a two-step wet chemical route (hydrosilylation of 1,8-nonadiyne and "click" reaction of azide tailored nitroxide). The prepared surface has been used to study the effect of electrostatic interactions between oxidized nitroxide (oxoammonium) and electrolyte anions or space charges in the interior of semiconductor on the electroactivity of nitroxide monolayers; indicating that the kinetic and thermodynamic parameters of redox couple electrode reactions are drastically altered while considering these electrostatic effects. They are also responsible for some non-ideal voltammetric performances such as contra-thermodynamic redox behavior and <90.6 mV full width at half maximum (FWHM).

Thermal-labile alkoxyamine molecules would be electrochemically oxidized to form alkoxyamine radical cations, followed by rapid fragmentation into carbocations and nitroxide radicals. Digital simulations and high-level theoretical calculations suggest that the electrostatic environment within electric double layers (explicit ions and solvents) other than explicit bonding interaction would help to promote the lysis of produced intermediates. However, the limitations of the inaccurate routine of including partial species during the modelling process as well as only qualitative analysis of the electrostatic effect have challenged us to think about whether there is a protocol which can quantify the electric field on the lysis of alkoxyamines. A scanning tunneling microscopy break-junction (STM-BJ) set-up allows us to wire an amino-functionalized

alkoxyamine molecule between an Au(111) substrate and a gold tip. While imposing an external bias around 150 mV to the built molecular circuit, we can observe two discrete conductance signals which are due to the parent alkoxyamines and putative nitroxides generated by the homolysis of parent alkoxyamines. We thus provide the concrete values of electric fields on the lysis of alkoxyamines.

Experimental evidence for validating electrostatic catalysis have recently emerged in initial work (electrostatic catalysis of a Diels-Alder reaction, ***Nature*** 531 (2016) 88). Although current experimental protocols have just remained at the proof-of-concept stage due to orientated issue (i.e., reactant vs. reaction axis), electrostatic effects have already been shown to be bright prospects for studies in some fields, for instance synthetic organic electrochemistry, field-effect transistor, and so forth. One can envision that electric fields can be used as versatile tools for manipulating various chemical reactions on a preparative scale in the future once the technologically-relevant obstacles are addressed.

Publications

1. **Long Zhang**, Benjamin B. Noble, Eduardo Laborda, Nadim Darwish, Sandra Pluczyk, Anton P. Le Brun, Gordon G. Wallace, Joaquin Gonzalez, Michelle L. Coote, Simone Ciampi. Electrochemical and Electrostatic Cleavage of Alkoxyamines. ***J. Am. Chem. Soc.*** 140 (2018) 766-774.
2. **Long Zhang**, Yan Boris Vogel, Benjamin B. Noble, Vinicius R. Goncales, Nadim Darwish, Anton Le Brun, J. Justin Gooding, Gordon G. Wallace, Michelle L. Coote, Simone Ciampi. TEMPO monolayers on Si(100) electrodes: electrostatic effects by the electrolyte and semiconductor space-charge on the electroactivity of a persistent radical. ***J. Am. Chem. Soc.*** 138 (2016) 9611-9619.
3. Yan B. Vogel, **Long Zhang**, Nadim Darwish, Vinicius R. Gonçales, Anton Le Brun, J. Justin Gooding, Angela Molina, Gordon G. Wallace, Michelle L. Coote, Joaquin Gonzalez, Simone Ciampi. Reproducible Flaws Unveil Electrostatic Aspects of Semiconductor Electrochemistry. ***Nat. Commun.*** 8 (2017) 2066-2074.
4. **Long Zhang**, Ruth Belinda Domínguez Espíndola, Benjamin B. Noble, Vinicius R. Goncales, Gordon G. Wallace, Nadim Darwish, Michelle L. Coote, and Simone Ciampi. Switchable Interfaces: Redox Monolayers on Si(100) by Electrochemical Trapping of Alcohol Nucleophiles. ***Surfaces*** 1 (2018) 3-11.
5. **Long Zhang**, Gordon G. Wallace, Simone Ciampi. Quantitative analysis of contra-thermodynamic peak-inversion phenomena of redox probe confined on the redox probe-confined semiconductor surfaces. (In preparation)

Conference Presentations

1. 2018 the International Conference on Nanoscience and Nanotechnology (ICONN), poster presentation, “Electrochemical and Electrostatic Cleavage of Alkoxyamine” (University of Wollongong, Wollongong, Australia).
2. 2017 12th Annual International Electromaterials Science Symposium, poster presentation, “Electrostatic Catalysis in the Anodic Cleavage of Alkoxyamines”, (University of Wollongong, Wollongong, Australia).
3. 2016 ARC Centre of Excellence for Electromaterials Science Meeting, I gave a talk titled “Electrostatic Effect on the Electroactivity of a Persistent Radical Monolayer”

(Australian National University, Canberra, Australia).

4. 2016 11th Annual International Electromaterials Science Symposium, poster presentation, “Assembly of Nitroxide Persistent Radicals Monolayers on Semiconductor Surface: Tweaking the Redox Thermodynamics and kinetics of TEMPO monolayers on Si(100)”, (Deakin University, Melbourne, Australia).

List of Names or Abbreviations

4-NH_2-TEMPO	4-Amino-2,2,6,6-tetramethylpiperidine-1-oxyl
4-N_3-TEMPO	4-Azido-2,2,6,6-tetramethyl-1-piperdinyloxy
4-N_3-TEMPO-PE	4-Azido-2,2,6,6-tetramethyl-1-(1-phenylethoxy)piperdine
4-OH-TEMPO	4-Hydroxy-2,2,6,6-tetramethyl-1-piperdinyloxy
BDE	Bond dissociation energy
BOC_2O	Di-tert-butyl decarbonate
Bu_4N	Tetrabutylammonium
ClO_4	Perchlorate
CT	Charger transfer
CuAAC	Copper-catalyzed alkyne-azide cycloaddition
CV	Cyclic voltammetry
MeCN	Acetonitrile
DCM	Dichloromethane
DFT	Density functional theory
di-amino-TEMPO-PE	1-(1-(4-Aminophenyl)ethoxy)-2,2,6,6-tetramethylpiperidin-4-amine
di-BOC-amino-TEMPO-PE	1-(1-(4-*Tert*-butylcarbamatephenyl)ethoxy)-2,2,6,6-tetramethylpiperidin-4-tert-butoxycarbonylamino
E_C	Conduction band edge
EEFs	External electric fields
E_F	Fermi level
EI	Electron impact
EPR	Electron paramagnetic resonance
E_{redox}	Solution redox potential
ESI	Electrospray ionization
E_V	Valence Band edge
Fc	Ferrocene
Fc^+/Fc	Ferricenium/ferrocene couple

FWHM	Full width at half maximum
GC-MS	Gas chromatography-mass spectrometry
HD	Highly-doped
HRMS	high resolution mass spectrometer
IHP	Inner Helmholtz plane
LD	Lowly-doped
MO	Molecular orbital
NaBARF	Sodium tetrakis[3,5-bis(trifluoromethyl)phenyl]borate
NMP	Nitroxide mediated radical polymerization,
NMR	Nuclear magnetic resonance
OCP	Open circuit potential
OHP	Outer Helmholtz plane
PF_6	Hexafluorophosphate
SLD	Scattering length density
SMD	Solvation model based on density
STM-BJ	Scanning tunneling microscopy break-junction
TEMPO	2,2,6,6-Tetramethylpiperidine-1-oxyl
TEMPO-PE	2,2,6,6-Tetramethyl-1-(1-phenylethoxy)piperdine
TLC	Thin-layer chromatography
Γ	Surface coverage
UHV	Ultra-high vacuum
VB	Valence bond
V_{FB}	Flat band potential
XPS	X-ray photoelectron spectroscopy
XRR	X-ray reflectivity
ΔG_{IP}	Ion-pairing energy

List of Schemes, Figures and Tables

of 1,8-nonadiyne (**S-1**). (a) Survey XPS scan. (b) High-resolution scan for the Si 2p region comprising two spin–orbit-split components. Silica-related emission (102–104 eV signal associated with SiO_x) were only minor - i.e. just above the spectrometer detection limit of *ca*. <0.05 SiO_x monolayers equivalents. (c) Narrow scan of the C 1s region. The signal was fit with three components at 285.0 (C–C), 286.4 (C–C/–N/–O) and 287.8 eV, comprising respectively of 8.1/10, 1.8/10, and 0.2/10 (adventitious oxidized carbon) of the total C 1s signal. (d) Narrow scan of the N 1s region with two main components at 401.7 and 400.4 eV (0.35:1 intensity ratio). The high binding energy satellite at 402.7 eV is assigned to a shake-up satellite of N–O electrons.

Figure 3.4 CV for **S-2** samples prepared on Si(100) electrodes (highly doped, 0.001–0.003 Ω cm). Background-subtracted observed (solid line) and simulated (symbols) voltammograms at 100 mV s^{-1} in MeCN containing 1.0×10^{-1} M Bu_4NClO_4. Figure inset shows the simulated voltammetry for a reversible and non-interacting electroactive monolayer system (*k* was set to 10^4 s^{-1} and Frumkin "*a*" was set to zero). Ideal adsorptive-shaped waves are symmetric with respect to E_f^0 and show a 90.6/*n* FWHM.

Figure 3.5 Representative CVs (v = 100 mV s^{-1}) for **S-2** samples (HD) before (black solid line) and upon (red dashed line) prolonged CV analysis (100 cycles) in 0.1 M Bu_4NClO_4/MeCN electrolytes. The measured nitroxide surface coverage, Γ, decreased by *ca*. 33% from 2.34×10^{-10} mol cm^{-2} to 1.56×10^{-10} mol cm^{-2} after the 100 cycles. This stability is comparable, or better, than what has been reported in literature for TEMPO monolayers on metallic electrodes. For example, when TEMPO was attached onto a graphite felt electrode the current–voltage response decreased by 50% after 50 repeated CV scans in acetonitrile- or water-based electrolytes. This chemical irreversibility is tentatively ascribed by Geneste and co-workers to reactions of the oxoammonium species.

Figure 3.6 Linear relationship between voltage scan rate and experimental peak current (symbols) for S-2 samples on HD electrodes in 0.1 M Bu_4NClO_4/MeCN systems.

Figure 3.7 CVs of **S-2** samples on HD silicon electrodes in MeCN solutions containing

different Bu_4N salts at a 0.1 M concentration (a-e). The experimental E_f^0 is indicated in each panel; with the exception of HSO_4^-, it moves progressively anodically with the decrease of the anions' Lewis basicity (see Table 3.2 for theoretical ΔG_{IP} values). The stronger than expected basicity of HSO_4^- compared with the other anions can be rationalized by the formation of a stabilizing H-bond with the 1,2,3-triazole ring.

Figure 3.8 Shifts of the experimental E_f^0 (●) and changes to the theoretical redox potential (+) as a function of the chemical composition of the electrolyte anion (Tables 3.1 and 3.2).

Figure 3.9 Chemical structures of all species examined in this work and their abbreviations.

Figure 3.10 M06-2*X*/6-31+G(d,p) optimized geometries of the complexes between electrolyte anions and a truncated model of the **S-2** film containing the oxidized TEMPO substituted with the 4-methyl-1,2,3-triazole substituent (denoted **T-cat**).

Figure 3.11 CVs of **S-2** samples on illuminated LD electrodes in 0.1 M Bu_4NClO_4/MeCN (voltage scan rate was 100 mV s^{-1}). The experimental FWHM is independent of surface charge (117 mV for 3.97×10^{-11} mol cm^{-2} and 116 mV for 1.31×10^{-10} mol cm^{-2}). The low coverage sample shown in the left panel (as well as in Figure 3.16) is obtained by reducing the CuAAC reaction time from 2 h to 1 min.

Figure 3.12 Simulated cyclic voltammograms for a reversible one-electron redox couple where both species are strongly adsorbed on the electrode surface. The Frumkin *a* term that leads to the isotherm under equilibrium was varied between -0.9 and 0.9. $A = 0.28$ cm^2, $\Gamma = 2 \times 10^{-10}$ mol cm^{-2} and the voltage sweep rate was set to 0.1 V s^{-1}. The calculated value of FWHM is indicated in the figure. The x-axis is $E - E_p$, that equals to the overpotential ($E - E_0$) if $b_o = b_r$ and $a_o = a_r$ where b_i is the absorption strength and a_i is the interaction parameter between *i* molecules (oxidized or reduced forms).

Figure 3.13 Observed CVs (lines) and simulated linear sweeps (symbols) for the dark HD **S-2** samples in the presence of 0.5×10^{-3} M Bu_4NBr in acetonitrile with 1.0×10^{-1} M of either Bu_4NPF_6, Bu_4NClO_4 or Bu_4NNO_3. The refined value of k_{cat} for the reaction between the adsorbed oxoammonium and non-adsorbed bromide relates to the

electrolyte anion and dropped progressively from 3.2×10^4 $dm^3mol^{-1}s^{-1}$ (PF_6^-), to 1.9×10^4 $dm^3mol^{-1}s^{-1}$ (ClO_4^-) and finally to 2.8×10^3 $dm^3mol^{-1}s^{-1}$ (NO_3^-). The higher value for k_{cat} in PF_6^- rules out the possibility of strong ion pairing reducing the rate of the heterogeneous reactions, hence potentially nulling the thermodynamic gain from the favorable oxoammonium/anion interactions on the redox potential of the surface couple. The potential axis of the simulated curves is shown offset by neg. 400 mV for clarity only.

Figure 3.14 CVs for **S-2** samples prepared on n-Si electrodes (LD, 1–10 Ω cm). (a) Dark oxidation and reduction waves (solid symbols) and their underpotential shift with supra band gap illumination (lines). CVs were obtained at a voltage sweep rate of 100 mV s^{-1} in MeCN containing 1.0×10^{-1} M of either Bu_4NClO_4 (solid line, FWHM = 91 mV) or Bu_4NPF_6 (empty symbols, FWHM = 120 mV). (b) Observed (lines) and simulated (symbols) CV of the electrocatalytic mechanism on illuminated LD or HD **S-2** samples, respectively, in the presence of 0.5×10^{-3} M Bu_4NBr in 1.0×10^{-1} M of Bu_4NPF_6. The refined value of k_{cat} for the reaction between the adsorbed oxoammonium and non-adsorbed bromide was 3.2×10^3 $M^{-1}s^{-1}$.

Figure 3.15 The chemical reversibility of **S-2** samples was studied by experiments on LD electrodes where the light was deliberately switched off at the anodic limit (0.4 V, 0.5 V or 0.6 V) in Bu_4NClO_4/MeCN systems. In contrast to the data on HD electrodes (Figure 3.4), the CVs shown in Figure 3.15 suggest there are no measurable changes in Γ for LD samples as no changes to the anodic wave can be observed after nine consecutive cycles. The difference in chemical reversibility between LD and HD samples was not further investigated as it is beyond the scope of the work and an explanation will require further studies.

Figure 3.16 Panel (a) shows the experimental OCP values for **S-2** samples on LD electrodes under variable illumination intensity. If (i) the material does not have very fast carrier recombination rates and (ii) the illumination is sufficiently intense to completely remove band bending within the semiconductor, the illuminated OCP value can be used to estimate the E_{fb}. In the cases at hand for **S-2** samples on LD electrodes the direction of the shift in the OCP upon illumination is consistent with the doping

type (n-type). There was no evidence of saturation of the OCP event at the highest light intensity (ca. 4500 lx), hence suggesting some degree of residual upward bending, i.e. a residual barrier for electron injection from the electrolyte even under strong illumination. Additional examples of "peak inversion" in CVs of **S-2** samples on LD silicon electrodes under continuous illumination (b-d). The phenomenon appears to be independent of coverage and electrolyte type. For example, data in (b) and (c) were recorded in Bu_4NClO_4/MeCN at coverage of 2.52×10^{-11} mol cm^{-2} and 2.02×10^{-10} mol cm^{-2}, respectively. Data in (c) and (d) were of a comparable coverage but recorded in Bu_4NClO_4/MeCN and Bu_4NPF_6/MeCN, respectively.

Figure 3.17 (a) Example of "peak inversion" in CVs of **S-2** electrodes of low doping under illumination (Bu_4NClO_4 and v = 100 mV s^{-1}). (b-d) "peak inversion" can be deliberately induced in CVs of **S-2** samples on lowly doped electrodes when illumination is switched off at the anodic vertex (0.4, 0.5 or 0.6 V) in Bu_4NClO_4 electrolytes using solvents of progressively lower dielectric constant (37.5 for acetonitrile, 8.9 for dichloromethane and 4.8 for chloroform). Simulated voltammograms (symbols) and refined values of the self-interaction parameter a are indicated in the figure.

Figure 3.18 Deliberate acceleration of the backward rate. CVs of **S-2** LD samples with high coverage (1.31×10^{-10} mol cm^{-2}, i.e., standard CuAAC reaction time of 2 h) where the light was deliberately switched off at the anodic limit (0.5, 0.6, 0.7, 0.8 or 0.9 V) in Bu_4NClO_4/MeCN systems. The experimental FWHMs for the cathodic waves were indicated in figure.

Figure 4.1 Synthesis of alkoxyamines used in this Chapter; 4-N_3-TEMPO-PE (**1**, R = N_3, electrochemistry on silicon surface systems) and TEMPO-PE (**2**, R = H, electrochemistry diffusive systems, EPR and theoretical modelling).

Figure 4.2 XPS spectra of 4-N_3-TEMPO-PE monolayers (**S-1**) assembled on highly-doped Si(100) electrodes by CuAAC reactions between 4-N_3-TEMPO-PE (**1**) and monolayers of 1,8-nonadiyne on Si(100). a) Survey XPS scan. b) High-resolution XPS scan for the Si 2p region. c) Narrow scan of the C 1s region. d) Narron scan of the N 1s region.

Figure 4.3 X-ray reflectivity of 4-N_3-TEMPO-PE monolayer (**S-1**) on silicon at the air-solid interface. The points with error bars show the collected data and the solid red line is the fit to the data. The lower trace is the residuals between collected and fitted data. The refined monolayer thickness is 14.2 ± 0.4 Å which is in good agreement with the theoretical values of 17 Å (Chem3D).

Figure 4.4 Anodic cleavage of a surface-tethered alkoxyamine (**S-1**) and its conversion into a Si(100) nitroxide-terminated monolayer (electrolyte is 1.0×10^{-1} M Bu_4NClO_4 in MeCN). The monolayer distal-end of **S-1** samples is the phenylethyl portion of an alkoxyamine molecule (**1**) and it is lost to the electrolyte upon electrolysis. (a) Cyclic voltammograms (100 mV s^{-1}) acquired before (black trace) and after (blue trace) applying a positive bias to **S-1** samples prepared on Si(100) electrodes. The potential is stepped from open circuit to 0.65 V (vs. Fc/Fc^+) for a 30 s period before recording a voltammogram and selected traces are presented in the figure (blue traces). Anodization of **S-1** results in the progressive appearance of a redox signature that is in good agreement with that of a surface-tethered TEMPO control (**S-2**, black trace). The TEMPO coverage rises in increments of about 2.6×10^{-11} mol cm^{-2}, and reaches a maximum of ca. 1.31×10^{-10} mol cm^{-2}, equivalent to ca. 25% of a close-packed TEMPO monolayer assembled on a gold surface. (b) Plot of the electrochemically-determined changes to the surface coverage of redox-active nitroxide radicals as a function of the anodization time of **S-1** samples. (c) Reaction schematics for the alkoxyamine surface model (**S-1**) and controls (**S-2**).

Figure 4.5 Anodic electrochemistry of alkoxyamines **2** at platinum electrodes. (a) Experimental (solid lines) and simulated (empty symbols) cyclic voltammograms of 0.5×10^{-3} M **2**, and experimental data (offset grey trace) of 0.5×10^{-3} M TEMPO controls. The best-fit parameters are D (**2**/**2**$^{\bullet+}$) = 7.8×10^{-6} cm^2 s^{-1}, D (TEMPO/oxoammonium) = 2.2×10^{-5} cm^2 s^{-1}, E_1^0 = 0.78 V, k_1^0 = 0.05 cm s^{-1}, E_2^0 = 0.195 V, k_2^0 = 0.08 cm s^{-1}, k_f = 5.0×10^6 s^{-1}. (Electrolyte is 1.0×10^{-1} M MeCN/Bu_4NClO_4, and scan rate is 100 mV s^{-1}, 0.7 cm^2 platinum macrodisk electrode). (b) *In-situ* electrochemical EPR measurements conducted in 1.0×10^{-1} M

DCM/Bu_4NPF_6 in the presence of 0.5×10^{-3} M of **2**. The specified electrolysis bias (labels to curves vs. Fc/Fc^+) was applied to a platinum wire electrode for 360 s with the EPR data being accumulated over the last 60 s of the potential step.

Figure 4.6 Current evolution with time in a typical three-step chronoamperometry experiment of 0.36×10^{-3} M **2** in MeCN with 1.0×10^{-1} M Bu_4NClO_4. Experimental (solid line) and simulated (symbols) transients with the potential being stepped from -0.03 V to 0.87 V, then from 0.87 V to 0.47 V, and from 0.47 V to -0.03 V (vs. Fc/Fc^+). The best-fit parameters are D (**TEMPO**/oxoammonium) = 2.2×10^{-5} cm^2 s^{-1}, D (**2**/**2**$^{\bullet+}$) = 7.8×10^{-6} cm^2 s^{-1} E_1^0 = 0.78 V (vs. Fc/Fc^+), k_1^0 = 0.05 cm s^{-1}, E_2^0 = 0.195 V (vs. Fc/Fc^+), k_2^0 = 0.08 cm s^{-1}, k_f = 5.0×10^6 s^{-1}. The electrochemically-determined effective area for the data in the figure is 0.07 cm^2.

Figure 4.7 a) Cyclic voltammograms at Pt microdisks (4.5 μm in radius) of a solution containing 0.53×10^{-3} M Fc and 0.63×10^{-3} M **TEMPO** in MeCN with 1.0×10^{-1} M Bu_4NClO_4 (voltage sweep rate is 10 mV s^{-1}). The refined parameters (E mechanism) are: $E^0(Fc/Fc^+)$ = 0.35 V *vs.* Ag/AgCl ("leakless", see experimental section), k^0 (Fc/Fc^+) = 0.20 cm s^{-1}, E^0 (**TEMPO**/oxoammonium) = 0.58 V, k^0(**TEMPO**/oxoammonium) = 0.10 cm s^{-1}, α = 0.5. b) Cyclic voltammograms at Pt microdisks (4.5 μm in radius) of 0.53×10^{-3} M Fc and 0.92×10^{-3} M **2** in MeCN with 1.0×10^{-1} M Bu_4NClO_4 (scan rate is 10 mV s^{-1}). The refined parameters ($EC_{irr}E$ mechanism) are: E^0 (Fc/Fc^+) = 0.26 V vs Ag/AgCl ("leakless"), k^0 (Fc/Fc^+) = 0.10 cm s^{-1}, E^0 (**2**/**2**$^{\bullet+}$) = 1.05 V, k^0 (**2**/**2**$^{\bullet+}$) = 0.08 cm s^{-1}, E^0 (**TEMPO**/oxoammonium) = 0.47 V, k^0 (**TEMPO**/oxoammonium) = 0.08 cm s^{-1}, α = 0.5. For the chemical step of **2**$^{\bullet+}$ → **TEMPO** + R^+, the refined k_f is 5.0×10^6 s^{-1}. The experimental and simulated curves are plotted as solid lines and empty symbols, respectively. The diffusivity of Fc was set equal to 2.3×10^{-5} cm^2 s^{-1}. The diffusivity of the **2**/**2**$^{\bullet+}$ couple was 7.8×10^{-6} cm^2 s^{-1}. The refined D value of 2.2×10^{-5} cm^2 s^{-1} for the **TEMPO**/oxoammonium couple was also independently estimated by fittings of experimental cyclic voltammetry at Pt macrodisk electrodes (Figure 4.8).

Figure 4.8 Experimental (solid line) and simulated (empty symbol) cyclic voltammograms for 0.5×10^{-3} M **TEMPO** solutions in MeCN containing 1.0×10^{-1} M

Bu_4NClO_4 at different scan rates (indicated as labels to the figures). The diffusion coefficients and the electron transfer rate constant used to fit the data were 2.2×10^{-5} cm^2 s^{-1} (D_{TEMPO}), 2.2×10^{-5} cm^2 s^{-1} ($D_{oxoammonium}$) and 0.08 cm s^{-1} (k^0_{TEMPO}), E^0_{TEMPO} = 0.21 V (vs. Fc/Fc^+). The electrochemically-determined effective area of the Pt disk electrode is 0.07 cm^2.

Figure 4.9 (a) EPR spectra (red trace) of anodized TEMPO-PE solutions (0.5×10^{-3} M **2** in DCM with 1.0×10^{-1} M Bu_4NPF_6). The working Pt bias is poised to 0.85 V vs. Fc/Fc^+, the anodization time is 360 s and the EPR spectra is accumulated during the last 60 s of the anodic pulse. The EPR spectra of **2** is plotted against the EPR spectra (acquired at OCP) of control **TEMPO** solutions (black trace). (b) Experimental (solid line) and simulated (symbols) current-time transients after a potential step from OCP to 0.85 V (vs. Fc/Fc^+, cylindrical geometry, 0.01 cm radius and length of either 2.5 cm (solid symbol) or 4 cm (empty symbol), and semi-infinite 1D diffusion). The electrolyte is a 0.5×10^{-3} M solution of **2** and for the simulations (symbols) consideration was given to an $EC_{irr}E$ mechanism that is described by the following parameters: E^0_1 = 0.80 V (vs. Fc/Fc^+), k^0_1 = 0.01 cm s^{-1}, E^0_2 = 0.30 V, k^0_2 = 0.01 cm s^{-1}, α = 0.5. D (**TEMPO**/oxoammonium) = 1.9×10^{-5} cm^2 s^{-1}, D (**2**/**2**$^{\bullet+}$) = 6.0×10^{-6} cm^2 s^{-1}. The value of k_f for the irreversible chemical step is 1.0×10^6 s^{-1}. (c) Simulated concentration profiles (**2**, oxoammonium and **TEMPO**, $EC_{irr}E$ parameters as at panel (b)) near the cylindrical Pt wire (0.01 cm radius and 2.5 cm in length) and (d) simulated cumulative number of **TEMPO** molecules (right y-axis) present in the EPR sample after the 360 s potential step.

Figure 4.10 Simulated concentration profiles; Effect of changes to the rate of the chemical step. Plots (a)-(d) illustrate the direction of the hypothetical changes to the cumulative number (n) of TEMPO molecules that would be present in the electrolyte compartment of the EPR experiment (semi-infinite 1D diffusion at a cylindrical electrode of 0.1 cm in radius and 2.5 cm in length) in response to changes to the rate of the chemical step. The simulated electrode reaction is the electrolysis of 0.5×10^{-3} M **2** induced by a potential step from 0.3 V to 1.1 V, 360 s of anodization time and considering an $EC_{irr}E$ mechanism that is described by the following parameters: E^0_1 =

1.01 V, k_1^0 = 0.04 cm s^{-1}, E_2^0 = 0.425 V, k_2^0 = 0.05 cm s^{-1}, α = 0.5. D (**TEMPO**/oxoammonium) = 2.2 × 10^{-5} cm^2 s^{-1}, D (**2**/**2**$^{\bullet+}$) = 7.0 × 10^{-6} cm^2 s^{-1}. The value of k_f describing the chemical step is dropped from 1.0 × 10^6 s^{-1} to 1.0 × 10^3 s^{-1} ((a)-(d), respectively).

Figure 4.11 Anodic electrochemistry of alkoxyamine **2**. Experimental (solid line) and simulated (empty symbols) voltammograms at different scan rates (25 to 4000 mV s^{-1}, as specified by labels in the figure) of 0.5 × 10^{-3} M **2** in MeCN with 1.0 × 10^{-1} M Bu_4NClO_4. Best-fit parameters ($EC_{irr}E$ mechanism) are: E_1^0 = 0.78 V (vs. Fc/Fc^+), k_1^0 = 0.05 cm s^{-1}, E_2^0 = 0.195 V (vs. Fc/Fc^+), k_2^0 = 0.08 cm s^{-1}, α = 0.5. D (**TEMPO**/oxoammonium) = 2.2 × 10^{-5} cm^2 s^{-1}, D (**2**/**2**$^{\bullet+}$) = 7.8 × 10^{-6} cm^2 s^{-1} and for the irreversible chemical step k_f is 5.0 × 10^6 s^{-1}. Only the first 4 segments are shown for clarity and the first segment is acquired ramping the bias in the anodic direction. The electrochemically-determined effective area for the data in the figure is 0.07 cm^2. An estimate of the Pt macrodisk effective area was obtained prior to each experiment on **2** by refining cyclic voltammograms of 0.5 × 10^{-3} M Fc in MeCN with 1.0 × 10^{-1} M Bu_4NClO_4 and using the following model: E mechanism, E^0 (Fc/Fc^+) = 0.23 V (vs. Ag/AgCl), k^0 (Fc/Fc^+) = 0.2 cm s^{-1}, D (Fc/Fc^+) = 2.3 × 10^{-5} cm^2 s^{-1}, α = 0.5.

Figure 4.12 Anodic electrochemistry of alkoxyamine **2**. Experimental (solid line) and simulated (empty symbols) voltammograms at different scan rates (100 to 1500 mV s^{-1}, as specified by labels in figure) of 0.5 × 10^{-4} M **2** in MeCN with 1.0 × 10^{-1} M Bu_4NClO_4. Best-fit parameters ($EC_{irr}E$ mechanism) are: E_1^0 = 0.81 V (vs. Fc/Fc^+), k_1^0 = 0.52 cm s^{-1}, E_2^0 = 0.24 V (vs. Fc/Fc^+), k_2^0 = 0.19 cm s^{-1}, α = 0.5. D (**TEMPO**/oxoammonium) = 2.2 × 10^{-5} cm^2 s^{-1}, D (**2**/**2**$^{\bullet+}$) = 7.8 × 10^{-6} cm^2 s^{-1} and for the irreversible chemical step k_f is 3.4 × 10^7 s^{-1}. Only the first 4 segments are shown for clarity and the first segment is acquired ramping the bias in the anodic direction. The effective area for the data in the figure is 0.07 cm^2.

Figure 4.13 Anodic electrochemistry of alkoxyamine **2**. Experimental (solid line) and simulated (empty symbols) voltammograms at different scan rates (100 to 4000 mV s^{-1}, as specified by labels in the figure) of 5.0 × 10^{-3} M **2** in MeCN with 1.0 × 10^{-1} M Bu_4NClO_4. Best-fit parameters ($EC_{irr}E$ mechanism) are: E_1^0 = 0.83 V (vs. Fc/Fc^+), k_1^0

= 0.06 cm s^{-1}, E_2^0 = 0.245 V (vs. Fc/Fc^+), k_2^0 = 0.02 cm s^{-1}, α = 0.5. *D* (**TEMPO**/oxoammonium) = 2.2 × 10^{-5} cm^2 s^{-1}, *D* (**2**/**2**$^{\bullet+}$) = 7.8 × 10^{-6} cm^2 s^{-1} and for the irreversible chemical step k_f is 5.0 × 10^6 s^{-1}. The electrochemically-determined effective area for the data in the figure is 0.017 cm^2. Only the first 4 segments are shown for clarity and the first segment is acquired ramping the bias in the anodic direction.

Figure 4.14 Theoretical potential energy surface for the oxidative cleavage of alkoxyamine **2** in MeCN. The homolysis of the unperturbed ('free') radical-cation (red pathway) is strongly thermodynamically disfavoured. However, homolysis can be made more favourable by a static electric field, and by interactions with an explicit anion and/or with an explicit solvent molecule.

Figure 4.15 Anodic electrochemistry of alkoxyamine **2**. Experimental (solid line) and simulated (empty symbols) voltammograms at different scan rates (10 to 100 mV s^{-1}, as specified by labels in the figure) of 0.57 × 10^{-3} M **2** in MeCN with 1.0 × 10^{-1} M Bu_4NPF_6. Best-fit parameters ($EC_{irr}E$ mechanism) are: E_1^0 = 0.81 V (vs. Fc/Fc^+), k_1^0 = 0.08 cm s^{-1}, E_2^0 = 0.225 V (vs. Fc/Fc^+), k_2^0 = 0.04 cm s^{-1}, α = 0.5. *D* (**TEMPO**/oxoammonium) = 2.2 × 10^{-5} cm^2 s^{-1}, *D* (**2**/**2**$^{\bullet+}$) = 7.7 × 10^{-6} cm^2 s^{-1} and for the irreversible chemical step k_f is 5.0 × 10^6 s^{-1}. The electrochemically-determined effective area for the data in the figure is 0.08 cm^2. Only the first 4 segments are shown for clarity and the first segment is acquired ramping the bias in the anodic direction.

Figure 4.16 Current evolution with time in a typical three-step chronoamperometry experiment of 0.6 × 10^{-3} M **2** in MeCN with 1.0 × 10^{-1} M Bu_4NPF_6. Experimental (solid line) and simulated (symbols) transients with the potential being stepped from -0.04 V to 0.86 V, then from 0.86 V to 0.46 V, and from 0.46 V to -0.04 V (vs. Fc/Fc^+). The electrochemically-determined effective area for the data in the figure is 0.07 cm^2. The best-fit parameters are *D* (**TEMPO**/oxoammonium) = 2.2 × 10^{-5} cm^2 s^{-1}, *D* (**2**/**2**$^{\bullet+}$) = 7.7 × 10^{-6} cm^2 s^{-1} E_1^0 = 0.81 V (vs. Fc/Fc^+), k_1^0 = 0.08 cm s^{-1}, E_2^0 = 0.225 V (vs. Fc/Fc^+), k_2^0 = 0.04 cm s^{-1}, k_f = 5.0 × 10^6 s^{-1}.

Figure 4.17 Cyclic voltammograms at Pt microdisks (5.0 μm in radius) of 0.50 × 10^{-3} M Fc and 0.64 × 10^{-3} M **2** in MeCN with 1.0 × 10^{-2} NaBARF (scan rate is 10 mV s^{-1}).

The refined parameters ($EC_{irr}E$ mechanism) are: E^0 (Fc/Fc$^+$) = 0.20 V vs Ag/AgCl ("leakless"), k^0 (Fc/Fc$^+$) = 0.2 cm s^{-1}, E^0 (**2**/**2**$^{\bullet+}$) = 1.025 V, k^0 (**2**/**2**$^{\bullet+}$) = 0.07 cm s^{-1}, E^0 (**TEMPO**/oxoammonium) = 0.435 V, k^0 (**TEMPO**/oxoammonium) = 0.05 cm s^{-1}, α = 0.5. For the chemical step of **2**$^{\bullet+}$ → **TEMPO** + R$^+$, the refined k_f is 5.2 × 10^6 s^{-1}. The experimental and simulated curves are plotted as solid lines and empty symbols, respectively. The diffusivity of Fc is set to 1.8 × 10^{-5} cm^2 s^{-1}, that for the **TEMPO**/oxoammonium couple is 2.0 × 10^{-5} cm^2 s^{-1} and the diffusivity of the **2**/**2**$^{\bullet+}$ couple is 7.3 × 10^{-6} cm^2 s^{-1}.

Figure 4.18 Anodic electrochemistry of alkoxyamine **2**. Experimental (solid line) and simulated (empty symbols) voltammograms at different scan rates (75 to 8000 mV s^{-1}, as specified by labels in the figure) for 0.5 × 10^{-3} M **3** in MeCN with 1.0 × 10^{-2} M NaBARF. Best-fit parameters ($EC_{irr}E$ mechanism) are: E_1^0 = 0.82 V (vs. Fc/Fc$^+$), k_1^0 = 0.07 cm s^{-1}, E_2^0 = 0.23 V (vs. Fc/Fc$^+$), k_2^0 = 0.05 cm s^{-1}, α = 0.5 D (**TEMPO**/oxoammonium). = 2.0 × 10^{-5} cm^2 s^{-1}, D (**2**/**2**$^{\bullet+}$) = 7.3 × 10^{-6} cm^2 s^{-1} and for the irreversible chemical step k_f is 5.2 × 10^6 s^{-1}. The electrochemically-determined effective area for the data in the figure is 0.07 cm^2. Only the first 4 segments are shown for clarity and the first segment is acquired ramping the bias in the anodic direction.

Figure 4.19. Current evolution with time in a typical three-step chronoamperometry experiment of 0.5 × 10^{-3} M **2** in MeCN with 1.0 × 10^{-2} M NaBARF. Experimental (solid line) and simulated (symbols) transients with the potential being stepped from -0.04 V to 1.06 V, then from 1.06 V to 0.46 V, and from 0.46 V to -0.04 V (vs. Fc/Fc$^+$). The electrochemically-determined effective area for the data in the figure is 0.07 cm^2. The best-fit parameters are D (**TEMPO**/oxoammonium) = 2.0 × 10^{-5} cm^2 s^{-1}, D (**2**/**2**$^{\bullet+}$) = 7.3 × 10^{-6} cm^2 s^{-1} E_1^0 = 0.82 V (vs. Fc/Fc$^+$), k_1^0 = 0.07 cm s^{-1}, E_2^0 = 0.23 V (vs. Fc/Fc$^+$), k_2^0 = 0.05 cm s^{-1}, k_f = 5.2 × 10^6 s^{-1}.

Figure 4.20 (a-b) Anodic electrochemistry of alkoxyamine **2** in DCM. Experimental (solid line) and simulated (empty symbols) voltammograms of 0.5 × 10^{-3} M **2** in DCM with 1.0 × 10^{-1} M Bu_4NPF_6 (50 mV s^{-1} for Pt ultramicroelectrodes 5.0 μm in radius in (a), the electrolyte is added with 0.6 × 10^{-3} M Fc. The refined parameters ($EC_{irr}E$

mechanism) are: E^0 (Fc/Fc$^+$) = 0.13 V vs Ag/AgCl ("leakless"), k^0 (Fc/Fc$^+$) = 0.10 cm s^{-1}, E^0 (**2**/**2**$^{\bullet+}$) = 0.82 V, k^0 (**2**/**2**$^{\bullet+}$) = 0.01 cm s^{-1}, E^0 (**TEMPO**/oxoammonium) = 0.32 V, k^0 (**TEMPO**/oxoammonium) = 0.01 cm s^{-1}, α = 0.5. For the chemical step of **2**$^{\bullet+}$ → **TEMPO** + R$^+$, the refined k_f is 1.0 × 10^6 s^{-1}. The diffusivity of Fc was set equal to 1.9 × 10^{-5} cm^2 s^{-1}. The diffusivity of the **2**/**2**$^{\bullet+}$ couple was 6.0 × 10^{-6} cm^2 s^{-1}. The refined D value of 1.9 × 10^{-5} cm^2 s^{-1} was for the **TEMPO**/oxoammonium couple; 50 mV s^{-1} for 0.07 cm^2 Pt macro-disks electrodes presented in (b)). Best-fit parameters ($EC_{irr}E$ mechanism) are: E_1^0 = 0.68 V (vs. Fc/Fc$^+$), k_1^0 = 0.01 cm s^{-1}, E_2^0 = 0.18 V (vs. Fc/Fc$^+$), k_2^0 = 0.01 cm s^{-1}, α = 0.5. D (**TEMPO**/oxoammonium) = 1.9 × 10^{-5} cm^2 s^{-1}, D (**2**/**2**$^{\bullet+}$) = 6.0 × 10^{-6} cm^2 s^{-1} and for the irreversible chemical step k_f is 1.0 × 10^6 s^{-1}. (c) Current evolution with time in a typical three-step chronoamperometry experiment of 0.4 × 10^{-3} M **2** in DCM with 1.0 × 10^{-1} M Bu_4NPF_6**.** Experimental (solid line) and simulated (symbols) transients with the potential being stepped from -0.07 V to 0.78 V, then from 0.78 V to 0.43 V, and from 0.43 V to -0.07 V (vs. Fc/Fc$^+$). The best-fit parameters are D (**TEMPO**/oxoammonium) = 1.9 × 10^{-5} cm^2 s^{-1}, D (**2**/**2**$^{\bullet+}$) = 6.0 × 10^{-6} cm^2 s^{-1} E_1^0 = 0.69 V (vs. Fc/Fc$^+$), k_1^0 = 0.01 cm s^{-1}, E_2^0 = 0.19 V (vs. Fc/Fc$^+$), k_2^0 = 0.01 cm s^{-1}, k_f = 1.0 × 10^6 s^{-1}. The electrochemically-determined effective area for the data in the figure is 0.07 cm^2. It can be noted that refinement of a model against the experimental voltammetry of **2** in DCM-based electrolytes was generally found to lead to poorer quality fits relative to the MeCN counterparts.

Figure 4.21 Electrochemical cleavage of alkoxyamines. Theoretical potential energy surface for the oxidative cleavage of alkoxyamine **2** in DCM. The figure shows the effect of electrostatic environment (either solvent or electrolyte anions) on the reaction energies of alkoxyamine cation radicals decomposition. The homolysis of the unperturbed ('free') radical-cation (red pathway) is strongly thermodynamically disfavoured. However, homolysis can is made more favourable by a static electric field, and by interactions with an explicit anion. Unlike acetonitrile, an explicit solvent molecule does not aid homolysis.

Figure 5.1 Synthesis of alkoxyamine **1** used in this Chapter (STM-BJ experiments on gold surfaces and theoretical models).

Figure 5.2 An external oriented electric field prompt the lysis of alkoxyamines. Schematics of a STM-BJ setup on alkoxyamines in low dielectric solvents. Detailed results and experimental procedures are in the Figures 5.3 and 5.4. The fate of the parent alkoxyamine **1** (left panel) is probed by measuring the single-molecule conductivity at different magnitudes of electric field. Molecules have very distinct electrical finger-prints in STM-BJ and for instance the 4-amino TEMPO molecule (right panel) is less electrically conducting than the parent alkoxyamine by one order of magnitude.

Figure 5.3 Electrostatic catalysis in the homolysis of alkoxyamines. (a-c) Schematic depiction of the STM-BJ setup for a single-molecule junction experiment used to investigate the effect of an external electrical field on the breaking of a C–ON bond. Single-molecule STM-BJ conductance measurements were used to probe the fate of the alkoxyamine molecule **1** under a variable electric field stimulus in a low dielectric solvent. The experiments capture discrete electrical signals from either the intact parent molecule **1** or from the putative 4-amino-TEMPO fragment that is produced upon the homolysis of **1**. A STM tip is brought into and out of contact with an Au(111) surface while this is covered with a diluted solution of the molecule of interest (either **1** or a 4-amino-TEMPO standard in mesitylene/DCM, 10:1, v/v). The surface is biased against the tip and the current versus distance signal is collected as the tip is moved away from the surface. (d-f) Typical current versus distance traces with conductance plateaus indicative of a single-molecular junction. The current drops from the current-saturation value to the current-amplifier detection limit, passing through breakage steps, "plateaus", each of a specific conductance value. (g-i) Conductance histograms showing the electrical "fingerprints" of either the intact alkoxyamine **1** (i.e. before splitting, tip-surface bias < 150 mV) at 1E-5 G_0 ($G_0 = (2e^2/h = 77.5$ μS, quantum of conductance) or the free nitroxide that is unmasked after splitting (bias > 150 mV) at 1E-6 G_0. The molecular conductance obtained upon homolysis of **1**, as shown in (h, **1**@300 mV), is a perfect match of the results from control experiments where the two electrodes are forming junctions in a standard sample of commercial 4-amino-TEMPO (c,f,i).

Figure 5.4 Electric fields and breaking probability of single-molecules. The plot

shows the effect of the bias between the STM tip and the Au(111) surface over the fate of several thousand molecular junctions (ca. 4000 for each data point) each obtained by electrically "wiring" molecules of alkoxyamine **1** in a STM-BJ experiment. At biases in the range between 150 and 200 mV, discrete conductance plateaus at both 1E-5 G_0 and 1E-6 G_0 appear, reflecting the co-existence of both the parent molecule **1** and its homolysis product (4-amino-TEMPO). The area of each data point reflects the relative bias-dependent abundance of the species.

Figure 5.5 Electrostatic catalysis in the homolysis of alkoxyamines. (a,b) Representative single-molecule STM-BJ conductance "pull" trace and statistical conductance histograms for samples of alkoxyamine **1** in mesitylene/DCM biased at 200 mV (gold STM tip-to-Au(111) substrate bias). The histograms that are built from the analysis of ca. 4000 pulling traces show the coexistence of the 1E-5 Go "signature" which is assigned to the parent molecule (**1**) with the 1E-6 G_0 population which is assigned to one of the lysis product (4-amino-TEMPO molecules, i.e. the putative nitroxide fragment originated from the C–O lysis in **1**). (c,d) STM-BJ control experiments of the molecule 4-amino-TEMPO held at 50 mV showing a representative conductance-distance trace alongside conductance histograms revealing a major contributor of electrical conductance centred at 1E-6 G_0. The conductance does not change between 50 mV and 300 mV (Figure 5.3) for the 4-amino-TEMPO control, indicating that this molecule is not affected by the electric field in this bias range and remains intact during the measurement. (e,f) STM-BJ experiments on samples of 4-vinylaniline molecule, one of the putative product of the lysis of **1**. Plateaus are absent from the STM-BJ curves and this is statistically evident as no "peak" can be observed in conductance histograms built from the data. It can be inferred that the original alkoxyamine molecule **1** breaks in response to an electric field (threshold of about 200 mV bias between the gold STM tip and the Au(111) substrate) to release a 4-amino-TEMPO fragment (electrical "fingerprinting" of 1E-6 G_0) and possibly a vinylaniline that however is not forming a top & bottom junction with the gold electrodes.

Figure 5.6 Alkoxyamine homolytic and heterolytic bond cleavage.

Figure 5.7 Selection of the x-, y- and z-directions (axes) for the reactant and product

Table of Contents

Chapter 1 General Introduction

1.1Abstract

There is a wealth of knowledge on the effect of oscillating fields (e.g. light) on chemical reactivity, but little is known on the role of external electric fields (EEFs) on rate and equilibrium position of chemical reactions. Numerous theoretical studies are available concerning the effects of static electricity on the stability of charged species and/or on chemical and biological reactions, but the scope of EEFs over these aspects is largely unexplored experimentally. The introductory chapter aims to review the development of electrostatic catalysis from long-standing theoretical predictions to experimental evidence, elucidating the mediator/catalysis role of static fields of electrode/electrolyte interfaces (both for diffusive systems as well as diffusion-less surface models), pH-switching of non-redox reactivity in solution systems to EEFs effects in low-dielectric solvents in the scanning tunneling microscopy break-junction (STM-BJ) technique.

1.2 Background

Increasing attention at present concentrates on the use of static electric fields to catalyze non-electrochemical reactions, namely electrostatic catalysis.[1-7] The concept that a controllable electric field (direction and magnitude) enables chemists to control catalysis/inhibition of chemical/biochemical reactions at will, and hence establish a new approach to future biology and chemistry, from the adjustment of enzyme activity in biological processes to the manipulation of barrier height of chemical reactions. Our interest in the catalytical effect of EEFs was inspired by the 70s-80s seminal work of Yeshayahu Pocker on electrostatic catalysis of dissociation[8], elimination[9] and isomerization[10] by ionic aggregates in concentrated $LiClO_4$ solutions. Subsequently, different theories and models were proposed to describe the role of electrostatic forces while demonstrating its effect to influence vibrational Stark effect[11], promote electron transfer and redox reactions[12-15], elicit spin-polarized conductivity[16, 17], control the ferromagnetism in a thin-film semiconducting alloy[18], even change the configurations and transitions of molecules[19-21]. Much research have then contributed to illustrate that electric fields might be regarded as “smart” tools to manipulate certain biological/chemical reactions, namely the movement and rearrangement of electrons,

on the basis of the properties mentioned above. However, the intrinsic feature of an EEF as a vector suffered from limitation dictated by both how to adjust the orientation of electric field against reaction axis and how to gauge the precise strength of electric field applied on the reactions. Further, the effect of electrostatic interaction is large in the gas phase,[22] whereas in solution it tends to progressively diminish with the increasing solvent polarity.[23] Despite its natural limitations, the concept of electrostatic catalysis provides scientists with a novel idea to revolutionize conventional reactions catalyzed by specific catalyst entities. Most work on electrostatic effects so far has been limited to theoretical investigations because of the orientation and strength issues, therefore development of versatile platforms to control the orientation and intensity of an EEF deliberately is an extremely attractive approach toward electrostatic catalysis experiments.

It was not until 2016 that Coote et al. provided proof-of-concept that an electric field could accelerate a carbon-carbon bond forming reaction through STM-BJ technique.[3] Although the proposed surface model system is not on a practical scale, and the limited molecules/specific reactions are employed to match this experimental setup, it opened up the possibility of using easily accessible model systems to explore electrostatic catalysis phenomena experimentally. Moreover, the molecule bridges attached to the STM electrodes are expected to complement and/or extend the application of the currently popular nanotechnology field towards the development of molecular devices and nanosensors.

The following sections aim to review the development of electrostatics as an effector of chemical chance. Particular emphasis is placed on the effect of electrostatic interactions on non-redox reactions. The layout of the remaining content of the introductory chapter is as follows: theoretical research relevant to the understanding of the electrostatic effect in different aspects, such as enzyme catalysis, the stability of resonance structures, non-redox reaction, are presented in Section 1.3, especially in the context of the theoretical studies involving electrostatic forces relevant to this thesis; followed by introducing a concise overview of established experimental strategies (diffusive systems and surface models) for studying electrostatic interactions in Section

1.4. The major items described in this thesis, including nitroxide radicals, alkoxyamines, semiconductor electrodes, and STM-BJ technique for demonstrating the electrostatic effect, are outlined in Section 1.5. Section 1.6 will attempt to summarize the following chapters. In addition, two notable areas of this thesis relevant to electrostatic studies are not illustrated, or only treated briefly, since they are either reviewed in detail elsewhere, described in the corresponding chapters of this thesis or because they are not considered crucial to the motif presented in this thesis. They consist of a) theoretical calculations and electrochemical simulations, and b) kinetic and thermodynamic analysis for some electrochemical/chemical reactions.

1.3 Theoretical investigation of the electrostatic effect

Many reactions need a catalyst to proceed at an appreciable rate. Some scientists are devoting themselves to design molecules to serve as catalysts. Beside the difficulty of designing and testing a catalyst, there are also issues associated with it becoming an impurity (removal of catalysts). But does a catalyst need to be a chemical entity? The answer is probably not, and evidence are growing pointing in the direction of an electric field acting as alternative means to catalyze a range of reactions. The beginning of electrostatic catalysis study may be dated from the reports of Yeshayahu Pocker in the 1970s, delineating an extremely powerful electrostatic catalysis that arose from the ion-pair aggregate of lithium perchlorate and diethyl ether which was accessible; involving the ionization process of triphenylmethyl chloride and hydrogen chloride.[8] In the following 4 decades several theories and models have been developed to describe and predict the catalytic role of electrostatics, with some notable examples outlined in the following pages.

1.3.1 Ionic structures of bonds and transition states under EEFs

A methodology utilized the connection between molecular orbital (MO) and valence bond (VB) theories that was initially developed by Sason S. Shaik and co-workers for unravelling the topology of this electronic reorganization during the chemical transformation of reactants to products.[24, 25] Moreover, the implementation of the VB diagram provides scientists with a visualized model to understand how an electric field

can mediate a number of reactions by destabilizing/stabilizing ionic structures in their corresponding transition states (i.e. how an electric field lowers the energy of charge transfer (CT) configurations during a reaction process). When it comes to an EEF, it is important to note that an EEF is either from electrostatic interaction between charged molecules or from an external field stimulus.

Shaik's group illustrated the acceleration of the heterolysis rate of polar covalent bonds catalyzed by inducing external positive charges or metal ions to lower the barrier height of ionic structures.[26] With the aid of quantum chemical calculations and density functional theory, Grimme et al. proposed a mechanistic insight which illustrated that Lewis pairs can drive the activation of dihydrogen due to the formed electric fields by positive/negative charges inside molecule cavities.[27, 28] On the other hand, the effect of an applied electric field on chemical properties of molecules has long been suggested by theoretical chemists; there are also some theoretical studies toward either controlling structural delocalization of a non-polar π-system[29], affecting the energies, geometries, and vibrational Stark shifts of diatomic molecules[30] or governing the energy landscape of carbon-nitrogen bond of nitromethane[31] by adjusting the directions and strengths of an applied external homogeneous electric field. In order to exactly understand the electrostatic effect, for example, Shaik et al. showed that the degree and direction of bond ionicity of homonuclear bonds (H-H and Li-Li) rely largely on the molecular polarizability (molecule species) and oriented EEF (direction and strength) in Figure 1.1a. As can be seen from Figure 1.1b, researchers can appreciate that the electron pair orbitals hybridization of Li-Li bond is influenced by an electric field with MO theory, on top of that, the VB scenario shows that an oriented electric field can wake up dormant ionic structure of H-H bond (Figure 1.1c). All these theoretical studies indeed validate the electric field has an effect on stabilization of ionic structure, even catalyzing heterolysis or S_N1 reactions of polar bonds.[25, 26, 32] Further, the electrostatic catalytic effects stem from the control of energetics of different transient states.

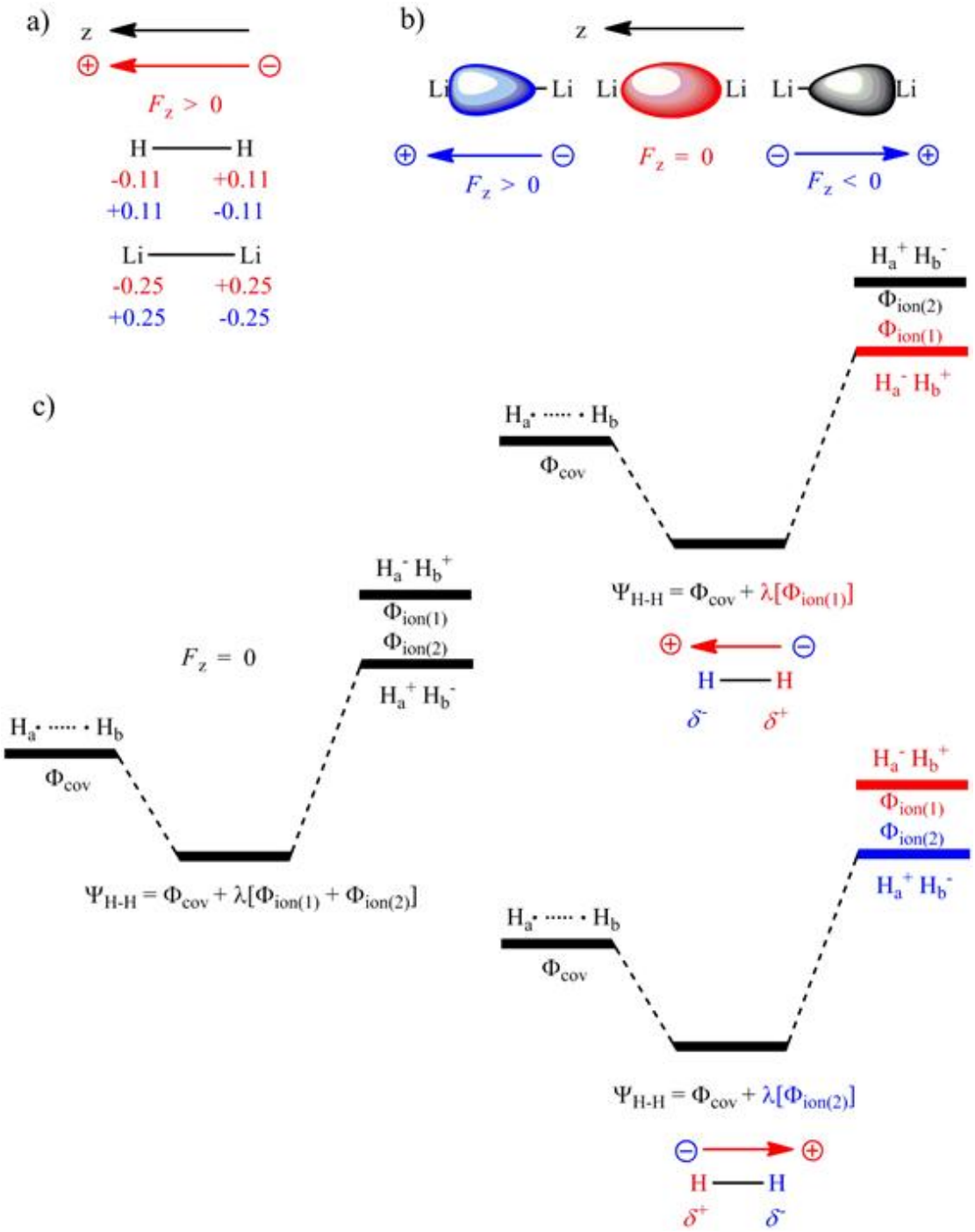

Figure 1.1 Analyses of charge distributions and dipole moments in two homonuclear bonds (H-H, Li-Li) affected by an oriented EEF with MO and VB theories. a) The ionicity of H_2 and Li_2 induced by oriented electric field along the bond-axis. b) Orbital hybridization of Li_2 under electric fields explained with MO-based polarization mechanism. c) Covalent-ionic bonds mixing of H_2 under electric fields illustrated with VB-based polarization mechanism. (This Figure is adapted from Ref. 4)

1.3.2 EEFs can control enzymatic catalysis

The cytochrome P450 enzymes play versatile roles in tuning hydrocarbon hydroxylation, heteroatom oxidation and olefin epoxidation.[33] Extensive earlier works,

including experimental evidence and theoretical calculations, have already underpinned the catalytic mechanisms which are due to the formed iron-based intermediates in the activation of oxygen by cytochrome P450.[33, 34] However, systematic exploration of the effect of oriented external electric fields on the catalytic power of P450 enzymes to date has been entirely a computational exercise. For example, Shaik's group by a QM/MM study emphasized the pronounced effects of EEFs on the key intermediate states and entire catalytic steps of P450 enzyme.[35] Further, compared with an electric field created at biological membranes and electrochemical interfaces, homogeneous external electric fields built have been based on computational works. They have a significant impact on the reactivity of cytochrome *c* compounds,[35] as well as can induce the electron mobility and structural distortion of cytochrome c,[36] allowing us to modulate the thermodynamic and kinetic parameters of electron transfer and enzymatic catalytic reactions.

It is worth noting that the built-in electric fields generated by chemical reagents themselves may catalyze a wide variety of reactions by lowering the energy of charge-transfer configurations or stabilizing ionic structure in each transient state. Warshel *et al.* reviewed the catalytic contributions of enzymes and showed that they are dependent largely on the pre-organized polar environment of the enzyme active sites that produce electrostatic effects to catalyze reactions.[32, 37] Besides P450 enzyme catalysis, electrostatic effects toward enzymatic catalysis were recently reported in several cases. The viewpoint of the role of electrostatic stabilization in catalysis has emerged based on mutation experiments, providing primary insights toward the importance of electrostatic effects.[38-43] Based on these studies, the horizon of electrostatic effects on enzymatic activities has been further expanded; for instance, the active site of ketosteroid isomerase creates a local electric field for inducing the electron rearrangement of C=O bond, affecting the rate-determining step of the corresponding enzymatic catalysis.[44] On the other hand, the conformational changes of all enzyme complexes occurring during the catalytic cycle of *Escherichia coli* dihydrofolate reductase will affect the magnitude of the electrostatic effect of active site microenvironments as well.[45]

1.3.3 EEFs can affect the regioselectivity and stereoselectivity

Controlling selectivity is the significant challenge for the development of any efficient chemical synthesis. The selectivity of an irreversible reaction is determined by the relative magnitudes of competing activation barriers, and consequently it is defined by the chemical structures of the reaction components. Therefore, numerous efforts to control selectivity have traditionally involved altering structural features. Identifying structural features that can influence selectivity can, however be extremely challenging. In principle EEFs could also be used to control selectivity through field-dipole interactions; this concept is particularly appealing because specific molecules and transition states have unique interactions with EEFs.[35]

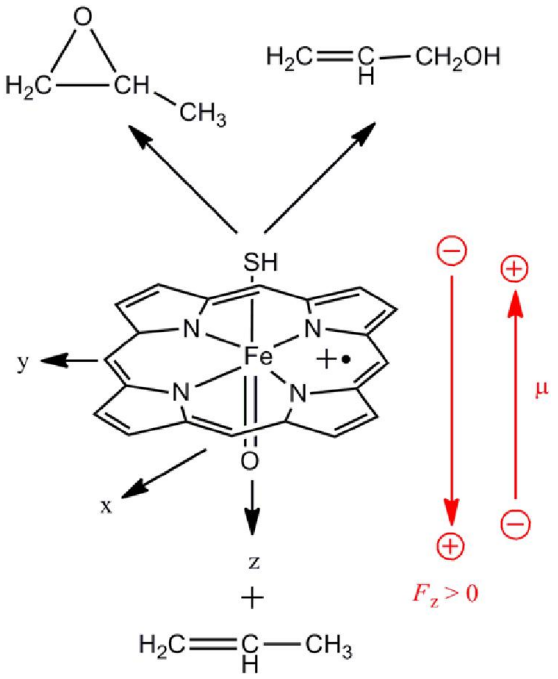

Figure 1.2 EEFs control the selectivity of a nonpolar reaction. When the direction of the electric field is oriented along the negative *z* axis (i.e. S-Fe=O), it will catalyze the epoxidation of propene. Reversing the field direction will favor propene hydroxylation. (This Figure is adjusted from Ref. 4 and 47, note; Shaik defined the direction of an EEF using the Gaussian convention which is opposite to the physics concept, i.e. positive is for the orientation of a negative test charge).

There are very few existing methods for the direct oxidation of some nonpolar aliphatic compounds; most known strategies are non-selective and, as a result, of limited scope. Following the content in Section 1.3.3, an electric field can predictably

drive selective bond activation of biomimetic reactions mediated by cytochrome P450, namely oxidation of nonpolar alkenes, and the catalyst itself shows no selectivity under zero electric field. QM/MM studies predict that EEFs could induce absolute chemical selectivity that can be controlled at will. As shown in Figure 1.2, reversing the direction of the external electric field along S-Fe=O axis of the enzyme cytochrome P450 is predicted to drive the system toward completely selective C-H bond hydroxylation ($F_z > 0$) or completely selective C=C epoxidation of propene ($F_z < 0$).[46] VB modelling of the above two reactions further demonstrated that the direction of the electric field will be responsible for the charge transfer either from propene to enzyme cytochrome P450 ($F_z < 0$, transition state dipole stretches from the positively-charged propene to the negatively-charged thiolate) or from thiolate to propene ($F_z > 0$, transition state dipole stretches from the positively-charged thiolate to the negatively charged oxo-ligand), leading to complete epoxidation or complete hydroxylation, respectively.[47, 48]

Computational practices in Figure 1.2 also indicate that the electric fields along the x and y axes can induce greater dipoles than those produced when the electric field is along the S-Fe=O axis and perpendicular to the porphine ring. However, applying electric fields along the x and y axes does not impart significant selectivity, which is due to higher selectivity for the transition states while changing dipoles in the z-direction as well as stable dipoles induced by x and y axes oriented fields between reactants and transition states. Shaik' et al therefore summarized that the effect obeys the following selection rule: the orientation of an EEF aligned along the axis where the electrons flow will lower the energy of transition states and selectively catalyze the reactions; this concept is referred to as the "reaction-axis" rule. Furthermore, this rule is also applied to regulate the hydroxylation rate of robust C-H bonds in cyclohexane by a non-heme iron-oxo complex.[49] It is known that $TMC(SR)Fe^{IV}O^{+}$ cannot really abstract a hydrogen from a poor electron donor like cyclohexane but can only react with weak C-H bonds like those in 9.10-dihydroanthracene. Density functional theory (DFT) calculations show that the H-abstraction barrier of cyclohexane molecules in the absence of an electric field is 11 times higher than that case when an EEF oriented in the negative direction of z axis is turned on, and the significant rebound barrier has

vanished as well. The application of an EEF will improve the rates of both H-abstraction and rebound step, and lead to the rate-controlling step being changed from the rebound step to the H-abstraction step. As such, one is able to predictably tune the reactivity of a synthetic non-heme iron-oxo species towards manipulating the rate and stereospecificity of a C-H bond activation by switching an EEF on/off, based on the "reaction-axis" rule.

In parallel to assessing EEF effects on the catalytic oxidation of small hydrocarbons, scientists will also expand the scope of "electrostatic catalysis" to the fine chemicals manufacturing. The recent computational data demonstrated EEFs are capable of tuning both the rate and *endo/exo* selectivity of a Diels-Alder reaction;[50] the intriguing features are that catalysis/inhibition of the reaction involves EEFs along the "reaction axis", while manipulation of products' *endo/exo* stereoselectivity is relevant to EEFs oriented perpendicular to the "reaction axis" in the direction of the individual molecule's dipole moments. The VB diagram model is used to further validate the selection rule for electric field effects on Diels-Alder reactions. A reaction was thought to be independent or little affected by a reactive environment (i.e. solvents), however, the computational results showed that the mechanism of a Diels-Alder reaction in DCM is changed to stepwise from concerted with increasing electric fields, while the mechanism always maintains concerted in a gas-phase. In addition, unlike the example of Diels-Alder reactions, most reactions are asymmetric and the reactive axis may be not well defined, hence requiring a viable treatment of solvents effects for quantum calculations and molecular dynamic simulations in the presence of EEFs. For example, a recent report shows the role of solvents in changing the regioselectivity of Au(I) – catalyzed hydroarylation controlled by electrostatic effects, emphasizing that the interactions between the ion-pair complex and the solvents contribute to the energy difference between transition states.[51]

1.3.4 More electrostatic effects on chemical changes

The above-mentioned theoretical studies highlight that not only does an oriented EEF along the reaction-axis allows chemists to accelerate/retard nonpolar reactions and

control their selectivity paths at will, but also to inhibit/catalyze the entire catalytic cycle of enzyme P450 by only flipping the direction of the external electric field along the reaction axis. There are also a wide number of other chemical changes caused by an EEF. For example, Coote et al. reported that the stability of nitroxide radicals can be changed by 3-4 orders of magnitude by using localized EEFs, due to remotely charged functionalized groups, whilst the Boxer's group published a series of papers illustrating that the electron-transfer reactions are promoted by EEFs.[12, 52-57] Importantly, the promotion of electron transfer in this way was further expanded to between surfaces[58], between molecules confined on surfaces[13, 59], and even in molecular devices[60-65]. Other theoretical works suggest that EEFs can affect the interactions of molecules and surfaces[66, 67], catalyze the proton transfer[68-70], modify biologically the structure and reactivity of *S*-nitrosothiols,[71] control the metal-ligand binding,[29, 72] and even regulate the formation of amino acids. In the light of these previous studies, this thesis reviews a few cases of substantial theoretical progress in EEFs-controlled chemical changes. Nonetheless, developing efficient protocols to enable EEFs to become real catalysts is still an extremely challenging domain. Limited experimental progress based on the electrostatic-effect will be reviewed in Section 1.4.

1.4 Experimental evidence of electrostatic effects

This section begins with a question. Why is electrostatic catalysis less developed in conventional synthetic chemistry but largely applied in enzymes-catalyzed biological reactions? This is because electrostatic effects are strongly oriented and are progressively attenuated with increasing polarity of media, but the solubility of charged residues is poor in non- or less-polar solvents.[23] In contrast, enzymes-involved reactions overcome these flaws by creating an oriented local electric field with charged species within a low-polarity active site[37]. In chemical systems, it is not uncommon that some experimental results have confirmed that electrostatics can affect isomerization reactions[1, 19, 20], tautomerization processes[73], and redox systems[13-15, 54]. However, extending electrostatic catalysis to a range of chemical reactions, but not limited to redox systems, is arguably the principal challenge while considering how to balance the

trade-off between solubility of charged species and magnitude of electric fields.

Inspired by the working principles of enzymes-catalyzed biological reactions, one can create a local electric field by using charged functional groups grafted onto the substrate. A few pioneering theoretical studies have predicted that electrostatic effects in principle could affect the stabilities of chemical species by destabilizing or stabilizing charge-separated resonance contributors.[22, 23, 46, 50] For example, Coote and co-workers discovered that delocalized radicals like nitroxides are massively stabilized by a negative charge located on an acid/base fragment (carboxylate, phosphate, sulfate, alkoxide). In other words, when a remote negatively charged functional group is anchored to the opposite of the N-O$^{\bullet}$ radical, the electrostatic stabilization of this neutral contributor leads to further stabilization of the species.[22, 23] The possibility of this stabilization arises because the resonance-stabilized radicals are more polarizable than non-resonance ones; so they can effectively redistribute electron density away from negative charges in order to minimize repulsion. Moreover, given that transition states tend to be more delocalized than reactants and products, the introduction of a negative charge or electric field should in principle catalyze the reaction, assuming no other effects are interfering. In order to ensure the progress of these reactions, there is a requirement to adjust the orientation of EEFs with respect to the approaching reactant; the percentage of resonance forms increases, leading to the overall stabilization of the molecule or transition state, which means that the kinetics and thermodynamics of non-redox chemical reactions possibly can be manipulated with EEFs.

Coote's group subsequently gave the experimental proof of the C-O bond-dissociation free energy of their carboxylated radicals switching by pH-induced orbital conversion. The results suggest that deprotonation of the carboxylic group weakens its C-O bond, promoting the dissociation of this chemical bond by as much as 20 kJ mol^{-1} in the gas phase at 25 °C, as compared with protonated or non-substituted forms.[22] Therefore, the electrostatic effect affords another significant ability as a 'pH switch' of radical stability. They used fluorescence spectroscopy to demonstrate significant pH-dependent electrostatic effects on the kinetics and thermodynamics of H atom transfer between a hydroxylamine and a profluorescent nitroxide. The results suggest that the

bond dissociation energy (BDE) is effectively decreased by half in low-polarity solvents such as dichloromethane,[2] however, the stabilizing interaction between a remote negative charge and stable radicals is completely lost in polar solvents.[74] Thus, one can imagine the possibility of designing some 'switchable' compounds through understanding the fact that the electrostatic effect is influenced by the stable radical species and properties of the explicit environment (i.e. electrolytes and solvents). For example, the ability to lower the BDE of a C-O or H-O bond through deprotonation of a remote carboxylic group (i.e. adjusting the pH of electrolyte systems), can be applied to manipulate the release/trapping of radicals in synthetic applications such as Diels-Alder reactions.[75]

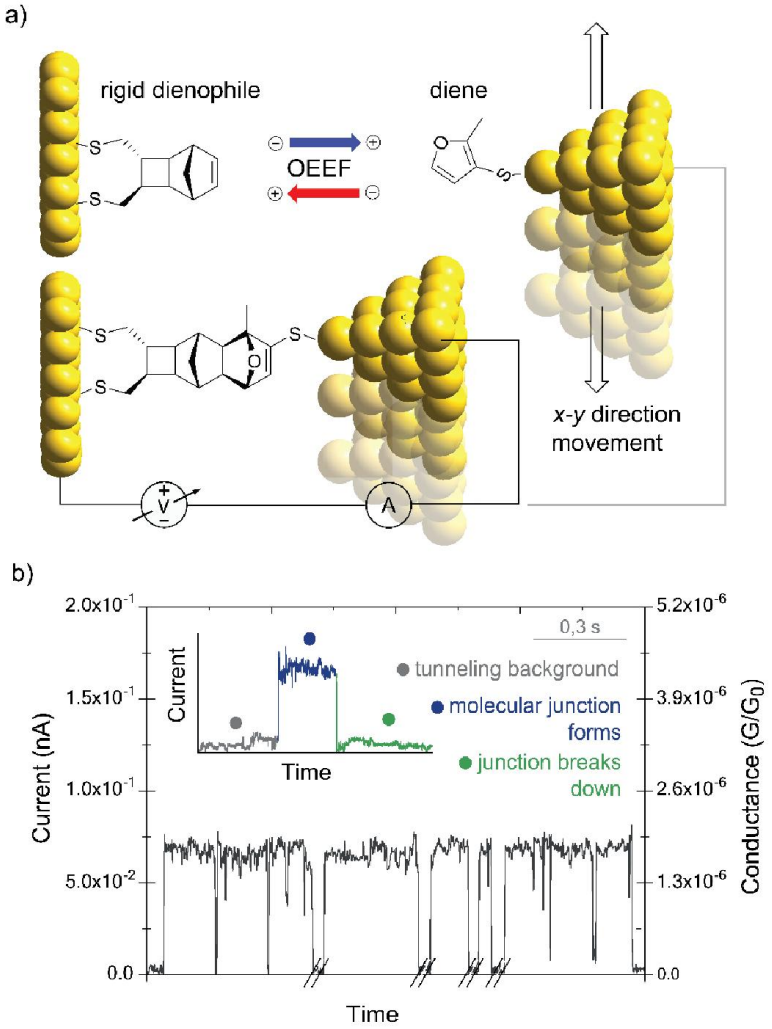

Figure 1.3 Electrostatic catalysis of a Diels-Alder reaction. a) The STM-BJ set up used to study the effect of an EEF on the rate of Diels-Alder reactions. b) Current indicatives of the formation and break of conduction junctions with time.

Yet, electrostatic effects derived from charged chemical species are only harnessed in limited reactions; manipulating in a tunable way a much wider range of reactions need to address the directional and magnitude issues of EEFs (vide supra). Surface chemistry provides a promising platform for immobilizing at least one of the reactants to build a favorable "reaction" axis. Aragonès et al. reported an unprecedented effect with the first experimental evidence that an oriented electric field can catalyze the Diels-Alder reactions.[3] They indeed developed a surface model system with advanced STM-BJ technique, which allows one to easily control the orientation of EEFs along the reaction axis as well as to make electric field stimuli effective in a nonpolar environment. As can be seen from Figure 1.3, when an oriented electric field stimulus is delivered across the diene and dienophile by imposing a voltage difference between a gold tip and gold surface, the rate of the electron transfer between these two molecules will be promoted, due to the formation of a conduction junction. The occurrence of this reaction is essentially due to the fact that electric fields are capable of stabilizing a minor charge separated resonance contributor of the transition states by lowering the energy. More importantly, their experimental results validate the previous prediction, showing a highly qualitatively consistent with the quantum chemical calculations.[50]

Similarly, this thesis work employed wet chemical routes to prepare surface monolayers (in particular on the semiconductor interfaces) for fixing reactant molecules within the electric field (i.e. electric double layer), to experimentally investigate the electrostatic effects on some chemical systems in a preparative scale. The following section will survey some essential items used in the experiments with the aim of conveying the purpose of this thesis.

1.5 Main objectives in this thesis

1.5.1 Nitroxides and alkoxyamines

Nitroxides and related persistent organic free radicals are known to possess excellent stability, so that they can be regarded as exceptionally good synthetic and functional tools to solve many problems in chemistry, physics, biology and biomedicine that take advantage of a great number of unique chemical and physical properties associated with

an unpaired electron.[76] The most prominent member of this class of compounds is 2,2,6,6-tetramethylpiperidine-1-oxyl (TEMPO). Because of their excellent stabilities in both aqueous and organic electrolytes, and intrinsic paramagnetic properties, TEMPO and its derivatives have attracted a lot of attention in different fields. Well-known applications are reported: in organic synthesis/electro-synthesis as catalysts[77-81], in biology and chemistry as spin labels/probes[82], in molecular magnetism as building blocks[83, 84], in medicine as antioxidant and imaging contrast agent[85, 86], in energy (organic radical batteries) as active electrode materials[87-89], and in material science (nitroxide mediated radical polymerization, NMP) as a mediator[90, 91].

Among these applications, it is known that until presently, much research have extensively contributed to the design TEMPO monolayers for electro-catalytic oxidations. Kashiwagi and coworkers prepared a TEMPO modified graphite felt electrode coated by poly(acrylic acid) for electrocatalytic oxidation of amines to nitriles.[92] They also provided two valuable electrochemical solutions for enantionselective oxidation of amines and alcohols by using: a gold electrode modified with a chiral nitroxyl radical-terminated self-assembled monolayer, and a graphite felt electrode modified by TEMPO in the presence of chiral sparteine, respectively.[93, 94] Recently, Sigman's group found that the electrocatalytic activity towards several biologically available alcohols can be dramatically enhanced when TEMPO is covalently immobilized onto linear poly(ethylenimine) followed by cross-linking onto a glassy carbon electrode surface.[95] Heterogeneous systems involving anodic regeneration of TEMPO oxoammonium proposed by Belgsir et al. were applied to oxidize carbohydrates on Nafion-TEMPO modified graphite felt electrodes.[96] Megiel et al. devised a promising system for electrocatalytic oxidation of benzyl alcohol using gold electrode surface nanostructured with gold nanoparticles coated with TEMPO radicals, which is more efficient than that achieved with electrode modified with TEMPO monolayer directly linked to the gold surface.[97] However, few works have been devoted to devise and explore the redox response of the TEMPO monolayer itself, resulting from the limited electrode materials and difficulty of preserving the unpaired electron (open-shell state) upon modification. Therefore, my first experiment (Chapter

3) uses a chemical route to tether TEMPO molecules onto a silicon semiconductor electrode, followed by investigations into the electrostatic effect (either from the electrolytes side or from semiconductor space charges side) on the redox response of self-assembled TEMPO monolayers.

When it comes to alkoxyamines, they are a class of alkylated nitroxide compounds, being synthesized by the trapping of carbon-centered radicals with persistent nitroxide radicals.[90] They can be considered as valuable precursors for industrial polymerization[91, 98], design of smart materials[99-102] and radical chemistry[103-106], as well as a means of opening up new perspectives of application in biology and medicine (in other words, such molecules can be applied as therapeutic agents, and they can be tuned so that either the therapeutic activity of alkyl radicals or the diagnostic property of nitroxide radicals is favored.)[107, 108]. However, they require relatively high temperatures (ca. 80-120 °C) to trigger their homolytic process, with some unfortunate consequences of unwanted side reactions occurring.[109] Therefore, the need of milder stimuli other than heat for decomposing alkoxyamines have motivated chemists to explore new trigger sources.

There have been some approaches for triggering alkoxyamine homolysis at room temperature where the molecules would otherwise be stable. An example is high energy irradiation stimulus which can also trigger the homolysis of alkoxyamine molecules for initiating NMP,[110-113] but is not suitable for biological and medicine applications due to possible carcinogenesis.[108] Further, Marque et al. published a series of papers about the possible activation/deactivation of the alkoxyamine C-ON bond homolysis based on chemical changes, in particular the appealing effect of protonation on the alkoxyamine lysis,[114-116] where these reactions in fact are controlled by remotely charged groups. From previously reviewed literature, it can be concluded that the electric field from the remote negatively charged functional groups could dramatically lower the BDE of alkoxyamines and facilitate their homolysis at temperatures lower than otherwise possible.[2, 22, 23, 117] The catalytic effect is delivered by the charges of ionized functional groups and can therefore be predictably adjusted according to pH (the pH effect is, in principle, electrostatic and highly oriented[22]).[2, 23, 118, 119] The kind of electric fields

created by local charged species can change the degree of charged-separated resonance contributors (i.e., $N–O^{\bullet} \leftrightarrow N^{+\bullet}–O^{-}$) and hence the extent of stabilization of the nitroxide. This ultimately leads to electrostatic catalysis of a reaction involving such "switchable" nitroxides, including alkoxyamine dissociation and hydroxyl amine hydrogen transfer. Some successful cases have been reported on pH-driven homolysis of alkoxyamines at ambient temperature where the molecules would otherwise be stable.[2, 120]

The electrostatic effect is greatest in the gas phase but, however, it progressively diminishes with the increase of solvent polarity. Although pH-induced electrostatic catalysis is possible in solvents of poor polarity, the limitation of low solubility of charged species will impede its practical applications. What needs to be addressed is: how to balance the discrepancy between solubility and magnitude. Another problem that is encountered is: how to control the orientation of C-ON bonds in alkoxyamine molecules to align with the field stimulus. In Chapter 5, these issues are addressed by devising a molecular circuit with the STM-BJ technique which allowed the imposition of an external potential between the STM gold tip and gold substrate for catalyzing C-ON bonds homolysis of alkoxyamine molecules. The same setup had been used to confirm that an EEF can accelerate/catalyze the C-C bonds formation in the Diels-Alder reactions.[3] Summing up, electrostatically controllable C-ON homolysis of alkoxyamine molecules will present a new perspective for their future development in different fields: being much less hazardous than conventional thermal- or irradiation-triggered homolysis.

1.5.2 Silicon semiconductor electrodes

As discussed above, the work described in this thesis is mainly intended for devising a surface model to explore the electrostatic catalysis effect. Therefore, selection of proper electrode substrates is of crucial importance for the successful implementation of studies in this work. Some of the most prominent materials including metals, alloys, semiconductors, carbons, conducting polymers have, so far, been used as electrode substrates for the development of sensors, supercapacitors, solar cells, molecular electronic devices, and so forth. Among these solid electrodes, semiconductors, and in

particular silicon electrodes, present unique potential in a variety of advanced fields, for example, the semiconductor silicon is still promoting the rapid development of electrochemistry[121-124], molecular electronics[125-129], quantum computing[130, 131], and spintronics[132-134]. The major reason why a silicon electrode was selected is the photoelectrochemical properties of the semiconductor-electrolyte interface while addressing surface chemical issues; in other words, the flow of electrons/holes in the semiconductor following exposure to light radiation. The electrochemical issues of silicon substrates as well as some fundamental concepts in semiconductors will be briefly introduced below for the reader to understand how the electrostatic studies in this thesis actually work on silicon surfaces.

1.5.2.1 Electronic structures of semiconductors

People can appreciate the difference between semiconductor electrodes and metallic electrodes by studying the electronic distributions inside these materials. The conducting properties of semiconductor materials can be deliberately altered by introducing "doping" impurities into their crystal structures. These extrinsic semiconductors are classified as either n-type or p-type with regard to the doped impurities; hence producing electron conductivity with electron donors, or holes conductivity with electron acceptors, respectively. In order to gain insight into the conductive mechanism of semiconductor materials, one is able to understand the electronic structure of these solids from the energy bands theory (i.e., atomic orbitals). As a result of small spacing distances between neighboring atomic orbitals within a given energy band, it is a convention to treat the band as a continuum of energy levels. The energy bands for describing electrons occupancy are constituted of fully or partially filled energy levels (allowed bands) and no energy levels (forbidden bands). In semiconductor materials, as can be seen from Figure 1.4, the highest occupied energy bond and the lowest unoccupied energy bond are referred to as the valence band and the conduction band, respectively. These two bands are separated by a forbidden band gap which determines the conductive properties of semiconductor materials. The most relevant parameters to the energy levels in a semiconductor are: the conduction band

edge E_C, valence band edge E_V and the Fermi level E_F. The E_F is used to characterize the equilibrium distribution of carriers (electrons or holes) in the energy bands.

Electrical conductivity in a semiconductor arises from the presence of partially occupied orbitals, allowing delocalized electrons to transport between states. Importantly, heat and light can provide energy to promote some electrons in the valence band across the band gap to partially fill the states in the conduction band. An intrinsic semiconductor, however, probably behaves less satisfactorily while involving some applications. One appealing feature of semiconductors is that their conductivity can be increased by introducing some types of elements (i.e., doping method) into them; where these doping elements can determine the charge carriers of prepared extrinsic semiconductors, namely, the charge carriers of doped semiconductors are dominated by dopant species. The extrinsic semiconductors are referred to as either n-type with electrons as charge carriers, or p-type with holes as charge carriers. Within an intrinsic semiconductor, the E_F lies in the middle position of the band gap, whereas doping impurities can change the distribution of electrons and increase the number of partially occupied states, hence change the E_F position. For example, the E_F level is close to the conduction band and valence band in n-type and p-type semiconductors, respectively.

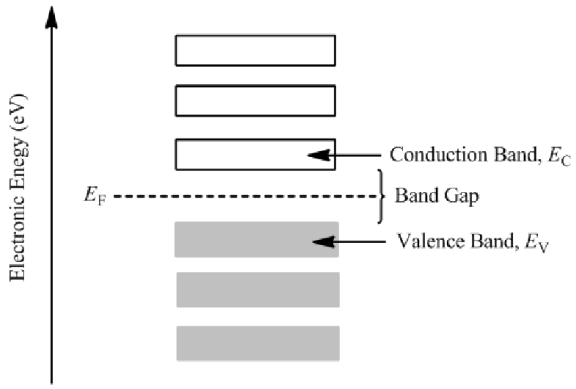

Figure 1.4 Filling of electronic states in intrinsic semiconductors at equilibrium.

1.5.2.2 Energy levels at the semiconductor/electrolyte interface

The electrochemistry of semiconductor electrodes behaves significantly differently in many aspects from the electrochemical processes occurring at conductor surfaces, resulting greatly from specific electronic structure within semiconductors. Some

concepts concerning the interface between a semiconductor electrode and an electrolyte solution is introduced below for the better understanding of the semiconductor electrode reactions. Generally, characterization of the energy level of a diffusive system is performed by calculating the redox potential (E_{redox}), which affords information on the ability of redox species of accepting and donating electrons. In Chapters 3 and 4 in this thesis, the two phases will tend to be in equilibrium (i.e., $E_F = E_{redox}$), when immersing modified silicon electrodes into electrolyte solutions, by the movement of electrons between solid electrodes and electrolytes. The excess charges in the semiconductors do not reside at the surface, but will extend into a region near the surface defined as the space charge region with a significant distance of approximate 10-1000 nm. For instance, while connecting a n-type semiconductor electrode to the three-electrode system (Figure 1.5), the Fermi level E_F is generally higher than the redox potential E_{redox} of the electrolyte and therefore the electrons will leave semiconductor electrodes to transfer to the electrolyte solution. The results are reflected in an electron-depleted positively charged space charge region and upward bent energy bands. A reversed phenomenon is observed in the case of p-type semiconductors; electrons are transferred from electrolyte solutions to the electrodes, leading to the formation of a holes-depleted negatively charged space charge region and hence causing a downward bending of the energy band. In addition, the formation of a space charge region will create an internal electric field inside the semiconductor, and an electric double layer between the electrode surface and electrolyte solution is also established in the solution side. These two electric double layers play key roles in the investigations of the electrostatic effect in this thesis; more details on them are introduced below.

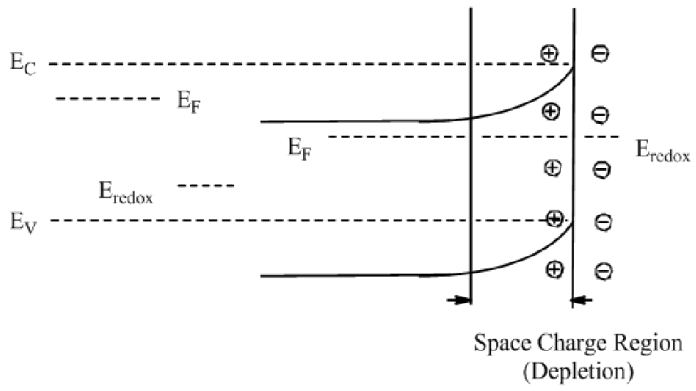

Figure 1.5 The changes of energy bands for an n-type semiconductor before and after immersing it into an electrolyte solution.

Apparently, the direction of the band bending depends on the charging species (i.e., electrons or holes) of the space charge region. However, an external applied potential can affect the direction and extent of band bending as well as band edges in the semiconductor. The space charge region can be classified into two types as per the magnitude of applied potentials. To account for the charges distribution and bands bending in these three cases, a potential called flat band potential (V_{FB}) need to be firstly defined, which is an important parameter used to connecting the energy levels of charge carriers in the semiconductor with the redox species dissolved in the electrolyte. When the Fermi energy level (E_F) is aligned with the solution redox potential (E_{redox}) with a certain external potential, leading to no charge transfer between electrode and solution and no band bending phenomenon (i.e., no space charge region), the potential is then referred to as the V_{FB}. Figure 1.6 illustrates the shifts of Fermi level position and the directions of band bending with different applied bias in an n-type semiconductor. While imposing a potential more positive than the V_{FB}, the electrons in the space charge region are forced away from this region and leave behind positive holes in the depleted region. The region is therefore referred to as the depletion region in this situation. Conversely, if an n-type semiconductor is biased towards potentials more negative of the V_{FB}, the majority carriers (electrons for an n-type semiconductor) are accumulated in the space charge region, which is then referred to as the accumulation region. In a p-type semiconductor, the accumulation and depletion regions are observed in which applied potentials with opposite tendency are imposed with respect to those of an n-type semiconductor case. Importantly, the performance of the charge transfer in semiconductor materials relies on whether the space charge region is in the accumulated or depleted state. The behavior of a semiconductor is similar to a conductor (i.e., metallic electrodes) if there is an accumulation region. In contrast, the charge transfer is largely limited or inhibited in a depletion region due to few charge carriers. However, the electrons in the semiconductor electrodes can be promoted to different energy levels under an illumination stimulus, leading to recombination of electrons and formation of

holes; on the other hand, the kinetic barrier is probably removed in the space charge region, allowing some reactions to occur. The charge separation of space charge regions will be highlighted in Section 1.5.2.3.

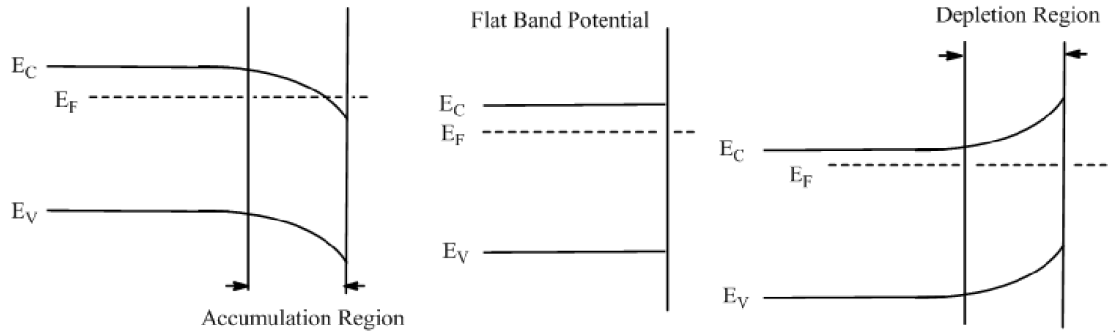

Figure 1.6 Effect of varying the external applied potentials on the Fermi level position and directions of band bending in the n-type semiconductor.

1.5.2.3 Photo-effect and electric field in depleted regions

Earlier, for this thesis work, the reason given for selecting a semiconductor (in particular, the silicon electrode) as surface model was the excellent photoelectrochemical property in the electrode-electrolyte interface. In general, when a semiconductor sample is illuminated with a light of energy larger than the energy gap between conduction band and valence band, the electrons in the valence band are then excited to the conduction band and leave behind an equal number of holes in the valence band. These generated electrons and holes in the interior of semiconductors recombine with the production of heat and emission of light. Similarly, this photo-effect also occurs in the depletion region with pronounced separation of charge carriers under a generated internal electric field. Take an n-type semiconductor as example, when an external potential greater than V_{FB} is applied to the semiconductor electrode, then energy bands in the space charge region bend upwards, a negligible current is measured in the dark condition. However, an obvious photocurrent is observed upon illumination, and simultaneously the formed internal electric field in the depleted region will separate the electrons from holes, that is, the holes move toward the interface, and electrons migrate to within the bulk of the semiconductor. Importantly, the holes close to the interface are high-energy species which will cause the reduction of redox species by extracting electrons from the

electrolyte solution; therefore, the n-type semiconductors can act as photoanodes under illumination. Based on the same analysis methods, the p-type semiconductors can be regarded as photocathodes.

In summary, the kinetics barrier of depleted dark semiconductor electrodes can be effectively controlled, or even removed, upon illumination with different energies; in particular, the formed internal electric field in the space charge region of semiconductors can predictably tune the electrochemical behavior of redox species attached to the electrode surface, hence revealing the electrostatic aspect in the semiconductor electrochemistry.[124] Relevant experimental evidence on this aspect will also be discussed in detail in Chapter 3. Notably, several important parameters/concepts (i.e., Fermi level, flat band potential, photocurrent, energy band) in semiconductor chemistry are constantly mentioned above, however, not much information will be provided on how to measure these parameters and to explain their relationship, because this thesis work is focused on the electrostatic effect on the chemistry. More knowledge on semiconductor (photo)electrochemistry can be found in many text books.[135-137]

1.5.2.4 Electric double layer

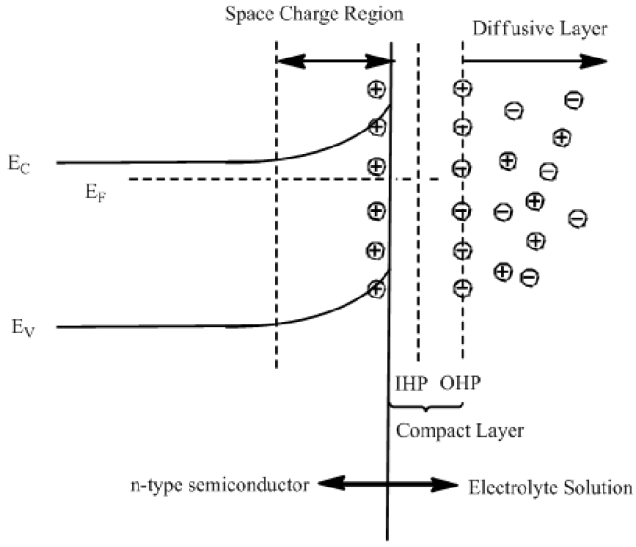

Figure 1.7 Helmholtz model illustration of the electric double layer in the n-type semiconductor/electrolyte interface at a depleted condition.

While discussing the internal electric field in the semiconductor, an associated external electric field (i.e., electric double layer) is also established between the solid electrode

surface and electrolyte solution. In fact, it is not possible to remove the electrostatic effects created by electric double layers when dealing with interfacial electrochemistry, regardless of whether the surfaces have been deliberately electrified or not. Figure 1.7 illustrates an electric double layer model in the n-type semiconductor/electrolyte region. Obviously, the solution side can be divided into a compact layer and a diffusive layer. The former in this model consists of two regions, the inner Helmholtz plane (IHP) which passes through the centers of the surface charged molecules, and the outer Helmholtz plane (OHP) lies at the position where solvated ions are the closest approach to the electrode surface. The diffusive layer extends from OHP to the bulk solution. The interest in this thesis is focused on the compact layer due to strong electrostatic forces and its major effect on electrode reaction kinetics, its structure (magnitude and/or thickness) which depends largely on the intrinsic conditions of the solid electrode-electrolyte system such as doping level of the semiconductor, electrolyte concentration, ions species. Take the Debye length formed near the electrode surface as an example, its length is gradually increased with decreasing electrolyte concentration (Figure 1.8), whereas the electrostatic magnitude within the Debye length relies largely on the distance from the electrode surface; that is, the size of the electrostatic effect is larger when closer to the electrode surface.

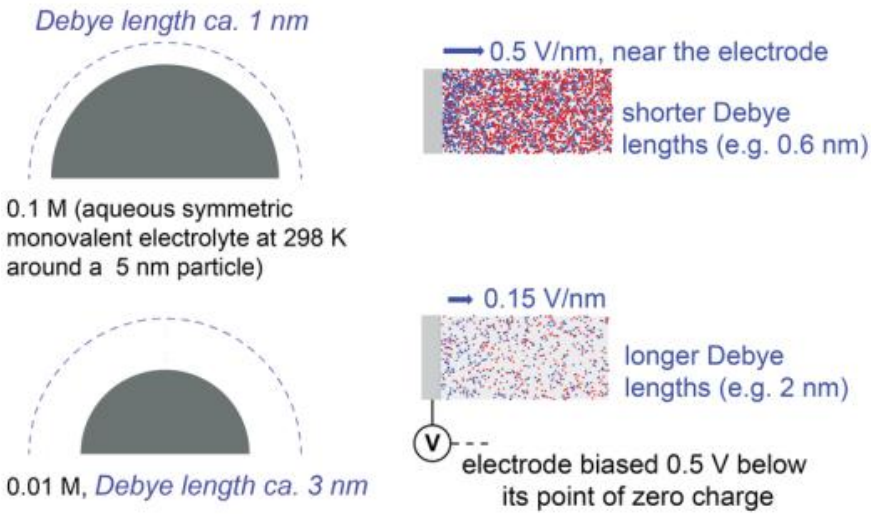

Figure 1.8 The dependence of electrostatic magnitude near the electrode surface on the electrolyte concentration and Debye distance.

In this thesis, in Chapter 3, the electrostatic interactions between oxoammonium

films and electrolyte anions are used to manipulate the oxidizing power of nitroxide monolayers, on the other hand, the dependency of electrode reactions on electric double layer (effect of solvents and anions) is also detailed in Chapter 4. In addition, the production of surface states from tethered molecules can redistribute the charges in the depletion region and hence influence the internal electric field in the semiconductor.

1.5.3 Preparation of monolayer films on silicon surfaces

A surface model provides us with an efficient strategy to address the orientation of EEFs with respect to reactants as well as balance the issue between solubility of charged species and magnitude of EEFs. Silicon electrodes/chips have already become the backbone towards the development of modern intelligent industry such as microscale devices,[138-142] hence intensive research into the surface chemistry of silicon electrodes has gained widespread attention and been reported in a systematic framework.[121, 143-146] When it comes to preparing chemically well-defined organic films on silicon electrodes, there are numerous protocols available to attain Si-C, Si-O and Si-N bound layers. In this thesis work, in particular, the main interest for silicon surface modifications is covalent attachment of Si-C bonds on a non-oxidized silicon surface (i.e., hydrogen-terminated silicon) by reacting with alkene molecules; this process is known as hydrosilylation. To obtain the Si-C linked monolayers, the native silicon oxide layers on silicon substrates typically need to be passivated with either fluoride-containing solutions, sodium hydroxide or ultra-high vacuum (UHV) technique, leading to the formation of hydrogen-terminated silicon surfaces. Different etching agents will cause changes to the hydrogen-terminated silicon configurations (mono-, di- and tri-hydrides) and microscopic morphology (smooth or rough atomically). For example, the single crystal Si(100) orientation wafers used in this thesis, are atomically flat and coated with a dihydride model while treating with 40% aqueous NH_4F;[147, 148] but the resultant hydrogen-terminated Si(100) are microscopically rough with mono-, coupled mono-, di- and tri-hydride mixture upon diluted HF treatment.[149] Si-H passivation as an appealing starting point of silicon surface functionalization because of easy preparation,[150] short-term tolerance to air and water,[151-154] inert reactivity towards some

common organic solvents.[155-161] These characteristics allow for covalent attachment of organic layers on silicon substrates by wet chemical routes.[162]

A wide variety of methods have so far been established for hydrosilylation processes involving insertion of unsaturated molecules (i.e., alkenes and alkynes) into Si-H bonds.[121, 145] The first experiment on the preparation of Si-C bound monolayers on non-oxidized Si-H surfaces was carried out by Linford and Chidsey in 1993.[162] Subsequently, they proposed a radical mechanism that the monolayers were yielded by the initiation of diacyl peroxides under a thermal condition (100 °C).[154] In contrast, Cidsey and co-workers also investigated the thermal hydrosilylation process in the absence of diacyl peroxides, indicating the formation of a poorer surface coverage. In Chapter 3 of this thesis, attachment of 1,8-nonadiyne to Si-H surfaces was achieved by thermal triggered hydrosilylation under neat conditions. Similar to the case with thermal induction, photochemical irradiation can also promote hydrosilylation of unsaturated compounds via homolytic cleavage of Si-H bonds. This method can be accomplished by both UV light[163, 164] and white light[165] at room temperature and therefore avoid thermally damaging modified molecules and silicon surfaces. Further, one can produce different images while photopatterning the electrode surfaces.[166] The light-mediated hydrosilylation of 1,8-nonadiyne is presented in Chapter 5. On top of these two approaches, hydrosilylation unsaturated alkenes and alkynes can take place by mediating with metal complexes[167-170], Lewis acid catalyzing reactions[171, 172], reacting with alkyl/aryl carbanions/direct attachment of alkyl Grignard reagents[173, 174], electrochemical reduction of diazonium[175-179] as well.

1.5.4 STM-BJ technique

Another surface model that was used in this thesis (Chapter 5) for conveying an electric field stimulus was constructed by the STM-BJ technique. This approach allowed us to bridge an individual molecule between an electrode tip and an electrode substrate where an electric circuit can be immediately formed. For better understanding of the working principles of the STM-BJ technique, a brief introduction about this method is presented below.

Many miniaturized devices wiring tailored molecules as conductive components have been devised and extensively employed in such microelectronic devices as molecular wire[180], rectifier and diode[181, 182], transistors[183, 184], switches[185-187], and sensors[188-190]. Measuring and controlling the electrical current of individual molecules is essential to the development of molecular-scale electronic devices.[191] It also affords an understanding of charge transport occurring in ubiquitous chemical and biological processes, and even to identify electronically chemical information of a single molecule, at an atomic-level basis. Common approaches have been used to make: molecular junctions and probe their electrical properties by STM-BJ,[192, 193] mechanically controllable break junction,[60] and conducting atomic-force-microscopy break junction.[194] In particular, the STM break junction technique has evolved into a versatile tool in electrostatic-catalysis of molecular-scale synthesis[3] as well as in modern nanoelectrochemistry for studying electron transport across single molecules[195].

In order to precisely measure and control electron transport of a molecule, one must first connect it to both a STM electrode tip and an electrode substrate, and the junction current response is measured as a function of bias voltage. Considerations for building efficient and reproducible electronic coupling contact between molecules and electrodes highlight the need to synthesize functionalized molecules with proper anchoring groups residing at two ends of the molecules. Apart from the robust connect (anchoring group effects),[196, 197] the measured conductance is also dependent on electrode substrates[128, 198], redox states of molecules[199, 200], solvents[201, 202], pH[203], even temperature[204, 205] and so forth[206, 207]. Precisely understanding how these factors affect the single molecule conductance, one is not only able to reconcile these discrepancies that exist between theoretically predicted conductance values and those measured experimentally, but also accelerate the development of molecular-devices by employing purpose-designed molecules with excellent optical, magnetic, thermoelectric, electrochemical, chiral recognition properties; which is an alternative complementary regime to the silicon-based microelectronics.

1.6 Thesis outline

Some fundamental concepts/items relevant to this thesis have been introduced in some detail above. The entire thesis work has been achieved and completed through electrochemical techniques with complementary further validations via simulations and calculations. This work aims mainly at studying the electrostatic effect on chemistry. A brief introduction for each chapter of this thesis is presented below:

Chapter 2 describes the experimental procedures and techniques routinely used throughout this thesis work. Chapter 3 deals with the effect of electrostatic interactions between grafted oxoammonium and electrolyte anions or space charge in the semiconductor on the electroactivity of persistent nitroxide monolayers. In addition, kinetic and thermodynamic analyses on electrode reactions are also partially documented in dark and under illumination conditions. In Chapter 4, one electron oxidation of an alkoxyamine leads to a cation radical intermediate that even at room temperature, where it would be otherwise stable, rapidly forms a nitroxide and a carbocation in diffusive systems. Simultaneously, anodization of a surface-tethered alkoxyamine shows gradual appearance of a TEMPO signature upon positive bias, and its coverage is a function of anodization time. High level quantum computations indicate that this lysis process is energetically unfavorable while not considering the explicit environment, namely electrolyte anions and solvents. Chapter 5 quantifies the magnitude of the electric effect on lysis of alkoxyamines, opening up a promising portal for development of an electrostatic switch to control molecule homolysis and/or polymerization on an electrified interface. An example of electrochemical conversion of alkoxyamine interfaces to redox monolayers by trapping of ferrocenemethanol nucleophiles is illustrated in Chapter 6, highlighting the renaissance of organic electrosynthesis on surfaces as well as laying the foundation to a new form of electrochemical lithography. Based on recently published experimental evidence on electrostatic catalysis, a future work framework, ranging from fundamental research to molecular devices design, is outlined in Chapter 7.

1.7 Reference

(1) Gorin, C. F.; Beh, E. S.; Kanan, M. W. An electric field–induced change in the selectivity of a metal oxide–catalyzed epoxide rearrangement. *J. Am. Chem. Soc.* **2012,** *134*, 186-189.

(2) Klinska, M.; Smith, L. M.; Gryn'ova, G.; Banwell, M. G.; Coote, M. L. Experimental demonstration of pH-dependent electrostatic catalysis of radical reactions. *Chem. Sci.* **2015,** *6*, 5623-5627.

(3) Aragonès, A. C.; Haworth, N. L.; Darwish, N.; Ciampi, S.; Bloomfield, N. J.; Wallace, G. G.; Diez-Perez, I.; Coote, M. L. Electrostatic catalysis of a Diels–Alder reaction. *Nature* **2016,** *531*, 88-91.

(4) Shaik, S.; Mandal, D.; Ramanan, R. Oriented electric fields as future smart reagents in chemistry. *Nat. Chem.* **2016,** *8*, 1091-1098.

(5) Geng, C.; Li, J.; Weiske, T.; Schlangen, M.; Shaik, S.; Schwarz, H. Electrostatic and charge-induced methane activation by a concerted double C-H bond insertion. *J. Am. Chem. Soc.* **2017,** *139*, 1684-1689.

(6) Akamatsu, M.; Sakai, N.; Matile, S. Electric-field-assisted anion-π catalysis. *J. Am. Chem. Soc.* **2017,** *139*, 6558-6561.

(7) Zhang, L.; Laborda, E.; Darwish, N.; Noble, B. B.; Tyrell, J. H.; Pluczyk, S.; Le Brun, A. P.; Wallace, G. G.; Gonzalez, J.; Coote, M. L. Electrochemical and electrostatic cleavage of alkoxyamines. *J. Am. Chem. Soc.* **2017,** *140*, 766-744.

(8) Pocker, Y.; Buchholz, R. F. Electrostatic catalysis of ionic aggregates. I. Ionization and dissociation of trityl chloride and hydrogen chloride in lithium perchlorate-diethyl ether solutions. *J. Am. Chem. Soc.* **1970,** *92*, 2075-2084.

(9) Pocker, Y.; Buchholz, R. F. Electrostatic catalysis by ionic aggregates. II. Reversible elimination of hydrogen chloride from tert-butyl chloride and the rearrangement of 1-phenylallyl chloride in lithium perchlorate-diethyl ether solutions. *J. Am. Chem. Soc.* **1970,** *92*, 4033-4038.

(10) Pocker, Y.; Buchholz, R. F. Electrostatic catalysis by ionic aggregates. III. Isomerization of (-)-menthone by hydrogen chloride and perchloric acid in lithium

perchlorate-diethyl ether solutions. *J. Am. Chem. Soc.* **1971,** *93*, 2905-2909.

(11) Fried, S. D.; Boxer, S. G. Measuring electric fields and noncovalent interactions using the vibrational Stark effect. *Acc. Chem. Res.* **2015,** *48*, 998-1006.

(12) Franzen, S.; Goldstein, R. F.; Boxer, S. G. Electric field modulation of electron transfer reaction rates in isotropic systems: long distance charge recombination in photosynthetic reaction centers. *J. Phys. Chem.* **1990,** *94*, 5135-5149.

(13) Murgida, D. H.; Hildebrandt, P. Electron-transfer processes of cytochrome c at interfaces. New insights by surface-enhanced resonance Raman spectroscopy. *Acc. Chem. Res.* **2004,** *37*, 854-861.

(14) Wahadoszamen, M.; Nakabayashi, T.; Kang, S.; Imahori, H.; Ohta, N. External electric field effects on absorption and fluorescence spectra of a fullerene derivative and its mixture with zinc-tetraphenylporphyrin doped in a PMMA film. *J. Phys. Chem. B* **2006,** *110*, 20354-20361.

(15) Ohta, N.; Koizumi, M.; Umeuchi, S.; Nishimura, Y.; Yamazaki, I. External electric field effects on fluorescence in an electron donor and acceptor system: Ethylcarbazole and dimethyl terephthalate in PMMA polymer films. *J. Phys. Chem.* **1996,** *100*, 16466-16471.

(16) Son, Y.-W.; Cohen, M. L.; Louie, S. G. Half-metallic graphene nanoribbons. *Nature* **2006,** *444*, 347-349.

(17) Naaman, R.; Waldeck, D. H. Spintronics and chirality: Spin selectivity in electron transport through chiral molecules. *Annu. Rev. Phys. Chem.* **2015,** *66*, 263-281.

(18) Ohno, H.; Chiba, D.; Matsukura, F.; Omiya, T.; Abe, E.; Dietl, T.; Ohno, Y.; Ohtani, K. Electric-field control of ferromagnetism. *Nature* **2000,** *408*, 944-946.

(19) Alemani, M.; Peters, M. V.; Hecht, S.; Rieder, K.-H.; Moresco, F.; Grill, L. Electric field-induced isomerization of azobenzene by STM. *J. Am. Chem. Soc.* **2006,** *128*, 14446-14447.

(20) Darwish, N.; Aragonès, A. C.; Darwish, T.; Ciampi, S.; Díez-Pérez, I. Multi-responsive photo-and chemo-electrical single-molecule switches. *Nano Lett.* **2014,** *14*, 7064-7070.

(21) Harzmann, G. D.; Frisenda, R.; van der Zant, H. S.; Mayor, M. Single-molecule

spin switch based on voltage-triggered distortion of the coordination sphere. *Angew. Chem. Int. Ed.* **2015,** *54*, 13425-13430.

(22) Gryn'ova, G.; Marshall, D. L.; Blanksby, S. J.; Coote, M. L. Switching radical stability by pH-induced orbital conversion. *Nat. Chem.* **2013,** *5*, 474-481.

(23) Gryn'ova, G.; Coote, M. L. Origin and scope of long-range stabilizing interactions and associated SOMO–HOMO conversion in distonic radical anions. *J. Am. Chem. Soc.* **2013,** *135*, 15392-15403.

(24) Shaik, S. S. What happens to molecules as they react? A valence bond approach to reactivity. *J. Am. Chem. Soc.* **1981,** *103*, 3692-3701.

(25) Pross, A.; Shaik, S. S. A qualitative valence-bond approach to organic reactivity. *Acc. Chem. Res.* **1983,** *16*, 363-370.

(26) Shaik, S.; Shurki, A. Valence bond diagrams and chemical reactivity. *Angew. Chem. Int. Ed.* **1999,** *38*, 586-625.

(27) Schirmer, B.; Grimme, S. Electric field induced activation of H_2–Can DFT do the job? *Chem. Commun.* **2010,** *46*, 7942-7944.

(28) Grimme, S.; Kruse, H.; Goerigk, L.; Erker, G. The mechanism of dihydrogen activation by frustrated Lewis pairs revisited. *Angew. Chem. Int. Ed.* **2010,** *49*, 1402-1405.

(29) Karafiloglou, P. Control of delocalization and structural changes by means of an electric field. *J. Comput. Chem.* **2006,** *27*, 1883-1891.

(30) Sowlati-Hashjin, S.; Matta, C. F. The chemical bond in external electric fields: Energies, geometries, and vibrational Stark shifts of diatomic molecules. *J. Chem. Phys.* **2013,** *139*, 144101-144114.

(31) Wei, Y.; Wang, X.; Wang, X.; Tao, Z.; Cui, Y.; Yang, M. A theoretical study of the activation of nitromethane under applied electric fields. *RSC Adv.* **2016,** *6*, 24712-24718.

(32) Warshel, A. Electrostatic basis of structure-function correlation in proteins. *Acc. Chem. Res.* **1981,** *14*, 284-290.

(33) Ortiz de Montellano, P. R.; De Voss, J. J. Oxidizing species in the mechanism of cytochrome P450. *Nat. Prod. Rep.* **2002,** *19*, 477-493.

(34) Shaik, S.; Kumar, D.; de Visser, S. P.; Altun, A.; Thiel, W. Theoretical perspective

on the structure and mechanism of cytochrome P450 enzymes. *Chem. Rev.* **2005,** *105*, 2279-2328.

(35) Lai, W.; Chen, H.; Cho, K. B.; Shaik, S. External electric field can control the catalytic cycle of Cytochrome P450cam: A QM/MM study. *J. Phys, Chem. Lett.* **2010,** *1*, 2082-2087.

(36) De Biase, P. M.; Paggi, D. A.; Doctorovich, F.; Hildebrandt, P.; Estrin, D. A.; Murgida, D. H.; Marti, M. A. Molecular basis for the electric field modulation of cytochrome c structure and function. *J. Am. Chem. Soc.* **2009,** *131*, 16248-16256.

(37) Warshel, A.; Sharma, P. K.; Kato, M.; Xiang, Y.; Liu, H.; Olsson, M. H. Electrostatic basis for enzyme catalysis. *Chem. Rev.* **2006,** *106*, 3210-3235.

(38) Winter, G.; Fersht, A. R.; Wilkinson, A. J.; Zoller, M.; Smith, M. Redesigning enzyme structure by site-directed mutagenesis: tyrosyl tRNA synthetase and ATP binding. *Nature* **1982,** *299*, 756-758.

(39) Benkovic, S.; Fierke, C.; Naylor, A. Insights into enzyme function from studies on mutants of dihydrofolate reductase. *Science* **1988,** *239*, 1105-1110.

(40) Harris, T. K.; Wu, G.; Massiah, M. A.; Mildvan, A. S. Mutational, kinetic, and NMR studies of the roles of conserved glutamate residues and of lysine-39 in the mechanism of the MutT pyrophosphohydrolase. *Biochemistry* **2000,** *39*, 1655-1674.

(41) Horton, N. C.; Otey, C.; Lusetti, S.; Sam, M. D.; Kohn, J.; Martin, A. M.; Ananthnarayan, V.; Perona, J. J. Electrostatic contributions to site specific DNA cleavage by Eco RV Endonuclease. *Biochemistry* **2002,** *41*, 10754-10763.

(42) Cho, K.-B.; Hirao, H.; Chen, H.; Carvajal, M. A.; Cohen, S.; Derat, E.; Thiel, W.; Shaik, S. Compound I in heme thiolate enzymes: a comparative QM/MM study. *J. Phys. Chem. A* **2008,** *112*, 13128-13138.

(43) Usharani, D.; Zazza, C.; Lai, W.; Chourasia, M.; Waskell, L.; Shaik, S. A single-site mutation (F429H) converts the enzyme CYP 2B4 into a heme oxygenase: a QM/MM study. *J. Am. Chem. Soc.* **2012,** *134*, 4053-4056.

(44) Fried, S. D.; Bagchi, S.; Boxer, S. G. Extreme electric fields power catalysis in the active site of ketosteroid isomerase. *Science* **2014,** *346*, 1510-1514.

(45) Liu, C. T.; Layfield, J. P.; Stewart III, R. J.; French, J. B.; Hanoian, P.; Asbury, J.

B.; Hammes-Schiffer, S.; Benkovic, S. J. Probing the electrostatics of active site microenvironments along the catalytic cycle for Escherichia coli dihydrofolate reductase. *J. Am. Chem. Soc.* **2014,** *136*, 10349-10360.

(46) Shaik, S.; de Visser, S. P.; Kumar, D. External electric field will control the selectivity of enzymatic-like bond activations. *J. Am. Chem. Soc.* **2004,** *126*, 11746-11749.

(47) Shaik, S.; Lai, W.; Chen, H.; Wang, Y. The valence bond way: reactivity patterns of cytochrome P450 enzymes and synthetic analogs. *Acc. Chem. Res.* **2010,** *43*, 1154-1165.

(48) Shaik, S.; Milko, P.; Schyman, P.; Usharani, D.; Chen, H. Trends in aromatic oxidation reactions catalyzed by cytochrome P450 enzymes: a valence bond modeling. *J. Chem. Theory. Comp.* **2011,** *7*, 327-339.

(49) Hirao, H.; Chen, H.; Carvajal, M. A.; Wang, Y.; Shaik, S. Effect of external electric fields on the C−H Bond activation reactivity of nonheme iron−oxo reagents. *J. Am. Chem. Soc.* **2008,** *130*, 3319-3327.

(50) Meir, R.; Chen, H.; Lai, W.; Shaik, S. Oriented electric fields accelerate Diels−Alder reactions and control the endo/exo selectivity. *ChemPhysChem* **2010,** *11*, 301-310.

(51) Lau, V. M.; Pfalzgraff, W. C.; Markland, T. E.; Kanan, M. W. Electrostatic control of regioselectivity in Au (I)-catalyzed hydroarylation. *J. Am. Chem. Soc.* **2017,** *139*, 4035-4041.

(52) Franzen, S.; Lao, K.; Boxer, S. G. Electric field effects on kinetics of electron transfer reactions: connection between experiment and theory. *Chem. Phys. Lett.* **1992,** *197*, 380-388.

(53) Franzen, S.; Boxer, S. G. Temperature dependence of the electric field modulation of electron-transfer rates: charge recombination in photosynthetic reaction centers. *J. Phys. Chem.* **1993,** *97*, 6304-6318.

(54) Lao, K.; Franzen, S.; Stanley, R. J.; Lambright, D. G.; Boxer, S. G. Effects of applied electric fields on the quantum yields of the initial electron-transfer steps in bacterial photosynthesis. 1. Quantum yield failure. *J. Phys. Chem.* **1993,** *97*, 13165-

13171.

(55) Lao, K.; Franzen, S.; Steffen, M.; Lambright, D.; Stanley, R.; Boxer, S. G. Effects of applied electric fields on the quantum yields for the initial electron transfer steps in bacterial photosynthesis II. Dynamic Stark effect. *Chem. Phys.* **1995,** *197*, 259-275.

(56) Zhou, H.; Boxer, S. G. Probing excited-state electron transfer by resonance Stark spectroscopy. 1. Experimental results for photosynthetic reaction centers. *J. Phys. Chem. B* **1998,** *102*, 9139-9147.

(57) Treynor, T. P.; Boxer, S. G. A theory of intervalence band stark effects. *J. Phys. Chem. A* **2004,** *108*, 1764-1778.

(58) Tóbik, J.; Dal Corso, A.; Scandolo, S.; Tosatti, E. Organic molecular crystals in electric fields. *Surf. Sci.* **2004,** *566*, 644-649.

(59) Murgida, D. H.; Hildebrandt, P. Heterogeneous electron transfer of cytochrome c on coated silver electrodes. Electric field effects on structure and redox potential. *J. Phys. Chem. B* **2001,** *105*, 1578-1586.

(60) Reed, M. A.; Zhou, C.; Muller, C.; Burgin, T.; Tour, J. Conductance of a molecular junction. *Science* **1997,** *278*, 252-254.

(61) Chen, J.; Reed, M.; Rawlett, A.; Tour, J. Large on-off ratios and negative differential resistance in a molecular electronic device. *Science* **1999,** *286*, 1550-1552.

(62) Blum, A. S.; Kushmerick, J. G.; Long, D. P.; Patterson, C. H.; Yang, J. C.; Henderson, J. C.; Yao, Y.; Tour, J. M.; Shashidhar, R.; Ratna, B. R. Molecularly inherent voltage-controlled conductance switching. *Nat. Mater.* **2005,** *4*, 167-172.

(63) Troisi, A.; Ratner, M. A. Molecular rectification through electric field induced conformational changes. *J. Am. Chem. Soc.* **2002,** *124*, 14528-14529.

(64) Li, Y.; Zhao, J.; Yin, X.; Yin, G. Ab initio investigations of the electric field dependence of the geometric and electronic structures of molecular wires. *J. Phys. Chem. A* **2006,** *110*, 11130-11135.

(65) Tao, N. J. Electron transport in molecular junctions. *Nat. Nanotechnol.* **2006,** *1*, 173-181.

(66) Leung, K.; Rempe, S. B.; Schultz, P. A.; Sproviero, E. M.; Batista, V. S.; Chandross, M. E.; Medforth, C. J. Density functional theory and DFT + U study of transition metal

porphines adsorbed on Au (111) surfaces and effects of applied electric fields. *J. Am. Chem. Soc.* **2006,** *128*, 3659-3668.

(67) Harikumar, K. R.; Polanyi, J. C.; Sloan, P. A.; Ayissi, S.; Hofer, W. A. Electronic switching of single silicon atoms by molecular field effects. *J. Am. Chem. Soc.* **2006,** *128*, 16791-16797.

(68) Carbonell, E.; Duran, M.; Lledos, A.; Bertran, J. Catalysis of Friedel-Crafts reactions by electric fields. *J. Phys. Chem.* **1991,** *95*, 179-183.

(69) Arabi, A. A.; Matta, C. F. Effects of external electric fields on double proton transfer kinetics in the formic acid dimer. *Phys. Chem. Chem. Phys.* **2011,** *13*, 13738-13748.

(70) Zhou, Z.-J.; Li, X.-P.; Liu, Z.-B.; Li, Z.-R.; Huang, X.-R.; Sun, C.-C. Electric field-driven acid−base chemistry: proton transfer from acid (HCl) to base (NH_3/H_2O). *J. Phys. Chem. A* **2011,** *115*, 1418-1422.

(71) Timerghazin, Q. K.; Talipov, M. R. Unprecedented external electric field effects on S-nitrosothiols: possible mechanism of biological regulation? *J. Phys. Chem. Lett.* **2013,** *4*, 1034-1038.

(72) De Biase, P. M.; Doctorovich, F.; Murgida, D. H.; Estrin, D. A. Electric field effects on the reactivity of heme model systems. *Chem. Phys. Lett.* **2007,** *434*, 121-126.

(73) Oklejas, V.; Uibel, R. H.; Horton, R.; Harris, J. M. Electric-field control of the tautomerization and metal ion binding reactivity of 8-hydroxyquinoline immobilized to an electrode surface. *Anal. Chem.* **2008,** *80*, 1891-1901.

(74) Franchi, P.; Mezzina, E.; Lucarini, M. SOMO–HOMO conversion in distonic radical anions: an experimental test in solution by EPR radical equilibration technique. *J. Am. Chem. Soc.* **2014,** *136*, 1250-1252.

(75) Aitken, H. M.; Coote, M. L. Can electrostatic catalysis of Diels–Alder reactions be harnessed with pH-switchable charged functional groups? *Phys. Chem. Chem. Phys.* **2018,** *20*, 10671-10676.

(76) Likhtenshtein, G. I.; Yamauchi, J.; Nakatsuji, S. i.; Smirnov, A. I.; Tamura, R., *Nitroxides: applications in chemistry, biomedicine, and materials science*. John Wiley & Sons: 2008.

(77) Vogler, T.; Studer, A. Applications of TEMPO in synthesis. *Synthesis* **2008,** *2008*, 1979-1993.

(78) Rafiee, M.; Miles, K. C.; Stahl, S. S. Electrocatalytic alcohol oxidation with TEMPO and bicyclic nitroxyl derivatives: Driving force trumps steric effects. *J. Am. Chem. Soc.* **2015,** *137*, 14751-14757.

(79) Chen, Q.; Fang, C.; Shen, Z.; Li, M. Electrochemical synthesis of nitriles from aldehydes using TEMPO as a mediator. *Electrochem. Commun.* **2016,** *64*, 51-55.

(80) Badalyan, A.; Stahl, S. S. Cooperative electrocatalytic alcohol oxidation with electron-proton-transfer mediators. *Nature* **2016,** *535*, 406-410.

(81) Qian, X.-Y.; Li, S.-Q.; Song, J.; Xu, H.-C. TEMPO-catalyzed electrochemical C–H thiolation: synthesis of benzothiazoles and thiazolopyridines from thioamides. *ACS Catal.* **2017,** *7*, 2730-2734.

(82) Kocherginsky, N.; Swartz, H. M., *Nitroxide spin labels: reactions in biology and chemistry*. CRC Press: 1995.

(83) Caneschi, A.; Gatteschi, D.; Sessoli, R.; Rey, P. Toward molecular magnets: the metal-radical approach. *Acc. Chem. Res.* **1989,** *22*, 392-398.

(84) Anzai, H. Recent progress in the development of organomagnetic materials based on neutral nitroxide radicals and charge transfer complexes derived from nitroxide radicals. *J. Mater. Chem.* **1997,** *7*, 2161-2174.

(85) Matsumoto, K.-i.; Hyodo, F.; Matsumoto, A.; Koretsky, A. P.; Sowers, A. L.; Mitchell, J. B.; Krishna, M. C. High-resolution mapping of tumor redox status by magnetic resonance imaging using nitroxides as redox-sensitive contrast agents. *Clin. Cancer Res.* **2006,** *12*, 2455-2462.

(86) Emoto, M.; Yamato, M.; Sato-Akaba, H.; Yamada, K.; Matsuoka, Y.; Fujii, H. Brain imaging in methamphetamine-treated mice using a nitroxide contrast agent for EPR imaging of the redox status and a gadolinium contrast agent for MRI observation of blood–brain barrier function. *Free Radical Res.* **2015,** *49*, 1038-1047.

(87) Nishide, H.; Iwasa, S.; Pu, Y.-J.; Suga, T.; Nakahara, K.; Satoh, M. Organic radical battery: nitroxide polymers as a cathode-active material. *Electrochim. Acta* **2004,** *50*, 827-831.

(88) Suguro, M.; Mori, A.; Iwasa, S.; Nakahara, K.; Nakano, K. Syntheses and electrochemical properties of TEMPO radical substituted silicones: active material for organic radical batteries. *Macromol. Chem. Phys.* **2009,** *210*, 1402-1407.

(89) Hansen, K.-A.; Nerkar, J.; Thomas, K.; Bottle, S. E.; O'Mullane, A. P.; Talbot, P. C.; Blinco, J. P. New spin on organic radical batteries–an isoindoline nitroxide-based high-voltage cathode material. *ACS Appl. Mater. Interfaces* **2018,** *10*, 7982-7988.

(90) Hawker, C. J.; Bosman, A. W.; Harth, E. New polymer synthesis by nitroxide mediated living radical polymerizations. *Chem. Rev.* **2001,** *101*, 3661-3688.

(91) Nicolas, J.; Guillaneuf, Y.; Lefay, C.; Bertin, D.; Gigmes, D.; Charleux, B. Nitroxide-mediated polymerization. *Prog. Polym. Sci.* **2013,** *38*, 63-235.

(92) Kashiwagi, Y.; Kurashima, F.; Kikuchi, C.; Anzai, J. I.; Osa, T.; Bobbin, J. M. Electrocatalytic oxidation of amines to nitriles on a TEMPO-modified graphite felt electrode (TEMPO = 2, 2, 6, 6-tetramethylpiperidin-1-yloxyl). *J. Chin. Chem. Soc.* **1998,** *45*, 135-138.

(93) Kashiwagi, Y.; Uchiyama, K.; Kurashima, F.; Anzai, J.-i.; Osa, T. Enantioselective oxidation of amines on a gold electrode modified by a self-assembled monolayer of a chiral nitroxyl radical compound. *Anal. Sci.* **1999,** *15*, 907-909.

(94) Kashiwagi, Y.; Yanagisawa, Y.; Kurashima, F.; Anzai, J.-i.; Osa, T.; Bobbitt, J. M. Enantioselective electrocatalytic oxidation of racemic alcohols on a TEMPO-modified graphite felt electrode by use of chiral base (TEMPO = 2, 2, 6, 6-tetramethylpiperidin-1-yloxyl). *Chem. Commun.* **1996**, 2745-2746.

(95) Hickey, D. P.; Milton, R. D.; Chen, D.; Sigman, M. S.; Minteer, S. D. TEMPO-modified linear poly (ethylenimine) for immobilization-enhanced electrocatalytic oxidation of alcohols. *Acs Catal.* **2015,** *5*, 5519-5524.

(96) Belgsir, E.; Schäfer, H. Selective oxidation of carbohydrates on Nafion®–TEMPO-modified graphite felt electrodes. *Electrochem. Commun.* **2001,** *3*, 32-35.

(97) Swiech, O.; Bilewicz, R.; Megiel, E. TEMPO coated Au nanoparticles: synthesis and tethering to gold surfaces. *RSC Adv.* **2013,** *3*, 5979-5986.

(98) Sciannamea, V.; Jérôme, R.; Detrembleur, C. In-situ nitroxide-mediated radical polymerization (NMP) processes: their understanding and optimization. *Chem. Rev.*

2008, *108*, 1104-1126.

(99) Otsuka, H.; Aotani, K.; Higaki, Y.; Takahara, A. Polymer scrambling: macromolecular radical crossover reaction between the main chains of alkoxyamine-based dynamic covalent polymers. *J. Am. Chem. Soc.* **2003,** *125*, 4064-4065.

(100) Schulte, B.; Tsotsalas, M.; Becker, M.; Studer, A.; De Cola, L. Dynamic microcrystal assembly by nitroxide exchange reactions. *Angew. Chem. Int. Ed.* **2010,** *49*, 6881-6884.

(101) Yuan, C. e.; Rong, M. Z.; Zhang, M. Q.; Zhang, Z. P.; Yuan, Y. C. Self-healing of polymers via synchronous covalent bond fission/radical recombination. *Chem. Mater.* **2011,** *23*, 5076-5081.

(102) Zhang, Z. P.; Rong, M. Z.; Zhang, M. Q.; Yuan, C. E. Alkoxyamine with reduced homolysis temperature and its application in repeated autonomous self-healing of stiff polymers. *Polym. Chem.* **2013,** *4*, 4648-4654.

(103) Studer, A. Tin-free radical cyclization reactions using the persistent radical effect. *Angew. Chem. Int. Ed.* **2000,** *39*, 1108-1111.

(104) Wetter, C.; Jantos, K.; Woithe, K.; Studer, A. Intermolecular radical addition and addition/cyclization reactions of alkoxyamines onto nonactivated alkenes. *Org. Lett.* **2003,** *5*, 2899-2902.

(105) Leroi, C.; Bertin, D.; Dufils, P.-E.; Gigmes, D.; Marque, S.; Tordo, P.; Couturier, J.-L.; Guerret, O.; Ciufolini, M. A. Alkoxyamine-mediated radical synthesis of indolinones and indolines. *Org. Lett.* **2003,** *5*, 4943-4945.

(106) Studer, A. Tin-free radical chemistry using the persistent radical effect: alkoxyamine isomerization, addition reactions and polymerizations. *Chem. Soc. Rev.* **2004,** *33*, 267-273.

(107) Audran, G.; Brémond, P.; Marque, S. R. Labile alkoxyamines: past, present, and future. *Chem. Commun.* **2014,** *50*, 7921-7928.

(108) Audran, G.; Brémond, P.; Franconi, J.-M.; Marque, S. R.; Massot, P.; Mellet, P.; Parzy, E.; Thiaudière, E. Alkoxyamines: a new family of pro-drugs against cancer. Concept for theranostics. *Org. Biomol. Chem.* **2014,** *12*, 719-723.

(109) Hodgson, J. L.; Roskop, L. B.; Gordon, M. S.; Lin, C. Y.; Coote, M. L. Side

reactions of nitroxide-mediated polymerization: N-O versus O-C cleavage of alkoxyamines. *J. Phys. Chem. A* **2010,** *114*, 10458-10466.

(110) Goto, A.; Scaiano, J.; Maretti, L. Photolysis of an alkoxyamine using intramolecular energy transfer from a quinoline antenna-towards photo-induced living radical polymerization. *Photoch. Photobio. Sci.* **2007,** *6*, 833-835.

(111) Guillaneuf, Y.; Bertin, D.; Gigmes, D.; Versace, D.-L.; Lalevée, J.; Fouassier, J.-P. Toward nitroxide-mediated photopolymerization. *Macromolecules* **2010,** *43*, 2204-2212.

(112) Telitel, S.; Amamoto, Y.; Poly, J.; Morlet-Savary, F.; Soppera, O.; Lalevée, J.; Matyjaszewski, K. Introduction of self-healing properties into covalent polymer networks via the photodissociation of alkoxyamine junctions. *Polym. Chem.* **2014,** *5*, 921-930.

(113) Bottle, S. E.; Clement, J.-L.; Fleige, M.; Simpson, E. M.; Guillaneuf, Y.; Fairfull-Smith, K. E.; Gigmes, D.; Blinco, J. P. Light-active azaphenalene alkoxyamines: fast and efficient mediators of a photo-induced persistent radical effect. *RSC Adv.* **2016,** *6*, 80328-80333.

(114) Bagryanskaya, E.; Brémond, P.; Edeleva, M.; Marque, S. R.; Parkhomenko, D.; Roubaud, V.; Siri, D. Chemically triggered C–ON bond homolysis in alkoxyamines. Part 2: DFT investigation and application of the pH effect on NMP. *Macromol. Rapid Commun.* **2012,** *33*, 152-157.

(115) Brémond, P.; Marque, S. R. First proton triggered C–ON bond homolysis in alkoxyamines. *Chem. Commun.* **2011,** *47*, 4291-4293.

(116) Bertin, D.; Gigmes, D.; Marque, S. R.; Tordo, P. Kinetic subtleties of nitroxide mediated polymerization. *Chem. Soc. Rev.* **2011,** *40*, 2189-2198.

(117) Gryn'ova, G.; Smith, L. M.; Coote, M. L. Computational design of pH-switchable control agents for nitroxide mediated polymerization. *Phys. Chem. Chem. Phys.* **2017,** *19*, 22678-22683.

(118) Smirnov, A. I.; Ruuge, A.; Reznikov, V. A.; Voinov, M. A.; Grigor'ev, I. A. Site-directed electrostatic measurements with a thiol-specific pH-sensitive nitroxide: differentiating local pK and polarity effects by high-field EPR. *J. Am. Chem. Soc.* **2004,**

126, 8872-8873.

(119) Gryn'ova, G.; Coote, M. L. Directionality and the role of polarization in electric field effects on radical stability. *Aust. J. Chem.* **2017,** *70*, 367-372.

(120) Edeleva, M. V.; Kirilyuk, I. A.; Zhurko, I. F.; Parkhomenko, D. A.; Tsentalovich, Y. P.; Bagryanskaya, E. G. pH-Sensitive C–ON bond homolysis of alkoxyamines of imidazoline series with multiple ionizable groups as an approach for control of nitroxide mediated polymerization. *J. Org. Chem.* **2011,** *76*, 5558-5573.

(121) Ciampi, S.; Harper, J. B.; Gooding, J. J. Wet chemical routes to the assembly of organic monolayers on silicon surfaces via the formation of Si–C bonds: Surface preparation, passivation and functionalization. *Chem. Soc. Rev.* **2010,** *39*, 2158-2183.

(122) Choudhury, M. H.; Ciampi, S.; Yang, Y.; Tavallaie, R.; Zhu, Y.; Zarei, L.; Gonçales, V. R.; Gooding, J. J. Connecting electrodes with light: one wire, many electrodes. *Chem. Sci.* **2015,** *6*, 6769-6776.

(123) Yang, Y.; Ciampi, S.; Choudhury, M. H.; Gooding, J. J. Light activated electrochemistry: light intensity and pH dependence on electrochemical performance of anthraquinone derivatized silicon. *J. Phys. Chem. C* **2016,** *120*, 2874-2882.

(124) Vogel, Y. B.; Zhang, L.; Darwish, N.; Gonçales, V. R.; Le Brun, A.; Gooding, J. J.; Molina, A.; Wallace, G. G.; Coote, M. L.; Gonzalez, J. Reproducible flaws unveil electrostatic aspects of semiconductor electrochemistry. *Nat. Commun.* **2017,** *8*, 2066-2074.

(125) Rakshit, T.; Liang, G.-C.; Ghosh, A. W.; Datta, S. Silicon-based molecular electronics. *Nano Lett.* **2004,** *4*, 1803-1807.

(126) Aswal, D.; Lenfant, S.; Guerin, D.; Yakhmi, J.; Vuillaume, D. Self assembled monolayers on silicon for molecular electronics. *Anal. Chim. Acta* **2006,** *568*, 84-108.

(127) Nakamura, M.; Yoshida, S.; Katayama, T.; Taninaka, A.; Mera, Y.; Okada, S.; Takeuchi, O.; Shigekawa, H. Mechanically activated switching of Si-based single-molecule junction as imaged with three-dimensional dynamic probe. *Nat. Commun.* **2015,** *6*, 8465-8472.

(128) Aragonès, A. C.; Darwish, N.; Ciampi, S.; Sanz, F.; Gooding, J. J.; Díez-Pérez, I. Single-molecule electrical contacts on silicon electrodes under ambient conditions.

Nat. Commun. **2017,** *8*, 15056-15063.

(129) Vilan, A.; Cahen, D. Chemical modification of semiconductor surfaces for molecular electronics. *Chem. Rev.* **2017,** *117*, 4624-4666.

(130) Hill, C. D.; Peretz, E.; Hile, S. J.; House, M. G.; Fuechsle, M.; Rogge, S.; Simmons, M. Y.; Hollenberg, L. C. A surface code quantum computer in silicon. *Sci. Adv.* **2015,** *1*, e1500707-e1500717.

(131) Tosi, G.; Mohiyaddin, F. A.; Schmitt, V.; Tenberg, S.; Rahman, R.; Klimeck, G.; Morello, A. Silicon quantum processor with robust long-distance qubit couplings. *Nat. Commun.* **2017,** *8*, 450-460.

(132) Flatté, M. E. Solid-state physics: Silicon spintronics warms up. *Nature* **2009,** *462*, 419-420.

(133) Jansen, R. Silicon spintronics. *Nat. Mater.* **2012,** *11*, 400-408.

(134) Sverdlov, V.; Selberherr, S. Silicon spintronics: progress and challenges. *Phys. Rep.* **2015,** *585*, 1-40.

(135) Zhang, X. G., *Electrochemistry of silicon and its oxide*. Springer Science & Business Media: 2007.

(136) Rajeshwar, K. Fundamentals of semiconductor electrochemistry and photoelectrochemistry. *Encyclopedia of electrochemistry* **2007**.

(137) Memming, R., *Semiconductor electrochemistry*. John Wiley & Sons: 2015.

(138) Roth, K. M.; Yasseri, A. A.; Liu, Z.; Dabke, R. B.; Malinovskii, V.; Schweikart, K.-H.; Yu, L.; Tiznado, H.; Zaera, F.; Lindsey, J. S. Measurements of electron-transfer rates of charge-storage molecular monolayers on Si(100). Toward hybrid molecular/semiconductor information storage devices. *J. Am. Chem. Soc.* **2003,** *125*, 505-517.

(139) Ruess, F. J.; Oberbeck, L.; Simmons, M. Y.; Goh, K. E. J.; Hamilton, A. R.; Hallam, T.; Schofield, S. R.; Curson, N. J.; Clark, R. G. Toward atomic-scale device fabrication in silicon using scanning probe microscopy. *Nano Lett.* **2004,** *4*, 1969-1973.

(140) Simmons, M.; Ruess, F.; Goh, K.; Hallam, T.; Schofield, S.; Oberbeck, L.; Curson, N.; Hamilton, A.; Butcher, M.; Clark, R. Scanning probe microscopy for silicon device fabrication. *Mol. Simulat.* **2005,** *31*, 505-515.

(141) Simmons, M.; Ruess, F.; Goh, K.; Pok, W.; Hallam, T.; Butcher, M.; Reusch, T.; Scappucci, G.; Hamilton, A.; Oberbeck, L. Atomic-scale silicon device fabrication. *Int. J. Nanotechnol.* **2008,** *5*, 352-369.

(142) Vilan, A.; Yaffe, O.; Biller, A.; Salomon, A.; Kahn, A.; Cahen, D. Molecules on Si: electronics with chemistry. *Adv. Mater.* **2010,** *22*, 140-159.

(143) Neergaard Waltenburg, H.; Yates, J. Surface chemistry of silicon. *Chem. Rev.* **1995,** *95*, 1589-1673.

(144) Bergerson, W.; Mulder, J.; Hsung, R.; Zhu, X.-Y. Assembly of organic molecules on silicon surfaces via the Si-N linkage. *J. Am. Chem. Soc.* **1999,** *121*, 454-455.

(145) Buriak, J. M. Organometallic chemistry on silicon surfaces: formation of functional monolayers bound through Si–C bonds. *Chem. Commun.* **1999**, 1051-1060.

(146) Zhu, X.-Y.; Boiadjiev, V.; Mulder, J.; Hsung, R.; Major, R. Molecular assemblies on silicon surfaces via Si−O linkages. *Langmuir* **2000,** *16*, 6766-6772.

(147) Niwano, M.; Takeda, Y.; Ishibashi, Y.; Kurita, K.; Miyamoto, N. Morphology of hydrofluoric acid and ammonium fluoride-treated silicon surfaces studied by surface infrared spectroscopy. *J. Appl. Phys.* **1992,** *71*, 5646-5649.

(148) Clark, I. T.; Aldinger, B. S.; Gupta, A.; Hines, M. A. Aqueous etching produces Si(100) surfaces of near-atomic flatness: Strain minimization does not predict surface morphology. *J. Phys. Chem. C* **2009,** *114*, 423-428.

(149) Chabal, Y.; Higashi, G.; Raghavachari, K.; Burrows, V. Infrared spectroscopy of Si(111) and Si(100) surfaces after HF treatment: hydrogen termination and surface morphology. *J. Vac. Sci. Technol. A* **1989,** *7*, 2104-2109.

(150) Higashi, G.; Chabal, Y.; Trucks, G.; Raghavachari, K. Ideal hydrogen termination of the Si(111) surface. *Appl. Phys. Lett.* **1990,** *56*, 656-658.

(151) Morita, M.; Ohmi, T.; Hasegawa, E.; Kawakami, M.; Ohwada, M. Growth of native oxide on a silicon surface. *J. Appl. Phys.* **1990,** *68*, 1272-1281.

(152) Higashi, G.; Becker, R.; Chabal, Y.; Becker, A. Comparison of Si(111) surfaces prepared using aqueous solutions of NH_4F versus HF. *Appl. Phys. Lett.* **1991,** *58*, 1656-1658.

(153) Niwano, M.; Kageyama, J. i.; Kurita, K.; Kinashi, K.; Takahashi, I.; Miyamoto, N. Infrared spectroscopy study of initial stages of oxidation of hydrogen-terminated Si surfaces stored in air. *J. Appl. Phys.* **1994,** *76*, 2157-2163.

(154) Linford, M. R.; Fenter, P.; Eisenberger, P. M.; Chidsey, C. E. Alkyl monolayers on silicon prepared from 1-alkenes and hydrogen-terminated silicon. *J. Am. Chem. Soc.* **1995,** *117*, 3145-3155.

(155) Cleland, G.; Horrocks, B. R.; Houlton, A. Direct functionalization of silicon via the self-assembly of alcohols. *J. Chem. Soc., Faraday Trans.* **1995,** *91*, 4001-4003.

(156) Yu, H.-Z.; Morin, S.; Wayner, D. D.; Allongue, P.; Henry de Villeneuve, C. Molecularly tunable “organic capacitors” at silicon/aqueous electrolyte interfaces. *J. Phys. Chem. B* **2000,** *104*, 11157-11161.

(157) Bansal, A.; Lewis, N. S. Electrochemical properties of (111)-oriented n-Si surfaces derivatized with covalently-attached alkyl chains. *J. Phys. Chem. B* **1998,** *102*, 1067-1070.

(158) Boukherroub, R.; Morin, S.; Bensebaa, F.; Wayner, D. New synthetic routes to alkyl monolayers on the Si(111) surface1. *Langmuir* **1999,** *15*, 3831-3835.

(159) Bateman, J. E.; Eagling, R. D.; Worrall, D. R.; Horrocks, B. R.; Houlton, A. Alkylation of porous silicon by direct reaction with alkenes and alkynes. *Angew. Chem. Int. Ed.* **1998,** *37*, 2683-2685.

(160) Sieval, A. B.; Opitz, R.; Maas, H. P.; Schoeman, M. G.; Meijer, G.; Vergeldt, F. J.; Zuilhof, H.; Sudhölter, E. J. Monolayers of 1-alkynes on the H-terminated Si(100) surface. *Langmuir* **2000,** *16*, 10359-10368.

(161) Sieval, A. B.; Linke, R.; Heij, G.; Meijer, G.; Zuilhof, H.; Sudhölter, E. J. Amino-terminated organic monolayers on hydrogen-terminated silicon surfaces. *Langmuir* **2001,** *17*, 7554-7559.

(162) Linford, M. R.; Chidsey, C. E. Alkyl monolayers covalently bonded to silicon surfaces. *J. Am. Chem. Soc.* **1993,** *115*, 12631-12632.

(163) Terry, J.; Linford, M. R.; Wigren, C.; Cao, R.; Pianetta, P.; Chidsey, C. E. Determination of the bonding of alkyl monolayers to the Si(111) surface using chemical-shift, scanned-energy photoelectron diffraction. *Appl. Phys. Lett.* **1997,** *71*,

1056-1058.

(164) Terry, J.; Mo, R.; Wigren, C.; Cao, R.; Mount, G.; Pianetta, P.; Linford, M. R.; Chidsey, C. E. Reactivity of the H-Si(111) surface. *Nucl. Instrum. Meth. B* **1997,** *133*, 94-101.

(165) Stewart, M. P.; Buriak, J. M. Photopatterned hydrosilylation on porous silicon. *Angew. Chem. Int. Ed.* **1998,** *37*, 3257-3260.

(166) Effenberger, F.; Götz, G.; Bidlingmaier, B.; Wezstein, M. Photoactivated preparation and patterning of self-assembled monolayers with 1-alkenes and aldehydes on silicon hydride surfaces. *Angew. Chem. Int. Ed.* **1998,** *37*, 2462-2464.

(167) Zazzera, L.; Evans, J.; Deruelle, M.; Tirrell, M.; Kessel, C.; McKeown, P. Bonding organic molecules to hydrogen-terminated silicon wafers. *J. Electrochem. Soc.* **1997,** *144*, 2184-2189.

(168) Holland, J. M.; Stewart, M. P.; Allen, M. J.; Buriak, J. M. Metal mediated reactions on porous silicon surfaces. *J. Solid State Chem.* **1999,** *147*, 251-258.

(169) Marciniec, B.; Guliński, J. Recent advances in catalytic hydrosilylation. *J. Organomet. Chem.* **1993,** *446*, 15-23.

(170) Ito, Y.; Suginome, M.; Murakami, M. Palladium(II) acetate-tert-alkyl isocyanide as a highly efficient catalyst for the inter-and intramolecular bis-silylation of carbon-carbon triple bonds. *J. Org. Chem.* **1991,** *56*, 1948-1951.

(171) Buriak, J. M.; Allen, M. J. Lewis acid mediated functionalization of porous silicon with substituted alkenes and alkynes. *J. Am. Chem. Soc.* **1998,** *120*, 1339-1340.

(172) Buriak, J. M.; Stewart, M. P.; Geders, T. W.; Allen, M. J.; Choi, H. C.; Smith, J.; Raftery, D.; Canham, L. T. Lewis acid mediated hydrosilylation on porous silicon surfaces. *J. Am. Chem. Soc.* **1999,** *121*, 11491-11502.

(173) Song, J. H.; Sailor, M. J. Functionalization of nanocrystalline porous silicon surfaces with aryllithium reagents: formation of Si−C bonds by cleavage of Si−Si bonds. *J. Am. Chem. Soc.* **1998,** *120*, 2376-2381.

(174) Bansal, A.; Li, X.; Lauermann, I.; Lewis, N. S.; Yi, S. I.; Weinberg, W. Alkylation of Si surfaces using a two-step halogenation/Grignard route. *J. Am. Chem. Soc.* **1996,** *118*, 7225-7226.

(175) Delamar, M.; Hitmi, R.; Pinson, J.; Saveant, J. M. Covalent modification of carbon surfaces by grafting of functionalized aryl radicals produced from electrochemical reduction of diazonium salts. *J. Am. Chem. Soc.* **1992,** *114*, 5883-5884.

(176) Allongue, P.; Delamar, M.; Desbat, B.; Fagebaume, O.; Hitmi, R.; Pinson, J.; Saveant, J.-M. Covalent modification of carbon surfaces by aryl radicals generated from the electrochemical reduction of diazonium salts. *J. Am. Chem. Soc.* **1997,** *119*, 201-207.

(177) Allongue, P.; De Villeneuve, C. H.; Pinson, J.; Ozanam, F.; Chazalviel, J.; Wallart, X. Organic monolayers on Si(111) by electrochemical method. *Electrochim. Acta* **1998,** *43*, 2791-2798.

(178) De Villeneuve, C. H.; Pinson, J.; Bernard, M.; Allongue, P. Electrochemical formation of close-packed phenyl layers on Si(111). *J. Phys. Chem. B* **1997,** *101*, 2415-2420.

(179) Hurley, P. T.; Ribbe, A. E.; Buriak, J. M. Nanopatterning of alkynes on hydrogen-terminated silicon surfaces by scanning probe-induced cathodic electrografting. *J. Am. Chem. Soc.* **2003,** *125*, 11334-11339.

(180) Robertson, N.; McGowan, C. A. A comparison of potential molecular wires as components for molecular electronics. *Chem. Soc. Rev.* **2003,** *32*, 96-103.

(181) Metzger, R. M. Unimolecular electrical rectifiers. *Chem. Rev.* **2003,** *103*, 3803-3834.

(182) Díez-Pérez, I.; Hihath, J.; Lee, Y.; Yu, L.; Adamska, L.; Kozhushner, M. A.; Oleynik, I. I.; Tao, N. Rectification and stability of a single molecular diode with controlled orientation. *Nat. Chem.* **2009,** *1*, 635-641.

(183) Díez-Pérez, I.; Li, Z.; Hihath, J.; Li, J.; Zhang, C.; Yang, X.; Zang, L.; Dai, Y.; Feng, X.; Muellen, K. Gate-controlled electron transport in coronenes as a bottom-up approach towards graphene transistors. *Nat. Commun.* **2010,** *1*, 31-35.

(184) Perrin, M. L.; Burzurí, E.; van der Zant, H. S. Single-molecule transistors. *Chem. Soc. Rev.* **2015,** *44*, 902-919.

(185) Jia, C.; Wang, J.; Yao, C.; Cao, Y.; Zhong, Y.; Liu, Z.; Liu, Z.; Guo, X. Conductance switching and mechanisms in single-molecule junctions. *Angew. Chem.*

Int. Ed. **2013,** *52*, 8666-8670.

(186) Darwish, N.; Díez-Pérez, I.; Da Silva, P.; Tao, N.; Gooding, J. J.; Paddon-Row, M. N. Observation of electrochemically controlled quantum interference in a single anthraquinone-based norbornylogous bridge molecule. *Angew. Chem. Int. Ed.* **2012,** *51*, 3203-3206.

(187) Schwarz, F.; Kastlunger, G.; Lissel, F.; Egler-Lucas, C.; Semenov, S. N.; Venkatesan, K.; Berke, H.; Stadler, R.; Lörtscher, E. Field-induced conductance switching by charge-state alternation in organometallic single-molecule junctions. *Nat. Nanotechnol.* **2016,** *11*, 170-176.

(188) Liu, S.; Zhang, X.; Luo, W.; Wang, Z.; Guo, X.; Steigerwald, M. L.; Fang, X. Single-molecule detection of proteins using aptamer-functionalized molecular electronic devices. *Angew. Chem. Int. Ed.* **2011,** *50*, 2496-2502.

(189) Kim, Y.; Jeong, W.; Kim, K.; Lee, W.; Reddy, P. Electrostatic control of thermoelectricity in molecular junctions. *Nat. Nanotechnol.* **2014,** *9*, 881.

(190) Gao, L.; Li, L.-L.; Wang, X.; Wu, P.; Cao, Y.; Liang, B.; Li, X.; Lin, Y.; Lu, Y.; Guo, X. Graphene–DNAzyme junctions: a platform for direct metal ion detection with ultrahigh sensitivity. *Chem. Sci.* **2015,** *6*, 2469-2473.

(191) Xiang, D.; Wang, X.; Jia, C.; Lee, T.; Guo, X. Molecular-scale electronics: from concept to function. *Chem. Rev.* **2016,** *116*, 4318-4440.

(192) Xu, B.; Tao, N. J. Measurement of single-molecule resistance by repeated formation of molecular junctions. *Science* **2003,** *301*, 1221-1223.

(193) Nichols, R. J.; Higgins, S. J. Molecular junctions: single-molecule contacts exposed. *Nat. Mater.* **2015,** *14*, 465-466.

(194) Cui, X.; Primak, A.; Zarate, X.; Tomfohr, J.; Sankey, O.; Moore, A.; Moore, T.; Gust, D.; Harris, G.; Lindsay, S. Reproducible measurement of single-molecule conductivity. *Science* **2001,** *294*, 571-574.

(195) Nichols, R. J.; Higgins, S. J. Single molecule nanoelectrochemistry in electrical junctions. *Acc. Chem. Res.* **2016,** *49*, 2640-2648.

(196) Chen, F.; Li, X.; Hihath, J.; Huang, Z.; Tao, N. Effect of anchoring groups on single-molecule conductance: comparative study of thiol-, amine-, and carboxylic-acid-

terminated molecules. *J. Am. Chem. Soc.* **2006,** *128*, 15874-15881.

(197) Li, Z.; Smeu, M.; Ratner, M. A.; Borguet, E. Effect of anchoring groups on single molecule charge transport through porphyrins. *J. Phys. Chem. C* **2013,** *117*, 14890-14898.

(198) Brooke, R. J.; Jin, C.; Szumski, D. S.; Nichols, R. J.; Mao, B.-W.; Thygesen, K. S.; Schwarzacher, W. Single-molecule electrochemical transistor utilizing a nickel-pyridyl spinterface. *Nano Lett.* **2014,** *15*, 275-280.

(199) Kubatkin, S.; Danilov, A.; Hjort, M.; Cornil, J.; Brédas, J.-L.; Stuhr-Hansen, N.; Hedegård, P.; Bjørnholm, T. Single-electron transistor of a single organic molecule with access to several redox states. *Nature* **2003,** *425*, 698-701.

(200) Haiss, W.; van Zalinge, H.; Higgins, S. J.; Bethell, D.; Höbenreich, H.; Schiffrin, D. J.; Nichols, R. J. Redox state dependence of single molecule conductivity. *J. Am. Chem. Soc.* **2003,** *125*, 15294-15295.

(201) Xu, B.; Zhang, P.; Li, X.; Tao, N. Direct conductance measurement of single DNA molecules in aqueous solution. *Nano Lett.* **2004,** *4*, 1105-1108.

(202) Osorio, H. M.; Catarelli, S.; Cea, P.; Gluyas, J. B.; Hartl, F. e.; Higgins, S. J.; Leary, E.; Low, P. J.; Martín, S.; Nichols, R. J. Electrochemical single-molecule transistors with optimized gate coupling. *J. Am. Chem. Soc.* **2015,** *137*, 14319-14328.

(203) Xiao, X.; Xu, B.; Tao, N. Conductance titration of single-peptide molecules. *J. Am. Chem. Soc.* **2004,** *126*, 5370-5371.

(204) Selzer, Y.; Cabassi, M. A.; Mayer, T. S.; Allara, D. L. Thermally activated conduction in molecular junctions. *J. Am. Chem. Soc.* **2004,** *126*, 4052-4053.

(205) Haiss, W.; van Zalinge, H.; Bethell, D.; Ulstrup, J.; Schiffrin, D. J.; Nichols, R. J. Thermal gating of the single molecule conductance of alkanedithiols. *Faraday Discuss.* **2006,** *131*, 253-264.

(206) Kuznetsov, A. M.; Sommer-Larsen, P.; Ulstrup, J. Resonance and environmental fluctuation effects in STM currents through large adsorbed molecules. *Surf. Sci.* **1992,** *275*, 52-64.

(207) Weiss, E. A.; Tauber, M. J.; Kelley, R. F.; Ahrens, M. J.; Ratner, M. A.; Wasielewski, M. R. Conformationally gated switching between superexchange and

hopping within oligo-p-phenylene-based molecular wires. *J. Am. Chem. Soc.* **2005,** *127*, 11842-11850.

Chapter 2 General Experimental

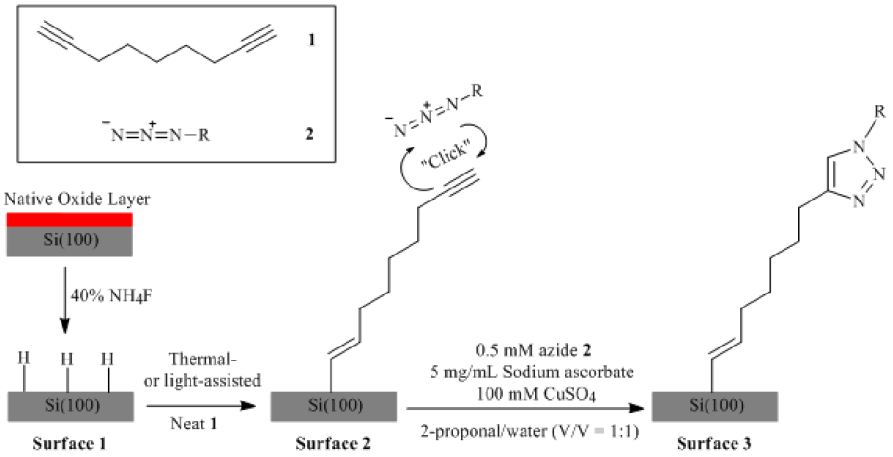

2.1 Introduction

This section mainly specifies the main materials, general experimental procedures and instrumentation used throughout this thesis work. More details including synthetic protocols, electrochemical analysis and surface modifications and characterizations on specific experiments are presented in the experimental sections of relevant chapters.

2.2 Materials

2.2.1 Chemicals

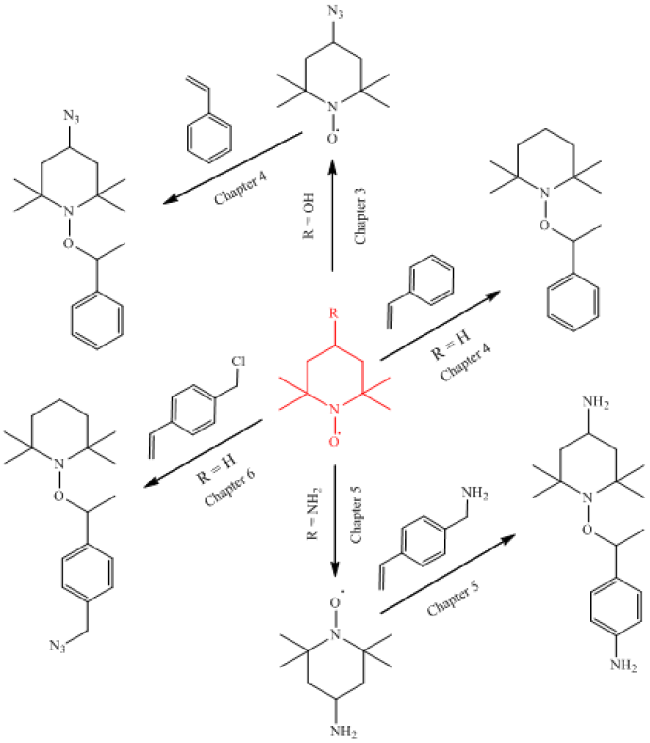

Figure 2.1 The structures of nitroxides and alkoxyamines studied in this thesis.

All chemicals used in this thesis, unless noted otherwise, were of analytical grade and used as received. The specifications of chemicals, solvents, and electrodes used in each chapter are detailed in the corresponding experimental sections. The main chemicals (nitroxides and alkoxyamines) studied in this thesis are summarized in Figure 2.1, where nitroxides highlighted in red are purchased from Sigma-Aldrich and used directly as received. These precursors are then either tailored to new nitroxides or reacted with alkenes to yield alkoxyamines. Nitroxides are stable persistent radicals with an unpaired electron located on the N-O resonance structure, whereas alkoxyamines are heat-labile

molecules which undergo thermal fragmentation processes into nitroxides and carbon-centered radicals. The nuclear magnetic resonance (NMR) and/or high resolution mass spectrometry (HRMS) techniques were used to characterize the synthesized products with detailed spectra listed in the corresponding chapters.

2.2.2 Electrode materials

There were three materials used as working electrodes in this thesis. In the diffusive systems (Chapter 4), either platinum disks or platinum microelectrodes were used as working electrodes. Using a smooth circular or figure-eight motion, the wet disk electrode surfaces were firstly cleaned by polishing the electrode on a microcloth pad with 0.03 μm alumina suspension. After ca. 5 minutes, the electrodes were rinsed with distilled water and sonicated in the sequential solvents of distilled water, methanol and distilled water for removing the residual abrasive particles. It is worth noting that the electrode response sometimes was attenuated due to slow oxidation of platinum material; the electrode surface therefore needed to be regenerated electrochemically. This issue was addressed by electrochemical treatment of the mechanically-polished platinum disk electrodes through performing cyclic voltammetry in the potential range of -0.2 V to 1.2 V (vs. Ag/AgCl), when the cleaned platinum electrode showed cyclic voltammetry as illustrated in Figure 2.2. Silicon wafers and crystal Au(111) as working electrodes used on surface models are presented in Chapters 3, 4 and 5. The silicon wafers were cleaned by freshly-made Piranha solution under ca. 100 °C and the cleaning procedure is detailed in the experimental section of relevant chapters. When assembling the silicon samples, the ohmic contact between the silicon electrodes and a copper plate was ensured by rubbing the back of the silicon electrodes and painting them evenly with gallium-indium eutectics, aiming to expose the bulk of the silicon samples. The single crystal Au(111) electrode substrate used in the STM-BJ setup was cleaned by flame annealing and then quenched with methanol. In addition, all glassware in STM-BJ experiments and PTFE components for assembling silicon electrodes were also cleaned with Piranha solution followed by washing with copious 18.2 MΩ cm^{-1} Milli-Q water.

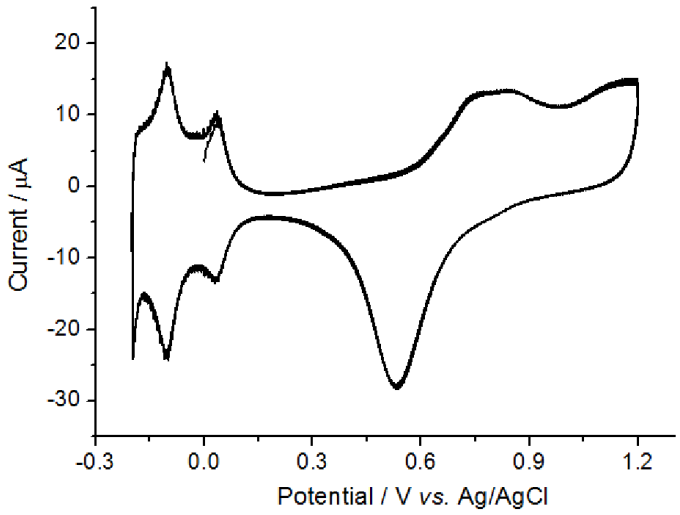

Figure 2.2 Cyclic voltammetry of 3 mm platinum disk electrode in 0.5 M H_2SO_4, the sweep rate was 100 mV s^{-1} and scanning cycles was 10.

2.3 Electrochemical experiments

All electrochemical measurements were performed using a CHI electrochemical workstation. A customized PTFE three-electrode cell was used on silicon surface experiments, while the electrochemical experiments in the diffusive system were carried out in glass vials. A coiled platinum wire was used as the auxiliary electrode and the reference electrode was either Ag/AgCl (in 3 M NaCl) in aqueous solutions or leakless Ag/AgCl in organic media. All potential values are referred to *E*, and reported against the Fc/Fc^+ redox couple. The electrolyte solutions had to be freshly prepared and de-oxygenated by bubbling with inert gas.

In this thesis, investigations were carried out on the kinetic and thermodynamic parameters for both the surface electrochemical reaction process (Chapter 3) and solution electrochemical-chemical-electrochemical mechanism (Chapter 4) using cyclic voltammetry and chronoamperometry techniques with the aid of digital simulations and quantum calculations. To be more specific, reasonable explanations have been given for the non-ideal electrochemical phenomena (anti-thermodynamic inverted redox peaks and < 90.6 mV FWHM value) on the surface models, which have been ascribed to electrostatic interplays between surface charged species and space charges in the semiconductor. Emphasis has also been placed on the effect of the electrostatic environment within an electric double layer on the C-ON bonds cleavage

in alkoxyamine molecules. Understanding the electrostatic role played in these cases has been of help in analyzing correctly the kinetic behavior of electron-transfer on the semiconductor surface as well as in manipulating the chemical reactivity in organic electrochemistry.

2.4 Analysis of peak inversion using the Laviron model

Peak inversion voltammetries (contra-thermodynamic cyclic voltammetries) on TEMPO monolayers experimented with in Chapter 3 were encountered. The attractive interactions in TEMPO monolayers were quantitatively analyzed based on a Laviron model for explaining the changes in FWHM values.

The idealized model assumes the following hypothesis:

i) o and r (oxidized and reduced species) are strongly adsorbed (the contribution to the current for dissolved species is negligible).
ii) The process is Nernstian.
iii) Adsorption and desorption do not occur during the scan or are fast compared with the overall process.
iv) Frumkin isotherm applies.
v) $a_{o,}$ a_r, a_{or}, b_o and b_r are potential independent.
vi) The surface occupied by one molecule of r is equal to the surface occupied by one molecule of o.

Where $a_{o,}$ a_r, a_{or} are the constants of interaction between molecules of o, r and o-r respectively. b_o and b_r are the adsorption coefficients of o and r respectively.

Under these assumptions the current expression for the cathodic peak is:

$$i = -\Psi \frac{n^2F^2vA\Gamma_T}{RT} \quad [1]$$

Where,

$$\Psi = \frac{f(1-f)}{1-2af(1-f)} \quad [2]$$

$$f = \frac{\theta_O}{\theta_T} \quad [3]$$

$$a = \ddot{u}G\theta_T \quad [4]$$

$$G = a_o + a_r - a_{or} \quad [5]$$

Where *n*, *F*, *R* and *T* have the usual meaning, A is the electrode area, *v* is the scan rate, Γ_T is the electrode surface concentration, ü are the number of molecules of water displaced by o or r and θ_O and θ_T are the coverages of o and o + r.

And the potential expression is:

$$E = E_p + \frac{RT}{F}\left[ln\left(\frac{f}{1-f}\right) + a(1-2f)\right] \qquad [6]$$

and

$$E_p = E^0 - \frac{RT}{nF} ln\left(\frac{b_o}{b_r}\right) + \frac{RT}{nF}(a_r - a_o)ü\theta_T \qquad [7]$$

Where E_p is the potential at which the current is maximum and E^0 is the formal potential.

For the fitting, "*a*" was calculated trough the FWHM according to the following expression that can be derived from [2] and [4]:

$$FWHM = \frac{2RT}{nF}\left[ln\left(\frac{1+\beta}{1-\beta}\right) - üG\theta_T\beta\right] \qquad [8]$$

where

$$\beta = \frac{\sqrt{2-}üG\theta_T}{\sqrt{4-}üG\theta_T} \qquad [9]$$

Thus the above model was applied to give a straightforward explanation of the shape of the backward peak, without explaining the change in E_p of the backward peak and the relative position and shape of the forward peak. This will be the subject of further studies.

It can be seen that a narrowing of the cathodic peak occurred as the "switching off" was made at more negative potentials, thus indicating an increase in attractive interactions. Importantly, it can also be observed that there is a broadening in the peaks as the dielectric constant of the solvent increases. This can be observed in the cathodic as well as in the anodic peaks.

It was seen that this behavior was independent of the coverage (see Figure 3.16 and Figure 3.17).

Ref. Laviron, E. *J. Electroanal. Chem. and Interfacial Electrochem.* **1974**, *52*, 395-402.

2.5 Surface characterizations

The monolayers attached to silicon surfaces were characterized with X-ray photoelectron spectroscopy (XPS) and X-ray reflectivity (XRR) techniques.

XPS was used to measure the elemental composition, providing the chemical and electronic states of elemental states that exist within the prepared monolayer. These spectra were recorded by irradiating a material with a beam of X-rays while measuring the kinetic energy and number of electrons that escape from the material interior. XRR was employed to characterize the thickness of monolayers. The working principle of this technique is to reflect a beam of X-rays from an electrode surface and to then monitor the intensity of X-rays from the reflected angle direction. The specifications for XPS and XRR instruments and parameters settings are detailed in the *Surface Characterization section* in Chapters 3 and 4. Detailed parameters and working environment can be found in relevant experiments.

Chapter 3 TEMPO Monolayers on Si(100) Electrodes: Electrostatic Effects by the Electrolyte and Semiconductor Space-Charge on the Electroactivity of a Persistent Radical

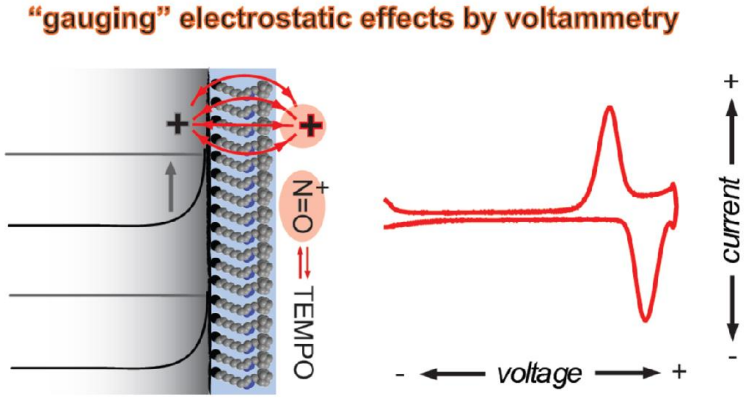

3.1 Abstract

This chapter demonstrates the effect of electrostatic interactions on the electroactivity of a persistent organic free radical. This was achieved by chemical modification of molecules of 4-azido-2,2,6,6-tetramethyl-1-piperdinyloxy (4-N_3-TEMPO) onto monolayer-modified Si(100) electrodes using a two-step chemical procedure to preserve the open-shell state and hence the electroactivity of the nitroxide radical. Kinetic and thermodynamic parameters for the surface electrochemical reaction were investigated experimentally and analyzed with the aid of electrochemical digital simulations and quantum-chemical calculations of a theoretical model of the tethered 2,2,6,6-tetramethyl-1-piperdinyloxy (TEMPO) system. Interactions between the electrolyte anions and the TEMPO grafted on highly doped (i.e., metallic) electrodes can be tuned to predictably manipulate the oxidizing power of surface nitroxide/oxoammonium redox couple, hence showing the practical importance of electrostatics on the electrolyte side of the radical monolayer. Conversely, for monolayers prepared on the poorly doped electrodes, the electrostatic interactions between the tethered TEMPO units and the semiconductor (i.e., space-charge) become dominant and result in drastic kinetic changes to the electroactivity of the radical monolayer as well as electrochemical non-idealities that can be explained as an increase in the self-interaction "*a*" parameter that leads to the Frumkin isotherm.

3.2 Introduction

To realize the full technological potential that molecular and supramolecular systems hold, the ability to control molecular topology, and hence function, needs to be coupled to the sturdiness of a solid device.[1, 2] Persistent organic free radicals have a key role in chemistry and biology,[3] and nitroxide radicals, such as the 2,2,6,6-tetramethyl-1-piperidinyloxyl radical generally referred to as TEMPO, and its derivatives are very interesting both from a fundamental[4-6] as well as from an applied[7] point of view. Assembly of persistent radicals on solid surfaces by physisorption is often complicated by the competition between the thermodynamic assembly and unwanted kinetic traps;[8] hence, chemical routes to tether TEMPO species onto a solid, such as gold- and carbon-

based materials are starting to appear.[9-11] Silicon, and in particular the (100) orientation, remains the technologically most relevant material of our age,[12, 13] and this material is still bringing fresh momentum to the fields of electrochemistry,[14] spintronics,[15] and molecular electronics.[16] No reports are available for the tethering of nitroxide radicals on silicon electrodes. This is presumably because of the ease of binding between silicon surface bonds and the unpaired valence electron of the singly-occupied molecular orbital of the TEMPO molecule, which would result in the loss of the free radical character.[17] Here, this thesis addresses this issue using a two-step chemical route to preserve the unpaired spin upon grafting. A Si(100)–H surface was first functionalized by the thermal hydrosilylation of α,ω-alkynes to yield a short functional monolayer where direct electrical communication between a grafted molecule and the substrate was still possible.[18, 19] Thereafter, TEMPO was attached with the radical preserved.

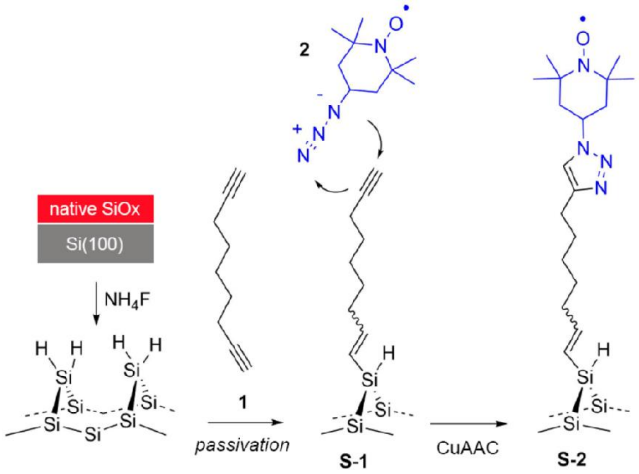

Scheme 3.1 Thermal hydrosilylation of 1,8-nonadiyne **1** at a Si(100)-H electrode (**S-1**) and covalent attachment of 4-azido-TEMPO **2** via CuAAC "Click" reactions to yield the redox-active radical film (**S-2**).

The properties of a near-surface region are remarkably different to the properties of the bulk. For instance, issues of mass transport can be neglected. Similarly, the chemical interactions of a grafted molecule with either the solid, neighboring molecules or supporting electrolyte molecules may dramatically change the chemical,[20] optical[21] or redox[22-24] properties. The purpose of the current study is to investigate how the electrostatic interactions between surface-grafted TEMPO units and residual charges in the semiconductor space-charge, or electrolyte ions, can predictably tune the

electroactivity of a common radical species. To achieve both the passivation of the substrate against anodic decomposition[18] as well as to circumvent the high reactivity of the Si–H surface toward the oxygen function in the TEMPO molecule, reliance on an established wet chemistry protocol to prepare alkyne-terminated monolayers (**S-1**, Scheme 3.1) was adopted.[19, 25] The chemical passivation of the Si(100) surface, as depicted in Scheme 3.1, is generally proven to be a difficult experimental task,[26] and a definitive mechanism for the thermal hydrosilylation of 1-alkynes is still debated.[27, 28] The mainly dihydride phase (=SiH_2) of the chemically etched (100) surface[29-31] does not allow for a complete reaction of Si–H sites,[32] but if the monolayer can retain a degree of π-π interactions, anodic decomposition of the substrate can be greatly limited.[18] The 1-alkyne moiety that remains exposed at the monolayer distal end in **S-1** samples can engage in highly selective copper-catalyzed alkyne-azide cycloaddition reactions (CuAAC[33]) to immobilize an azide-tagged version of TEMPO (**S-2**). This chemistry opens up access to an interface where (i) the Si/C contrast enables one to complement analytical electrochemical methods with surface-sensitive X-ray spectroscopic techniques,[18] and (ii) the presence of a band gap in the semiconducting substrate allows one to shift redox reactions contra-thermodynamically if assisted by visible radiation (i.e. energetic gain in a catalytic application of the radical film).

3.3 Experimental methods

3.3.1 Chemicals and materials

Unless otherwise noted, all chemicals were of analytical grade and used as received. Chemicals used in surface modification procedures and electrochemical experiments were of high purity (>99%). Hydrogen peroxide (30 wt.% in water), ammonium fluoride (PuranalTM, 40 wt.% in water), and sulfuric acid (PuranalTM, 95-97%) used in wafers cleaning and etching procedures were of semiconductor grade from Sigma-Aldrich. 1,8-Nonadiyne (**1**, Sigma-Aldrich, 98%) was redistilled from sodium borohydride (Sigma-Aldrich, 99+%) under reduced pressure (80 °C, 10−12 Torr) and stored under a high purity argon atmosphere prior to use. 4-Azido-2,2,6,6-tetramethyl-1-piperdinyloxy (**2**, 4-N_3-TEMPO) was prepared in two-steps from 4-hydroxy-2,2,6,6-

tetramethyl-1-piperdinyloxy (4-OH-TEMPO, Sigma-Aldrich, 97%) through published methods[34] with minor modifications (Figure 3.1). Thin-layer chromatography (TLC) was performed on silica gel using Merck aluminium sheets (60 F254). Merck 60 Å silica gel (220−400 mesh particle size) was used for column chromatography. Gas chromatography-mass spectrometry (GC-MS) analyses were performed by means of an Agilent Technologies 7890A GC system equipped with a HP-5 capillary column (5% phenyl methyl siloxan, 30 m × 250 μm × 0.25 μm) and interfaced with an Agilent 5975N MSD scheme operating in electron impact (EI) mode. The helium carrier gas flow-rate was 14 mL/min and the temperature was increased from 100 to 280 °C at a temperature ramp rate of 15 °C/min. The column was held at the initial and final temperatures for 5 min. Tetrabutylammonium perchlorate (Bu_4NClO_4, Sigma-Aldrich, >99%) used as supporting electrolyte was recrystallized twice from 2-propanol. Milli-Q™ water (> 18 MΩ cm) was used to prepare solutions, chemical reactions and surface cleaning procedures. Dichloromethane, 2-propanol and ethanol for surface cleaning procedures were redistilled prior to use. Prime grade, single-side polished silicon wafers, 100-oriented (<100> ± 0.5°), p-type (boron-doped), 500 ± 25 μm thick, with nominal resistivity of 0.001–0.003 Ω cm were obtained from Siltronix, S.A.S. (Archamps, France) and are referred to as highly doped. Prime grade, single-side polished silicon wafers, 100-oriented (<100> ± 0.09°), n-type (phosphorous-doped), 500 ± 25 μm thick, 1–10 Ω cm resistivity were purchased from Virginia Semiconductors, Inc. (Fredericksburg, VA) and are referred to as lowly doped.

3.3.2 Syntheses

High-resolution mass spectral data (HRMS, mass accuracy 2-4 ppm) of compounds **A** and **2** were obtained using a Waters Xevo QTof MS via electrospray ionization (ESI) experiments and infusing the sample at 8 μL/min. Electron paramagnetic resonance (EPR) spectra of a 100 μM solution of 4-azido-TEMPO **2** in hexane were recorded on a Bruker EMX EPR spectrometer. The microwave frequency was set to 9.87 GHz, attenuator to 30.0 Db, sweep width of 100 G, modulation frequency of 100 kHz, modulation amplitude of 1 G, time constant of 20.49 ms, conversion time of 81.92 ms

and sweep time of 83.89 s.

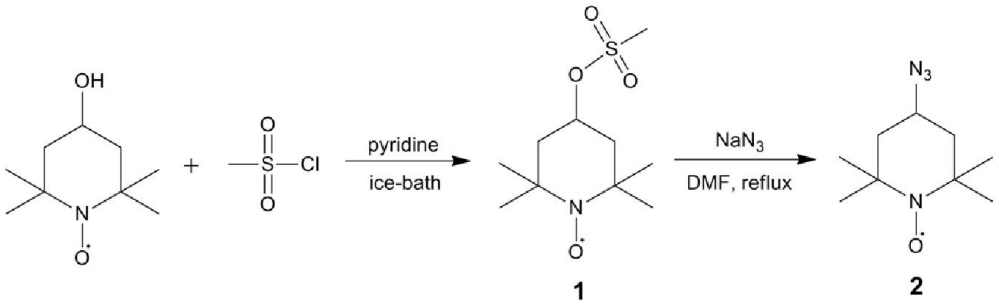

Figure 3.1 Synthesis of 4-azido-TEMPO **2**.

4-Methanesulfonyl-oxy-2,2,6,6-tetramethylpiperidine-1-oxyl (1). To an ice-cold solution of 4-hydroxy-TEMPO (0.86 g, 5 mmol) in anhydrous pyridine (5 mL), methane sulfonyl chloride (0.8 mL, 10.3 mmol) was added dropwise under an argon atmosphere. The mixture was allowed to warm up to room temperature and stirred for a 6 hours period. An ice-cold aqueous saturated solution of sodium bicarbonate (10 mL) was added to the reaction mixture and the solution was extracted with chloroform (4 × 15 mL). The combined organic extracts were washed with saturated sodium bicarbonate (2 × 15 mL) and water (2 × 15 mL), dried over anhydrous magnesium sulfate, filtered, and the filtrate was dried under vacuum to give **1** as an orange solid (1.13 g, 90%). HRMS (*m*/*z*): $[M+H]^+$ calcd for $C_{10}H_{21}NO_4S$ 251.1191; found 251.1185.

4-Azido-TEMPO (2). Sodium azide (162 mg, 2.5 mmol) was added in one portion to a stirred solution of 4-methanesulfonyl-oxy-2,2,6,6-tetramethylpiperidine-1-oxyl (**1**, 312 mg, 1.25 mmol) in *N*,*N*-dimethylformamide (10 mL). The suspension was stirred at 110 °C under argon atmosphere overnight. Upon cooling, diethyl ether (50 mL) was added to the reaction mixture. The organic solution was washed with a saturated solution of sodium bicarbonate (25 mL) and water (4 × 25 mL). The organic layer was separated and dried with anhydrous magnesium sulfate. After filtration and removal of the solvent under vacuum, the crude product was purified by column chromatography (silica gel, hexane/ethyl acetate, 25/1, v/v) to give 57.21 mg of **2** as an orange solid (0.29 mmol, 58%). The EPR signal of **2** was centered at a magnetic field of 3516 G (*g* factor occurred at around 1.9), which is in good agreement with TEMPO species. HRMS (*m*/*z*): $[M+H]^+$ calcd for $C_9H_{18}N_4O$, 198.1481; found 198.1485.

3.3.3 Surface modification

Acetylene-functionalized Silicon(100) Electrodes (S-1). Assembly of the acetylenylated Si(100) surface (**S-1**) by covalent attachment of the diyne **1** followed a previously reported procedure (Scheme 3.1).[18, 19] In brief, silicon wafers were cut into pieces (approximately 10 × 30 mm^2), cleaned for 20−30 min in hot Piranha solution (100 °C, a 3:1 (v/v) mixture of concentrated sulfuric acid to 30% hydrogen peroxide ***Caution:*** *piranha solution is a strong oxidant and reacts violently with organic substances*), rinsed with water and then etched with a deoxygenated 40% aqueous ammonium fluoride solution for 5 min. The samples were then transferred, taking extra care to exclude air completely from the reaction vessel (a custom-made Schlenk flask), to a degassed (through a minimum of 30 min of argon bubbling) sample of diyne **1**. The samples were kept under a stream of argon while the reaction vessel was immersed in an oil bath set to 160 °C for 3 h. The flask was then opened to the atmosphere, and the functionalized surface samples (**S-1**) were rinsed several times with dichloromethane and rested for a 12 h period in a sealed vial at +4 °C under dichloromethane, before being further reacted with the TEMPO molecule **2**.

CuAAC Attachment of 4-Azido TEMPO onto the Acetylenyl Surface (S-2). CuAAC reactions were used to attach 4-azido-TEMPO (**2**) to the acetylenyl surface (**S-1**). To a reaction vial containing the alkyne-functionalized silicon surface (**S-1**) was added (i) the azide (**2**, 0.5 mM, 2-propanol/water, 1:1), (ii) copper(II) sulfate pentahydrate (20 mol% relative to the azide) and (iii) sodium ascorbate (100 mol% relative to the azide). Reactions were carried out in air, at room temperature, under ambient light, and unless noted otherwise, they were stopped by removal of the samples from the reaction vessel after a reaction time of 2 h. The surface-bound [1,2,3]-triazoles (**S-2**) were rinsed consecutively with copious amounts of ethanol, water, ethanol and dichloromethane and blown dry in argon before being analyzed.

3.3.4 Surface characterization

X-ray Photoelectron Spectroscopy. X-ray photoelectron spectra (XPS) were obtained on an ESCALAB 220iXL spectrometer fitted with a monochromatic Al Kα source

(1486.6 eV), a hemispherical analyzer and a 6 multichannel detector. Spectra of Si 2p (89–108 eV), C 1s (276–295 eV), N 1s (391–410 eV) and O 1s (523–542 eV) were recorded in normal emission (θ = 90°) with the analyzing chamber operating below 10^{-9} mbar. The resolution of the spectrometer is *ca*. 0.6 eV as measured from the Ag $3d_{5/2}$ signal (full width at half maximum, FWHM) with 20 eV pass energy. High-resolution scans were run with 0.1 eV step size, dwell time of 100 ms and the analyzer pass energy set to 20 eV. After background subtraction, spectra were fitted with Voigt functions. All energies are binding energies expressed in eV, obtained by applying to all samples a rigid shift to bring the energy of the C 1s peak to a value of 285.0 eV.

X-ray Reflectometry. X-ray reflectivity (XRR) profiles of **S-2** samples (highly doped) were measured under ambient conditions on a Panalytical Ltd X'Pert Pro Reflectometer using Cu Kα X-ray radiation (λ = 1.54056 Å). The X-ray beam was focused using a Göbel mirror and collimated with 0.2 mm pre-sample slit and a post-sample parallel plate collimator. Reflectivity data were collected over the angular range $0.05° \leq \theta \leq 5.00°$, with a step size of 0.010° and counting times of 10 s per step. Prior to measurements, samples were stored under argon and exposed to air for approximately 10 min in order to be aligned on the reflectometer. From the experimental data, structural parameters of the self-assembled structures were refined using the MOTOFIT analysis software with reflectivity data presented as a function of the momentum transfer vector normal to the surface $Q = 4\pi(\sin\theta)/\lambda$.[35] The Levenverg-Marquardt method was used to minimize χ^2 values in the fitting routines.

Electrochemical Characterization. Electrochemical experiments of the silicon electrodes (**S-2** samples) were performed in a PTFE three-electrode cell with the modified silicon surface as the working electrode, a platinum wire (ca. 30 mm^2) as the counter electrode, and a plastic body silver/silver chloride "leakless" as the reference electrode (eDAQ, part ET072-1). The reference electrode was checked against the ferrocene/ferricenium couple (Fc/Fc^+) at a glassy carbon electrode before and after each experiment. All potentials are reported versus the formal potential, E_f^0, for the Fc^+/Fc couple (1.0×10^{-3} M ferrocene solutions in acetonitrile containing either Bu_4NPF_6,

Bu_4NClO_4, Bu_4NO_3, Bu_4HSO_4 or $Bu_4NCF_3SO_3$). All solutions for electrochemical measurements of contained 1.0×10^{-1} M of the Bu_4N salt as supporting electrolyte. The surface coverage, Γ, in mol cm^{-2} was calculated from the faradaic charge taken as the background-subtracted integrated anodic current. All electrochemical experiments were performed at room temperature (23 ± 2 °C) in a grounded Faraday cage in air and either shielded from ambient light or deliberately illuminated (lowly doped samples, when stated) using a fiber-coupled high-power tungsten source from World Precision Instruments (model Novaflex optical illuminator) with an output of approximately 4500 lx. A rectilinear cross-section Viton gasket defined the geometric area of the working electrode to 28 mm^2. The back-side of the silicon sample was exposed with emery paper and rubbed with gallium-indium eutectic. A planar copper electrode was pressed against the sample backside and served as ohmic contact. Electrochemical measurements were performed using a CH instruments 650D electrochemical analyzer (CH Instruments, Inc.). The 95% confidence limit of the mean of experimentally-determined quantities, such as surface coverage Γ, and the voltage of the current peaks were calculated as $t_{n-1}s/n^{1/2}$, where t_{n-1} depended on the number of repeats and varied between 3.18 and 2.23,[36] s is the standard deviation, and n is the number of repeated measurements (n was between 3 and 10). The device flat-band potential (V_{FB}) was estimated for **S-2** samples on lowly doped electrodes from measurements of the open-circuit voltage (OCP) under illumination (Figure 3.15a).[37] Experimental cyclic voltammograms (CVs) of **S-2** samples were analyzed by a commercial digital simulation program (DigiElch 7©, ElchSoft). Butler-Volmer kinetics was used to estimate charge transfer parameters. A semi-infinite 1D diffusion at an electrode of planar geometry was assumed, all diffusion coefficients were set to 1×10^{-5} cm^2 s^{-1}. The number of equally- spaced nodes in the spatial grid perpendicular to the electrode was set to 39. The adsorption process was simulated on the basis of the Frumkin isotherm using different values for the self-interaction parameter a. Simulations in DigiElch of the surface redox reaction requires modeling a system made up by two redox couples and charge-transfer is assumed to proceed only by direct reduction/oxidation of the adsorbed species. The first couple (*sln.*), does not undergo a charge-transfer reaction (k was set to 0.0 s^{-1}) and it is entered

for the sole purpose of mimicking a species which is adsorbed on the electrode surface. The independent variables that describe the adsorption, i.e. the forward rate constant, k_f and the equilibrium constant, $K = k_f/k_b$ describing the adsorption process were set to 1×10^{10} and 1×10^{14}, respectively. Observed electrocatalytic curves were compared against simulations for a system comprising two redox-couples. One of these redox couples was the TEMPO unit strongly adsorbed on the electrode surface and played the role of a redox-mediator for the heterogeneous oxidation of bromide to bromine (written in DigiElch as $Br^- \rightarrow Br^{\bullet} + e^-$). The anodic wave did not plateau because this process is not the more common diffusive EC' mechanism. The follow-up homogeneous chemical step for the formation of tribromide anion from bromide was not considered in the simulation.[38] The standard potential and rate constant of the adsorbed redox couple were set to the experimental values of **S-2** samples on either illuminated lowly doped or dark highly doped electrodes, $D_{Br-} = D_{Br\bullet} = 1 \times 10^{-5}$ cm^2 s^{-1}, the $Br^-/Br^{\bullet}$ electrochemical process was neglected (k_0 = 0 cm s^{-1}) and the speed (k_f) of the heterogeneous reaction occurring between the adsorbed and not adsorbed redox couple was varied (oxoammonium + $Br^- \xrightarrow{k_f}$ TEMPO + $Br^{\bullet}$).

3.3.5 Computational methods

High-level *ab initio* calculations were used to predict the interaction energies between the Bu_4N counter-anions (HSO_4^-, NO_3^-, ClO_4^-, $CF_3SO_3^-$ and PF_6^-) and the oxidized **S-2** film. For these calculations, a truncated model of the **S-2** film containing the (oxidized) TEMPO ring substituted with the 4-methyl-1,2,3-triazole substituent (denoted **T-cat** for short) was utilized. Calculations were performed at a high level of theory, chosen on the basis of previous studies of the redox behavior of nitroxide radicals.[39-41] The high-level composite *ab initio* G3(MP2,CC)(+) method was utilized, which is a variation of standard G3(MP2,CC) theory[42] where calculations with the 6-31G(d) basis set are replaced with the 6-31+G(d) basis set (for better treatment of anions). This high-level methodology was utilized in conjugation with an ONIOM inspired approximation,[43, 44] with RMP2/GTMP2Large employed to model remote substituent effects. All geometry optimizations and frequencies calculations were performed at the M06-2X/6-31+G(d,p)

level of theory[45] and frequencies were scaled by recommended factors.[46] The SMD model was used to correct for implicit solvation effects.[47] All standard *ab initio* calculations were performed using the Gaussian 09[48] and Molpro 2012 Software packages.[49, 50]

To ensure maximum systematic error cancellation, consideration was only given to the relative ΔG_{IP} values. These were converted to absolute values using the experimental redox potential for the HSO_4^- salt as the reference species. This approach is analogous to the proton exchange method, which is able to provide accurate pK_a values, even when absolute pK_a predictions (those that do not use a reference acid) are significantly less accurate.[51] The calculated absolute ΔG_{IP} values and the optimized geometries are provided below.

3.4 Results and discussions

The grafting of the TEMPO moieties (**S-2**, Scheme 3.1) onto the acetylene-terminated Si(100) surfaces (**S-1**) was initially verified by XRR and XPS. XRR allows the thickness (*d*) of thin films to be measured with atomic resolution as a result of the high contrast in scattering length density (SLD)[52] of the organic molecules in the SAM (SLD ~1×10^{-5} Å^{-2}) compared to air (SLD = 0) and the silicon substrate (SLD = 2.01×10^{-5} Å^{-2}). Figure 3.2 shows the measured specular XRR curve for **S-2** samples. The theoretical fit to the experimental data is shown as a solid line.[35] Unlike the Fresnel-like decay of the Si(100)–H surface,[53] XRR profiles for **S-2** show clear interference thickness oscillations that could be simulated using a one-layer model of 16 Å thickness, which is close to the theoretical length of 14 Å. The refined value of SLD for the CuAAC-modified substrates (**S-2**) is 14.1×10^{-6} Å^{-2} and as high as to those achieved for SAMs on gold substrates in close-packed Langmuir-Blodgett films.[54] The surface roughness between the silicon surface and the monolayer, as determined by XRR refinement, was 2.9 Å, which is typical for high-quality silicon substrates.[55-57]

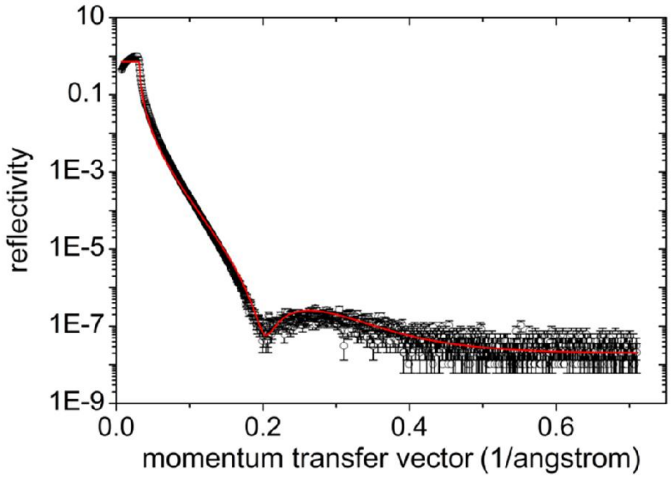

Figure 3.2 XRR profile of TEMPO monolayers (**S-2**) assembled on Si(100) electrodes by CuAAC reactions of 4-azido-TEMPO on monolayers of 1,8-nonadiyne.

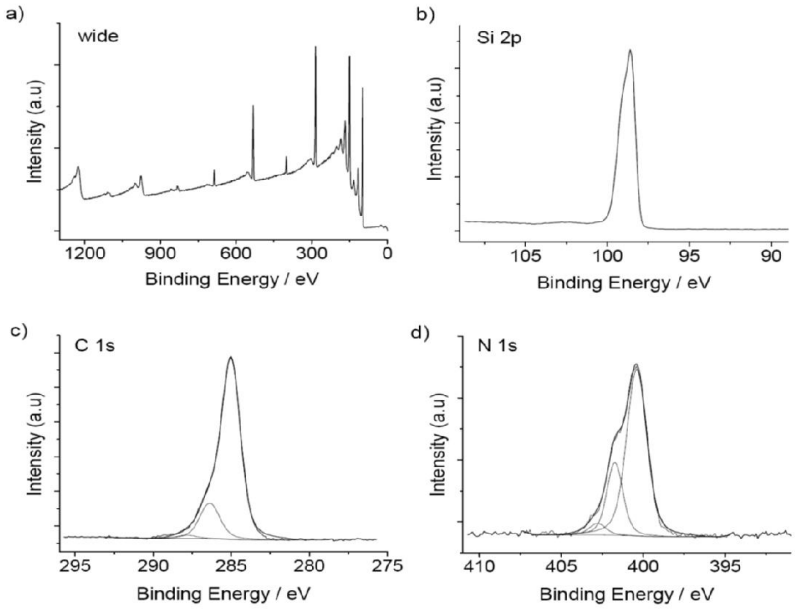

Figure 3.3 XPS spectra of TEMPO monolayers (**S-2**) assembled on highly-doped (HD hereafter) Si(100) electrodes by CuAAC reactions of 4-azido TEMPO **2** on monolayers of 1,8-nonadiyne (**S-1**). (a) Survey XPS scan. (b) High-resolution scan for the Si 2p region comprising two spin–orbit-split components. Silica-related emission (102–104 eV signal associated with SiO_x) were only minor - i.e. just above the spectrometer detection limit of *ca*. <0.05 SiO_x monolayers equivalents. (c) Narrow scan of the C 1s region. The signal was fit with three components at 285.0 (C–C), 286.4 (C–C/–N/–O) and 287.8 eV, comprising respectively of 8.1/10, 1.8/10, and 0.2/10 (adventitious oxidized carbon) of the total C 1s signal. (d) Narrow scan of the N 1s region with two main components at 401.7 and 400.4 eV (0.35:1 intensity ratio). The high binding energy satellite at 402.7 eV is assigned to a shake-up satellite of N–O electrons.

XPS spectra acquired for **S-2** samples are shown in Figure 3.3. This appearance of the N 1s electrons after the CuAAC reaction is in good agreement with the literature

for analogous derivatization procedures on solid surfaces.[19] There was no evidence for the high binding energy N 1s signal (*ca*. 405 eV[58, 59]) that corresponds to the electron-deficient nitrogen atom in the azido group, hence confirming negligible physisorption of the radical species in the film. A least-squares refinement of the N 1 emission gives three fitted peaks with binding energies of 400.4, 401.7 and 402.7 eV. The position of the main low binding energy line in the **S-2** samples is in agreement with the 400.6 eV previously assigned to nitroxide nitrogen atoms in thin films of the *p*-nitrophenyl nitroxide radical.[60] Electrons from the triazole heterocycle contributed to the 400.4 and 401.7 emissions only, with an expected ratio of the peak areas being *ca*. 2:1.[19, 61, 62] The weak shoulder observed on the high binding-energy side (402.7 eV) is be tentatively assigned to a shake-up satellite[63, 64] of N–O electrons.

Figure 3.4 shows CVs for **S-2** samples prepared on highly doped electrodes. The TEMPO films exhibited cyclic voltammetry (CV) waves of moderate stability (Figure 3.5) attributable to the chemically reversible nitroxide/oxoammonium ion oxidation/reduction process[23] and with a surface coverage, $\Gamma = (2.21 \pm 0.09) \times 10^{-10}$ mol cm^{-2} and the magnitude of the peak scales with the voltage scan rate (v) and not with the square root of v, which is indicative of an electroactive substrate-bound monolayer (Figure 3.6). With only few exceptions,[65] for most electrochemical experiments, a large excess of an inert electrolyte salt is necessary. This is done to restrict the potential gradient only within a distance of few nanometers from the surface and to compensate for charges created upon electron transfer, hence preventing an increase in local resistivity during the experiment. In a high dielectric constant solvent like acetonitrile, the electrochemical behavior of self-assembled monolayers depends strongly on the nature of the supporting electrolytes,[66, 67] and ion pairing with the redox unit is known to affect both kinetics and thermodynamics.[68]

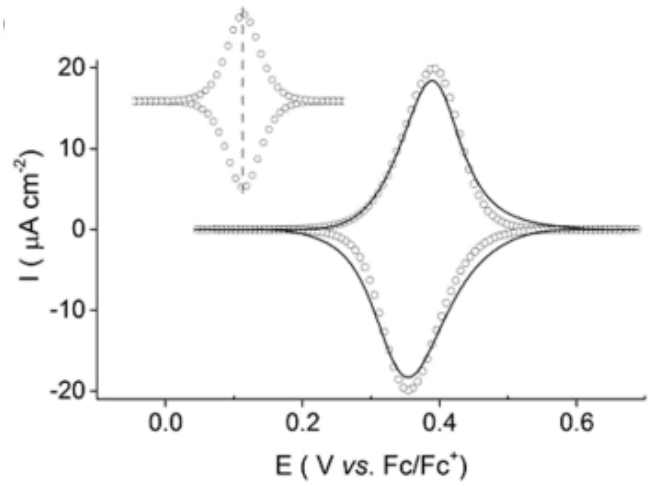

Figure 3.4 CV for **S-2** samples prepared on Si(100) electrodes (highly doped, 0.001–0.003 Ω cm). Background-subtracted observed (solid line) and simulated (symbols) voltammograms at 100 mV s^{-1} in MeCN containing 1.0 × 10^{-1} M Bu_4NClO_4. Figure inset shows the simulated voltammetry for a reversible and non-interacting electroactive monolayer system (*k* was set to 10^4 s^{-1} and Frumkin "*a*" was set to zero). Ideal adsorptive-shaped waves are symmetric with respect to E_f^0 and show a 90.6/*n* FWHM.

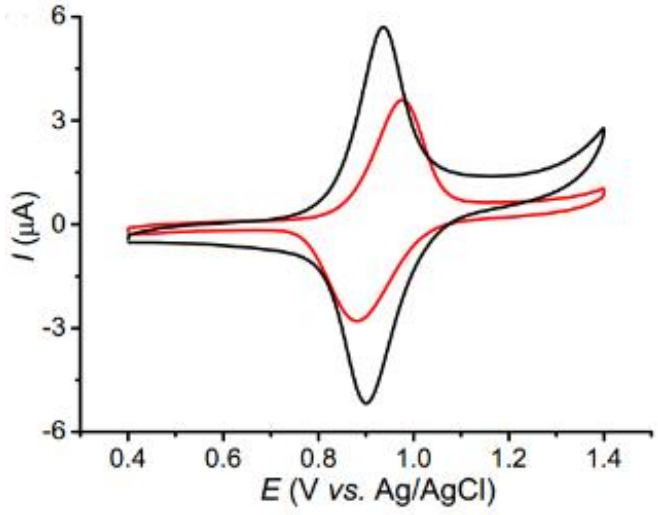

Figure 3.5 Representative CVs (v = 100 mV s^{-1}) for **S-2** samples (HD) before (black solid line) and upon (red dashed line) prolonged CV analysis (100 cycles) in 0.1 M Bu_4NClO_4/MeCN electrolytes. The measured nitroxide surface coverage, Γ, decreased by *ca*. 33% from 2.34× 10^{-10} mol cm^{-2} to 1.56 × 10^{-10} mol cm^{-2} after the 100 cycles. This stability is comparable, or better, than what has been reported in literature for TEMPO monolayers on metallic electrodes. For example, when TEMPO was attached onto a graphite felt electrode the current–voltage response decreased by 50% after 50 repeated CV scans in acetonitrile- or water-based electrolytes.[69] This chemical irreversibility is tentatively ascribed by Geneste and co-workers[69] to reactions of the oxoammonium species.

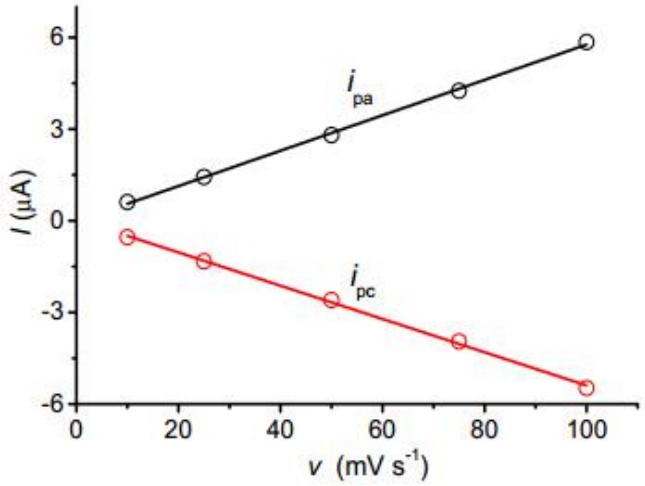

Figure 3.6 Linear relationship between voltage scan rate and experimental peak current (symbols) for S-2 samples on HD electrodes in 0.1 M Bu_4NClO_4/MeCN systems.

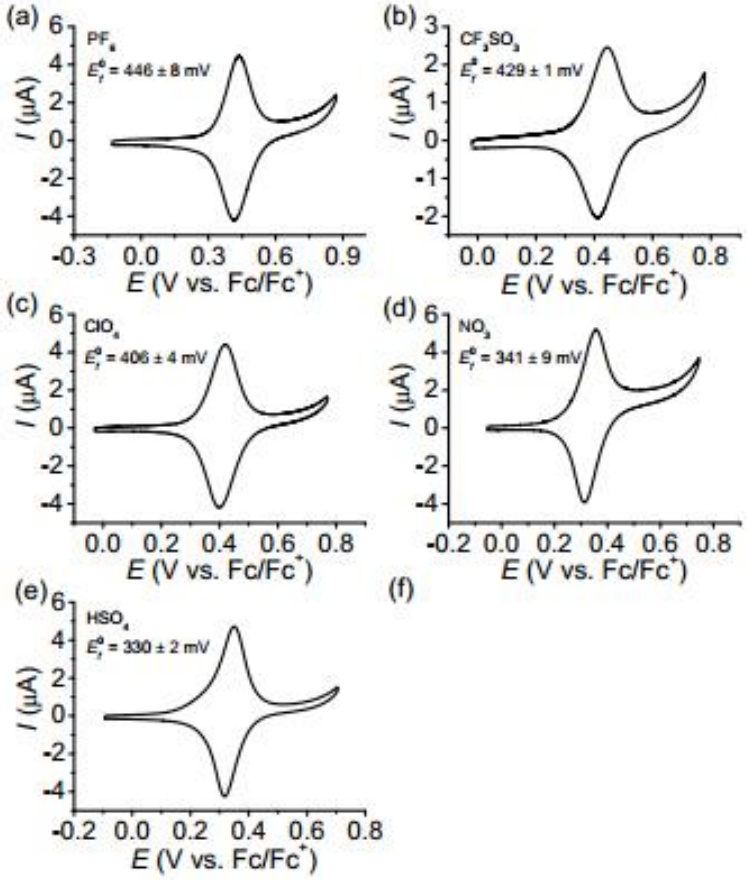

Figure 3.7 CVs of **S-2** samples on HD silicon electrodes in MeCN solutions containing different Bu_4N salts at a 0.1 M concentration (a-e). The experimental E_f^0 is indicated in each panel; with the exception of HSO_4^-, it moves progressively anodically with the decrease of the anions' Lewis basicity (see Table 3.2 for theoretical ΔG_{IP} values). The stronger than expected basicity of HSO_4^- compared with the other anions can be rationalized by the formation of a stabilizing H-bond with the 1,2,3-triazole ring.

Figure 3.7 displays CV data of TEMPO monolayers in acetonitrile solutions containing different Bu_4N salts. Notably, the position of the anodic and cathodic peaks appears to relate to the anion chemistry; the apparent formal potential (E_f^o) moves progressively anodically in the sequence $HSO_4^- < NO_3^- < ClO_4^- < CF_3SO_3^- < PF_6^-$ (Figure 3.8 and Table 3.1). With the exception of HSO_4^-, the magnitude of the displacement in E_f^0 tracks the empirical value of the anion Lewis basicity (Figure 3.8 and Table 3.2, *vide infra*). In the case of HSO_4^-, theoretical calculations (Tables 3.3-3.5) indicate that the additional stabilization is due to formation of a hydrogen bond with the azole ring (see Figure 3.9 and 3.10).

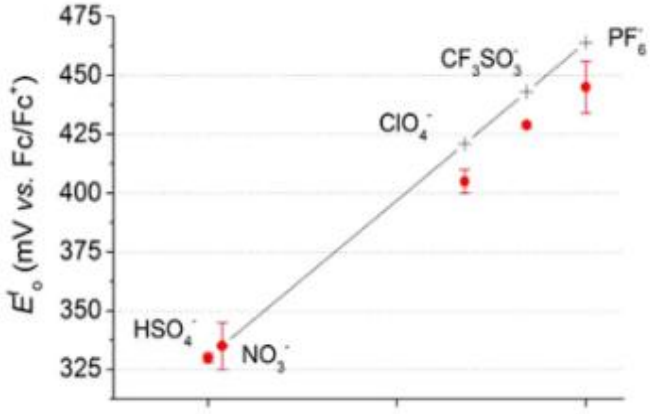

Figure 3.8 Shifts of the experimental E_f^0 (●) and changes to the theoretical redox potential (+) as a function of the chemical composition of the electrolyte anion (Tables 3.1 and 3.2).

Table 3.1 Experimental values of E_f^0 and FWHM for samples of **S-2** on HD electrodes in different electrolytes.

	[a]MeCN-PF_6	[a]MeCN-CF_3SO_3	[a]MeCN-ClO_4	[a]MeCN-NO_3	[a]MeCN-HSO_4
E_f^0	446 ± 8 mV	429 ± 1 mV	406 ± 4 mV	341 ± 9 mV	330 ± 2 mV
FWHM	119 ± 3 mV	112 ± 1 mV	102 ± 1 mV	94 ± 6 mV	95 ± 2 mV

[a]The number of independently prepared and analyzed samples was six for PF_6^-, three for $CF_3SO_3^-$, seven for ClO_4^-, five for NO_3^- and three for HSO_4^-.

Table 3.2 Absolute and relative ion-pairing energies (ΔG_{IP}) and theoretically predicted redox potentials.

Anion Species	Theoretical ΔG_{IP} (kJ mol^{-1})			Redox Potential (mV)	
	Absolute (Gas-phase)	Absolute (Solution)	Relative to HSO_4^- (Solution)	Theoretically Predicted (using HSO_4^- as a reference)	Experimental[a]
HSO_4^-	-357.89	-13.14	0.00	-	330 ± 2 mV
NO_3^-	-385.69	-12.67	0.48	335	341 ± 9 mV
ClO_4^-	-368.99	-4.35	8.79	421	406 ± 4 mV
$CF_3SO_3^-$	-355.13	-2.29	10.86	443	429 ± 1 mV
PF_6^-	-351.89	-0.24	12.90	464	446 ± 8 mV

[a]From Table 3.1

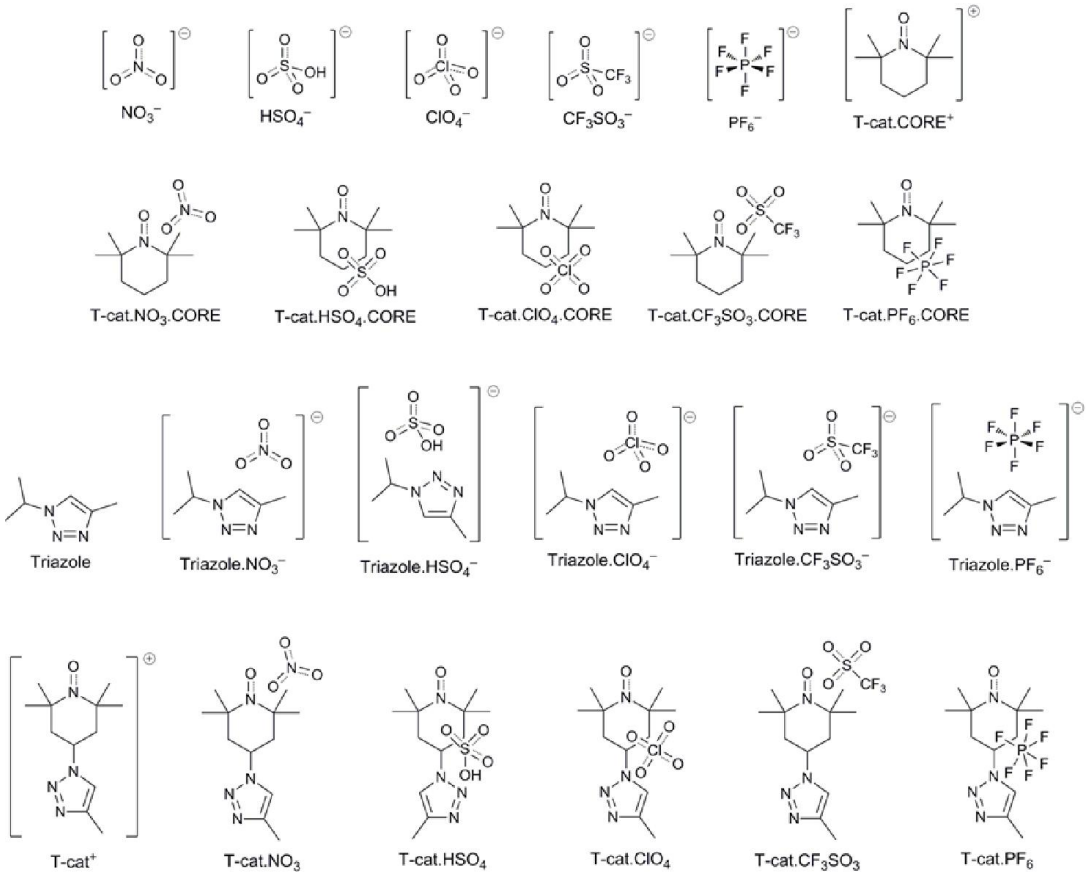

Figure 3.9 Chemical structures of all species examined in this work and their abbreviations.

Table 3.3 Raw electronic energies, thermal and entropic corrections and solvation energies. (Unless otherwise noted, units are given in Hartree)

Species	Corrections (25 °C)			Raw Energies					Thermochemistry and Solvation (25 °C)		
	S ($Jmol^{-1}K^{-1}$)	TC	ZPVE	M06-2X/ 6-31+G(d,p)	RMP2/ 6-31+G(d)	RMP2/ GTMP2Large	URCCSD(T)/ 6-31+G(d)	G3(MP2,CC)(+)	G_{gas} RMP2/Large	G_{gas} G3(MP2,CC)(+)	ΔG_{solv}
NO_3^-	245.49	0.004095	0.014175	-280.262886	-279.672565	-279.950505	-279.692192	-279.970132	-279.960114	-279.979741	-0.085166
HSO_4^-	300.82	0.005834	0.026394	-699.578238	-698.431818	-698.886156	-698.460133	-698.914471	-698.888089	-698.916404	-0.088232
ClO_4^-	265.83	0.005029	0.014974	-760.674608	-759.511145	-759.991598	-759.541332	-760.021785	-760.001783	-760.031970	-0.080608
$CF_3SO_3^-$	347.46	0.008101	0.027075	-961.320764	-959.658416	-960.371245	-959.701494	-960.414323	-960.375528	-960.418606	-0.075708
PF_6^-	301.77	0.007076	0.018826	-940.487981	-938.840109	-939.569234	-938.868521	-939.597646	-939.577601	-939.606013	-0.080185
T-cat.CORE$^+$	432.16	0.012952	0.257021	-483.266593	-481.853581	-482.419218	-482.011711	-482.577348	-482.198321	-482.356451	-
Tcat.NO_3.CORE	517.70	0.017068	0.273648	-763.686369	-761.684329	-762.529696	-761.862157	-762.707523	-762.297770	-762.475597	-
T-cat.HSO_4.CORE	562.22	0.019152	0.285415	-1182.997762	-1180.437245	-1181.460129	-1180.623885	-1181.646769	-1181.219409	-1181.406048	-
T-cat.ClO_4.CORE	545.10	0.018322	0.274040	-1244.084733	-1241.508825	-1242.557843	-1241.696644	-1242.745662	-1242.327382	-1242.515202	-
T-cat. CF_3SO_3.CORE	620.96	0.021628	0.286054	-1444.728493	-1441.654281	-1442.934328	-1441.855625	-1443.135671	-1442.697162	-1442.898505	-
T-cat.PF_6.CORE	595.55	0.020655	0.277639	-1423.889143	-1420.828020	-1422.126861	-1421.015559	-1422.314400	-1421.896198	-1422.083737	-
Triazole	408.03	0.010586	0.167094	-399.333293	-398.221613	-398.653164	-398.329157	-398.760708	-398.521819	-398.629363	-
Triazole.NO_3^-	529.79	0.015463	0.182570	-679.628304	-677.926942	-678.637280	-678.053774	-678.764112	-678.499411	-678.626243	-
Triazole.HSO_4^-	572.38	0.016811	0.195230	-1098.927358	-1096.669585	-1097.556250	-1096.805453	-1097.692118	-1097.409208	-1097.545076	-
Triazole.ClO_4^-	557.00	0.016558	0.183136	-1160.034716	-1157.761572	-1158.674856	-1157.898972	-1158.812256	-1158.538414	-1158.675814	-
Triazole. $CF_3SO_3^-$	637.79	0.019788	0.195211	-1360.680909	-1357.909262	-1359.054394	-1358.059736	-1359.204867	-1358.911822	-1359.062296	-
Triazole.PF_6^-	592.81	0.018722	0.186905	-1339.845409	-1337.087797	-1338.250141	-1337.224221	-1338.386564	-1338.111832	-1338.248256	-
T-cat$^+$	566.36	0.018697	0.322168	-763.509364	-761.397386	-762.224139	-	-	-761.947590	-	-0.104726
T-cat.NO_3	651.73	0.022732	0.339124	-1043.935155	-1041.235900	-1042.342383	-	-	-1042.054537	-	-0.047814
T-cat.HSO_4	664.64	0.024155	0.351795	-1463.247271	-1459.991239	-1461.272263	-	-	-1460.971789	-	-0.061650
T-cat.ClO_4	665.47	0.023904	0.339877	-1524.342510	-1521.070291	-1522.378955	-	-	-1522.090743	-	-0.046450
T-cat. CF_3SO_3	753.41	0.027318	0.351743	-1724.982654	-1721.211274	-1722.751749	-	-	-1722.458245	-	-0.046043
T-cat.PF_6	714.39	0.026267	0.343500	-1704.145101	-1700.387010	-1701.946395	-	-	-1701.657754	-	-0.050977

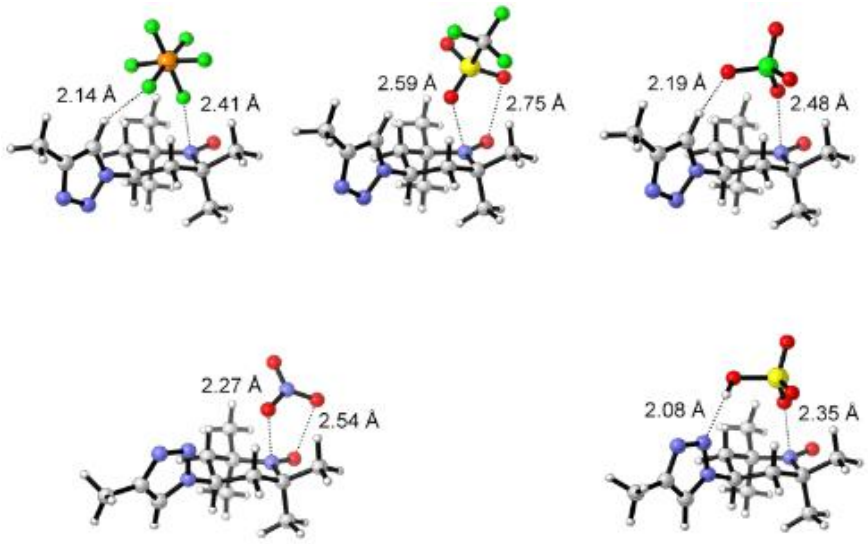

Figure 3.10 M06-2*X*/6-31+G(d,p) optimized geometries of the complexes between electrolyte anions and a truncated model of the **S-2** film containing the oxidized TEMPO substituted with the 4-methyl-1,2,3-triazole substituent (denoted **T-cat**).

Table 3.4 The ONIOM corrections used for each ion-pairing complex.

Anion Species	T-cat.CORE$^+$ Binding Energy (kJ mol^{-1})			Triazole Binding Energy (kJ mol^{-1})			Overall Correction
	RMP2/ GTMP2L	G3(MP2,CC)(+)	Correction	RMP2/ GTMP2L	G3(MP2,CC)(+)	Correction	
NO_3^-	-420.01	-420.19	-0.18	-88.25	-87.36	0.89	-0.18*
HSO_4^-	-406.31	-406.82	-0.51	-44.45	-44.47	-0.02	-0.54
ClO_4^-	-386.02	-384.71	1.31	-79.01	-78.14	0.87	2.18
$CF_3SO_3^-$	-377.72	-378.07	-0.35	-78.73	-78.33	0.39	-0.35*
PF_6^-	-363.39	-366.01	-2.62	-72.84	-74.07	-1.23	-3.84

*Triazole correction was not included because the lowest energy conformation of the respective T-cat. anion ion-pair complex did not have significant aromatic C-H anion interaction.

Table 3.5 Theoretically predicted ion-pairing energies (ΔG_{IP}).

Anion Species	Theoretical ΔG_{IP} (kJ mol^{-1})			
	Uncorrected RMP2 (Gas-phase)	ONIOM Corrected (Gas-phase)	ONIOM (Solution)	Relative to HSO_4^- (Solution)
NO_3^-	-385.5	-385.69	-12.67	0.48
HSO_4^-	-357.4	-357.89	-13.14	-
ClO_4^-	-371.2	-368.99	-4.35	8.79
$CF_3SO_3^-$	-354.8	-355.13	-2.29	10.86
PF_6^-	-348.0	-351.89	-0.24	12.90

The value of Γ was approximately 50% of that reported for close-packed TEMPO monolayers assembled on gold electrodes,[70] but even for this "diluted" system, the shape of the experimental redox waves is not ideal,[23] showing a minor asymmetry. The experimental FWHM is also independent of surface coverage in the range of Γ explored (Figure 3.11), and yet is larger than the theoretical values of 90.6/n mV (Figure 3.4 inset). For instance, the observed FWHM is ca. 100 mV for ClO_4^- or NO_3^--based electrolytes (102 ± 1 mV and 94 ± 6 mV, respectively) and upward to ca. 112 ± 1 mV and 119 ± 3 mV in $CF_3SO_3^-$ and PF_6^- solutions, respectively (Table 3.1). A small peak asymmetry coupled to a small increase (ca. 5-10 mV) over the ideal FWHMs can be simulated and accounted for in terms of slow charge transfer kinetics (Figure 3.4, simulated CV in symbols with refined electrochemical rate constant k and refined FWHM being 3.6 s^{-1} and 96 mV, respectively). At present, there is uncertainty as to what factors other than slow kinetics contribute to the nonideal FWHMs in the ClO_4^- and PF_6^- systems; especially because these nonidealities persist when the rate is enhanced by up to 5-fold for illuminated lowly doped substrates (*vide infra*).

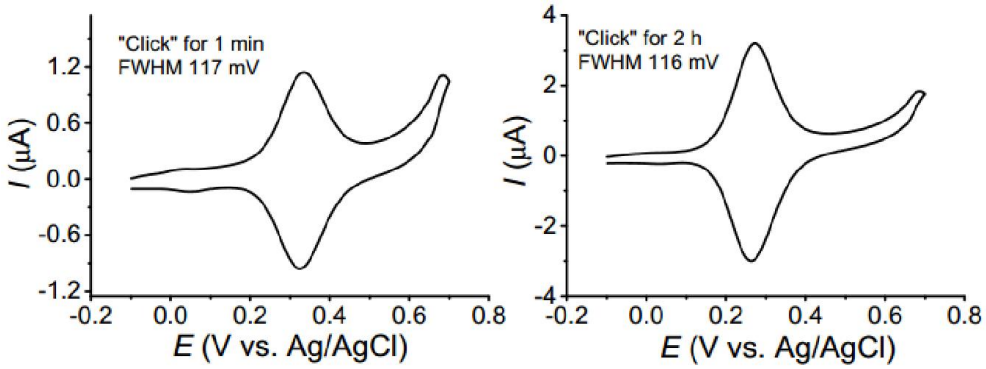

Figure 3.11 CVs of **S-2** samples on illuminated LD electrodes in 0.1 M Bu_4NClO_4/MeCN (voltage scan rate was 100 mV s^{-1}). The experimental FWHM is independent of surface charge (117 mV for 3.97×10^{-11} mol cm^{-2} and 116 mV for 1.31×10^{-10} mol cm^{-2}). The low coverage sample shown in the left panel (as well as in Figure 3.16) is obtained by reducing the CuAAC reaction time from 2 h to 1 min.

It is noted, however, that a large number of models have been proposed to explain such nonidealities,[71] and in the Nernstian case of an electrochemically reversible systems ($k \rightarrow \infty$),[72] when the energy of interaction between like molecules is larger than that between unlike molecules, the observed FWHM will be larger than that for the ideal noninteracting case.

In reversible systems, the extent of these putative electrostatic interactions have often been parameterized simply by introducing changes to the Frumkin *a* factor that leads to the corresponding isotherm (Figure 3.12).[73] However as noted above, the highly doped **S-2** systems in this thesis work have a finite electron transfer kinetics; hence using this approach would probably lead to an oversimplification and would fail to give a meaningful quantitative explanation on both peak broadening and shifts in E_f^0 values. Therefore, the discussion in this work focuses exclusively on the electrolyte-related shifts to E_f^0 and interpret the data by showing a correlation between the observed voltammograms and calculated quantities. Notably, the displacement in E_f^0 (Table 3.2) tracks the empirical values of the anions Lewis basicity with the exception of HSO_4^- for which, as noted above, a favorable hydrogen bond with the azole ring leads to additional stabilization. An electrostatic component can be separated for the Lewis acid-base interaction (oxoammonium-electrolyte anion interaction) and this electrostatic scheme brings about a reduction in the thermodynamic cost for the TEMPO oxidation. This is supported by the theoretical calculations of the oxoammonium-electrolyte anion interaction energies which are stabilizing overall and predict a progressive anodic shift in the redox potential in the same order as experiment: $HSO_4^- < NO_3^- < ClO_4^- < CF_3SO_3^- < PF_6^-$. In brief, the nature of the electrolyte anion appears to have a large effect on *i-E* curves in a way that is not quantifiable as a commonly reported adjustment of the Frumkin *a* term (Figure 3.12).

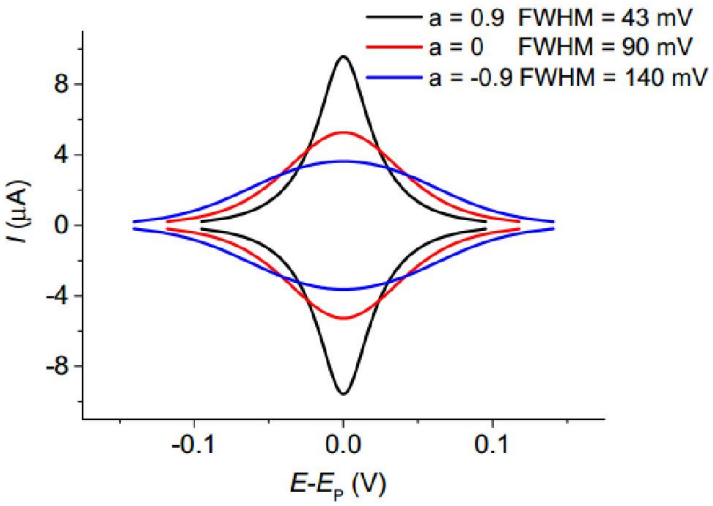

Figure 3.12 Simulated cyclic voltammograms for a reversible one-electron redox couple where both species are strongly adsorbed on the electrode surface. The Frumkin a term that leads to the isotherm under equilibrium was varied between -0.9 and 0.9. A = 0.28 cm^2, $\Gamma = 2 \times 10^{-10}$ mol cm^{-2} and the voltage sweep rate was set to 0.1 V s^{-1}. The calculated value of FWHM is indicated in the figure. The x-axis is E - E_p, that equals to the overpotential (E - E_0) if $b_o = b_r$ and $a_o = a_r$ where b_i is the absorption strength and a_i is the interaction parameter between i molecules (oxidized or reduced forms).

The direction of the displacement in E_f^0 values is consistent with the chemistry involved, and this implies that for a given bias, one is able to predictably alter the ratio of surface reductant to surface oxidant, i.e. surface nitroxide to oxoammonium, by a simple change in the electrolyte; for instance, increasing the oxidizing power of a TEMPO film by increasing the Lewis base character of the electrolyte anion. This aspect is potentially of great significance when one considers applications of TEMPO films in heterogeneous catalysis.[74] To illustrate this, the homogeneous TEMPO charge transfer reaction has been coupled to the heterogeneous oxidation of bromide ions thus affording the extraction of the dependency of the apparent heterogeneous rate constant as a function of electrolyte, with the highest k_{cat} measured for PF_6^- systems (Figure 3.13).

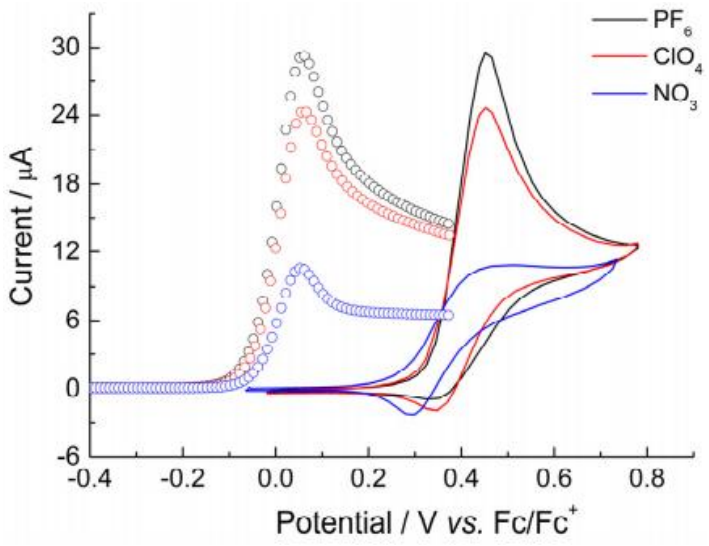

Figure 3.13 Observed CVs (lines) and simulated linear sweeps (symbols) for the dark HD **S-2** samples in the presence of 0.5×10^{-3} M Bu_4NBr in acetonitrile with 1.0×10^{-1} M of either Bu_4NPF_6, Bu_4NClO_4 or Bu_4NNO_3. The refined value of k_{cat} for the reaction between the adsorbed oxoammonium and non-adsorbed bromide relates to the electrolyte anion and dropped progressively from 3.2×10^4 $dm^3mol^{-1}s^{-1}$ (PF_6^-), to 1.9×10^4 $dm^3mol^{-1}s^{-1}$ (ClO_4^-) and finally to 2.8×10^3 $dm^3mol^{-1}s^{-1}$ (NO_3^-). The higher value

for k_{cat} in PF_6^- rules out the possibility of strong ion pairing reducing the rate of the heterogeneous reactions,[75] hence potentially nulling the thermodynamic gain from the favorable oxoammonium/anion interactions on the redox potential of the surface couple. The potential axis of the simulated curves is shown offset by neg. 400 mV for clarity only.

As introduced above, this work's chemical strategy to immobilize the nitroxide radical on the highly doped substrate can be expanded to a Si(100) electrode of low doping where the internal electrical field of the semiconductor space-charge[76] can be used to drive the redox reaction(s) contra-thermodynamically (Figure 3.14). The same surface chemistry used for the **S-2** samples on the highly doped electrodes (Scheme 3.1) was applied to n-type Si(100) electrodes of low doping (LD, ~ 4.5×10^{14} cm^{-3} to 5.0×10^{15} cm^{-3}, resistivity 1–10 Ω cm), followed by studying the chemical reversibility of **S-2** samples on LD electrodes (Figure 3.15), which indicated an excellent reversible nitroxide/oxoammonium oxidation/reduction process.

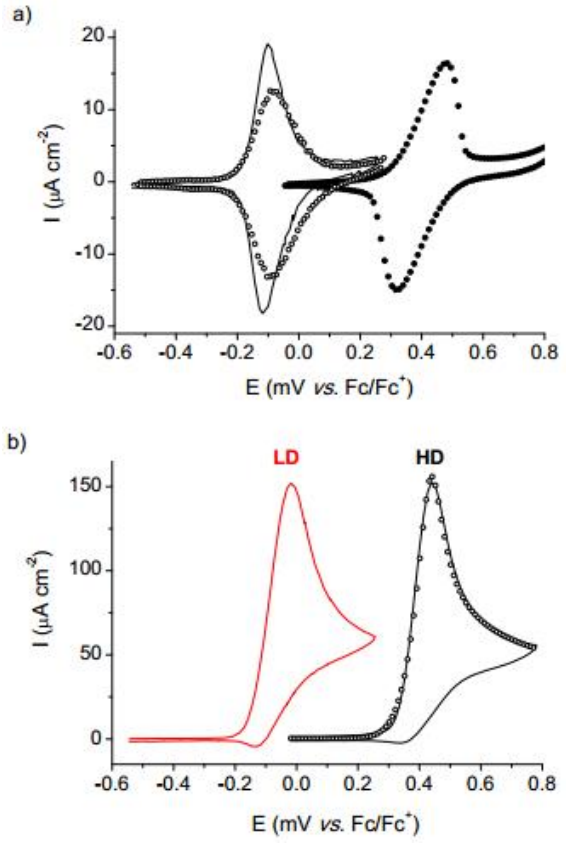

Figure 3.14 CVs for **S-2** samples prepared on n-Si electrodes (LD, 1–10 Ω cm). (a) Dark oxidation and reduction waves (solid symbols) and their underpotential shift with supra band gap illumination (lines). CVs were obtained at a voltage sweep rate of 100 mV s^{-1} in MeCN containing 1.0×10^{-1} M of either Bu_4NClO_4 (solid line, FWHM = 91

mV) or Bu_4NPF_6 (empty symbols, FWHM = 120 mV). (b) Observed (lines) and simulated (symbols) CV of the electrocatalytic mechanism on illuminated LD or HD **S-2** samples, respectively, in the presence of 0.5×10^{-3} M Bu_4NBr in 1.0×10^{-1} M of Bu_4NPF_6. The refined value of k_{cat} for the reaction between the adsorbed oxoammonium and non-adsorbed bromide was 3.2×10^3 $M^{-1}s^{-1}$.

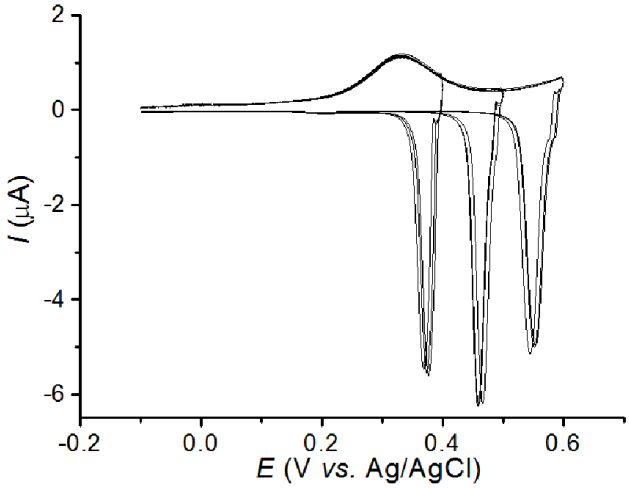

Figure 3.15 The chemical reversibility of **S-2** samples was studied by experiments on LD electrodes where the light was deliberately switched off at the anodic limit (0.4 V, 0.5 V or 0.6 V) in Bu_4NClO_4/MeCN systems. In contrast to the data on HD electrodes (Figure 3.4), the CVs shown in Figure 3.15 suggest there are no measurable changes in Γ for LD samples as no changes to the anodic wave can be observed after nine consecutive cycles. The difference in chemical reversibility between LD and HD samples was not further investigated as it is beyond the scope of the work and an explanation will require further studies.

The dark current-voltage characteristics of the **S-2** electrode (Figure 3.14a, solid symbols) reveal the extent of the expected kinetic limitations for the tunneling across the semiconductor space-charge; both asymmetry in the peaks[77] and a sizable peak-to-peak separation are a manifestation of slow charge transfer kinetics ($k_{et} \approx 0.01$ s^{-1}) in the dark lowly doped samples. In the light-activated faradaic response,[14, 78] this kinetic barrier is largely removed (Figure 3.14a, solid line, $k_{et} \approx 15$ s^{-1}), and the values of E_f^0 are shifted approximately 500 mV more negative with respect to the low or high doping **S-2** samples in the dark (Figure 3.4). Peak shapes in the illuminated lowly doped samples are near-to-ideal (FWHM = 95 ± 7 mV) in ClO_4^- electrolytes, but remain significantly broader in PF_6^- (FWHM = 131 ± 5 mV), hence reinforcing on the notion that factors other than kinetics are causing this nonideality (*vide supra*). The up-hill shift is consistent with the measured OCP under illumination (Figure 3.16a) and it is a result

of a process mediated by photo-generated valence band holes as previously reported for gallium and germanium photoanodes.[76, 79] As anticipated in the introduction, the shift in the E_f^0 of the homogeneous TEMPO reaction can translate in an energetic gain for a heterogeneous reaction, such as the oxidation of bromide ions in solution. The electrocatalytic process that is mediated by the surface TEMPO molecule on illuminated lowly doped samples (Figure 3.14b) is shifted uphill by about 500 mV compared to the same heterogeneous reaction on highly-doped (metallic) samples (Figure 3.14).

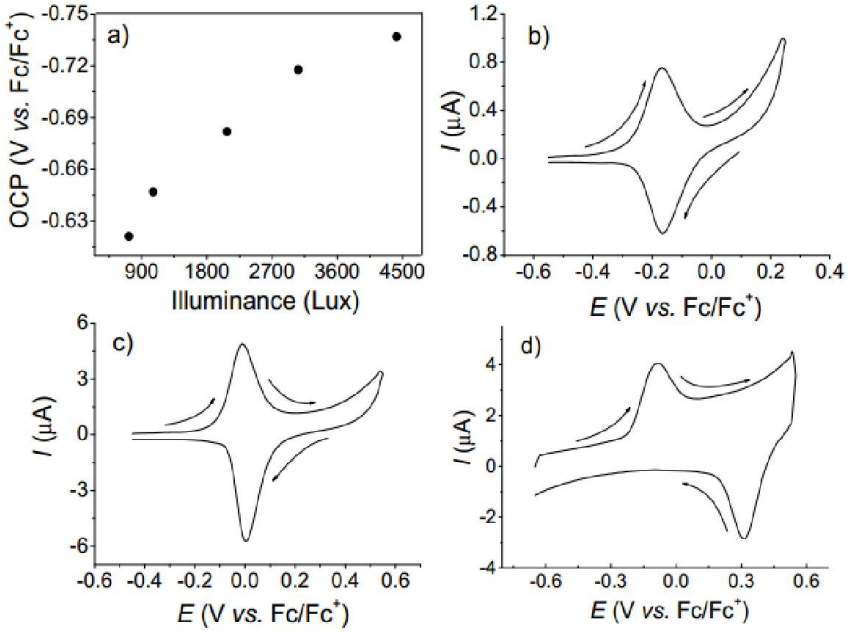

Figure 3.16 Panel (a) shows the experimental OCP values for **S-2** samples on LD electrodes under variable illumination intensity. If (i) the material does not have very fast carrier recombination rates and (ii) the illumination is sufficiently intense to completely remove band bending within the semiconductor, the illuminated OCP value can be used to estimate the E_{fb}. In the cases at hand for **S-2** samples on LD electrodes the direction of the shift in the OCP upon illumination is consistent with the doping type (n-type). There was no evidence of saturation of the OCP event at the highest light intensity (ca. 4500 lx), hence suggesting some degree of residual upward bending, i.e. a residual barrier for electron injection from the electrolyte even under strong illumination. Additional examples of "peak inversion" in CVs of **S-2** samples on LD silicon electrodes under continuous illumination (b-d). The phenomenon appears to be independent of coverage and electrolyte type. For example, data in (b) and (c) were recorded in Bu_4NClO_4/MeCN at coverage of 2.52×10^{-11} mol cm^{-2} and 2.02×10^{-10} mol cm^{-2}, respectively. Data in (c) and (d) were of a comparable coverage but recorded in Bu_4NClO_4/MeCN and Bu_4NPF_6/MeCN, respectively.

The CV data for illuminated **S-2** samples of low doping have been reproduced several times, with no major differences in peak-to-peak separations (11.5 ± 1.5 mV), FWHM (95 ± 7 mV) and Γ (2.05 ± 0.04 × 10^{-10} mol cm^{-1}) values (ClO_4^- data); however, a remarkable phenomenon was observed in at least four independently prepared and analyzed samples (Figure 3.16 and Figure 3.17a). In these four samples, the cathodic current peaked at a more anodic potential than that of the anodic peak. A current across an electrified interface is always indicative of an overall rate; hence, this "inversion" would immediately be disregarded as an artefact on a common metallic surface. However, a similar observation was reported in 1979 by Wrighton and co-workers for illuminated n-type gallium arsenide electrodes[76] that were modified with surface-bound ferrocenes. As tentatively suggested by Wrighton, a reduction rate being higher than the oxidation rate at an anodic regime may result from the charges of the adsorbed oxidized species affecting the electrostatics of the semiconductor electrode.[80] In the cases at hand (**S-2**, n-type, low doping), the flat-band potential of the system, E_{fb}, may be forced to shift anodically when during the voltammetric sweep the relative amount of neutral nitroxide radical to positively charged oxoammonium ion changes in favour of the latter. The observed sudden dominance of the reduction rate at a bias that is anodic of the oxidation wave may result from an electrostatic effect on the semiconductor space-charge, such that the oxoammonium species force bands to flatten, removing the tunneling barrier for the electrons leaving the electrode. It is important to note that the light intensity used in these experiments appears not to be high enough to force the bands to "flatten" completely (Figure 3.16a), and that the high dielectric medium (ε_{MeCN} = 37.5) is not completely masking interactions between the ionized semiconductor space-charge and oxoammonium species. Because of this electrostatic "push" by the oxoammonium species on the space charge, the onset of depletion requires a more positive bias, hence resulting in an oxoammonium-assisted smaller barrier to the flow of cathodic currents across the interface.

To support this electrostatic explanation for the "peak inversion" phenomenon, further work was performed on voltammetry in solvents of different dielectric constants to minimize or amplify this putative electrostatic effect, and deliberately switching off

the illumination source precisely at the anodic vertex. Figure 3.17b-d shows a series of CVs for **S-2** samples on lowly doped electrodes, with only the sweep toward the anodic region performed under illumination.

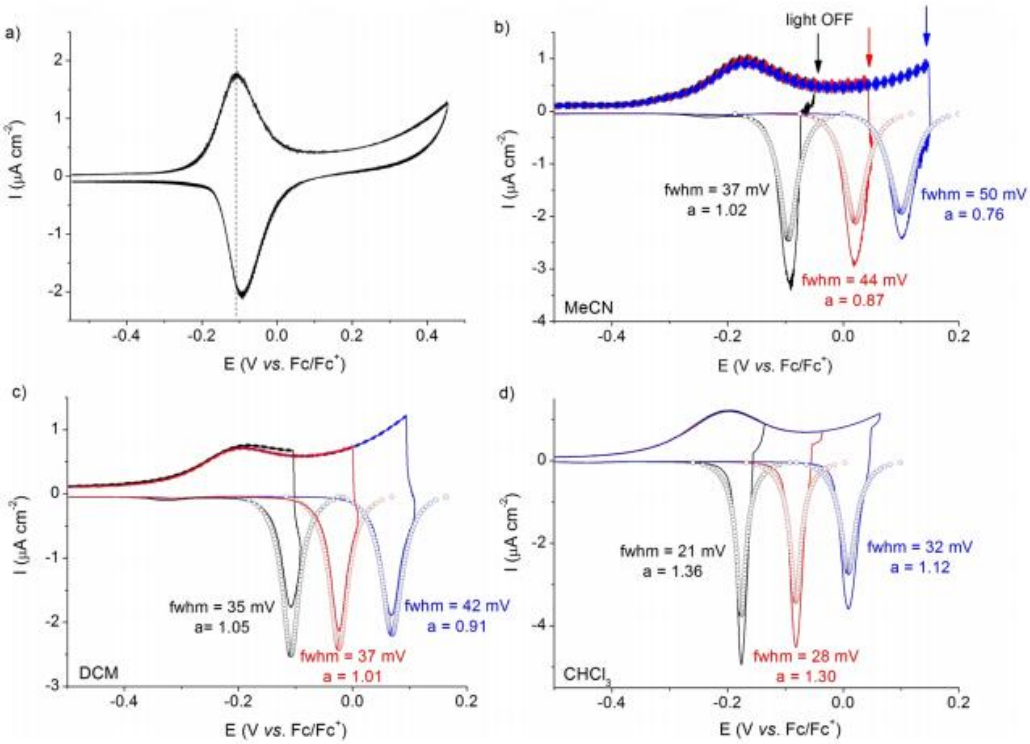

Figure 3.17 (a) Example of "peak inversion" in CVs of **S-2** electrodes of low doping under illumination (Bu_4NClO_4 and v = 100 mV s^{-1}). (b-d) "peak inversion" can be deliberately induced in CVs of **S-2** samples on lowly doped electrodes when illumination is switched off at the anodic vertex (0.4, 0.5 or 0.6 V) in Bu_4NClO_4 electrolytes using solvents of progressively lower dielectric constant (37.5 for acetonitrile, 8.9 for dichloromethane and 4.8 for chloroform). Simulated voltammograms (symbols) and refined values of the self-interaction parameter a are indicated in the figure.

The anodic "illuminated" wave in Figure 3.17 shows nothing unusual; hence, the theoretical current-voltage characteristics can be simulated on the basis of the Frumkin isotherm using a "zero" value of the Laviron self-interaction parameters a, i.e., the Langmuir isotherm without interactions[81] involving TEMPO units (*vide infra*). From a different angle, the observed peak shape implies ideality in the sense that the surface concentrations of the reduced and oxidized species equals their activities.[77] The light was then switched off at the anodic vertex (set either as 0.4, 0.5, or 0.6 V) in order to deliberately introduce a space-charge barrier for electrons to enter the semiconductor (anodic reaction). The flux of photo-generated holes is brought to a sudden halt and a

very sharp reductive peak appears instantly. The net result is a sudden increase in the reduction rate when the light was switched off, i.e., under these conditions the reductive peaks occur at a potential that is more positive than the oxidative peak. By doing this, the results obtained support the above hypothesis on the "peak inversion" (Figure 3.17a) being the result of an electrostatic effect of the oxoammonium on the semiconductor space-charge.

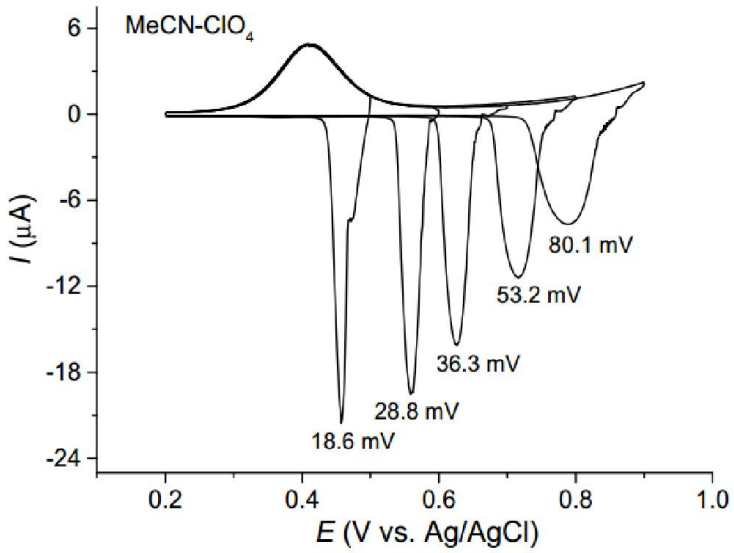

Figure 3.18 Deliberate acceleration of the backward rate. CVs of **S-2** LD samples with high coverage (1.31×10^{-10} mol cm^{-2}, i.e., standard CuAAC reaction time of 2 h) where the light was deliberately switched off at the anodic limit (0.5, 0.6, 0.7, 0.8 or 0.9 V) in Bu_4NClO_4/MeCN systems. The experimental FWHMs for the cathodic waves are indicated in the figure.

Furthermore, an assumption is made that the reduction event is fast and behaves like a Nernstian process; hence, tentative analysis can be done on this adsorbed system by using models that hold for reversible systems. As introduced above, a conventional approach to quantify the observed drop in experimental FWHMs in terms of attractive forces is the parametrization developed by Laviron based on the Frumkin isotherm (Figure 3.12, 3.17 and 3.18 and Chapter 2). In this model, the voltammetry response is derived, under Nernstian conditions by taking into account a simple isotherm, the so-called Frumkin isotherm, which introduces the *a* parameter. This is a dimensionless constant describing the extent of attractive and repulsive interactions between molecules,[82] and is directly related to the FWHM value (Chapter 2). When the light

source is switched off at the anodic vertex, band-bending in the depleted semiconductor space-charge is rapidly restored, and the balance of attractive to repulsive forces experienced by the adsorbed oxoammonium species appears to tilt in favor of the attractions, with the refined *a* increasing above the zero value (Figure 3.16b-d). In line with this explanation, this putative electrostatic effect on the *a* self-interaction parameter, which is ascribed tentatively to a space-charge effect on the oxoammonium/anion attractions, becomes in fact more pronounced as the solvent dielectric is reduced by moving from acetonitrile to chloroform solutions (Figure 3.16b and 3.16d).

3.5 Conclusions

This chapter presented a two-step acetyenylation/click procedure as a wet chemistry approach to tether a nitroxide radical to a silicon surface and preserve its open-shell state. This is the first example of the attachment of a redox-active stable free radical onto a semiconducting surface. From a fundamental standpoint, these surfaces can be used as a laboratory model to explore the recently reported electrostatic effects on chemical bonding and reactivity.[4-6, 83] This work has explored to what extent electrostatic effects arising either from electrolyte species or ionized dopants in the semiconductor space-charge can influence the redox activity of the free radical. It has been shown experimentally that it is possible to gauge these effects as changes to voltammetric responses. This knowledge may aid the development of electrocatalytic heterogeneous systems where the redox reaction of interest can be coupled to semiconductor effects and therefore driven contra-thermodynamically by up to 0.5 V.

All experimental results show good agreement with theoretical calculations and show that the redox properties of a nitroxide radical monolayer can indeed be predictably manipulated by controlling the electrostatic between the tethered persistent radical and electrolytes and semiconductor.

3.6 References

(1) Gooding, J. J.; Ciampi, S. The molecular level modification of surfaces: from self-assembled monolayers to complex molecular assemblies. *Chem. Soc. Rev.* **2011,** *40*,

2704-2718.

(2) Chia, S.; Cao, J.; Stoddart, J. F.; Zink, J. I. Working supramolecular machines trapped in glass and mounted on a film surface. *Angew. Chem. Int. Ed.* **2001,** *113*, 2447-2451.

(3) Fischer, H. The persistent radical effect: a principle for selective radical reactions and living radical polymerizations. *Chem. Rev.* **2001,** *101*, 3581-3610.

(4) Klinska, M.; Smith, L. M.; Gryn'ova, G.; Banwell, M. G.; Coote, M. L. Experimental demonstration of pH-dependent electrostatic catalysis of radical reactions. *Chem. Sci.* **2015,** *6*, 5623-5627.

(5) Gryn'ova, G.; Marshall, D. L.; Blanksby, S. J.; Coote, M. L. Switching radical stability by pH-induced orbital conversion. *Nat. Chem.* **2013,** *5*, 474-481.

(6) Gryn'ova, G.; Coote, M. L. Origin and scope of long-range stabilizing interactions and associated SOMO–HOMO conversion in distonic radical anions. *J. Am. Chem. Soc.* **2013,** *135*, 15392-15403.

(7) Knoop, C. A.; Studer, A. Hydroxy-and silyloxy-substituted TEMPO derivatives for the living free-radical polymerization of styrene and n-butyl acrylate: synthesis, kinetics, and mechanistic studies. *J. Am. Chem. Soc.* **2003,** *125*, 16327-16333.

(8) Niermann, N.; Degefa, T. H.; Walder, L.; Zielke, V.; Steinhoff, H.-J.; Onsgaard, J.; Speller, S. Galvinoxyl monolayers on Au(111) studied by STM, EPR, and cyclic voltammetry. *Phys. Rev. B* **2006,** *74*, 235424-235436.

(9) Lloveras, V.; Badetti, E.; Chechik, V.; Vidal-Gancedo, J. Magnetic interactions in spin-labeled Au nanoparticles. *J. Phys. Chem. C* **2014,** *118*, 21622-21629.

(10) Blinco, J. P.; Chalmers, B. A.; Chou, A.; Fairfull-Smith, K. E.; Bottle, S. E. Spin-coated carbon. *Chem. Sci.* **2013,** *4*, 3411-3415.

(11) Swiech, O.; Bilewicz, R.; Megiel, E. TEMPO coated Au nanoparticles: synthesis and tethering to gold surfaces. *RSC Adv.* **2013,** *3*, 5979-5986.

(12) Ball, P. Material witness: silicon still supreme. *Nat. Mater.* **2005,** *4*, 119-119.

(13) Ciampi, S.; Harper, J. B.; Gooding, J. J. Wet chemical routes to the assembly of organic monolayers on silicon surfaces via the formation of Si–C bonds: Surface preparation, passivation and functionalization. *Chem. Soc. Rev.* **2010,** *39*, 2158-2183.

(14) Choudhury, M. H.; Ciampi, S.; Yang, Y.; Tavallaie, R.; Zhu, Y.; Zarei, L.; Gonçales, V. R.; Gooding, J. J. Connecting electrodes with light: one wire, many electrodes. *Chem. Sci.* **2015,** *6*, 6769-6776.

(15) Jansen, R. Silicon spintronics. *Nat. Mater.* **2012,** *11*, 400-408.

(16) Nakamura, M.; Yoshida, S.; Katayama, T.; Taninaka, A.; Mera, Y.; Okada, S.; Takeuchi, O.; Shigekawa, H. Mechanically activated switching of Si-based single-molecule junction as imaged with three-dimensional dynamic probe. *Nat. Commun.* **2015,** *6*, 8465-8472.

(17) Greene, M. E.; Guisinger, N. P.; Basu, R.; Baluch, A. S.; Hersam, M. C. Nitroxyl free radical binding to Si(100): a combined scanning tunneling microscopy and computational modeling study. *Surf. Sci.* **2004,** *559*, 16-28.

(18) Ciampi, S.; Eggers, P. K.; Le Saux, G.; James, M.; Harper, J. B.; Gooding, J. J. Silicon (100) electrodes resistant to oxidation in aqueous solutions: an unexpected benefit of surface acetylene moieties. *Langmuir* **2009,** *25*, 2530-2539.

(19) Ciampi, S.; Böcking, T.; Kilian, K. A.; James, M.; Harper, J. B.; Gooding, J. J. Functionalization of acetylene-terminated monolayers on Si(100) surfaces: a click chemistry approach. *Langmuir* **2007,** *23*, 9320-9329.

(20) Squires, T. M.; Messinger, R. J.; Manalis, S. R. Making it stick: convection, reaction and diffusion in surface-based biosensors. *Nat. Biotechnol.* **2008,** *26*, 417-426.

(21) Hartstein, A.; Kirtley, J.; Tsang, J. Enhancement of the infrared absorption from molecular monolayers with thin metal overlayers. *Phys. Rev. Lett.* **1980,** *45*, 201-204.

(22) Zanetti-Polzi, L.; Daidone, I.; Bortolotti, C. A.; Corni, S. Surface packing determines the redox potential shift of cytochrome c adsorbed on gold. *J. Am. Chem. Soc.* **2014,** *136*, 12929-12937.

(23) Alévêque, O.; Blanchard, P.-Y.; Breton, T.; Dias, M.; Gautier, C.; Levillain, E.; Seladji, F. Nitroxyl radical self-assembled monolayers on gold: Experimental data vs. Laviron's interaction model. *Electrochem. Commun.* **2009,** *11*, 1776-1780.

(24) Kwon, Y.; Mrksich, M. Dependence of the rate of an interfacial Diels−Alder reaction on the steric environment of the immobilized dienophile: an example of enthalpy−entropy compensation. *J. Am. Chem. Soc.* **2002,** *124*, 806-812.

(25) Ng, A.; Ciampi, S.; James, M.; Harper, J. B.; Gooding, J. J. Comparing the reactivity of alkynes and alkenes on silicon (100) surfaces. *Langmuir* **2009,** *25*, 13934-13941.

(26) Rohde, R. D.; Agnew, H. D.; Yeo, W.-S.; Bailey, R. C.; Heath, J. R. A non-oxidative approach toward chemically and electrochemically functionalizing Si(111). *J. Am. Chem. Soc.* **2006,** *128*, 9518-9525.

(27) Coletti, C.; Marrone, A.; Giorgi, G.; Sgamellotti, A.; Cerofolini, G.; Re, N. Nonradical mechanisms for the uncatalyzed thermal functionalization of silicon surfaces by alkenes and alkynes: A density functional study. *Langmuir* **2006,** *22*, 9949-9956.

(28) Kondo, M.; Mates, T. E.; Fischer, D. A.; Wudl, F.; Kramer, E. J. Bonding structure of phenylacetylene on hydrogen-terminated Si(111) and Si(100): surface photoelectron spectroscopy analysis and ab initio calculations. *Langmuir* **2010,** *26*, 17000-17012.

(29) Ubara, H.; Imura, T.; Hiraki, A. Formation of Si-H bonds on the surface of microcrystalline silicon covered with SiO_x by HF treatment. *Solid State Commun.* **1984,** *50*, 673-675.

(30) Chabal, Y.; Higashi, G.; Raghavachari, K.; Burrows, V. Infrared spectroscopy of Si(111) and Si(100) surfaces after HF treatment: hydrogen termination and surface morphology. *J. Vac. Sci. Technol. A* **1989,** *7*, 2104-2109.

(31) Niwano, M.; Takeda, Y.; Ishibashi, Y.; Kurita, K.; Miyamoto, N. Morphology of hydrofluoric acid and ammonium fluoride-treated silicon surfaces studied by surface infrared spectroscopy. *J. Appl. Phys.* **1992,** *71*, 5646-5649.

(32) Nemanick, E. J.; Hurley, P. T.; Webb, L. J.; Knapp, D. W.; Michalak, D. J.; Brunschwig, B. S.; Lewis, N. S. Chemical and electrical passivation of single-crystal silicon (100) surfaces through a two-step chlorination/alkylation process. *J. Phys. Chem. B* **2006,** *110*, 14770-14778.

(33) Meldal, M.; Tornøe, C. W. Cu-catalyzed azide−alkyne cycloaddition. *Chem. Rev.* **2008,** *108*, 2952-3015.

(34) Tansakul, C.; Lilie, E.; Walter, E. D.; Rivera III, F.; Wolcott, A.; Zhang, J. Z.; Millhauser, G. L.; Braslau, R. Distance-dependent fluorescence quenching and binding

of CdSe quantum dots by functionalized nitroxide radicals. *J. Phys. Chem. C* **2010,** *114*, 7793-7805.

(35) Nelson, A. Co-refinement of multiple-contrast neutron/X-ray reflectivity data using MOTOFIT. *J. Appl. Crystallogr.* **2006,** *39*, 273-276.

(36) Miller, J. N.; Miller, J. C. Statistics and chemometrics for analytical chemistry, 6th ed.; Prentice Hall: Essex, U.K. **2010**, p 266.

(37) Gerischer, H. Electrochemical photo and solar cells principles and some experiments. *J. Electroanal. Chem. Interfacial Electrochem.* **1975,** *58*, 263-274.

(38) Allen, G. D.; Buzzeo, M. C.; Villagrán, C.; Hardacre, C.; Compton, R. G. A mechanistic study of the electro-oxidation of bromide in acetonitrile and the room temperature ionic liquid, 1-butyl-3-methylimidazolium bis(trifluoromethylsulfonyl)imide at platinum electrodes. *J. Electroanal. Chem.* **2005,** *575*, 311-320.

(39) Gryn'ova, G.; Barakat, J. M.; Blinco, J. P.; Bottle, S. E.; Coote, M. L. Computational design of cyclic nitroxides as efficient redox mediators for dye sensitized solar cells. *Chem. A Eur. J.* **2012,** *18*, 7582-7593.

(40) Blinco, J. P.; Hodgson, J. L.; Morrow, B. J.; Walker, J. R.; Will, G. D.; Coote, M. L.; Bottle, S. E. Experimental and theoretical studies of the redox potentials of cyclic nitroxides. *J. Org. Chem.* **2008,** *73*, 6763-6771.

(41) Hodgson, J. L.; Namazian, M.; Bottle, S. E.; Coote, M. L. One-electron oxidation and reduction potentials of nitroxide antioxidants: A theoretical study. *J. Phys. Chem. A* **2007,** *111*, 13595-13605.

(42) Curtiss, L. A.; Raghavachari, K.; Redfern, P. C.; Baboul, A. G.; Pople, J. A. Gaussian-3 theory using coupled cluster energies. *Chem. Phys. Lett.* **1999,** *314*, 101-107.

(43) Izgorodina, E. I.; Brittain, D. R.; Hodgson, J. L.; Krenske, E. H.; Lin, C. Y.; Namazian, M.; Coote, M. L. Should contemporary density functional theory methods be used to study the thermodynamics of radical reactions? *J. Phys. Chem. A* **2007,** *111*, 10754-10768.

(44) Coote, M. L.; Krenske, E. H.; Izgorodina, E. I. Computational studies of RAFT

polymerization–mechanistic insights and practical applications. *Macromol. Rapid Commun.* **2006,** *27*, 473-497.

(45) Zhao, Y.; Truhlar, D. G. The M06 suite of density functionals for main group thermochemistry, thermochemical kinetics, noncovalent interactions, excited states, and transition elements: two new functionals and systematic testing of four M06-class functionals and 12 other functionals. *Theor. Chem. Acc.* **2008,** *120*, 215-241.

(46) Alecu, I. M.; Zheng, J.; Zhao, Y.; Truhlar, D. G. Computational thermochemistry: scale factor databases and scale factors for vibrational frequencies obtained from electronic model chemistries. *J. Chem. Theory Comput.* **2010,** *6*, 2872-2887.

(47) Marenich, A. V.; Cramer, C. J.; Truhlar, D. G. Universal solvation model based on solute electron density and on a continuum model of the solvent defined by the bulk dielectric constant and atomic surface tensions. *J. Phys. Chem. B* **2009,** *113*, 6378-6396.

(48) Frisch, M. J.; Trucks, G. W.; Schegel, H. B.; Scuseria, G. E.; Robb, M. A.; Cheeseman, J. R.; Scalmani, G.; Barone, V.; Mennucci, B.; Petersson, G. A.; Nakatsuji, H.; Caricato, M.; Li, X.; Hratchian, H. P.; Izmaylov, A. F.; Bloino, J.; Zheng, G.; Sonnenberg, J. L.; Hada, M.; Ehara, M.; Toyota, K.; Fukuda, R.; Hasegawa, J.; Ishida, M.; Nakajima, T.; Honda, Y.; Kitao, O.; Nakai, H.; Vreven, T.; Montgomery, J. A.; Jr. Peralta, J. E.; Ogliaro, F.; Bearpark, M.; Heyd, J. J.; Brothers, E.; Kudin, K. N.; Staroverov, V. N.; Keith, T.; Kobayashi, R.; Normand, J.; Raghavachari, K.; Rendell, A.; Burant, J. C.; Iyengar, S. S.; Tomasi, J.; Cossi, M.; Rega, N.; Millam, J. M.; Klene, M.; Knox, J. E.; Cross, J. B.; Bakken, V.; Adamo, C.; Jaramillo, J.; Gomperts, R.; Stratmann, R. E.; Yazyev, O.; Austin, A. J.; Cammi, R.; Pomelli, C.; Ochterski, J. W.; Martin, R. L.; Morokuma, K.; Zakrzewski, V. G.; Voth, G. A.; Salvador, P.; Dannenberg, J. J.; Dapprich, S.; Daniels, A. D.; Farkas, O.; Foresman, J. B.; Ortiz, J. V.; Cioslowski, J.; Fox, D. J. *Gaussian 09, revision E.01* **2009**, Gaussian, Inc., Wallingford CT.

(49) Werner, H.; Knowles, P.; Knizia, G.; Manby, F.; Schütz, M.; Celani, P.; Györffy, W.; Kats, D.; Korona, T.; Lindh, R.; Mitrushenkov, A.; Rauhut, G.; Shamasundar, K. R.; Adler, T. B.; Amos, R. D.; Bernhardsson, A.; Berning, A.; Cooper, D. L.; Deegan, M. J. O.; Dobbyn, A. J.; Eckert, F.; Goll, E.; Hampel, C.; Hesselmann, A.; Hetzer, G.; Hrenar, T.; Jansen, G.; Köppl, C.; Liu, Y.; Lloyd, A. W.; Mata, R. A.; May, A. J.;

McNicholas, S. J.; Meyer, W.; Mura, M. E.; Nicklass, A.; O'Neill, D. P.; Palmieri, P.; Peng, D.; Pflüger, K.; Pitzer, R.; Reiher, M.; Shiozaki, T.; Stoll, H.; Stone, A. J.; Tarroni, R.; Thorsteinsson, T.; Wang, M. MOLPRO, a package of *ab Initio* programs, version 2012.1. *University College Cardiff Consultants Ltd.: Wales, UK* **2012**, http://www.molpro.net.

(50) Werner, H. J.; Knowles, P. J.; Knizia, G.; Manby, F. R.; Schütz, M. Molpro: a general-purpose quantum chemistry program package. *WIREs Comput. Mol. Sci.* **2012,** *2*, 242-253.

(51) Ho, J.; Coote, M. L. A universal approach for continuum solvent pKa calculations: are we there yet? *Theor. Chem. Acc.* **2010,** *125*, 3-21.

(52) SLD for X-rays is obtained by multiplying the electron density (e-/Å^3) of the material by the factor 2.82 × 10^{-5} Å.

(53) Ciampi, S.; James, M.; Darwish, N.; Luais, E.; Guan, B.; Harper, J. B.; Gooding, J. J. Oxidative acetylenic coupling reactions as a surface chemistry tool. *Phys. Chem. Chem. Phys.* **2011,** *13*, 15624-15632.

(54) Ulman, A., *An introduction to ultrathin organic films: from Langmuir-Blodgett to self-assembly*. Academic Press Limited: London, U.K.: 1991.

(55) Linford, M. R.; Fenter, P.; Eisenberger, P. M.; Chidsey, C. E. Alkyl monolayers on silicon prepared from 1-alkenes and hydrogen-terminated silicon. *J. Am. Chem. Soc.* **1995,** *117*, 3145-3155.

(56) Böcking, T.; James, M.; Coster, H. G.; Chilcott, T. C.; Barrow, K. D. Structural characterization of organic multilayers on silicon (111) formed by immobilization of molecular films on functionalized Si−C linked monolayers. *Langmuir* **2004,** *20*, 9227-9235.

(57) James, M.; Darwish, T. A.; Ciampi, S.; Sylvester, S. O.; Zhang, Z.; Ng, A.; Gooding, J. J.; Hanley, T. L. Nanoscale condensation of water on self-assembled monolayers. *Soft Matter* **2011,** *7*, 5309-5318.

(58) Ciampi, S.; James, M.; Michaels, P.; Gooding, J. J. Tandem “click” reactions at acetylene-terminated Si(100) monolayers. *Langmuir* **2011,** *27*, 6940-6949.

(59) Devadoss, A.; Chidsey, C. E. Azide-modified graphitic surfaces for covalent

attachment of alkyne-terminated molecules by "click" chemistry. *J. Am. Chem. Soc.* **2007,** *129*, 5370-5371.

(60) Caro, J.; Fraxedas, J.; Jürgens, O.; Santiso, J.; Rovira, C.; Veciana, J.; Figueras, A. The first oriented thin films based on a nitronyl nitroxide radical. *Adv. Mater.* **1998,** *10*, 608-610.

(61) Liu, H.; Duclairoir, F.; Fleury, B.; Dubois, L.; Chenavier, Y.; Marchon, J.-C. Porphyrin anchoring on Si(100) using a β-pyrrolic position. *Dalton Trans.* **2009**, 3793-3799.

(62) Qin, G.; Santos, C.; Zhang, W.; Li, Y.; Kumar, A.; Erasquin, U. J.; Liu, K.; Muradov, P.; Trautner, B. W.; Cai, C. Biofunctionalization on alkylated silicon substrate surfaces via "click" chemistry. *J. Am. Chem. Soc.* **2010,** *132*, 16432-16441.

(63) Fraxedas, J.; Caro, J.; Figueras, A.; Gorostiza, P.; Sanz, F. Surface characterization of thin films of tetrathiofulvalene 7, 7, 8, 8-tetracyano-p-quinodimethane evaporated on NaCl (001). *J. Vac. Sci. Technol. A* **1998,** *16*, 2517-2523.

(64) Grobman, W. D.; Pollak, R. A.; Eastman, D. E.; Maas, E. T.; Scott, B. A. Valence electronic structure and charge transfer in tetrathiofulvalinium tetracyanoquinodimethane (TTF-TCNQ) from photoemission spectroscopy. *Phys. Rev. Lett.* **1974,** *32*, 534-537.

(65) Compton, R. G.; Laborda, E.; Ward, K. R., *Understanding voltammetry: simulation of electrode processes*. World Scientific: 2014; p 145.

(66) Gautier, C.; Alévêque, O.; Seladji, F.; Dias, M.; Breton, T.; Levillain, E. Nitroxyl radical self assembled monolayers: Ion pairing investigation in organic and aqueous media. *Electrochem. Commun.* **2010,** *12*, 79-82.

(67) Valincius, G.; Niaura, G.; Kazakevičienė, B.; Talaikytė, Z.; Kažemėkaitė, M.; Butkus, E.; Razumas, V. Anion effect on mediated electron transfer through ferrocene-terminated self-assembled monolayers. *Langmuir* **2004,** *20*, 6631-6638.

(68) Andreu, R.; Calvente, J. J.; Fawcett, W. R.; Molero, M. Role of ion pairing in double-layer effects at self-assembled monolayers containing a simple redox couple. *J. Phys. Chem. B* **1997,** *101*, 2884-2894.

(69) Geneste, F.; Moinet, C.; Ababou-Girard, S.; Solal, F. Covalent attachment of

TEMPO onto a graphite felt electrode and application in electrocatalysis. *New J. Chem.* **2005,** *29*, 1520-1526.

(70) Blanchard, P.-Y.; Alévêque, O.; Breton, T.; Levillain, E. TEMPO mixed SAMs: electrocatalytic efficiency versus surface coverage. *Langmuir* **2012,** *28*, 13741-13745.

(71) Honeychurch, M. J.; Rechnitz, G. A. Voltammetry of adsorbed molecules. part 1: reversible redox systems. *Electroanal.* **1998,** *10*, 285-293.

(72) Laviron, E. The use of linear potential sweep voltammetry and of ac voltammetry for the study of the surface electrochemical reaction of strongly adsorbed systems and of redox modified electrodes. *J. Electroanal. Chem. Interfacial Electrochem.* **1979,** *100*, 263-270.

(73) Forces betweeen like species are parameterized as a_A or a_B, while those between unlike species are indicated as a_{AB}. The peak shape relates to a, with $a = a_A + a_B - 2a_{AB}$. An a value > 0 is used for attractions, and a value < 0 for repulsions. For large values of a, the forward and backward peaks appear at different potential, regardles of kinetics.

(74) Kashiwagi, Y.; Uchiyama, K.; Kurashima, F.; Anzai, J.-i.; Osa, T. Enantioselective oxidation of amines on a gold electrode modified by a self-assembled monolayer of a chiral nitroxyl radical compound. *Anal. Sci.* **1999,** *15*, 907-909.

(75) Kazakevičienė, B.; Valincius, G.; Niaura, G.; Talaikytė, Z.; Kažemėkaitė, M.; Razumas, V.; Plaušinaitis, D.; Teišerskienė, A.; Lisauskas, V. Mediated oxidation of ascorbic acid on a homologous series of ferrocene-terminated self-assembled monolayers. *Langmuir* **2007,** *23*, 4965-4971.

(76) Bolts, J. M.; Wrighton, M. S. Chemically derivatized n-type semiconducting gallium arsenide photoelectrodes. Thermodynamically uphill oxidation of surface-attached ferrocene centers. *J. Am. Chem. Soc.* **1979,** *101*, 6179-6184.

(77) Brown, A. P.; Anson, F. C. Cyclic and differential pulse voltammetric behavior of reactants confined to the electrode surface. *Anal. Chem.* **1977,** *49*, 1589-1595.

(78) Yang, Y.; Ciampi, S.; Choudhury, M. H.; Gooding, J. J. Light activated electrochemistry: light intensity and pH dependence on electrochemical performance of anthraquinone derivatized silicon. *J. Phys. Chem. C* **2016,** *120*, 2874-2882.

(79) Bolts, J. M.; Wrighton, M. S. Chemically derivatized n-type semiconducting

germanium photoelectrodes. Persistent attachment and photoelectrochemical activity of ferrocene derivatives. *J. Am. Chem. Soc.* **1978,** *100*, 5257-5262.

(80) Ginley, D.; Butler, M. Flatband potential of cadmium sulfide (CdS) photoanodes and its dependence on surface ion effects. *J. Electrochem. Soc.* **1978,** *125*, 1968-1974.

(81) Compton, R. G.; Banks, E. C. Understanding Voltammetry; Imperial College Press: London, U.K., 2011; p 282.

(82) Laviron, E. Surface linear potential sweep voltammetry: equation of the peaks for a reversible reaction when interactions between the adsorbed molecules are taken into account. *J. Electroanal. Chem. Interfacial Electrochem.* **1974,** *52*, 395-402.

(83) Aragonès, A. C.; Haworth, N. L.; Darwish, N.; Ciampi, S.; Bloomfield, N. J.; Wallace, G. G.; Diez-Perez, I.; Coote, M. L. Electrostatic catalysis of a Diels–Alder reaction. *Nature* **2016,** *531*, 88-91.

Chapter 4 Electrostatic Catalysis in the Anodic Cleavage of Alkoxyamines

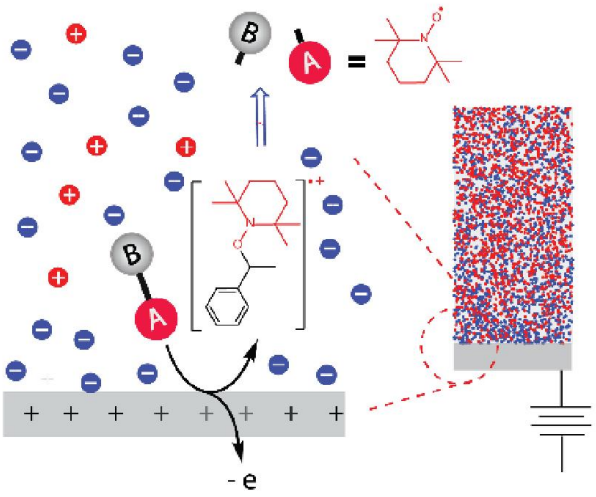

4.1 Abstract

Alkoxyamines are heat-liable molecules, widely used as *in-situ* source of nitroxides in polymer and materials sciences. Here is shown that the one-electron oxidation of an alkoxyamine leads to an anodic intermediate that even at room temperature rapidly fragments releasing a nitroxide species. Digital simulations of experimental voltammetry and current-time transients suggest that unimolecular decomposition which yields the "unmasked" nitroxide (TEMPO) is exceedingly rapid and irreversible. High-level quantum computations indicate the collapse of the alkoxyamine cation radical is likely to yield a neutral nitroxide radical and a secondary phenylethyl cation. However, this fragmentation is predicted to be slow and very energetically unfavorable. To attain qualitative agreement between the experimental kinetics and computational modeling for this fragmentation step, the explicit electrostatic environment of the electric double layer must be considered. This work highlights the participation of electrolytes in a bond breaking process, defines the magnitude of this type of electrostatic catalytic effect, and suggest a redox on/off switch to guide the cleavage of alkoxyamines at an electrified interface.

4.2 Introduction

Nitroxide radicals ($R_1R_2N–O^{\bullet}$) are stabilized free-radicals that resist dimerization and many other chemical reactions but make excellent traps for carbon-centered radicals. They are key intermediates in the Denisov cycle, the process by which hindered amine light stabilizers protect polymers from auto-oxidation,[1, 2] and in nitroxide-mediated polymerization, the first successful controlled radical polymerization process.[3-5] Their oxidized close-shell counterparts are also of great practical value as electron shuttles in organic electro-synthesis.[6-8] For example a very recent report has elegantly shown the use of 2,2,6,6-tetramethyl-1-piperidinyloxy (TEMPO) in electrolytic dehydrogenative coupling reactions of small pharmaceuticals.[9]

Alkoxyamines are arguably the prime source of nitroxides for both chemists and material scientists. They are heat-labile molecules but relatively high temperatures (*ca.* 80-120 °C) are required to trigger their homolysis, with the unfortunate consequence of

unwanted side reactions occurring.[10] The ability to manipulate alkoxyamine and nitroxide radical stability through external stimuli, other than temperature or chemical design, has been a long-standing quest for chemists. There has been some success in the use of light[11-14] and pH[15-18] to trigger alkoxyamine lysis at temperatures where the molecule would otherwise be stable. The case of pH is particularly intriguing; here the effect is electrostatic in origin and highly directional (field vs reactant).[19-21] The catalytic effect is delivered by remote molecular charges of acid or base substituents, and can therefore be predictably adjusted according to pH.[17, 18] The electric field that is associated with the ionized functional group alters the stability of charge-separated resonance contributors ($N–O^{\bullet} \leftrightarrow N^{+\bullet}–O^{-}$) hence the extent of stabilization of the nitroxide, and ultimately it governs the radical exchange reaction. However, whilst this electrostatic effect is large in the gas phase,[17] in solution it progressively diminishes as the polarity of the solvent increases.[18] Further, whilst this type of pH switch is possible in solvents of low polarity, its practical use here is hampered by the low solubility of charged species, leading to a trade-off between solubility and magnitude of the electrostatic catalytic effect. This raises the question as to whether there is a better and more general method of introducing charges and ensuring they align with reaction axes.

Inspired by the seminal work of Yeshayahu Pocker in the 1970s and 80s on electrostatic catalysis by ionic aggregates,[22, 23] and guided by the more recent experimental and theoretical developments in the field,[24-27] this thesis work explores the prospect of using electricity as an alternative trigger of alkoxyamine decomposition. Recently, this PhD candidate has demonstrated that the oxidation potential and reactivity of a surface tethered nitroxide could be predictably manipulated via electrolyte ion-pairing.[28] Herein, it is shown that molecular charges introduced upon an anodic reaction in electrolytes guide the fragmentation of the TEMPO-derived alkoxyamine **2** (synthetic details in Figure 4.1). Alkoxyamine **2** and the surface chemistry construct **S-1** in Scheme 4.1 has been used to illustrate electrostatic catalysis in a diffusive and surface tether system, respectively. In this work, conventional electrochemical experiments were performed in electrolyte solutions of different

dielectric constants and different supporting electrolytes and at temperatures under which the molecules would otherwise be thermally stable. Electrochemical and spectroscopic techniques, digital simulations of voltammetry and quantum chemistry have been used to explore and conceptualize the role of charges on the follow-up chemical reaction that, at room temperature, rapidly converts the anodic intermediate into a free nitroxide persistent radical, with emphasis on demonstrating the role played by electrolyte anions on this technologically-relevant unimolecular decomposition reaction.

4.3 Experimental methods

4.3.1 Chemicals and materials

Chemicals. Unless noted otherwise, all chemicals were of analytical grade and used as received. Milli-Q™ water (> 18 MΩ cm) was used to prepare solutions, for chemical reactions and in surface cleaning procedures. Acetonitrile (MeCN), dichloromethane (DCM), 2-propanol and ethanol for substrate cleaning and chemical reactions were redistilled prior to use. Hydrogen peroxide (30 wt.% in water), ammonium fluoride (PuranalTM, 40 wt.% in water), and sulfuric acid (PuranalTM, 95-97%) used in wafer cleaning and etching procedures were of semiconductor grade. 1,8-Nonadiyne (Sigma-Aldrich, 98%) was redistilled from sodium borohydride (Sigma-Aldrich, 99+%) under reduced pressure (80 °C, 10−12 Torr) and stored under a high purity argon atmosphere prior to use. Styrene (ReagentPlus®, Sigma-Aldrich ≥99%) was washed with aqueous 5% sodium hydroxide for removing the inhibitors and/or stabilizers. Tetrabutylammonium (Bu_4N) salts (Sigma-Aldrich) of perchlorate (ClO_4, ≥98%) and hexafluorophosphate (PF_6, purum, ≥98%) were recrystallized twice from 2-propanol before using as supporting electrolytes. Sodium tetrakis[3,5-bis(trifluoromethyl)phenyl]borate (Alfa Aesar, NaBARF, 97%, may cont. 1-5% water) was directly used for a control supporting electrolyte without any refinements. Ferrocene (Fc, 98%), ammonium sulfite and TEMPO (98%) were purchased from Sigma-Aldrich. 4-azido-2,2,6,6-tetramethyl-1-(1-phenylethoxy)piperdine (**1**, 4-N_3-TEMPO-PE in shorthand notation) and 2,2,6,6-Tetramethyl-1-(1-

phenylethoxy)piperdine (**2**, TEMPO-PE) were synthesized from 4-azido-2,2,6,6-tetramethyl-1-piperdine-1-oxyl (4-N_3-TEMPO, synthesis procedure given in Chapter 3)[29] and from 2,2,6,6-tetramethylpiperidine-1-oxyl (TEMPO, 98%, Sigma-Aldrich), respectively, through published methods with minor modifications (see Section 4.3.2).[30]

Silicon wafers. Prime grade, single-side polished silicon wafers, 100-oriented (<100> ± 0.5°), p-type (boron-doped), 500 ± 25 μm thick, with nominal resistivity of 0.001–0.003 Ω cm were obtained from Siltronix, S.A.S. (Archamps, France).

4.3.2 Purification and analysis of synthesized compounds

Thin-layer chromatography (TLC) was performed on silica gel using Merck aluminum sheets (60 F254). Merck 60 Å silica gel (220−400 mesh particle size) was used for column chromatography. High-resolution mass spectral data (HRMS, MASS accuracy 2-4 ppm) of compounds 4-azido-2,2,6,6-tetramethyl-1-(1-phenylethoxy)piperdine (**1**, 4-N_3-TEMPO-PE) and 2,2,6,6-Tetramethyl-1-(1-phenylethoxy)piperdine (**2**, TEMPO-PE) were obtained using a Waters Xevo QTof MS via ESI experiments and infusing the sample at 8 μL/min. Nuclear magnetic resonance (NMR) spectra were recorded on a Bruker Avance 400 spectrometer.

Alkoxyamines 4-N_3-TEMPO-PE (**1**, surface systems, silicon electrodes) and TEMPO-PE (**2**, diffusive systems) were synthesized via the following procedures. The nitroxide radicals (4-N_3-TEMPO, 0.99 g, 5 mmol or TEMPO, 0.78 g, 5 mmol) were dissolved in a 150-mL mixture of toluene/ethanol (1/1), and a ten-fold molar excess of styrene (5.2 g, 50 mmol, freshly distilled) and $Mn(OAc)_3$ $2H_2O$ (13.4 g, 50 mmol) were added to the solutions. The mixtures were stirred in open 250-ml round-bottomed flasks. Three aliquots of $NaBH_4$ (15-fold molar excess with respect to nitroxides, 3.15 g, 75 mmol) were added portion-wise in 15-min intervals to avoid the boiling of the reaction mixtures. After the filtration of the inorganics, the solvents were evaporated off and the products were separated on a silica column using pure hexane as the eluent, yielding 0.82 g (2.7 mmol, 54%) of pale yellow oil (**1**) or 0.81 g (3.1 mmol, 62%) of white solid (**2**).

HRMS (**1**, *m*/*z*): $[M+H]^+$ calcd for $C_{17}H_{27}N_4O$ 303.2185; found 303.2193.

HRMS (**2**, *m*/*z*): $[M+H]^+$ calcd for $C_{17}H_{28}NO$ 262.2171; found 262.2161.

^1H NMR (**1**, 500 MHz, *d*-DMSO) δ = 7.35-7.18 (m, 5H), 4.77 (q, 1H), 1.82-1.48 (m, 5H), 1.47-1.26 (m, 6H), 1.18 (s, 3H), 1.13 (s, 3H), 0.63 (s, 3H).

^1H NMR (**2**, 500 MHz, *d*-DMSO) δ = 7.34-7.28 (m, 4H), 7.25-7.20 (m, 1H), 4.75 (q, 1H), 1.54-1.38 (m, 6H), 1.37-1.19 (m, 6H), 1.12 (s, 3H), 0.97 (s, 3H), 0.59 (s, 3H).

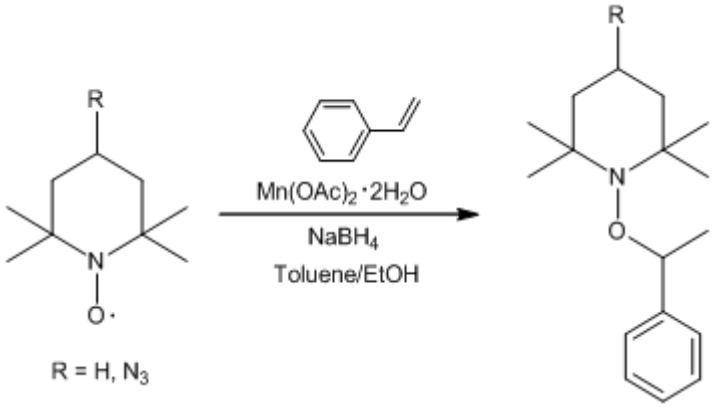

Figure 4.1 Synthesis of alkoxyamines used in this Chapter; 4-N_3-TEMPO-PE (**1**, R = N_3, electrochemistry on silicon surface systems) and TEMPO-PE (**2**, R = H, electrochemistry diffusive systems, EPR and theoretical modelling).

4.3.3 Electrochemical methods and digital simulations

Electrochemical experiments were carried out using a CH 650D electrochemical analyzer (CH Instruments, Austin, TX) and a single compartment three-electrode PTFE cell. Platinum disks or chemically modified Si(100) surfaces (**S-1** and **S-2**, vide infra) served as the working electrodes (analysis of diffusive systems of alkoxyamine **2** or surface-tethered model using alkoxyamine **1**, respectively), a platinum coil was used as counter electrode, and a plastic body silver/silver chloride "leakless" as the reference electrode (eDAQ, part ET072-1). The active area of the platinum disk was electrochemically determined prior to each experiment from the refinement of an E model against experimental voltammograms measured in 1.0×10^{-1}M $MeCN/Bu_4NClO_4$ in the presence of 0.5×10^{-3} M ferrocene (Fc in shorthand hereafter). The geometric area of the Si(100) working electrode was defined to 28 mm^2 by a Viton gasket of rectilinear cross-section. The backside of the silicon sample was scratched with emery paper and rubbed with gallium-indium eutectic. A planar copper plate was

pressed against the sample backside and served as ohmic contact. The reference electrode was calibrated before and after each experiment against the apparent formal potential of the ferricenium/ferrocene couple (Fc^+/Fc) at a platinum disk electrode in 0.5×10^{-3} M Fc. All potentials are reported against the Fc^+/Fc couple. Electrochemical experiments were performed at room temperature (23 ± 2 °C) in a grounded Faraday cage under either argon or air. *In situ* electrochemical electron paramagnetic resonance (EPR) spectra were acquired in a cylindrical cell equipped with a platinum wire as a working electrode (2.5 cm length and 0.2 mm diameter), a platinum coil as an auxiliary electrode and a silver wire as a pseudo-reference electrode. The experiments were conducted using a JEOLJES-FA 200, X-band CW-EPR spectrometer operating at 100 kHz field modulation coupled with the Ecochemie AUTOLAB Autolab PGSTAT302N+BA potentiostat-galvanostat. During measurement, the microwave power was equal to 0.995 mW and modulation width was equal to 0.1 mT and the influence of modulation width on registered spectra was also verified. Digital simulations of cyclic voltammetry and chronoamperometry experiments were performed in DigiElch-Professional v7 (ElchSoft). Simulated kinetic, thermodynamic and transport parameters for the electrode reaction were determined from fittings of experimental data sets that covered a range of concentrations assuming an $EC_{irr}E$ mechanism. Butler-Volmer kinetics was used to estimate charge transfer parameters. A semi-infinite 1D diffusion was assumed at both macrodisk planar and cylindrical electrodes (chronoamperometry and EPR experiments). For microdisks, we considered semi-infinite 2D diffusion fronts with 27 (X) and 23 (Y) grid points. The cell *iR* drop was not compensated during measurement. Values of cell resistance were measured by electrochemical impedance spectroscopy and used in the simulations (data of resistance are 140 Ω for MeCN/Bu_4NPF_6, 144 Ω for MeCN/Bu_4NClO_4, 1466 Ω for MeCN/NaBARF, 1220 Ω for DCM/Bu_4NPF_6; with the exception of the borate salt, which was present at 1.0×10^{-2} M, all supporting salts were at a concentration of 1.0×10^{-1} M). Adsorption steps were neglected in the simulations and the transfer coefficients for both electrons transfer reactions (TEMPO/oxoammonium and **2/2**$^{\bullet+}$) were assumed as constants (α, 0.5) for fitting purposes. Including a DISP-COMP

pathway[31] does not improve the results. In the simulations the homogeneous chemical steps for the fate of the putative benzylic cation fragment (R^+) was not considered as this has no effect on the quality of the fits. The diffusion coefficients of **2** and $\mathbf{2}^{\bullet+}$ were obtained from the best fits of an $EC_{irr}E$ model of the linear sweep voltammogram at platinum microdisk electrodes and were assumed equal. For the chemical step, only the forward (k_f) constant was considered. The second-order backward (k_b) constant tends to zero (i.e., backward chemical reaction is not operative in the time scale of the experiments). The refined values of formal potential and rate constant obtained from the fitting of the independent experiments show some minor differences (*vide infra*). These differences, which are statistically non-significant in the case of the rate constants, are most likely reflecting deviations from the assumptions made in the modeling, namely assumptions of linear diffusion conditions and equal diffusion coefficients. The possibility of adsorption events contributing to these shifts was also not disregarded, and it is discussed in the Figure 4.9. Moreover, the refinement of thermodynamic data for the $\mathbf{2}/\mathbf{2}^{\bullet+}$ and TEMPO/oxoammonium couples were guided by independent quantum chemistry calculations of a theoretical model of the system.[32]

4.3.4 Si(100) surface modification

Assembly of monolayers of 1,8-nonadiyne on Si(100). Silicon wafers were firstly cut into pieces (approximately 10 × 30 mm in size), cleaned by 30 min of Soxhlet reflux with chloroform and immersed for 20−30 min in hot Piranha solution (100 °C, a 3:1 (v/v) mixture of concentrated sulfuric acid to 30% hydrogen peroxide ***Caution:*** *piranha solution reacts violently with organic substances*). The wafers were then rinsed with copious amounts of water and immediately etched with a deoxygenated 40% aqueous ammonium fluoride solution for 5 min. A small amount (ca. 5 mg) of ammonium sulfite was added to the etching bath. The assembly of the acetylenylated Si(100) surface by covalent attachment of 1,8-nonadiyne on hydrogen-terminated silicon was done by using a light-assisted hydrosilylation method.[33-36] The freshly etched samples were then washed sequentially with water and DCM, and blown dry in argon before the dropping of a small deoxygenated sample of 1,8-nonadiyne (approximate 50 μL) on the

hydrogen-terminated wafers, followed by covering it with a quartz slide to limit evaporation, rapidly transferred to an air-tight and light-proof reaction chamber, and kept under a stream of argon. A collimated LED source (λ = 365 nm, nominal power output > 190 mW, Thorlabs part M365L2 coupled to a SM1P25-A collimator adapter) was fixed over the sample at a distance of about 10 cm. After illumination for a 2 h period, the acetylene-functionalized samples (Scheme 4.1) were removed from the reaction chamber, rinsed several times with DCM and rested for a 12 h period in a sealed vial at +4 °C under DCM, before being further reacted with **1** (4-N_3-TEMPO-PE) or 4-N_3-TEMPO.

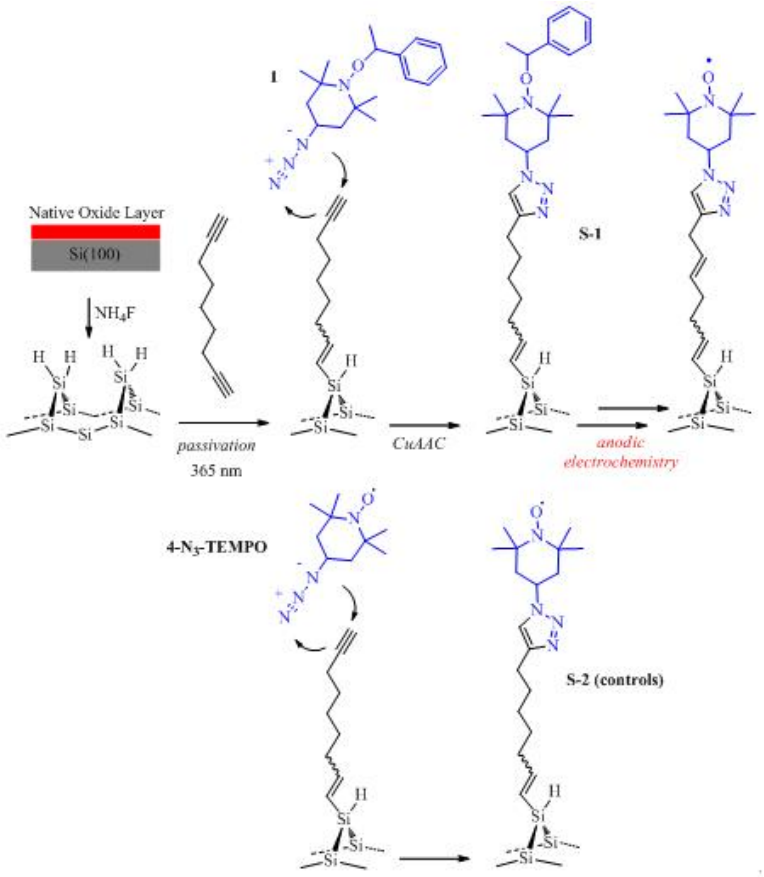

Scheme 4.1 Light-assisted (365 nm) hydrosilylation of 1,8-nonadiyne to passivate an hydrogen-terminated Si(100) electrode and covalent attachment of **1** (upper panel) and 4-N_3-TEMPO (lower panel) via CuAAC "click" reactions to yield either alkoxyamine (**S-1**) or nitroxide (**S-2**, TEMPO controls) monolayers, respectively.

Click derivatization of acetylene-terminated Si (100) surface. In the "click" procedure, copper(I)-catalyzed alkyne-azide cycloaddition (CuAAC) reactions were used to graft 4-N_3-TEMPO-PE (**1**) to the acetylenylated surfaces.[37] In brief, to a reaction vial

containing the alkyne-functionalized silicon surface was added (i) the azide (**1**, 0.5×10^{-3} M, 2-propanol/water, 1:1), (ii) copper(II) sulfate pentahydrate (1.0×10^{-4} M) and (iii) sodium ascorbate (5 mg/mL). Reactions were carried out without excluding air from the reaction environment at room temperature and under ambient light. Samples were removed from the reaction vessel after a reaction time of 2 h. The surface-bound [1,2,3]-triazoles Si(100) samples (**S-1**, Scheme 4.1) were rinsed consecutively with copious amounts of ethanol, water, ethanol and DCM, and blown dry in argon before being analyzed. An analogous procedure was used for the attachment of 4-N_3-TEMPO to yield redox-active monolayers of TEMPO (**S-2,** Scheme 4.1) used in control experiments.

4.3.5 Surface characterization

X-ray photoelectron spectroscopy (XPS). The formation of the alkoxyamine monolayer (**S-1**) was confirmed by XPS measurements. X-ray photoelectron spectra were obtained on an ESCALAB 220iXL spectrometer fitted with a monochromatic Al Kα source (1486.6 eV), a hemispherical analyzer and a 6 multi-channel detector. Spectra were recorded in normal emission with the analyzing chamber operating below 10^{-9} mbar. The resolution of the spectrometer is ca. 0.6 eV as measured from the Ag $3d_{5/2}$ signal (full width at half maximum, FWHM) with 20 eV pass energy. High-resolution scans were run with 0.1 eV step size, dwell time of 100 ms and the analyzer pass energy set to 20 eV. After background subtraction, spectra were fitted with Voigt functions.

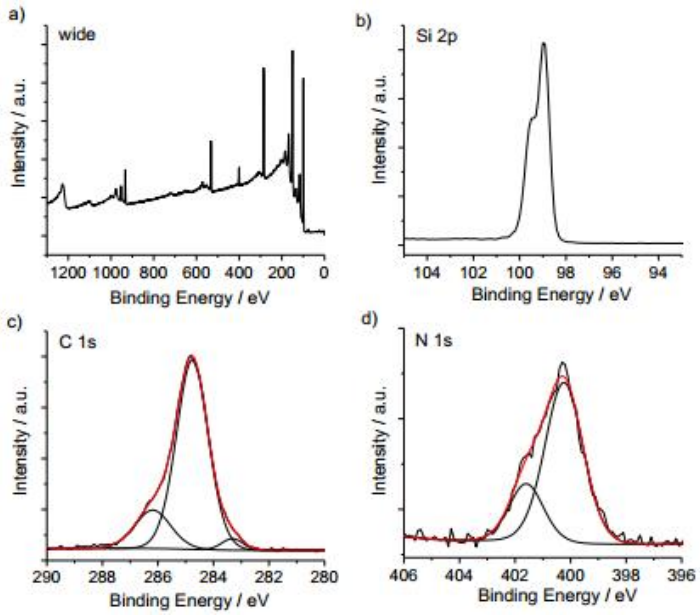

Figure 4.2 XPS spectra of 4-N_3-TEMPO-PE monolayers (**S-1**) assembled on highly-doped Si(100) electrodes by CuAAC reactions between 4-N_3-TEMPO-PE (**1**) and monolayers of 1,8-nonadiyne on Si(100). a) Survey XPS scan. b) High-resolution XPS scan for the Si 2p region. c) Narrow scan of the C 1s region. d) Narron scan of the N 1s region.

From the high resolution scans in Figure 4.2, it is evident that alkoxyamine **1** is covalently attached to the electrode. The electrode oxidation is also negligible. High-resolution scan for the Si 2p region comprising two spin–orbit-split components are shown in panel (b) and the silica-related emission (102–104 eV signal associated with SiO_x) were below the spectrometer detection limit of ca. <0.05 SiO_x monolayers equivalents. The XPS C 1s region can be deconvoluted into three contributions of mean binding energies of 283.4, 284.8, 286.2 eV (panel (c)). The smallest peak centered at 283.4 eV is ascribed to sp2 C-C in the benzene ring.[38] The peak at 284.8 eV is characteristic of carbon-bound carbon atoms (C-C). Signals from C-O and C-N are suggested to contribute to the 286.2 eV signal.[39] The high-resolution N 1s data (panel (d)) shows good agreement with the literature for analogous derivatization procedures on solid surfaces.[33] The lack of *ca.* 405 eV[40, 41] N 1s emission from electron-deficient nitrogen atom in the azido group confirm negligible physisorption of alkoxyamine **1** molecules in the film. The N 1s peak is resolved into two peaks assigned at 400.2 and 401.6 eV, with an expected ratio of the peak areas being *ca*. 3:1, which indicates a successful triazole formation.[33, 42, 43] There are not any binding energy signals for the

free nitroxide nitrogen atom[44] or a shakeup satellite of N-O electrons[45, 46], which confirms that the chemical structure of alkoxyamine **1** is preserved upon surface attachment.[47]

***X-ray reflectometry* X-ray reflectivity (XRR)**. XRR profiles of **S-1** sample (Figure 4.3) were measured under ambient conditions on a Panalytical Ltd X'Pert Pro Reflectimeter using radiation wavelength of $\lambda = 1.54$ Å from a Cu Kα source. The X-ray beam was focused and collimated using a Göbel mirror and pre-sample slit with a 0.1 mm horizontal opening. The reflectivity data were collected over an incident angle range $0.05° \leq \theta \leq 5.00°$ with a step size of 0.01° and a counting time of 7 seconds per step. All data were collected in the specular regime where angle of incidence is equal to angle of reflection. The data were normalized so that the critical edge is equal to unity and presented as reflectivity *versus* momentum transfer, Q ($= 4\pi \sin\theta / \lambda$, where θ is the angle of incidence and λ the wavelength). Structural parameters were refined using MOTOFIT analysis software.[47] The model used described the 4-N_3-TEMPO-PE monolayer (**S-1**) as a single layer defined by its thickness, roughness and X-ray scattering length density (SLD) calculated as:

$SLD = (\sum Z_i r_e) / V_m$

Where Z_i is the atomic number for each atom in 4-N_3-TEMPO-PE, r_e is the Bohr electron radius (2.818×10^{-15} m) and V_m is the molecular volume (calculated to be 471.29 $Å^3$ from http://www.molinspiration.com/cgi-bin/properties). This gives a theoretical SLD for **S-1** of 15.06×10^{-6} $Å^{-2}$. In the fitting, a least squares regression employing a generic algorithm was used to minimize χ^2 values by varying the thickness and SLD of the monolayer and the roughness of the monolayer-air and silicon-monolayer interfaces. The errors reported from the fitting are ±1 standard deviation.

The refined XRR parameters results of **S-1** monolayers are listed in the table below:

Layer	Thickness (Å)	SLD ($\times 10^{-6}$ $Å^{-2}$)	Roughness (Å)
Air	-	0.0 (fixed parameter)	-
S-1	14.2 ± 0.4	15.0 ± 0.1	8.9 ± 0.1
Silicon	-	20.1 (fixed parameter)	2.7 ± 0.2

The fitted SLD gives a volume fraction of 0.99 for the **S-1** monolayer. Therefore, a near-complete monolayer has been formed.

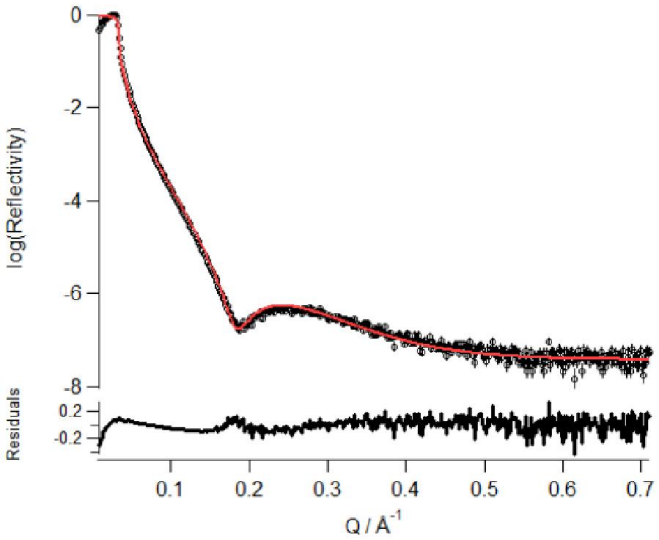

Figure 4.3 X-ray reflectivity of 4-N_3-TEMPO-PE monolayer (S-1) on silicon at the air-solid interface. The points with error bars show the collected data and the solid red line is the fit to the data. The lower trace is the residuals between collected and fitted data. The refined monolayer thickness is 14.2 ± 0.4 Å which is in good agreement with the theoretical values of 17 Å (Chem3D).

4.3.6 Computational methods

For the electrochemical experiments, accurate absolute values of the oxidation potentials and homolysis energies were required and so higher levels of theory were used, based on extensive benchmarking studies, including for alkoxyamine homolysis energies,[48] and nitroxide oxidation potentials and ion-pairing energies.[28, 49] All geometry optimizations and frequency calculations were performed at the M06-2X/31+G(d,p) level of theory. Entropies, thermal corrections and zero-point vibrational energies were scaled by recommended scale factors.[50] Improved single-point energies were calculated using the high-level composite *ab initio* G3(MP2,CC)(+) method, a variation of standard G3(MP2,CC)[51] where calculations with the 6-31G(d) basis set are replaced with corresponding 6-31+G(d). These high-level calculations were utilized in conjunction with the ONIOM approximation[52, 53] for larger systems, with either standard G3(MP2,CC) or UMP2 used to model remote substituents effects. The solvation model based on density (SMD)[54] was used to relax gas-phase structures to the

solution-phase (at the UM06-2X/6-31+G(d,p) level of theory). Free energies of solvation were then calculated on solution-phase geometries using the COSMO-RS model,[55-57] using the ADF package,[58] at the BP/TZP level of theory (as it was parameterized for), and the remaining parameters were kept as default values.[59] All standard *ab initio* molecular orbital theory, density functional theory (DFT) calculations were carried out using Gaussian 09[60] and Molpro 2015[61, 62] software packages. Full details of all theoretical procedures used for computing electrochemical experiments (including optimized geometries, oxidation potential of different species and ion-pairing energies) can be found in our published paper.[63]

4.4 Results and discussions

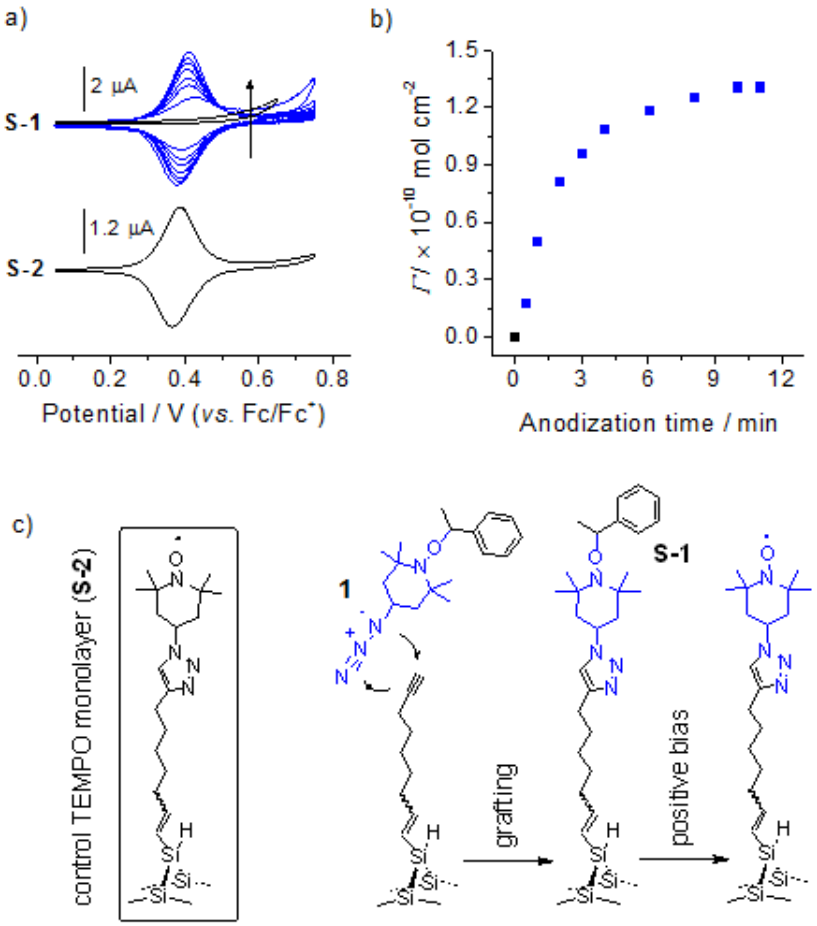

Figure 4.4 Anodic cleavage of a surface-tethered alkoxyamine (**S-1**) and its conversion into a Si(100) nitroxide-terminated monolayer (electrolyte is 1.0×10^{-1} M Bu_4NClO_4 in MeCN). The monolayer distal-end of **S-1** samples is the phenylethyl portion of an alkoxyamine molecule (**1**) and it is lost to the electrolyte upon electrolysis. (a) Cyclic voltammograms (100 mV s^{-1}) acquired before (black trace) and after (blue trace) applying a positive bias to **S-1** samples prepared on Si(100) electrodes. The potential is

stepped from open circuit to 0.65 V (vs. Fc/Fc^+) for a 30 s period before recording a voltammogram and selected traces are presented in the figure (blue traces). Anodization of **S-1** results in the progressive appearance of a redox signature that is in good agreement with that of a surface-tethered TEMPO control (**S-2**, black trace). The TEMPO coverage rises in increments of about 2.6×10^{-11} mol cm^{-2}, and reaches a maximum of ca. 1.31×10^{-10} mol cm^{-2}, equivalent to ca. 25% of a close-packed TEMPO monolayer assembled on a gold surface.[64] (b) Plot of the electrochemically-determined changes to the surface coverage of redox-active nitroxide radicals as a function of the anodization time of **S-1** samples. (c) Reaction schematics for the alkoxyamine surface model (**S-1**) and controls (**S-2**).

Chemists appreciate that the condition of bulk electroneutrality is not valid at interfaces, and strong field gradients are ubiquitous at electrode/electrolyte interfaces (i.e., electrical double layer).[65, 66] Anodization of a surface-tethered alkoxyamine **1** in a perchlorate-based electrolyte (**S-1** surface construct in Figure 4.4, surface modification and XPS/XRR characterizations in Scheme 4.1 and Figures 4.2 and 4.3, respectively) shows the gradual appearance of a TEMPO redox signature[28, 67, 68] upon positive biases. A similar electrochemical pre-treatment with negative bias has only a minor effect on the cleavage. Under these conditions, the greater yield with positive bias was unexpected as the alkoxyamine (and product nitroxide radical) is tethered with the nitrogen-side of the polar $N^{\delta+}$–$O^{\bullet\delta-}$ bond closest to the electrode, hence it was initially assumed that a negative electrode would better stabilize the nitroxide radical product.

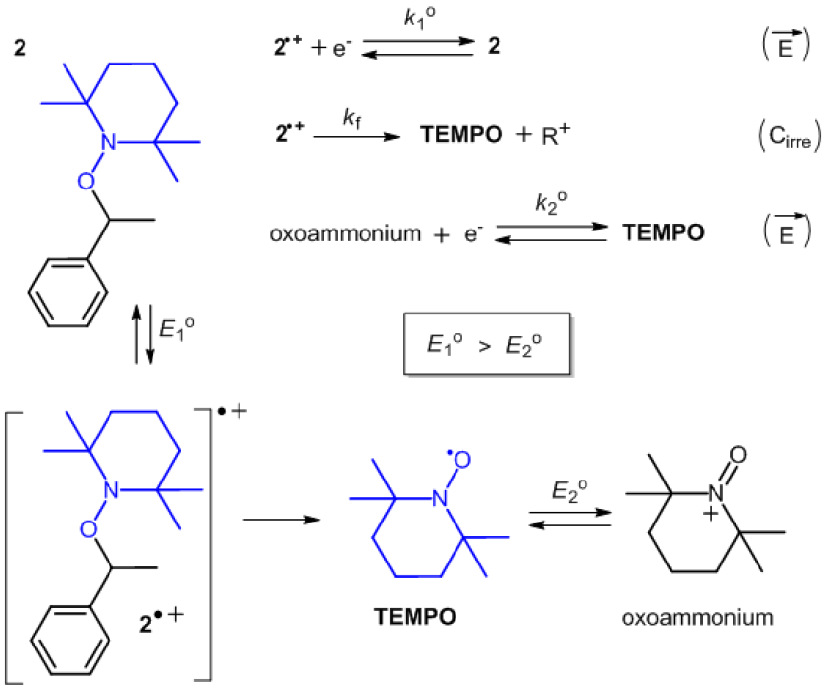

Scheme 4.2 $EC_{irre}E$ mechanism accounting for the anodic fragmentation of alkoxyamine **2**. The anodic intermediate $\mathbf{2}^{\bullet+}$ is an unstable transient species which is found to undergo rapid unimolecular decomposition (C_{irre}, k_f in the order 10^6 s^{-1}, see the details on individual electrolyte systems below), releasing at room temperature the redox-active nitroxide fragment (**TEMPO**).

The monolayer distal end of **S-1** samples is the phenylethyl portion of the alkoxyamine, which is lost in the electrolyte upon electrolysis (vide infra, follow-up chemical fragmentation) leaving behind surface tethered and redox-active nitroxide units. This surface chemistry construct permits the "trapping" of the putative product of alkoxyamine lysis and to fine-tune and measure the surface concentration of the newly formed nitroxides (see Figure 4.4). Such a fine control – an ON/OFF switch of alkoxyamine homolysis – would be beyond reach using conventional thermal ramps. However, follow up diffusive experiments revealed that the situation is much more complicated than was first anticipated (*i.e.* simple stabilization of charge-separated contributors by distal negative charges) and that in electrolytes the positive bias was actually leading to oxidation of the alkoxyamine. This in turn led to its cleavage to a carbocation and nitroxide, followed by oxidation of the latter to oxoammonium (Scheme 4.2). Subsequently this same behavior was observed in non-surface tethered nitroxide radicals, where digital simulations of voltammetry and *in-situ* electrochemical EPR experiments were able to help validate an $EC_{irr}E$ mechanism and measure the thermodynamic and kinetic parameters of the process.

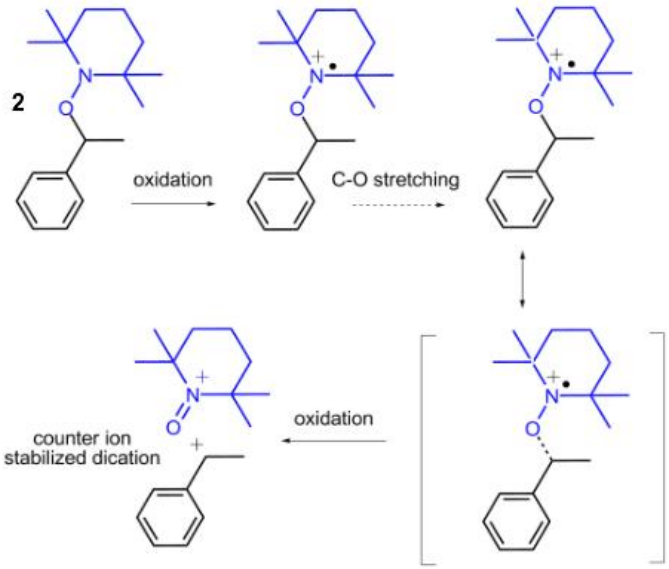

Scheme 4.3 In the electrochemical model applied here, the electrochemical and chemical steps were "uncoupled" and assigned the corresponding thermodynamics and kinetics. That is, changing the position of the chemical step, i.e., to go from an ECE mechanism to an EEC-like mechanism, with very fast breaking of the C-O bond in a dication of **2.** This alternative mechanism is theoretically (quantum model of the system) justifiable, but cannot account for the accumulation of the TEMPO EPR signal.

It can also be noted that there is a second and very intriguing mechanistic possibility. It would be theoretically not inconceivable to change the place of the chemical step, i.e. to go from an ECE mechanism to an EEC-like mechanism, with very fast breaking of the C-O bond in the dication formed from **2** (see Scheme 4.3). The refinement of the voltammetry would marginally drop in quality, but this path could, in principle, align with the observations of a prevalent lack of "anion-sensitivity" in terms of current shapes and positions, and agree with a mainly-Coulombic stabilization of the final di-cation. In fact, a quantum model of the system for this scenario is satisfactory, but on the other hand this mechanism would be in disagreement with the EPR signal (*vide infra*). This would become complex to explain and, therefore, the $EC_{irr}E$ process is the only framework where all of the observations are accounted for, fit with a quantum model, and very satisfactorily. In short, this work has further expanded the analysis to validate the ECE mechanism.

Furthermore, an addition was made of an explicit reference to the possibility of a DISP/COMP contribution. Hence, analysis of the voltammetry included a DISP/COMP pathway and simulations based on a theoretical treatment have been reported recently on this specific subject.[31] The results indicate that including the possibility of DISP/COMP is not found to affect the conclusions on a simple $EC_{irre}E$ mechanism in any significant way. The latter contents show representative experimental voltammograms, current-time transients (chronoamperometry) and digital simulations for the electrochemical oxidation of **2** at platinum electrodes in different electrolyte solutions. Extensive data sets where the voltage sweep rate and concentration of the alkoxyamine reagent were varied over two orders of magnitude range are also presented.

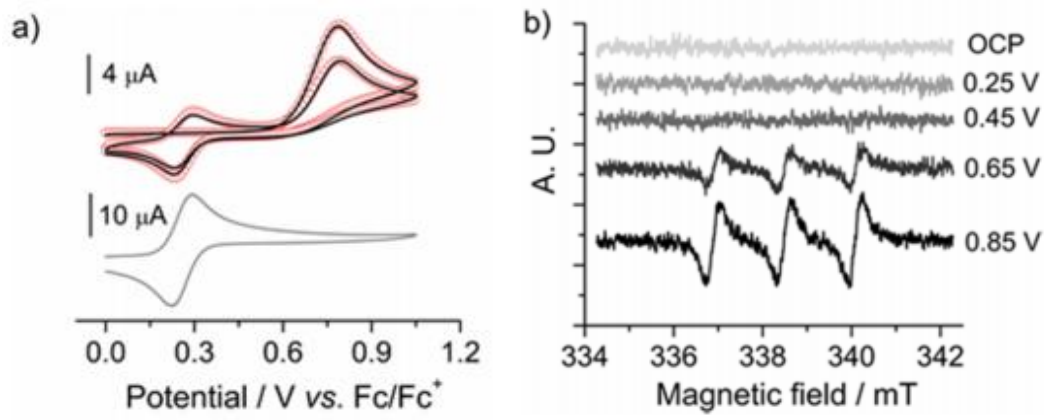

Figure 4.5 Anodic electrochemistry of alkoxyamines **2** at platinum electrodes. (a) Experimental (solid lines) and simulated (empty symbols) cyclic voltammograms of 0.5×10^{-3} M **2**, and experimental data (offset grey trace) of 0.5×10^{-3} M TEMPO controls. The best-fit parameters are D (**2**/**2**$^{\bullet+}$) = 7.8×10^{-6} cm^2 s^{-1}, D (TEMPO/oxoammonium) = 2.2×10^{-5} cm^2 s^{-1}, E_1^0 = 0.78 V, k_1^0 = 0.05 cm s^{-1}, E_2^0 = 0.195 V, k_2^0 = 0.08 cm s^{-1}, k_f = 5.0×10^6 s^{-1}. (Electrolyte is 1.0×10^{-1} M MeCN/Bu_4NClO_4, and scan rate is 100 mV s^{-1}, 0.7 cm^2 platinum macrodisk electrode). (b) *In-situ* electrochemical EPR measurements conducted in 1.0×10^{-1} M DCM/Bu_4NPF_6 in the presence of 0.5×10^{-3} M of **2**. The specified electrolysis bias (labels to curves vs. Fc/Fc$^+$) was applied to a platinum wire electrode for 360 s with the EPR data being accumulated over the last 60 s of the potential step.

The first anodic segment is featureless, i.e., it displays only a capacitive-like current until the potential is extended to about 0.7 V, where the current rises rapidly to show a clear oxidative wave before the onset of background processes. This anodic process is irreversible over the time scale of the experiment. The lack of a reverse peak in cyclic voltammetry (Figure 4.5a), as well as the modelling of current-time transients (triple potential step chronoamperometry data in Figure 4.6), indicate that the electron-transfer step is followed by a fast follow-up homogeneous chemical reaction. A satisfactory fit of both types of experiments does not require inclusion of a second-order reverse process in the chemical step; hence it is apparent that alkoxyamine **2** undergoes fragmentation after its initial electrochemical oxidation with a rather large chemical rate (k_f = 5.0×10^6 s^{-1}). The current magnitude of the most anodic wave, as well as the appearance of a redox signature upon scan reversal, both indicate that one of the two fragments is electrochemically-active. The electrode kinetics and thermodynamics for this fragment are a perfect match of those obtained for control experiments using

TEMPO solutions (E^0_{TEMPO}= 0.21 V *vs.* Fc/Fc$^+$, k^0_{TEMPO} = 0.08 cm s^{-1}, lower grey trace in Figure 4.5a and extensive data sets in Figures 4.7 and 4.8).

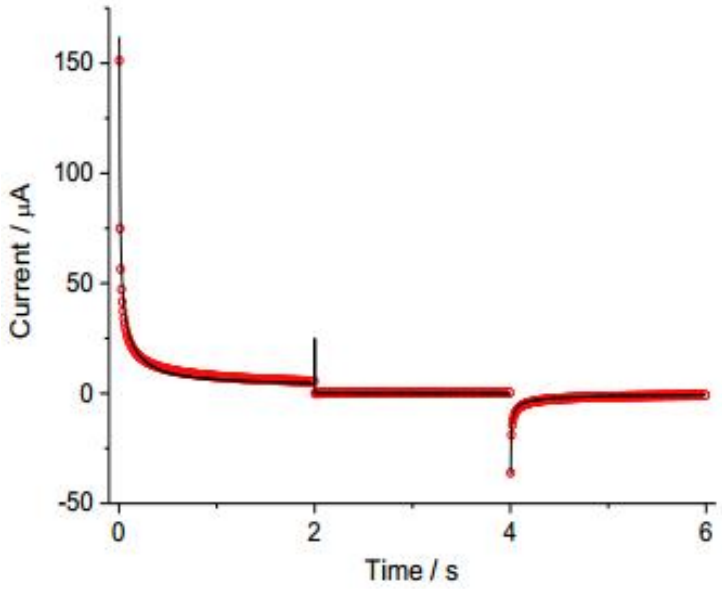

Figure 4.6 Current evolution with time in a typical three-step chronoamperometry experiment of 0.36 × 10^{-3} M **2** in MeCN with 1.0 × 10^{-1} M Bu_4NClO_4. Experimental (solid line) and simulated (symbols) transients with the potential being stepped from -0.03 V to 0.87 V, then from 0.87 V to 0.47 V, and from 0.47 V to -0.03 V (vs. Fc/Fc$^+$). The best-fit parameters are D (**TEMPO**/oxoammonium) = 2.2 × 10^{-5} cm^2 s^{-1}, D (**2**/**2**$^{\bullet+}$) = 7.8 × 10^{-6} cm^2 s^{-1} E^0_1 = 0.78 V (vs. Fc/Fc$^+$), k^0_1 = 0.05 cm s^{-1}, E^0_2 = 0.195 V (vs. Fc/Fc$^+$), k^0_2 = 0.08 cm s^{-1}, k_f = 5.0 × 10^6 s^{-1}. The electrochemically-determined effective area for the data in the figure is 0.07 cm^2.

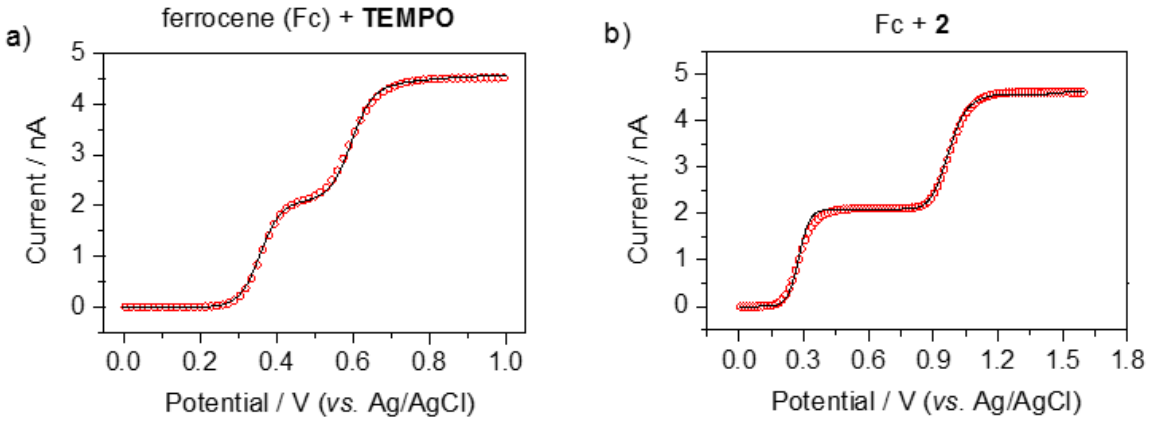

Figure 4.7 a) Cyclic voltammograms at Pt microdisks (4.5 μm in radius) of a solution containing 0.53 × 10^{-3} M Fc and 0.63 × 10^{-3} M **TEMPO** in MeCN with 1.0 × 10^{-1} M Bu_4NClO_4 (voltage sweep rate is 10 mV s^{-1}). The refined parameters (E mechanism) are: E^0(Fc/Fc$^+$) = 0.35 V *vs.* Ag/AgCl ("leakless", see experimental section), k^0 (Fc/Fc$^+$) = 0.20 cm s^{-1}, E^0 (**TEMPO**/oxoammonium) = 0.58 V, k^0(**TEMPO**/oxoammonium) =

0.10 cm s^{-1}, α =0.5. b) Cyclic voltammograms at Pt microdisks (4.5 µm in radius) of 0.53 × 10^{-3} M Fc and 0.92 × 10^{-3} M **2** in MeCN with 1.0 × 10^{-1} M Bu_4NClO_4 (scan rate is 10 mV s^{-1}). The refined parameters ($EC_{irr}E$ mechanism) are: E^0 (Fc/Fc^+) = 0.26 V vs Ag/AgCl ("leakless"), k^0 (Fc/Fc^+) = 0.10 cm s^{-1}, E^0 (**2**/**2**$^{\bullet+}$) = 1.05 V, k^0 (**2**/**2**$^{\bullet+}$) = 0.08 cm s^{-1}, E^0 (**TEMPO**/oxoammonium) = 0.47 V, k^0 (**TEMPO**/oxoammonium) = 0.08 cm s^{-1}, α = 0.5. For the chemical step of **2**$^{\bullet+}$ → **TEMPO** + R^+, the refined k_f is 5.0 × 10^6 s^{-1}. The experimental and simulated curves are plotted as solid lines and empty symbols, respectively. The diffusivity of Fc was set equal to 2.3 × 10^{-5} cm^2 s^{-1}.[69] The diffusivity of the **2**/**2**$^{\bullet+}$ couple was 7.8 × 10^{-6} cm^2 s^{-1}. The refined D value of 2.2 × 10^{-5} cm^2 s^{-1} for the **TEMPO**/oxoammonium couple was also independently estimated by fittings of experimental cyclic voltammetry at Pt macrodisk electrodes (Figure 4.8).

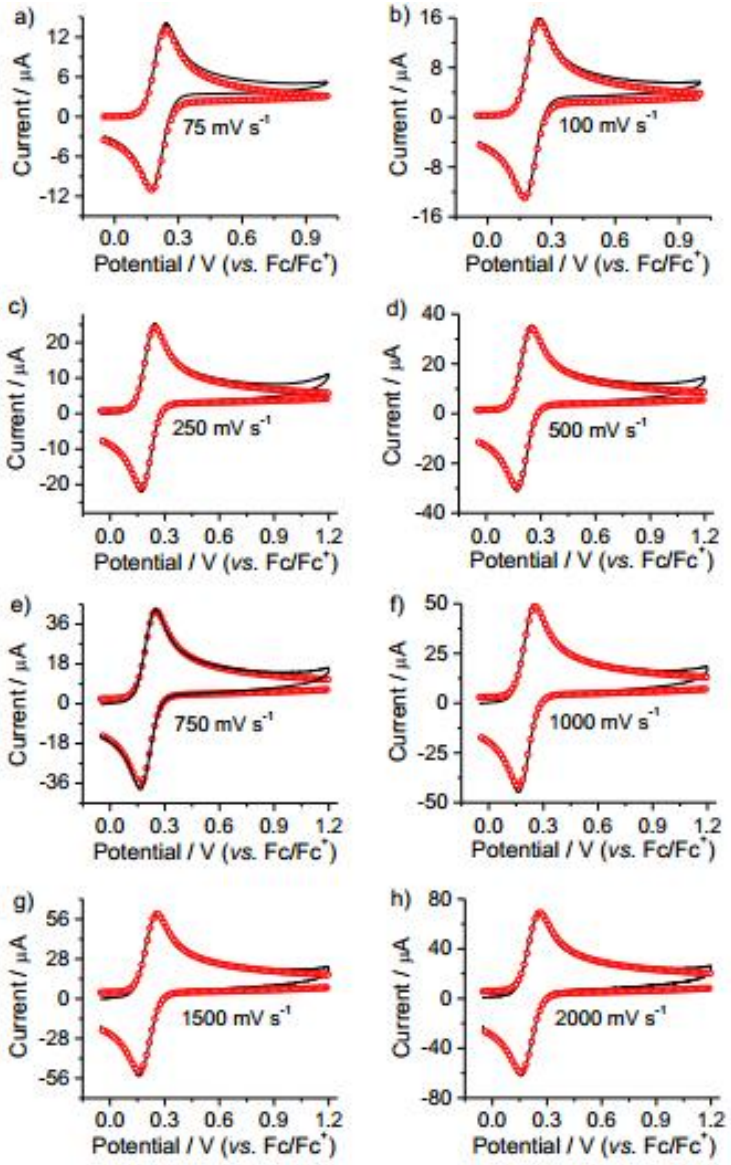

Figure 4.8 Experimental (solid line) and simulated (empty symbol) cyclic voltammograms for 0.5 × 10^{-3} M **TEMPO** solutions in MeCN containing 1.0 × 10^{-1} M Bu_4NClO_4 at different scan rates (indicated as labels to the figures). The diffusion coefficients and the electron transfer rate constant used to fit the data were 2.2 × 10^{-5}

cm^2 s^{-1} (D_{TEMPO}), 2.2 × 10^{-5} cm^2 s^{-1} ($D_{oxoammonium}$) and 0.08 cm s^{-1} (k^0_{TEMPO}), E^0_{TEMPO} = 0.21 V (vs. Fc/Fc^+). The electrochemically-determined effective area of the Pt disk electrode is 0.07 cm^2.

These controls, in conjunction with *in-situ* electrochemical EPR data (Figure 4.5b and Figure 4.9), indicate that lysis of the oxidized alkoxyamine (**2**$^{\bullet+}$) is most likely occurring on its C–ON bond with release of the parent nitroxide (i.e., TEMPO, *vide infra* for the discussion on a quantum model of the system). Figure 4.9 shows the simulated TEMPO concentration profiles and cumulative number of TEMPO molecules across the EPR cell obtained upon the anodization of alkoxyamine **2**. As seen from panel (a) in Figure 4.9, the EPR signal emerging during the anodization of **2** (0.5 mM solutions, 0.4 mL total sample volume) is in agreement with the pure EPR signal of a TEMPO control solution. The standard based on Mn^{2+} was used to calibrate g-factor. EPR spectra of Mn^{2+} consists of six spectral lines. Organic radicals absorb energy in the range of magnetic field between the third and the fourth spectral line of Mn^{2+}. In order to calculate the g-factor, the spectra of Mn^{2+} (the third and fourth line) together with investigated sample was measured. Based on known values of g-factor of corresponding lines of Mn^{2+}spectra (2.03277 for 3rd and 1.98104 for 4th spectral line) the g-factor of investigated sample was calculated. G-factor of pure TEMPO as well as **2**$^{\bullet+}$ is equal to 2.00619 (calculated for the center of spectra).

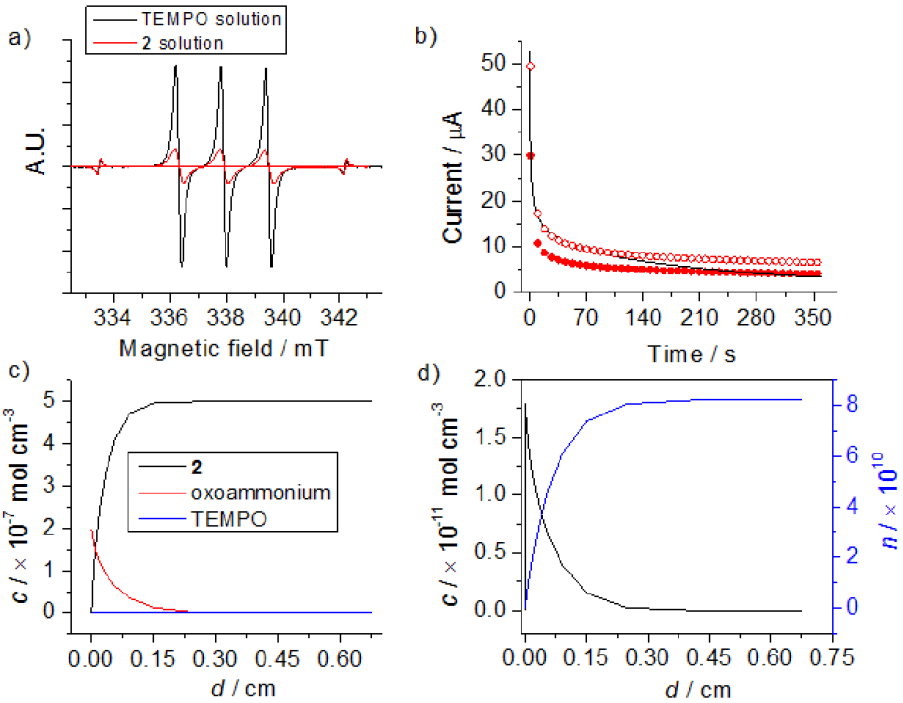

Figure 4.9 (a) EPR spectra (red trace) of anodized TEMPO-PE solutions (0.5×10^{-3} M **2** in DCM with 1.0×10^{-1} M Bu_4NPF_6). The working Pt bias is poised to 0.85 V vs. Fc/Fc^+, the anodization time is 360 s and the EPR spectra is accumulated during the last 60 s of the anodic pulse. The EPR spectra of **2** is plotted against the EPR spectra (acquired at OCP) of control **TEMPO** solutions (black trace). (b) Experimental (solid line) and simulated (symbols) current-time transients after a potential step from OCP to 0.85 V (vs. Fc/Fc^+, cylindrical geometry, 0.01 cm radius and length of either 2.5 cm (solid symbol) or 4 cm (empty symbol), and semi-infinite 1D diffusion). The electrolyte is a 0.5×10^{-3} M solution of **2** and for the simulations (symbols) consideration was given to an $EC_{irr}E$ mechanism that is described by the following parameters: $E_1^0 = 0.80$ V (vs. Fc/Fc^+), $k_1^0 = 0.01$ cm s^{-1}, $E_2^0 = 0.30$ V, $k_2^0 = 0.01$ cm s^{-1}, $\alpha = 0.5$. D (**TEMPO**/oxoammonium) = 1.9×10^{-5} cm^2 s^{-1}, D (**2**/**2**$^{\bullet+}$) = 6.0×10^{-6} cm^2 s^{-1}. The value of k_f for the irreversible chemical step is 1.0×10^6 s^{-1}. (c) Simulated concentration profiles (**2**, oxoammonium and **TEMPO**, $EC_{irr}E$ parameters as at panel (b)) near the cylindrical Pt wire (0.01 cm radius and 2.5 cm in length) and (d) simulated cumulative number of **TEMPO** molecules (right y-axis) present in the EPR sample after the 360 s potential step.

Further, the potential of the pseudo-reference used in the EPR cell was checked against the Fc/Fc^+ couple prior to experiment and the anodization bias was specified in the figure caption and reported against Fc/Fc^+ ("*Pt bias is 0.85 V vs. Fc/Fc*$^+$ "). On top of the reported simulated transients by using the $EC_{irr}E$ parameters extracted from voltammetry and chronoamperometry at macrodisk electrodes while accounting for the cylindrical geometry (EPR electrode) and semi-infinite 1D diffusion (panel (c)), the actual current transients have been obtained in the EPR experiment and plotted against simulations in panel (b). There is an apparent reduction of current signal during the long chronoamperometric experiments and it is concluded that electrode fouling is taking place over this time scale (360 s). Thin-layer effects could also account for the drop in current, but it is relatively unlikely to be operating as the working electrode-cell wall distance is more than 0.2 mm (after 100-200 s the linear diffusion layer for a 0.1 mm-radius cylindrical electrode is around 0.2 mm). Electrode fouling seems a more reasonable explanation. To account for this use has been made of a lower effective area as a conservative value when calculating the cumulative number of EPR-active TEMPO molecules in the EPR cavity, as illustrated in panel (d), the estimated number of spins (cumulative number of TEMPO molecules after 360 s of sample anodization) is in line with the detection limit of nitroxide radicals by EPR.[70]

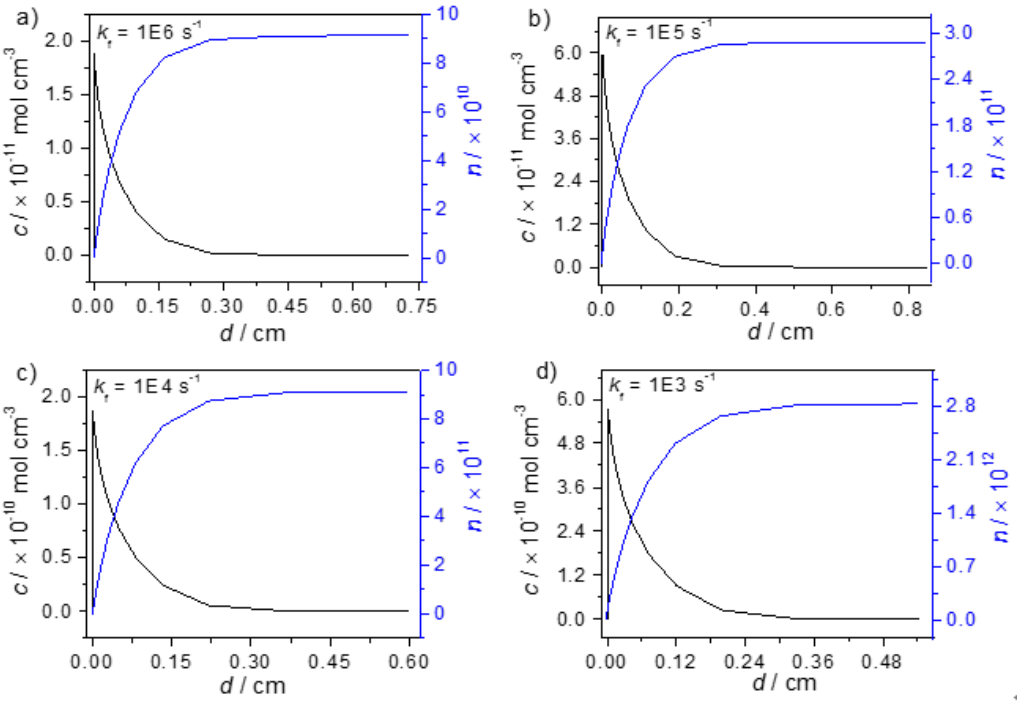

Figure 4.10 Simulated concentration profiles; Effect of changes to the rate of the chemical step. Plots (a)-(d) illustrate the direction of the hypothetical changes to the cumulative number (n) of TEMPO molecules that would be present in the electrolyte compartment of the EPR experiment (semi-infinite 1D diffusion at a cylindrical electrode of 0.1 cm in radius and 2.5 cm in length) in response to changes to the rate of the chemical step. The simulated electrode reaction is the electrolysis of 0.5 × 10^{-3} M **2** induced by a potential step from 0.3 V to 1.1 V, 360 s of anodization time and considering an EC$_{irr}$E mechanism that is described by the following parameters: E_1^0 = 1.01 V, k_1^0 = 0.04 cm s^{-1}, E_2^0 = 0.425 V, k_2^0 = 0.05 cm s^{-1}, α = 0.5. D (**TEMPO**/oxoammonium) = 2.2 × 10^{-5} cm^2 s^{-1}, D (**2**/**2**$^{\bullet+}$) = 7.0 × 10^{-6} cm^2 s^{-1}. The value of k_f describing the chemical step is dropped from 1.0 × 10^6 s^{-1} to 1.0 × 10^3 s^{-1} ((a)-(d), respectively).

In summary, the accumulation of TEMPO molecules in the EPR cavity is measurable and it is a function of the rate of the chemical step (k_f). Reproduced simulated concentration profiles to expand briefly on this aspect are given in Figure 4.10. The "cumulative" number of TEMPO molecules in the EPR cavity decreases when (k_f) increases from 10^3 s^{-1} to 10^6 s^{-1}.

In brief, digital simulations of the electrochemical data lead to the following main conclusions: (i) the overall mechanism needs to be analyzed as an EC$_{irr}$E process (i.e., sequential electrochemical-chemical-electrochemical steps, Scheme 4.2); (ii) a large cation radical decay reaction rate constant (k_f) is needed to reproduce the shapes of all the experimental curves; (iii) the anodic wave at ca. 0.7 V includes two one-electron

processes, the oxidation of **2** (refined E_1^0 = 0.78 V) and the oxidation of a portion of the newly-formed TEMPO units (refined E_2^0 = 0.195 V). In brief, after the oxidation of the parent alkoxyamine, $\mathbf{2}^{\bullet+}$ participates in a fast homogeneous chemical reaction, explaining the mechanistic framework that leads to a free nitroxide and a carbocation at the electrified interface ($\mathbf{2}^{\bullet+} \rightleftarrows$ TEMPO + R^+, $k_b \rightarrow 0$).

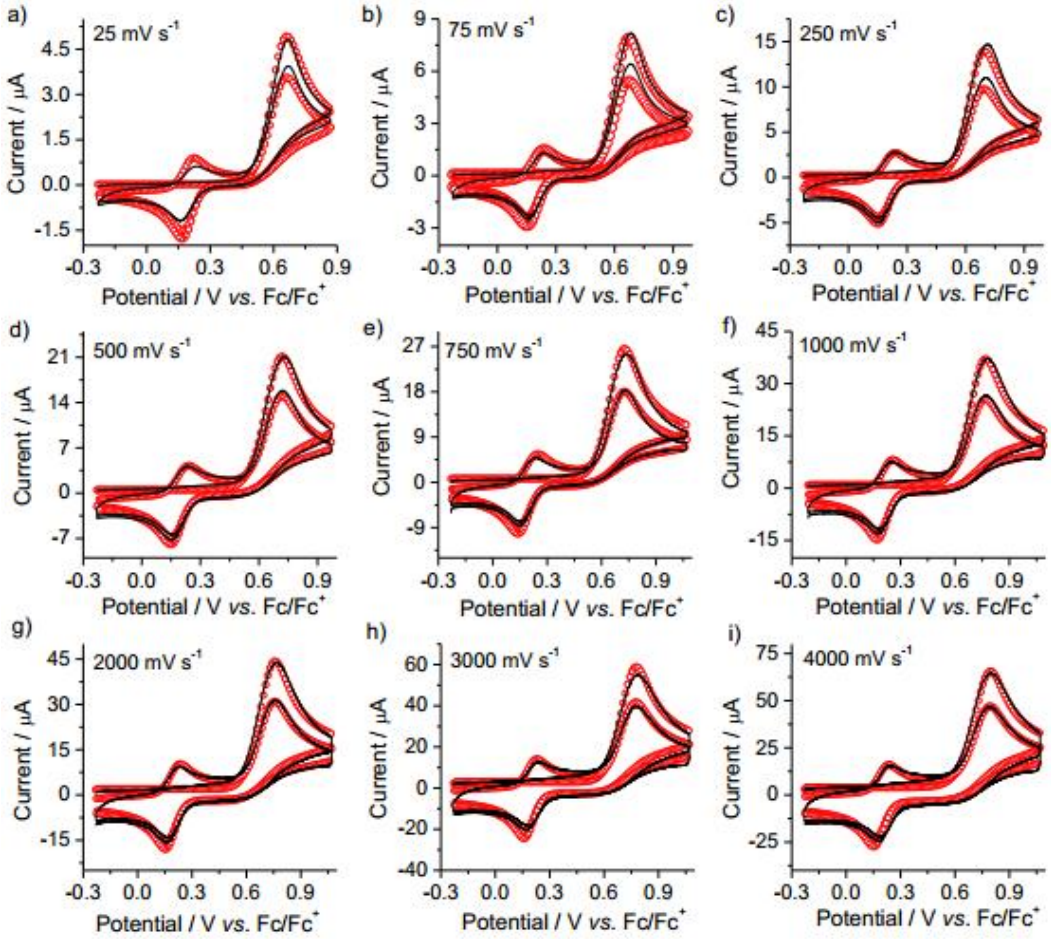

Figure 4.11 Anodic electrochemistry of alkoxyamine **2**. Experimental (solid line) and simulated (empty symbols) voltammograms at different scan rates (25 to 4000 mV s^{-1}, as specified by labels in the figure) of 0.5 × 10^{-3} M **2** in MeCN with 1.0 × 10^{-1} M Bu_4NClO_4. Best-fit parameters ($EC_{irr}E$ mechanism) are: E_1^0 = 0.78 V (vs. Fc/Fc^+), k_1^0 = 0.05 cm s^{-1}, E_2^0 = 0.195 V (vs. Fc/Fc^+), k_2^0 = 0.08 cm s^{-1}, α = 0.5. D (**TEMPO**/oxoammonium) = 2.2 × 10^{-5} cm^2 s^{-1}, D ($\mathbf{2}/\mathbf{2}^{\bullet+}$) = 7.8 × 10^{-6} cm^2 s^{-1} and for the irreversible chemical step k_f is 5.0 × 10^6 s^{-1}. Only the first 4 segments are shown for clarity and the first segment is acquired ramping the bias in the anodic direction. The electrochemically-determined effective area for the data in the figure is 0.07 cm^2. An estimate of the Pt macrodisk effective area was obtained prior to each experiment on **2** by refining cyclic voltammograms of 0.5 × 10^{-3} M Fc in MeCN with 1.0 × 10^{-1} M Bu_4NClO_4 and using the following model: E mechanism, E^0 (Fc/Fc^+) = 0.23 V (vs. Ag/AgCl), k^0 (Fc/Fc^+) = 0.2 cm s^{-1}, D (Fc/Fc^+) = 2.3 × 10^{-5} cm^2 s^{-1}, α =0.5.

Further experiments were performed for collecting representative voltammetric data on fast sweep rates (up to 5-10 V/s, Figure 4.11) and larger range of concentrations of **2** (0.5 to 5 mM, Figure 4.12 and 4.13). Voltammetry at extremely low concentrations of **2** (0.05 mM, Figure 4.12 shown below) did reproduce qualitatively all of the features generally observed for the data in 0.5 mM and 5 mM, but were generally of lower reproducibility. However, and most importantly, the modelling of this wider data set (voltage sweep rates and concentrations) does not appear to alter the conclusions in the last paragraph. Overall, the remarkable finding is that at room temperature after an initial oxidation, the lysis of C-ON bonds of both diffusive and tethered alkoxyamines are quite favorable.

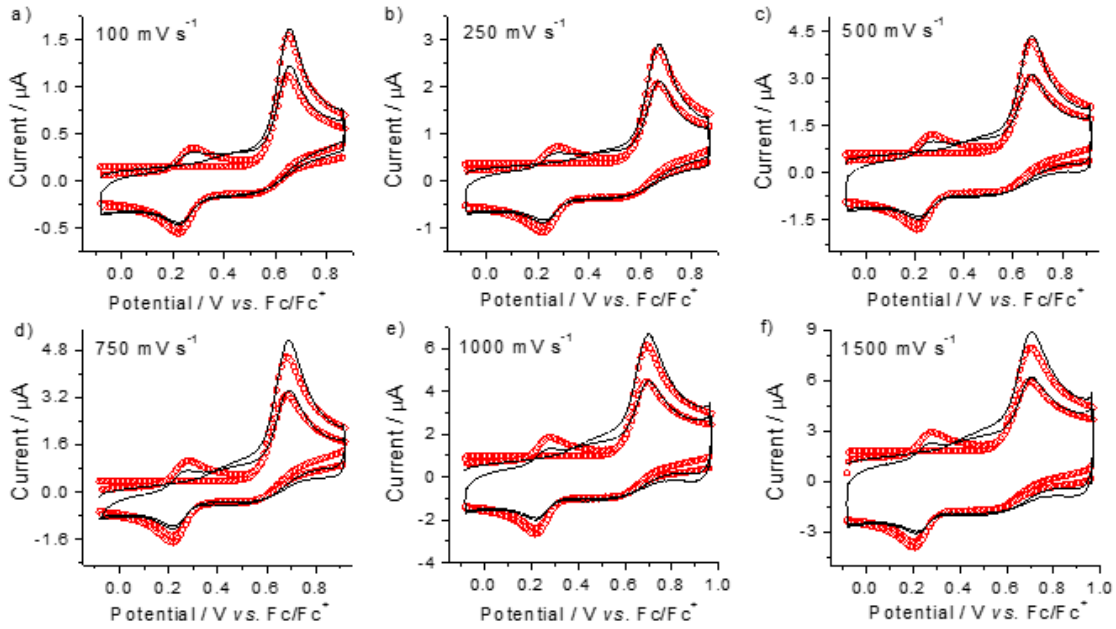

Figure 4.12 Anodic electrochemistry of alkoxyamine **2**. Experimental (solid line) and simulated (empty symbols) voltammograms at different scan rates (100 to 1500 mV s^{-1}, as specified by labels in figure) of 0.5 × 10^{-4} M **2** in MeCN with 1.0 × 10^{-1} M Bu_4NClO_4. Best-fit parameters ($EC_{irr}E$ mechanism) are: E_1^0 = 0.81 V (vs. Fc/Fc^+), k_1^0 = 0.52 cm s^{-1}, E_2^0 = 0.24 V (vs. Fc/Fc^+), k_2^0 = 0.19 cm s^{-1}, α = 0.5. D (**TEMPO**/oxoammonium) = 2.2 × 10^{-5} cm^2 s^{-1}, D (**2**/**2**$^{\bullet+}$) = 7.8 × 10^{-6} cm^2 s^{-1} and for the irreversible chemical step k_f is 3.4 × 10^7 s^{-1}. Only the first 4 segments are shown for clarity and the first segment is acquired ramping the bias in the anodic direction. The effective area for the data in the figure is 0.07 cm^2.

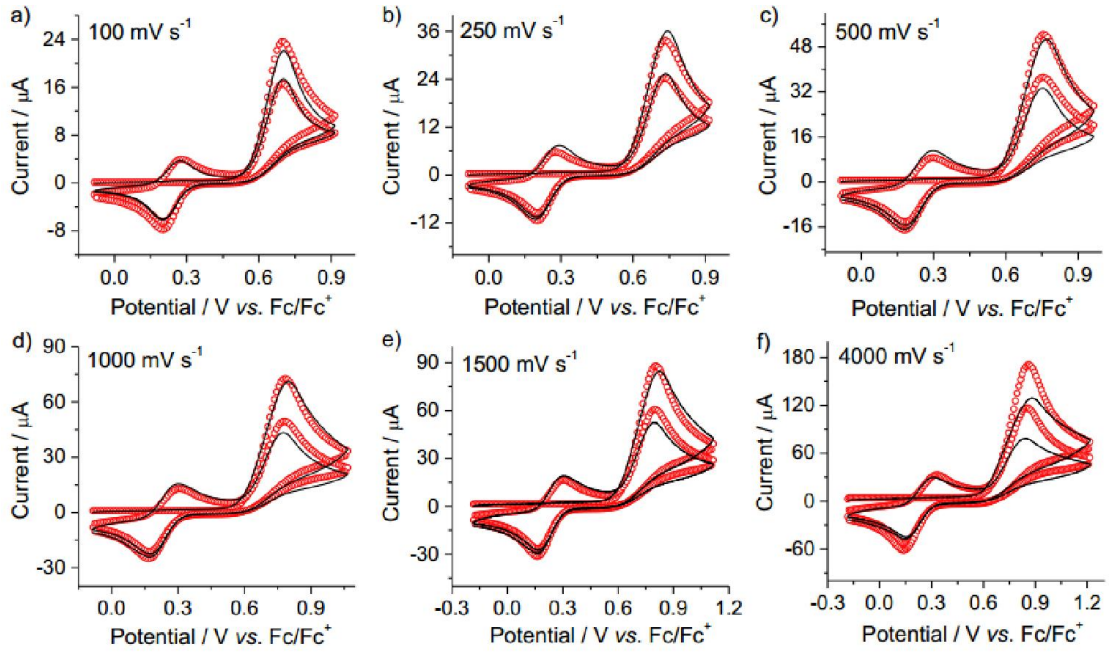

Figure 4.13 Anodic electrochemistry of alkoxyamine **2**. Experimental (solid line) and simulated (empty symbols) voltammograms at different scan rates (100 to 4000 mV s^{-1}, as specified by labels in the figure) of 5.0 × 10^{-3} M **2** in MeCN with 1.0 × 10^{-1} M Bu_4NClO_4. Best-fit parameters ($EC_{irr}E$ mechanism) are: E_1^0 = 0.83 V (vs. Fc/Fc^+), k_1^0 = 0.06 cm s^{-1}, E_2^0 = 0.245 V (vs. Fc/Fc^+), k_2^0 = 0.02 cm s^{-1}, α = 0.5. D (**TEMPO**/oxoammonium) = 2.2 × 10^{-5} cm^2 s^{-1}, D (**2**/**2**$^{\bullet+}$) = 7.8 × 10^{-6} cm^2 s^{-1} and for the irreversible chemical step k_f is 5.0 × 10^6 s^{-1}. The electrochemically-determined effective area for the data in the figure is 0.017 cm^2. Only the first 4 segments are shown for clarity and the first segment is acquired ramping the bias in the anodic direction.

The experimental finding that alkoxyamines, normally stable at room temperature, undergo rapid and irreversible room temperature homolysis upon oxidation is remarkable when analyzed in terms of the expected energetics of the process. High-level *ab initio* calculations were conducted at a level of theory previously demonstrated to reproduce experimental redox potentials of nitroxides[49] and homolysis equilibrium constants of neutral alkoxyamines[48]. The computed oxidation potentials versus Fc/Fc^+ of **2** (0.83 V) and TEMPO (0.20 V) in this work are also in excellent agreement with the corresponding best-fit experimental values (E_1^0 = 0.78 V and E_2^0 = 0.195 V). Moreover, the calculations predict the correct preferred fragmentation pattern (i.e., to a nitroxide and carbocation rather than an oxoammonium cation and a carbon centered radical) further validating their accuracy. However, when the energetics of the homolysis of the oxidized alkoxyamine is calculated in MeCN it is unfavorable by 35

kJ mol^{-1}; a finding that is inconsistent with the rapid decomposition observed experimentally.

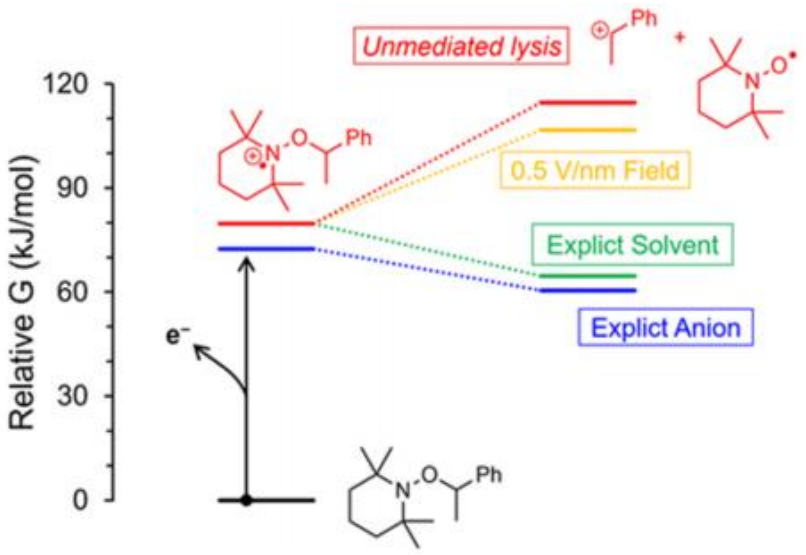

Figure 4.14 Theoretical potential energy surface for the oxidative cleavage of alkoxyamine **2** in MeCN. The homolysis of the unperturbed ('free') radical-cation (red pathway) is strongly thermodynamically disfavoured. However, homolysis can be made more favourable by a static electric field, and by interactions with an explicit anion and/or with an explicit solvent molecule.

Importantly, the calculations only take account of the solvent and fail to consider the electric fields experienced in the near-surface double-layer. When these were taken into account, it is then clear that the homolysis is promoted (Figure 4.14). For instance, by using only a simple background electric field of 0.5 V nm^{-1}, a value which reflects the potential gradient that is most likely experienced by species reaching the electrified interface,[71] the homolysis energies were lowered but not by enough to explain the experimentally observed reaction rates. However, combination of a static electric field and a continuum solvent model (in which the solvent is itself modelled as an electric field) is likely to provide a rather crude approximation of the true environment. Unfortunately, modelling a full ensemble of explicit ions and solvent molecules while maintaining a suitably high level of theory is impractical. However, it can be shown that when either an explicit ion or an explicit solvent molecule is included in the calculations, further lowering is observed (Figure 4.14). Hence it is most likely that the electrostatic environment within the double-layer is helping to promote homolysis of a

compound that would otherwise be stable.

While the calculations suggest that the environment in the double layer is promoting homolysis, it is difficult to establish whether this is due to explicit bonding interactions or electrostatics; as full ensemble of species cannot be modelled accurately (*vide supra*). To examine whether the effects were primarily electrostatic, experiments were thus conducted with anions that are significantly less coordinating than perchlorate, such as hexafluorophosphate and tetrakis[3,5-bis(trifluoromethyl)phenyl]borate (BARF hereafter) (see Supporting Figures 4.15-4.19).

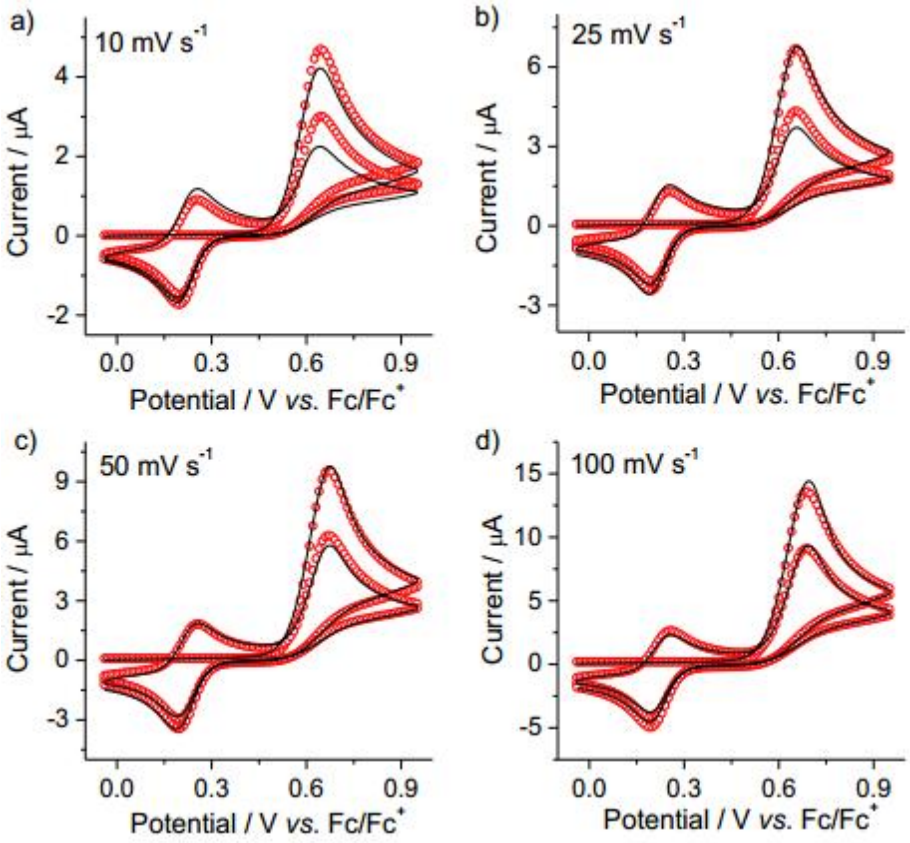

Figure 4.15 Anodic electrochemistry of alkoxyamine **2**. Experimental (solid line) and simulated (empty symbols) voltammograms at different scan rates (10 to 100 mV s^{-1}, as specified by labels in the figure) of 0.57 × 10^{-3} M **2** in MeCN with 1.0 × 10^{-1} M Bu_4NPF_6. Best-fit parameters ($EC_{irr}E$ mechanism) are: E_1^0 = 0.81 V (vs. Fc/Fc^+), k_1^0 = 0.08 cm s^{-1}, E_2^0 = 0.225 V (vs. Fc/Fc^+), k_2^0 = 0.04 cm s^{-1}, α = 0.5. D (**TEMPO**/oxoammonium) = 2.2 × 10^{-5} cm^2 s^{-1}, D (**2**/**2**$^{\bullet+}$) = 7.7 × 10^{-6} cm^2 s^{-1} and for the irreversible chemical step k_f is 5.0 × 10^6 s^{-1}. The electrochemically-determined effective area for the data in the figure is 0.08 cm^2. Only the first 4 segments are shown for clarity and the first segment is acquired ramping the bias in the anodic direction.

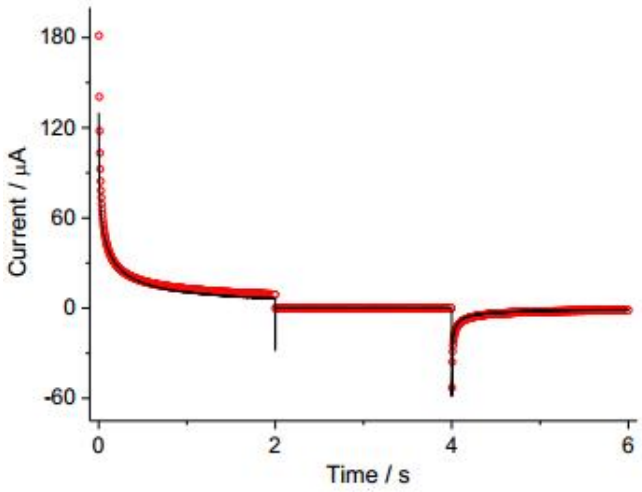

Figure 4.16 Current evolution with time in a typical three-step chronoamperometry experiment of 0.6×10^{-3} M **2** in MeCN with 1.0×10^{-1} M Bu_4NPF_6. Experimental (solid line) and simulated (symbols) transients with the potential being stepped from -0.04 V to 0.86 V, then from 0.86 V to 0.46 V, and from 0.46 V to -0.04 V (vs. Fc/Fc^+). The electrochemically-determined effective area for the data in the figure is 0.07 cm^2. The best-fit parameters are D (**TEMPO**/oxoammonium) = 2.2×10^{-5} cm^2 s^{-1}, D (**2**/**2**$^{\bullet+}$) = 7.7×10^{-6} cm^2 s^{-1} E_1^0 = 0.81 V (vs. Fc/Fc^+), k_1^0 = 0.08 cm s^{-1}, E_2^0 = 0.225 V (vs. Fc/Fc^+), k_2^0 = 0.04 cm s^{-1}, k_f = 5.0×10^6 s^{-1}.

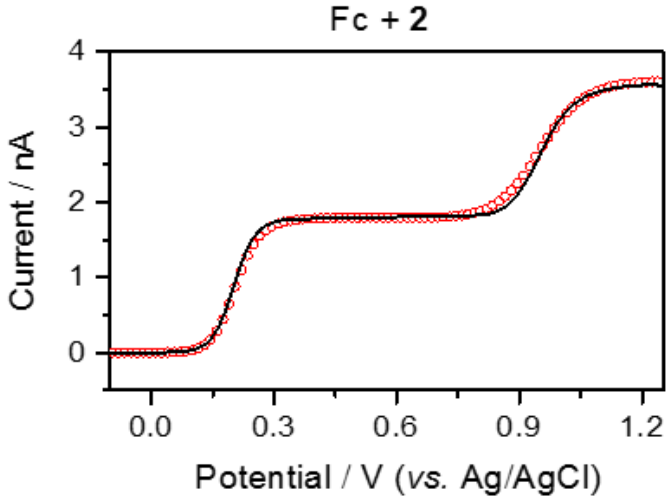

Figure 4.17 Cyclic voltammograms at Pt microdisks (5.0 μm in radius) of 0.50×10^{-3} M Fc and 0.64×10^{-3} M **2** in MeCN with 1.0×10^{-2} NaBARF (scan rate is 10 mV s^{-1}). The refined parameters ($EC_{irr}E$ mechanism) are: E^0 (Fc/Fc^+) = 0.20 V vs Ag/AgCl ("leakless"), k^0 (Fc/Fc^+) = 0.2 cm s^{-1}, E^0 (**2**/**2**$^{\bullet+}$) = 1.025 V, k^0 (**2**/**2**$^{\bullet+}$) = 0.07 cm s^{-1}, E^0 (**TEMPO**/oxoammonium) = 0.435 V, k^0 (**TEMPO**/oxoammonium) = 0.05 cm s^{-1}, α = 0.5. For the chemical step of **2**$^{\bullet+}$ → **TEMPO** + R^+, the refined k_f is 5.2×10^6 s^{-1}. The experimental and simulated curves are plotted as solid lines and empty symbols, respectively. The diffusivity of Fc is set to 1.8×10^{-5} cm^2 s^{-1}, that for the **TEMPO**/oxoammonium couple is 2.0×10^{-5} cm^2 s^{-1} and the diffusivity of the **2**/**2**$^{\bullet+}$ couple is 7.3×10^{-6} cm^2 s^{-1}.

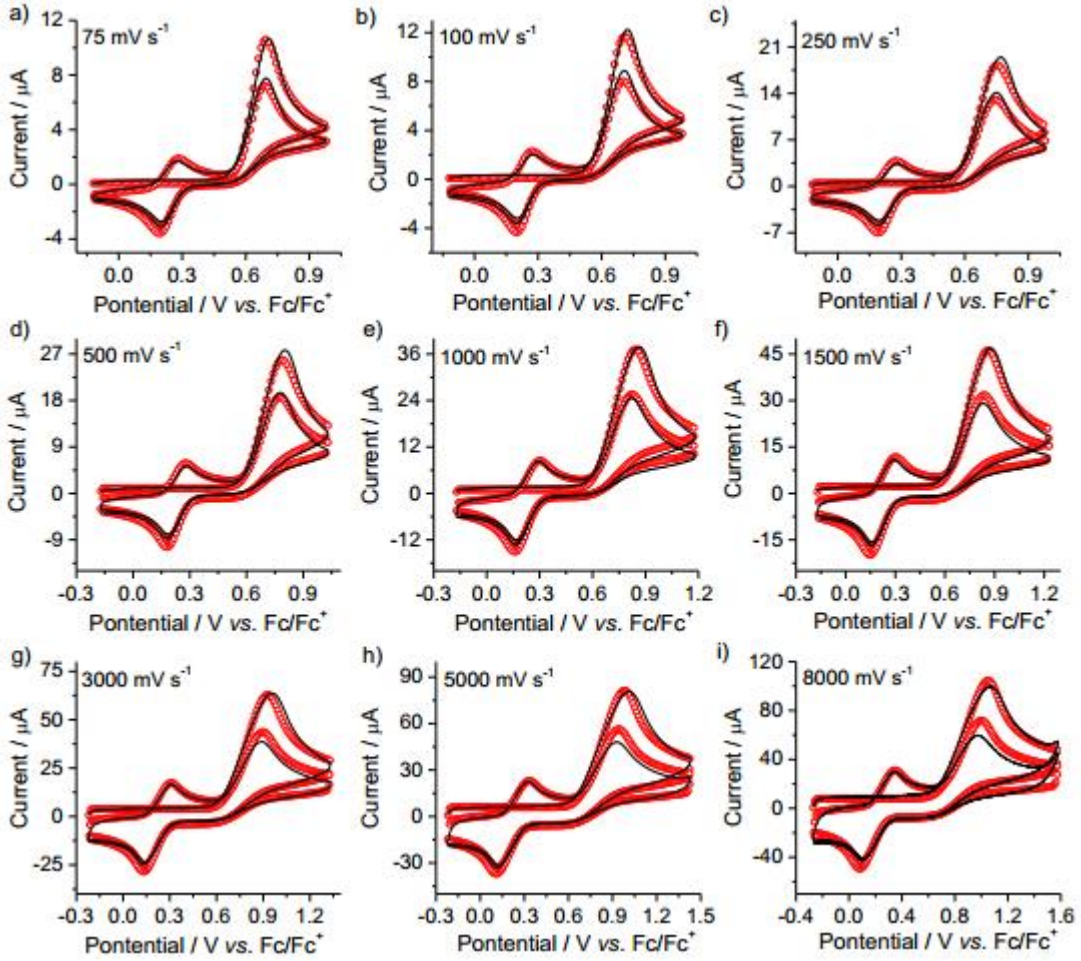

Figure 4.18 Anodic electrochemistry of alkoxyamine **2**. Experimental (solid line) and simulated (empty symbols) voltammograms at different scan rates (75 to 8000 mV s^{-1}, as specified by labels in the figure) for 0.5 × 10^{-3} M **3** in MeCN with 1.0 × 10^{-2} M NaBARF. Best-fit parameters ($EC_{irr}E$ mechanism) are: E_1^0 = 0.82 V (vs. Fc/Fc^+), k_1^0 = 0.07 cm s^{-1}, E_2^0 = 0.23 V (vs. Fc/Fc^+), k_2^0 = 0.05 cm s^{-1}, α = 0.5 D (**TEMPO**/oxoammonium). = 2.0 × 10^{-5} cm^2 s^{-1}, D (**2**/**2**$^{\bullet+}$) = 7.3 × 10^{-6} cm^2 s^{-1} and for the irreversible chemical step k_f is 5.2 × 10^6 s^{-1}. The electrochemically-determined effective area for the data in the figure is 0.07 cm^2. Only the first 4 segments are shown for clarity and the first segment is acquired ramping the bias in the anodic direction.

The results are in line with the observations in the perchlorate system, pointing to an $EC_{irr}E$ mechanism with the backward chemical reaction not being operative in the time scale of the experiments. For example, with scan rates that varied over three orders of magnitude (from 75 mV s^{-1} to 8 V s^{-1}, Figure 4.18) the refinement of the voltammograms of alkoxyamine **2** in BARF electrolytes (k_f = 5.2 × 10^6 s^{-1}) suggest kinetic, as well as mass transport, parameters that are a close match of those obtained in Bu_4NClO_4 electrolytes (k_f = 5.0 × 10^6 s^{-1}) (Figures 4.11). Within the same solvent,

the results remained unchanged (see Figure 4.11, 4.15 and 4.18), however, there were small differences between solvents (MeCN versus DCM, see Figure 4.11 and Figure 4.20). Indeed, this was also supported by theoretical calculations (Figure 4.21).

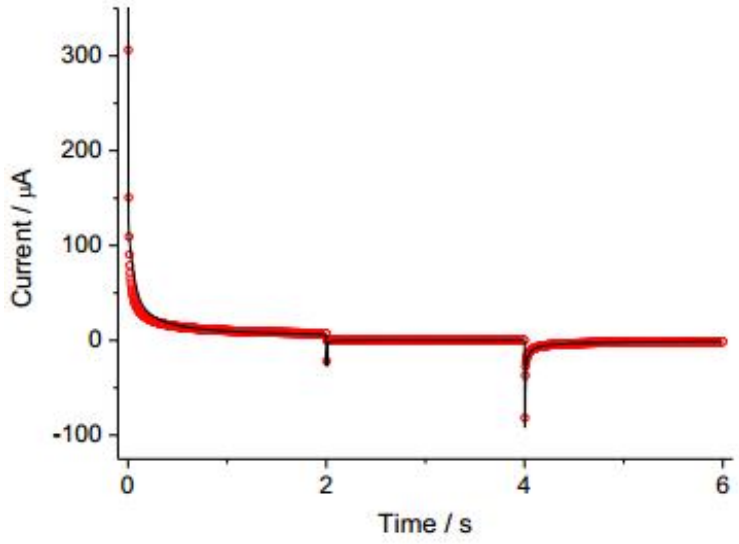

Figure 4.19. Current evolution with time in a typical three-step chronoamperometry experiment of 0.5×10^{-3} M **2** in MeCN with 1.0×10^{-2} M NaBARF. Experimental (solid line) and simulated (symbols) transients with the potential being stepped from -0.04 V to 1.06 V, then from 1.06 V to 0.46 V, and from 0.46 V to -0.04 V (vs. Fc/Fc^+). The electrochemically-determined effective area for the data in the figure is 0.07 cm^2. The best-fit parameters are D (**TEMPO**/oxoammonium) = 2.0×10^{-5} cm^2 s^{-1}, D (**2**/**2**$^{\bullet+}$) = 7.3×10^{-6} cm^2 s^{-1} E_1^0 = 0.82 V (vs. Fc/Fc^+), k_1^0 = 0.07 cm s^{-1}, E_2^0 = 0.23 V (vs. Fc/Fc^+), k_2^0 = 0.05 cm s^{-1}, k_f = 5.2×10^6 s^{-1}.

The quality of the fits is high in the MeCN systems and only satisfactory when DCM is the solvent. In both cases there seems to be something that the $EC_{irre}E$ mechanism does not fully describe and it does not enable one to reach perfect fits, though it is consistent with the general picture of the problem, which is, most notably, the lack of influence of the anion. It would appear that there are secondary processes that, in some way, "dirty" the electrochemical response and distort the current, mainly in the TEMPO potential region. The true nature of these secondary processes is not clear. Adsorption could only partially explain the issue since experiments at smaller concentrations are generally leading to perfect fits. Another possibility is related with the presence of reactive species; which aligns with the common notion that oxoammoniums or carbon cations are highly reactive species and far from being ideal redox species. Nevertheless,

the simplest $EC_{irre}E$ mechanism with a backward chemical reaction not being operative on the time scale of the experiments remain consistent with EPR, voltammetric and current-transient data. Collectively, the experiments suggest that it is primarily the electrostatic environment in the double layer that is driving cleavage rather than explicit covalent interactions with the electrolyte ions.

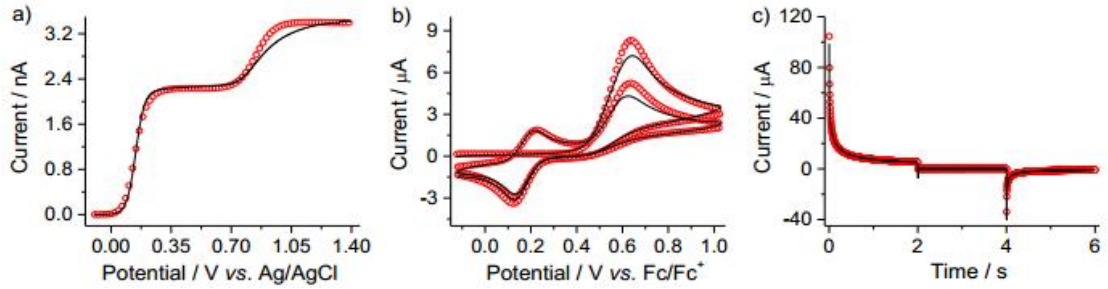

Figure 4.20 (a-b) Anodic electrochemistry of alkoxyamine **2** in DCM. Experimental (solid line) and simulated (empty symbols) voltammograms of 0.5×10^{-3} M **2** in DCM with 1.0×10^{-1} M Bu_4NPF_6 (50 mV s^{-1} for Pt ultramicroelectrodes 5.0 µm in radius in (a), the electrolyte is added with 0.6×10^{-3} M Fc. The refined parameters ($EC_{irr}E$ mechanism) are: E^0 (Fc/Fc^+) = 0.13 V vs Ag/AgCl ("leakless"), k^0 (Fc/Fc^+) = 0.10 cm s^{-1}, E^0 (**2**/**2**$^{\bullet+}$) = 0.82 V, k^0 (**2**/**2**$^{\bullet+}$) = 0.01 cm s^{-1}, E^0 (**TEMPO**/oxoammonium) = 0.32 V, k^0 (**TEMPO**/oxoammonium) = 0.01 cm s^{-1}, α = 0.5. For the chemical step of **2**$^{\bullet+}$ → **TEMPO** + R^+, the refined k_f is 1.0×10^6 s^{-1}. The diffusivity of Fc was set equal to 1.9 $\times 10^{-5}$ cm^2 s^{-1}. The diffusivity of the **2**/**2**$^{\bullet+}$ couple was 6.0×10^{-6} cm^2 s^{-1}. The refined D value of 1.9×10^{-5} cm^2 s^{-1} was for the **TEMPO**/oxoammonium couple; 50 mV s^{-1} for 0.07 cm^2 Pt macro-disks electrodes presented in (b)). Best-fit parameters ($EC_{irr}E$ mechanism) are: E_1^0 = 0.68 V (vs. Fc/Fc^+), k_1^0 = 0.01 cm s^{-1}, E_2^0 = 0.18 V (vs. Fc/Fc^+), k_2^0 = 0.01 cm s^{-1}, α = 0.5. D (**TEMPO**/oxoammonium) = 1.9×10^{-5} cm^2 s^{-1}, D (**2**/**2**$^{\bullet+}$) = 6.0×10^{-6} cm^2 s^{-1} and for the irreversible chemical step k_f is 1.0×10^6 s^{-1}. (c) Current evolution with time in a typical three-step chronoamperometry experiment of 0.4×10^{-3} M **2** in DCM with 1.0×10^{-1} M Bu_4NPF_6**.** Experimental (solid line) and simulated (symbols) transients with the potential being stepped from -0.07 V to 0.78 V, then from 0.78 V to 0.43 V, and from 0.43 V to -0.07 V (vs. Fc/Fc^+). The best-fit parameters are D (**TEMPO**/oxoammonium) = 1.9×10^{-5} cm^2 s^{-1}, D (**2**/**2**$^{\bullet+}$) = 6.0×10^{-6} cm^2 s^{-1} E_1^0 = 0.69 V (vs. Fc/Fc^+), k_1^0 = 0.01 cm s^{-1}, E_2^0 = 0.19 V (vs. Fc/Fc^+), k_2^0 = 0.01 cm s^{-1}, k_f = 1.0×10^6 s^{-1}. The electrochemically-determined effective area for the data in the figure is 0.07 cm^2. It can be noted that the refinement of a model against the experimental voltammetry of **2** in DCM-based electrolytes was generally found to lead to poorer quality fits relative to the MeCN counterparts.

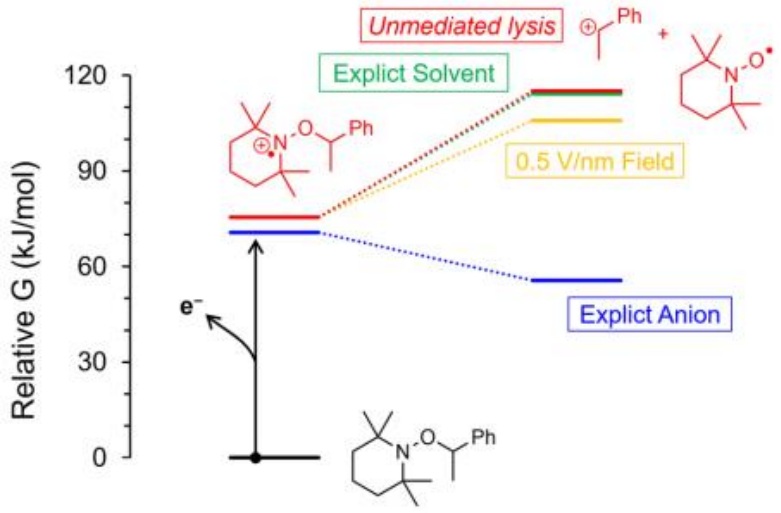

Figure 4.21 Electrochemical cleavage of alkoxyamines. Theoretical potential energy surface for the oxidative cleavage of alkoxyamine **2** in DCM. The figure shows the effect of electrostatic environment (either solvent or electrolyte anions) on the reaction energies of alkoxyamine cation radicals decomposition. The homolysis of the unperturbed ('free') radical-cation (red pathway) is strongly thermodynamically disfavoured. However, homolysis can is made more favourable by a static electric field, and by interactions with an explicit anion. Unlike acetonitrile, an explicit solvent molecule does not aid homolysis.

4.5 Conclusions

The role of static charges in controlling bond breaking and reformation is largely unexplored,[26] and electrostatic catalysis is starting to emerge as a synthetic tool available to the chemist.[25, 26] This work provides the first insights on the use of external electric fields to cleave alkoxyamines at room temperature or using electricity to generate surface-tethered persistent radicals in a switchable manner. Importantly, even under the oxidative conditions used, a theoretical model of the system indicates that the cleavage is kinetically assisted by specific interactions between the substrate and the electrolyte anions, highlighting the key, and often unappreciated, role that such interactions play in chemical reactions.[72] These results offer the conceptual basis to start exploring electrochemical control on electrophile substitutions and cationic polymerization,[73] an ON/OFF switch in the electro-synthesis of small organic molecules[9], or possibly a new way of making inferences on the energy of ionic aggregates within electric double layers[22].

4.6 References

(1) Hodgson, J. L.; Coote, M. L. Clarifying the mechanism of the Denisov cycle: how do hindered amine light stabilizers protect polymer coatings from photo-oxidative degradation? *Macromolecules* **2010,** *43*, 4573-4583.

(2) Gryn'ova, G.; Ingold, K. U.; Coote, M. L. New insights into the mechanism of amine/nitroxide cycling during the hindered amine light stabilizer inhibited oxidative degradation of polymers. *J. Am. Chem. Soc.* **2012,** *134*, 12979-12988.

(3) Hawker, C. J.; Bosman, A. W.; Harth, E. New polymer synthesis by nitroxide mediated living radical polymerizations. *Chem. Rev.* **2001,** *101*, 3661-3688.

(4) Sciannamea, V.; Jérôme, R.; Detrembleur, C. In-situ nitroxide-mediated radical polymerization (NMP) processes: their understanding and optimization. *Chem. Rev.* **2008,** *108*, 1104-1126.

(5) Nicolas, J.; Guillaneuf, Y.; Lefay, C.; Bertin, D.; Gigmes, D.; Charleux, B. Nitroxide-mediated polymerization. *Prog. Polym. Sci.* **2013,** *38*, 63-235.

(6) Rafiee, M.; Miles, K. C.; Stahl, S. S. Electrocatalytic alcohol oxidation with TEMPO and bicyclic nitroxyl derivatives: driving force trumps steric effects. *J. Am. Chem. Soc.* **2015,** *137*, 14751-14757.

(7) Chen, Q.; Fang, C.; Shen, Z.; Li, M. Electrochemical synthesis of nitriles from aldehydes using TEMPO as a mediator. *Electrochem. Commun.* **2016,** *64*, 51-55.

(8) Badalyan, A.; Stahl, S. S. Cooperative electrocatalytic alcohol oxidation with electron-proton-transfer mediators. *Nature* **2016,** *535*, 406-410.

(9) Qian, X.-Y.; Li, S.-Q.; Song, J.; Xu, H.-C. TEMPO-catalyzed electrochemical C–H thiolation: synthesis of benzothiazoles and thiazolopyridines from thioamides. *ACS Catal.* **2017,** *7*, 2730-2734.

(10) Gryn'ova, G.; Lin, C. Y.; Coote, M. L. Which side-reactions compromise nitroxide mediated polymerization? *Poly. Chem.* **2013,** *4*, 3744-3754.

(11) Goto, A.; Scaiano, J.; Maretti, L. Photolysis of an alkoxyamine using intramolecular energy transfer from a quinoline antenna-towards photo-induced living radical polymerization. *Photoch. Photobio. Sci.* **2007,** *6*, 833-835.

(12) Guillaneuf, Y.; Bertin, D.; Gigmes, D.; Versace, D.-L.; Lalevée, J.; Fouassier, J.-P. Toward nitroxide-mediated photopolymerization. *Macromolecules* **2010,** *43*, 2204-2212.

(13) Telitel, S.; Amamoto, Y.; Poly, J.; Morlet-Savary, F.; Soppera, O.; Lalevée, J.; Matyjaszewski, K. Introduction of self-healing properties into covalent polymer networks via the photodissociation of alkoxyamine junctions. *Polym. Chem.* **2014,** *5*, 921-930.

(14) Bottle, S. E.; Clement, J.-L.; Fleige, M.; Simpson, E. M.; Guillaneuf, Y.; Fairfull-Smith, K. E.; Gigmes, D.; Blinco, J. P. Light-active azaphenalene alkoxyamines: fast and efficient mediators of a photo-induced persistent radical effect. *RSC Adv.* **2016,** *6*, 80328-80333.

(15) Bagryanskaya, E.; Brémond, P.; Edeleva, M.; Marque, S. R.; Parkhomenko, D.; Roubaud, V.; Siri, D. Chemically triggered C–ON bond homolysis in alkoxyamines. Part 2: DFT investigation and application of the pH effect on NMP. *Macromol. Rapid Commun.* **2012,** *33*, 152-157.

(16) Edeleva, M. V.; Kirilyuk, I. A.; Zhurko, I. F.; Parkhomenko, D. A.; Tsentalovich, Y. P.; Bagryanskaya, E. G. pH-Sensitive C–ON bond homolysis of alkoxyamines of imidazoline series with multiple ionizable groups as an approach for control of nitroxide mediated polymerization. *J. Org. Chem.* **2011,** *76*, 5558-5573.

(17) Gryn'ova, G.; Marshall, D. L.; Blanksby, S. J.; Coote, M. L. Switching radical stability by pH-induced orbital conversion. *Nat. Chem.* **2013,** *5*, 474-481.

(18) Klinska, M.; Smith, L. M.; Gryn'ova, G.; Banwell, M. G.; Coote, M. L. Experimental demonstration of pH-dependent electrostatic catalysis of radical reactions. *Chem. Sci.* **2015,** *6*, 5623-5627.

(19) Smirnov, A. I.; Ruuge, A.; Reznikov, V. A.; Voinov, M. A.; Grigor'ev, I. A. Site-directed electrostatic measurements with a thiol-specific pH-sensitive nitroxide: differentiating local pK and polarity effects by high-field EPR. *J. Am. Chem. Soc.* **2004,** *126*, 8872-8873.

(20) Gryn'ova, G.; Coote, M. L. Origin and scope of long-range stabilizing interactions and associated SOMO–HOMO conversion in distonic radical anions. *J. Am. Chem. Soc.*

2013, *135*, 15392-15403.

(21) Gryn'ova, G.; Coote, M. L. Directionality and the role of polarization in electric field effects on radical stability. *Aust. J. Chem.* **2017,** *70*, 367-372.

(22) Pocker, Y.; Buchholz, R. F. Electrostatic catalysis of ionic aggregates. I. Ionization and dissociation of trityl chloride and hydrogen chloride in lithium perchlorate-diethyl ether solutions. *J. Am. Chem. Soc.* **1970,** *92*, 2075-2084.

(23) Pocker, Y.; Buchholz, R. F. Electrostatic catalysis by ionic aggregates. II. Reversible elimination of hydrogen chloride from tert-butyl chloride and the rearrangement of 1-phenylallyl chloride in lithium perchlorate-diethyl ether solutions. *J. Am. Chem. Soc.* **1970,** *92*, 4033-4038.

(24) Gorin, C. F.; Beh, E. S.; Bui, Q. M.; Dick, G. R.; Kanan, M. W. Interfacial electric field effects on a carbene reaction catalyzed by Rh porphyrins. *J. Am. Chem. Soc.* **2013,** *135*, 11257-11265.

(25) Aragonès, A. C.; Haworth, N. L.; Darwish, N.; Ciampi, S.; Bloomfield, N. J.; Wallace, G. G.; Diez-Perez, I.; Coote, M. L. Electrostatic catalysis of a Diels–Alder reaction. *Nature* **2016,** *531*, 88-91.

(26) Shaik, S.; Mandal, D.; Ramanan, R. Oriented electric fields as future smart reagents in chemistry. *Nat. Chem.* **2016,** *8*, 1091-1098.

(27) Lau, V. M.; Pfalzgraff, W. C.; Markland, T. E.; Kanan, M. W. Electrostatic control of regioselectivity in Au (I)-catalyzed hydroarylation. *J. Am. Chem. Soc.* **2017,** *139*, 4035-4041.

(28) Zhang, L.; Vogel, Y. B.; Noble, B. B.; Gonçales, V. R.; Darwish, N.; Brun, A. L.; Gooding, J. J.; Wallace, G. G.; Coote, M. L.; Ciampi, S. TEMPO monolayers on Si(100) electrodes: electrostatic effects by the electrolyte and semiconductor space-charge on the electroactivity of a persistent radical. *J. Am. Chem. Soc.* **2016,** *138*, 9611-9619.

(29) Yapici, N. B.; Jockusch, S.; Moscatelli, A.; Mandalapu, S. R.; Itagaki, Y.; Bates, D. K.; Wiseman, S.; Gibson, K. M.; Turro, N. J.; Bi, L. New rhodamine nitroxide based fluorescent probes for intracellular hydroxyl radical identification in living cells. *Org. Lett.* **2011,** *14*, 50-53.

(30) Danko, M.; Szabo, E.; Hrdlovic, P. Synthesis and spectral characteristics of

fluorescent dyes based on coumarin fluorophore and hindered amine stabilizer in solution and polymer matrices. *Dyes Pigments* **2011,** *90*, 129-138.

(31) Molina, Á.; Laborda, E.; Gómez-Gil, J. M.; Martínez-Ortiz, F.; Compton, R. G. A comprehensive voltammetric characterisation of ECE processes. *Electrochim. Acta* **2016,** *195*, 230-245.

(32) Marenich, A. V.; Ho, J.; Coote, M. L.; Cramer, C. J.; Truhlar, D. G. Computational electrochemistry: prediction of liquid-phase reduction potentials. *Phys. Chem. Chem. Phys.* **2014,** *16*, 15068-15106.

(33) Ciampi, S.; Böcking, T.; Kilian, K. A.; James, M.; Harper, J. B.; Gooding, J. J. Functionalization of acetylene-terminated monolayers on Si(100) surfaces: a click chemistry approach. *Langmuir* **2007,** *23*, 9320-9329.

(34) Ciampi, S.; Eggers, P. K.; Le Saux, G.; James, M.; Harper, J. B.; Gooding, J. J. Silicon (100) electrodes resistant to oxidation in aqueous solutions: an unexpected benefit of surface acetylene moieties. *Langmuir* **2009,** *25*, 2530-2539.

(35) Ciampi, S.; Harper, J. B.; Gooding, J. J. Wet chemical routes to the assembly of organic monolayers on silicon surfaces via the formation of Si–C bonds: Surface preparation, passivation and functionalization. *Chem. Soc. Rev.* **2010,** *39*, 2158-2183.

(36) Ciampi, S.; James, M.; Le Saux, G.; Gaus, K.; Justin Gooding, J. Electrochemical "switching" of Si(100) modular assemblies. *J. Am. Chem. Soc.* **2011,** *134*, 844-847.

(37) Meldal, M.; Tornøe, C. W. Cu-catalyzed azide−alkyne cycloaddition. *Chem. Rev.* **2008,** *108*, 2952-3015.

(38) Chen, L.; Xu, Z.; Li, J.; Zhou, B.; Shan, M.; Li, Y.; Liu, L.; Li, B.; Niu, J. Modifying graphite oxide nanostructures in various media by high-energy irradiation. *Rsc Adv.* **2014,** *4*, 1025-1031.

(39) Ciampi, S.; Guan, B.; Darwish, N. A.; Zhu, Y.; Reece, P. J.; Gooding, J. J. A multimodal optical and electrochemical device for monitoring surface reactions: redox active surfaces in porous silicon Rugate filters. *Phys. Chem. Chem. Phys.* **2012,** *14*, 16433-16439.

(40) Ciampi, S.; James, M.; Michaels, P.; Gooding, J. J. Tandem "click" reactions at acetylene-terminated Si(100) monolayers. *Langmuir* **2011,** *27*, 6940-6949.

(41) Devadoss, A.; Chidsey, C. E. Azide-modified graphitic surfaces for covalent attachment of alkyne-terminated molecules by "click" chemistry. *J. Am. Chem. Soc.* **2007,** *129*, 5370-5371.

(42) Liu, H.; Duclairoir, F.; Fleury, B.; Dubois, L.; Chenavier, Y.; Marchon, J.-C. Porphyrin anchoring on Si(100) using a β-pyrrolic position. *Dalton Trans.* **2009**, 3793-3799.

(43) Qin, G.; Santos, C.; Zhang, W.; Li, Y.; Kumar, A.; Erasquin, U. J.; Liu, K.; Muradov, P.; Trautner, B. W.; Cai, C. Biofunctionalization on alkylated silicon substrate surfaces via "click" chemistry. *J. Am. Chem. Soc.* **2010,** *132*, 16432-16441.

(44) Caro, J.; Fraxedas, J.; Jürgens, O.; Santiso, J.; Rovira, C.; Veciana, J.; Figueras, A. The first oriented thin films based on a nitronyl nitroxide radical. *Adv. Mater.* **1998,** *10*, 608-610.

(45) Grobman, W. D.; Pollak, R. A.; Eastman, D. E.; Maas, E. T.; Scott, B. A. Valence electronic structure and charge transfer in tetrathiofulvalinium tetracyanoquinodimethane (TTF-TCNQ) from photoemission spectroscopy. *Phys. Rev. Lett.* **1974,** *32*, 534-537.

(46) Fraxedas, J.; Caro, J.; Figueras, A.; Gorostiza, P.; Sanz, F. Surface characterization of thin films of tetrathiofulvalene 7, 7, 8, 8-tetracyano-p-quinodimethane evaporated on NaCl (001). *J. Vac. Sci. Technol. A* **1998,** *16*, 2517-2523.

(47) Wagner, H.; Brinks, M. K.; Hirtz, M.; Schäfer, A.; Chi, L.; Studer, A. Chemical surface modification of self-assembled monolayers by radical nitroxide exchange reactions. *Chem. A Eur. J.* **2011,** *17*, 9107-9112.

(48) Hodgson, J. L.; Lin, C. Y.; Coote, M. L.; Marque, S. R. A.; Matyjaszewski, K. Linear free-energy relationships for the alkyl radical affinities of nitroxides: a theoretical study. *Macromolecules* **2010,** *43*, 3728-3743.

(49) Gryn'ova, G.; Barakat, J. M.; Blinco, J. P.; Bottle, S. E.; Coote, M. L. Computational design of cyclic nitroxides as efficient redox mediators for dye sensitized solar cells. *Chem. A Eur. J.* **2012,** *18*, 7582-7593.

(50) Alecu, I. M.; Zheng, J.; Zhao, Y.; Truhlar, D. G. Computational thermochemistry: scale factor databases and scale factors for vibrational frequencies obtained from

electronic model chemistries. *J. Chem. Theory Comput.* **2010,** *6*, 2872-2887.

(51) Curtiss, L. A.; Raghavachari, K.; Redfern, P. C.; Baboul, A. G.; Pople, J. A. Gaussian-3 theory using coupled cluster energies. *Chem. Phys. Lett.* **1999,** *314*, 101-107.

(52) Izgorodina, E. I.; Coote, M. L. Reliable low-cost theoretical procedures for studying addition-fragmentation in RAFT polymerization. *J. Phys. Chem. A* **2006,** *110*, 2486-2492.

(53) Izgorodina, E. I.; Brittain, D. R.; Hodgson, J. L.; Krenske, E. H.; Lin, C. Y.; Namazian, M.; Coote, M. L. Should contemporary density functional theory methods be used to study the thermodynamics of radical reactions? *J. Phys. Chem. A* **2007,** *111*, 10754-10768.

(54) Marenich, A. V.; Cramer, C. J.; Truhlar, D. G. Universal solvation model based on solute electron density and on a continuum model of the solvent defined by the bulk dielectric constant and atomic surface tensions. *J. Phys. Chem. B* **2009,** *113*, 6378-6396.

(55) Klamt, A. Conductor-like screening model for real solvents: a new approach to the quantitative calculation of solvation phenomena. *J. Phys. Chem.* **1995,** *99*, 2224-2235.

(56) Klamt, A.; Jonas, V.; Bürger, T.; Lohrenz, J. C. Refinement and parametrization of COSMO-RS. *J. Phys. Chem.* **1998,** *102*, 5074-5085.

(57) Klamt, A., *COSMO-RS: from quantum chemistry to fluid phase thermodynamics and drug design*. Elsevier: 2005.

(58) Louwen, J. N.; Pye, C. C.; Van Lenthe, E.; McGarrity, E. S.; Xiong, R.; Sandler, S. I.; Burnett, R. I., In http://www.scm.com, ADF2014 COSMO-RS, SCM, Theoreoretical Chemistry, Vrije Universiteit, Amsterdam, The Netherlands: 2014.

(59) Pye, C. C.; Ziegler, T.; Van Lenthe, E.; Louwen, J. N. An implementation of the conductor-like screening model of solvation within the Amsterdam density functional package—Part II. COSMO for real solvents 1. *Can. J. Chem.* **2009,** *87*, 790-797.

(60) Frisch, M. J.; Trucks, G. W.; Schegel, H. B.; Scuseria, G. E.; Robb, M. A.; Cheeseman, J. R.; Scalmani, G.; Barone, V.; Mennucci, B.; Petersson, G. A.; Nakatsuji, H.; Caricato, M.; Li, X.; Hratchian, H. P.; Izmaylov, A. F.; Bloino, J.; Zheng, G.; Sonnenberg, J. L.; Hada, M.; Ehara, M.; Toyota, K.; Fukuda, R.; Hasegawa, J.; Ishida,

M.; Nakajima, T.; Honda, Y.; Kitao, O.; Nakai, H.; Vreven, T.; Montgomery, J. A.; Jr. Peralta, J. E.; Ogliaro, F.; Bearpark, M.; Heyd, J. J.; Brothers, E.; Kudin, K. N.; Staroverov, V. N.; Keith, T.; Kobayashi, R.; Normand, J.; Raghavachari, K.; Rendell, A.; Burant, J. C.; Iyengar, S. S.; Tomasi, J.; Cossi, M.; Rega, N.; Millam, J. M.; Klene, M.; Knox, J. E.; Cross, J. B.; Bakken, V.; Adamo, C.; Jaramillo, J.; Gomperts, R.; Stratmann, R. E.; Yazyev, O.; Austin, A. J.; Cammi, R.; Pomelli, C.; Ochterski, J. W.; Martin, R. L.; Morokuma, K.; Zakrzewski, V. G.; Voth, G. A.; Salvador, P.; Dannenberg, J. J.; Dapprich, S.; Daniels, A. D.; Farkas, O.; Foresman, J. B.; Ortiz, J. V.; Cioslowski, J.; Fox, D. J. *Gaussian 09, revision E.01* **2009**, Gaussian, Inc., Wallingford CT.

(61) Werner, H. J.; Knowles, P. J.; Knizia, G.; Manby, F. R.; Schütz, M. Molpro: a general-purpose quantum chemistry program package. *WIREs Comput. Mol. Sci.* **2012,** *2*, 242-253.

(62) Werner, H. J.; Knowles, P. J.; Knizia, G.; Manby, F. R.; Schütz, M.; Celani, P.; Györffy, W.; Kats, D.; Korona, T.; Lindh, R.; Mitrushenkov, A.; Rauhut, G.; Shamasundar, K. R.; Adler, T. B.; Amos, R. D.; Bernhardsson, A.; Berning, A.; Cooper, D. L.; Deegan, M. J. O.; Dobbyn, A. J.; Eckert, F.; Goll, E.; Hampel, C.; Hesselmann, A.; Hetzer, G.; Hrenar, T.; Jansen, G.; Köppl, C.; Liu, Y.; Lloyd, A. W.; Mata, R. A.; May, A. J.; McNicholas, S. J.; Meyer, W.; Mura, M. E.; Nicklass, A.; O'Neill, D. P.; Palmieri, P.; Peng, D.; Pflüger, K.; Pitzer, R.; Reiher, M.; Shiozaki, T.; Stoll, H.; Stone, A. J.; Tarroni, R.; Thorsteinsson, T.; Wang, M. *MOLPRO, version 2015.1, a package of ab initio programs,* http://www.molpro.net **2015**.

(63) Zhang, L.; Laborda, E.; Darwish, N.; Noble, B. B.; Tyrell, J. H.; Pluczyk, S.; Le Brun, A. P.; Wallace, G. G.; Gonzalez, J.; Coote, M. L. Electrochemical and electrostatic cleavage of alkoxyamines. *J. Am. Chem. Soc.* **2017,** *140*, 766-744.

(64) Blanchard, P.-Y.; Alévêque, O.; Breton, T.; Levillain, E. TEMPO mixed SAMs: electrocatalytic efficiency versus surface coverage. *Langmuir* **2012,** *28*, 13741-13745.

(65) Parsegian, A. Energy of an ion crossing a low dielectric membrane: solutions to four relevant electrostatic problems. *Nature* **1969,** *221*, 844-846.

(66) Hurth, C.; Li, C.; Bard, A. J. Direct probing of electrical double layers by scanning electrochemical potential microscopy. *J. Phys. Chem. C* **2007,** *111*, 4620-4627.

(67) Alévêque, O.; Seladji, F.; Gautier, C.; Dias, M.; Breton, T.; Levillain, E. Nitroxyl radical self-assembled monolayers on gold: versatile electroactive centers in aqueous and organic media. *ChemPhysChem* **2009,** *10*, 2401-2404.

(68) Alévêque, O.; Blanchard, P.-Y.; Breton, T.; Dias, M.; Gautier, C.; Levillain, E.; Seladji, F. Nitroxyl radical self-assembled monolayers on gold: experimental data vs. Laviron's interaction model. *Electrochem. Commun.* **2009,** *11*, 1776-1780.

(69) Wang, Y.; Rogers, E. I.; Compton, R. G. The measurement of the diffusion coefficients of ferrocene and ferrocenium and their temperature dependence in acetonitrile using double potential step microdisk electrode chronoamperometry. *J. Electroanal. Chem.* **2010,** *648*, 15-19.

(70) Witting, P. K.; Douglas, D.; Mauk, A. G. Reaction of human myoglobin and H_2O_2 involvement of a thiyl radical produced at cysteine 110. *J. Biol. Chem.* **2000,** *275*, 20391-20398.

(71) Yoon, Y. H.; Woo, D. H.; Shin, T.; Chung, T. D.; Kang, H. Real-space investigation of electrical double layers. potential gradient measurement with a nanometer potential probe. *J. Phys. Chem. C* **2011,** *115*, 17384-17391.

(72) Carbonell, E.; Duran, M.; Lledos, A.; Bertran, J. Catalysis of Friedel-Crafts reactions by electric fields. *J. Phys. Chem.* **1991,** *95*, 179-183.

(73) Matyjaszewski, K. Direct NMR observation of model and macromolecular esters in polymerization of styrene by perchloric acid. *Macromolecules* **1988,** *21*, 933-937.

Chapter 5 Electrostatic Catalysis in Homolytic Process of Alkoxyamines

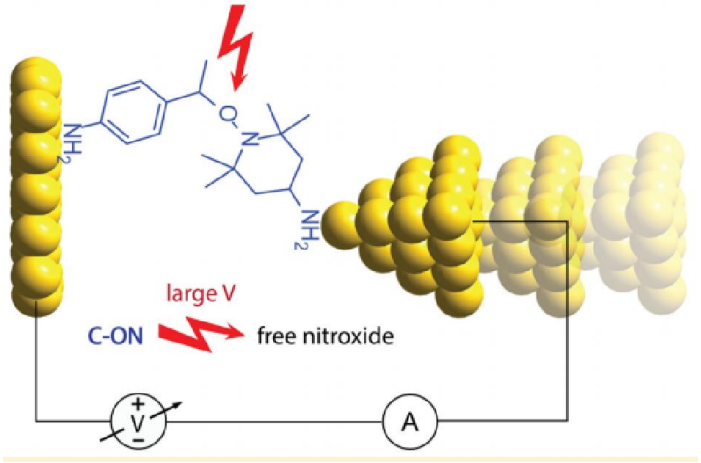

5.1 Abstract

The concept of "electrostatic catalysis of alkoxyamine lysis" is mentioned in Chapter 4 because while the oxidation of the alkoxyamine is triggered by a standard electrochemical process, its cleavage cannot however be explained without taking into account an explicit electrostatic environment (i.e., solvents and anions). This catalytic effect is not quantitatively sufficient to explain the lysis but only validated based theoretical frameworks. This is likely due to the limitations in the computational model (modelling the electric double layer by a background static field rather than an ensemble of ions and solvent molecules, something which cannot be done accurately because of computational cost). Here, therefore, this work has been further expanded to include an independent experimental demonstration of pure electrostatic cleavage of the neutral alkoxyamine molecule (1-(1-(4-aminophenyl)ethoxy)-2,2,6,6-tetramethylpiperidin-4-amine (molecule **1**). This is achieved using single molecule break junction experiments in a scanning tunneling microscope in low dielectric solvents (STM-BJ technique), defining the magnitude of this catalytic effect by looking at an independent electrical signal in non-electrolyte systems. Quantum calculations modelling the role of electric fields (magnitude and alignment, *i.e.* field *vs* reaction axis) in guiding the homolysis of the STM-BJ system also support the electrostatic role in assisting the rupture of C-O bonds.

5.2 Introduction

Electrostatic catalysis refers to the use of static electric fields to catalyze ordinary chemical reactions.[1] Conversion of reactants into products is synonymous of electronic reorganization, yet little is known on the effect of static charges on chemical catalysis. Chemists appreciate that redox currents at electrodes respond predictably to changes in voltage – for instance a bias of about 1 V pointing in the right direction can lead to changes in redox currents by a factor of up to 10^8. These currents are the manifestation of the rate at which electrons are either lost or gained; hence, the field-effect is easily explained and accounted for. On the other hand, the effect of static electricity on non-redox reactivity, long suggested by theoretical chemists,[2-4] is not intuitive and it is just

starting now to emerge as an important branch of chemical catalysis.[1, 5-7] The chemical implications are expected to be broad since electrolytes and electrostatic interactions are ubiquitous in chemical, material and biological sciences,[4, 8-11] to the point of dominating the entire reaction space in natural or technological environments, such as cell membranes,[12] fluidic channels[13] or the confined electrolyte space of a porous electrode.[14] The theories and models describing the role of electrostatic forces on the formation or rupture of chemical bonds were pioneered by Pocker,[15] Bertrán,[4] Warshel,[16] and Shaik[17] starting in the 1970s. This form of catalysis arises because formally covalent species can be stabilized via minor charge-separated resonance contributors. A non-polar covalent bond A–B might be written as [A–B ↔ A^+–B^- ↔ A^-–B^+], but in the absence of an electrostatic force A–B is dominant and the extent of resonance stabilization is small. Only in the presence of an appropriately-oriented electric field can one of the charge-separated contributors be stabilized. The electrostatic "awakening" of the ionic character of bonds, and the effect on reaction barriers that follows can be dramatic.[1, 6, 18] The obvious and perceived challenge is how to align molecules and field so as to take advantage of these effects.[6, 19-21]

Earlier work has shown that the electric field from remote negatively charged functional groups could dramatically lower the bond dissociation energy of alkoxyamines and facilitate their homolysis at temperatures lower than otherwise possible.[19, 22-24] It has also been shown in Chapter 4 that the lysis of alkoxyamine radical cations is energetically inaccessible in the absence of electrostatic factors, that is, their rupture processes are energetically infeasible if one neglected orbital-based interactions with solvents or anions. For example, validated theoretical calculations suggest that the cleavage in a continuum solvent without an electric field is thermodynamically uphill 30 kJ/mol, which can also be facilitated by presence of a background electric field and when the coordinating anion is replaced by a point charge as well.[25] However, the electrostatic effect is currently only qualitatively confirmed based on theoretical calculations and, moreover, the calculated effect is limited to a background electric field but not an ensemble of ions and solvents molecules. Another challenge that needs to be

addressed is how to balance the trade off between solubility and magnitude of the electrostatic catalytic effect.[19, 22, 23]

This raises two questions as to whether there are better and more general methods of introducing charges and ensuring they align with reaction axes as well as concerning whether the role of a static electric field can be quantified, that is described by voltage/distance. One strategy successfully used in this work relies on electrification of molecules while these are held under bias in the nanoscale gap between metal electrodes of a STM-BJ set-up. STM-BJ is the only technique available to bring together single molecule reactants between nanoscale electrodes, and it is unparalleled in its ability to deliver a large oriented electric field (V/nm) which is tunable and can catalyze several thousands of chemical events over short periods of time. Using STM-BJ (in mesitylene as solvent) one has recently demonstrated a link between electrostatic forces and the rate of formation of a carbon–carbon covalent bond.[6] Therefore, similar measurement were made here to capture the field-sensitivity on the homolysis of alkoxyamines. The new STM-BJ single molecule experiments performed are complementary to the electrochemical data and quantum data in Chapter 4, stressing on the electrostatic factors at play in the bond breaking energetics. However, it remains that while this technique can be key in an experimental scrutiny leading to proof-of-concept data, it is clearly not practical to process workable quantities of materials in STM-BJ. The single molecule experiments show a direct link between the electric field magnitude and the extent of C–O lysis (electrostatic lysis of the "symmetrically" substituted di-amino alkoxyamine **1**). Once more, besides this, by using the technologically-relevant case of alkoxyamines this work seeks to demonstrate the analytical value of the STM-BJ technique in chemistry.

5.3 Experimental methods

5.3.1 Chemicals and materials

Chemicals. Unless noted otherwise, all chemicals were of analytical grade and used as received. The main chemicals, 4-Vinylbenzyl chloride (90%), 4-vinylaniline, di-tert-butyl dicarbonate (BOC_2O, ReagentPlus®, ≥99%), and 4-amino-2,2,6,6-

tetramethylpiperidine-1-oxyl (4-NH_2-TEMPO) were purchased from Sigma-Aldrich. 1-(1-(4-aminophenyl)ethoxy)-2,2,6,6-tetramethylpiperidin-4-amine (**1**, di-amino-TEMPO-PE), was synthesized through published methods with minor modifications.[26]

STM-BJ surface model: Both tip and substrate where alkoxyamine 1 is bridged are gold material, in particular, the orientation of gold substrate is Au(111).

5.3.2 Purification and analysis of synthesized compounds

Thin-layer chromatography (TLC) was performed on silica gel using Merck aluminium sheets (60 F254). Merck 60 Å silica gel (220−400 mesh particle size) was used for column chromatography. High-resolution mass spectral data (HRMS, MASS accuracy 2-4 ppm) of compound di-amino-TEMPO-PE (alkoxyamine **1**) was obtained using a Waters Xevo QTof MS via ESI experiments and infusing the sample at 8 μL/min. Nuclear magnetic resonance (NMR) spectra were recorded on a Bruker Avance 400 spectrometer. Alkoxyamine **1a** (precursor of alkoxyamine **1** used in STM-BJ experiments, gold electrodes) was synthesized in one-step from nitroxide **A** and olefin **B**. Synthetic details for **A** and **B** are shown below.

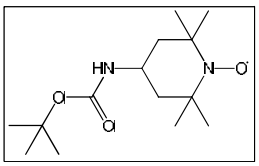

4-*Tert*-butoxycarbonylamino-2,2,6,6-tetramethylpiperidin-1-oxyl (A). Three molar equivalents of $NaHCO_3$ (1.26 g, 15 mmol) and a 20% molar excess of BOC_2O (1.31 g, 6 mmol) were added in portions to an ice-cold solution of 4-amino-TEMPO (0.86 g, 5 mmol) in a mixture of THF/water (1/1, 50 mL). The reaction mixture was stirred under argon atmosphere in an ice-bath for 45 min followed by stirring overnight (12 h) at room temperature. The crude solution was poured into 100 mL ether and the organic phases were washed with water (3 × 50 mL). The combined organic layers were then dried over $MgSO_4$, and the ether was removed under reduced pressure. The obtained orange solid residue was purified by silica gel column chromatography (ethyl acetate/hexane, 1/4, v/v) to give an orange solid that was used in the following step without further characterization (1.14 g, 4.2 mmol).

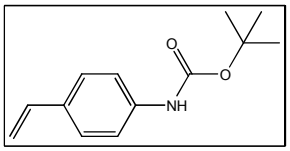

***Tert*-butyl-4-vinylphenylcarbamate (B).** To a stirred solution of 4-vinylaniline (1.79 g, 15 mmol) in 30 mL anhydrous THF, a solution of BOC_2O (3.93 g, 18 mmol) in anhydrous THF (30 mL) was added dropwise at room temperature under nitrogen atmosphere while stirring. The solution was refluxed overnight (12 h), the mixture was then allowed to cool to room temperature, diluted with DCM and then partitioned between water and DCM. The aqueous solution was further extracted with DCM (3 × 50 mL), the organic layers were combined, washed with water and brine, then dried over $MgSO_4$. After removal of the solid residue by filtration, the solvent was removed under reduced pressure and the crude material was purified by silica gel column chromatography (ethyl acetate/hexane, 1/10, v/v) to yield the title compound as a white solid (2.8 g, 12.8 mmol).

^{1}H NMR (400 MHz, *d*-DMSO): δ (ppm) = 9.38 (s, BOC-N**H**, 1H), 7.43 (d, Ar-**H**, *J* = 8.68 Hz, 2H), 7.35 (d, Ar-**H**, *J* = 8.56 Hz, 2H), 6.63 (dd, Ar-C**H**=CH_2, *J* = 17.62 Hz, 10.92 Hz, 1H), 5.68 (dd, Ar-CH=C**H$_2$**, *J* = 17.70 Hz, 1.06 Hz, 1H), 5.12 (dd, Ar-CH=C**H$_2$**, *J* = 10.92 Hz, 1.00 Hz, 1H), 1.47 (s, **BOC**, 9H).

^{13}C NMR (400 MHz, *d*-DMSO): δ (ppm) = 152.64, 139.26, 136.20, 131.00, 126.48, 117.96, 112.08, 79.06, 28.09.

Alkoxyamine 1 synthesis 1-(1-(4-*tert*-butylcarbamatephenyl)ethoxy)-2,2,6,6-tetramethylpiperidin-4-tert-butoxycarbonylamino (di-BOC-amino-TEMPO-PE, **1a**) was synthesized via the following procedures. To a 100 mL rounded-bottom flask equipped with a magnetic stirrer and placed in an ice-bath, sequential additions were made of: i) 2 mmol of the nitroxide precursors dissolved in 60 mL of a toluene/ethanol (1/1, v/v) mixture, ii) a ten-fold molar excess of styrene or its derivative, and iii) $Mn(OAc)_3$ $2H_2O$ (5.36 g, 20 mmol). A 15-fold molar excess of $NaBH_4$ (with respect to the nitroxide) was added in portions at 15-min intervals. After stirring overnight under nitrogen atmosphere, the crude reaction mixture was filtered, the filtrate was transferred into water and the aqueous suspension was then washed three times with DCM. The combined organic layers were evaporated under reduced pressure and the crude materials were purified on silica gel column chromatography using eluents (ethyl

acetate/hexane, 1/5, v/v,) to yield **1a** (white solid, 0.42 g, 0.9 mmol). Di-amino-TEMPO-PE (**1**) di-BOC-amino-TEMPO-PE (**1a**, 1 g, 2 mmol) was deprotected with CF_3COOH (6.84 g, 60 mmol) in 20 mL DCM with stirring at room temperature. After 6 h of stirring, the reaction mixture was adjusted to neutral pH with saturated $NaHCO_3$ aqueous solution and the water phase was then extracted with DCM (3 × 20 mL). The combined organic extracts were dried over $MgSO_4$, filtered, and then concentrated under reduced pressure. Alkoxyamine **1** was purified by chromatography over an alkalified silica gel column (ethyl acetate/MeOH, 5/1 v/v with 1% v/v of Et_3N) as a yellow oil (0.18 g, 0.6 mmol).

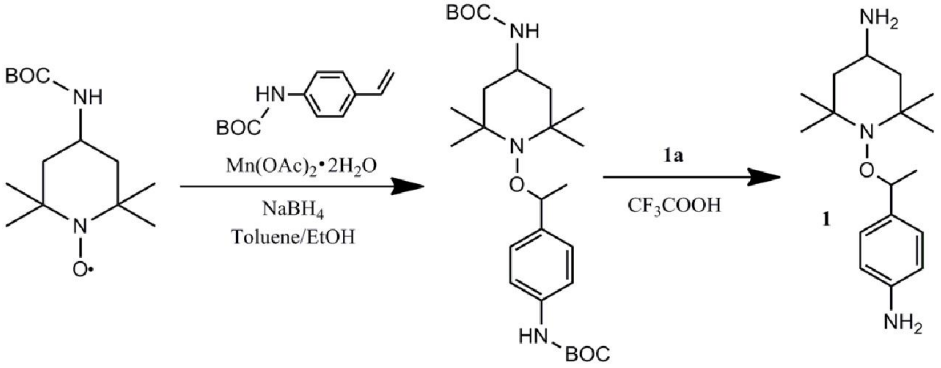

Figure 5.1 Synthesis of alkoxyamine **1** used in this Chapter (STM-BJ experiments on gold surfaces and theoretical models).

^{1}H NMR (**1a**, 400 MHz, *d*-DMSO) δ (ppm) = 9.27 (s, BOC-N**H**-Ar, 1H), 7.38 (d, Ar-**H**, *J* = 8.28 Hz, 2H), 7.16 (d, Ar-**H**, *J* = 8.52 Hz, 2H), 6.64 (d, BOC-N**H**-TEMPO, *J* = 7.88 Hz, 1H), 4.65 (q, NO-C**H**-Ar, *J* = 6.56 Hz, 1H), 3.62-3.48 (m, 1H), 1.50-1.34 (m, 24H), 1.28-1.19 (m, 4H), 1.14 (s, 3H), 0.99 (s, 3H), 0.55 (s, 3H).

^{13}C NMR (**1a**, 400 MHz, *d*-DMSO): δ (ppm) = 154.84, 152.76, 138.54, 138.36, 126.87, 117.76, 82.10, 78.88, 77.49, 59.62, 59.17, 45.67, 45.13, 33.78, 28.25, 28.12, 22.80, 20.61

HRMS (**1a**, *m*/*z*): $[M+H]^+$ calcd for $C_{27}H_{46}N_3O_5$ 492.3432, found 492.3428.

^{1}H NMR (**1**, 400 MHz, *d*-DMSO) δ (ppm) = 7.32 (d, Ar-**H**, *J* = 8.48 Hz, 2H), 7.23 (d, Ar-**H**, *J* = 8.54 Hz, 2H), 6.35 (s, N**H**$_2$-Ar, 2H), 5.56 (s, N**H**$_2$-TEMPO, 2H), 4.76 (q, NO-C**H**-Ar, *J* = 6.52 Hz, 1H), 2.97-2.85 (m, 1H), 1.72-1.62 (m, 1H), 1.57-1.48 (m, 1H), 1.46-1.40 (m, 3H), 1.31-1.23 (m, 4H), 1.20-1.16 (m, 4H), 1.02 (s, 3H), 0.61 (s, 3H).

HRMS (**1**, *m*/*z*): $[M+H]^+$ calcd for $C_{17}H_{30}N_3O$ 292.2383, found 292.2381.

5.3.3 STM-BJ measurement

Measurements of single-molecule conductivity using the STM-BJ technique were carried out using PicoSPM I microscope controlled by a Picoscan-2500 electronics (all from Agilent Technologies) and using a custom PTFE-STM cell for solid/liquid samples. The current versus distance curves (gold STM tip-to-Au(111) substrate distance) were captured using a NI-DAQmx/BNC-2110 National Instruments (LabVIEW) and analyzed with a LabVIEW code. The procedure of break-junction experiment is based on moving the STM tip to tunneling distance over an Au(111) surface that is covered with a dilute sample containing the molecules of interest (alkoxyamine **1**, 4-amino-TEMPO and 4-vinylaniline in mesitylene /DCM, 10:1, v/v). The STM current-feedback is then turned off and the tip is driven into and out of contact with the surface at a speed of ca. 50 nm/s. This 2-points cycle is repeated thousands of times enabling capturing of ca. 4000 distance versus current curves (current decays) for each set of data. Plateaus, indicative of the formation and subsequent rupture of single-molecule electrical junctions, appear during the pulling cycle of the externally driven two-point loop. The current decays are then accumulated in conductance histograms. The peak maximum in the conductance histogram resemble the single-molecule conductivity of the sample (conductance (G) was calculated using the equation $G = I_{step}/V_{bias}$, where I_{step} is the plateau current and V_{bias} is the voltage difference between the tip and surface).

5.3.4 Computational methods

As for the STM-BJ experiments, the principle aims were to study the effect of EEFs on the reaction energies, rather than assess absolute reaction energies. For this purpose the M06-2X/6-31+G(d) level of theory, which has been benchmarked and used in previous studies of EEFs,[6] was sufficient. Full conformer searching and geometry relaxation of each species were performed and the lowest energy conformer then used for subsequent calculations involving fields. Solvation energies in mesitylene solvent were calculated with the SMD solvent model, and all calculations were performed in Gaussian 09.[27] Full details of all theoretical procedures used for computing the effect of external

electric field on homolysis of alkoxyamines are summarized in my reported paper.[25]

5.4 Results and discussions

To establish whether electrostatic effects can trigger alkoxyamine homolysis, STM-BJ experiments were performed. STM-BJ experiments can pick-up the electrical "finger printing" of reactants and products by probing the magnitude of molecular resistance of over several (5-6) orders of magnitude. This technique is the state-of-the-art approach in terms of delivering an electrostatic stimulus across a reactant and acquiring statistically significant data. The repetitive formation of molecular junctions in the STM-BJ technique is an established method of accessing conductance measurements on single-molecules.[28-30] It also allows access to a statistically significant pool of data on bond breaking (and/or reformation[6]) in response to changes in field magnitude. The schematic directly below (Figure 5.2) is only intended as a guide on the STM-BJ technique and as a cartoon to aid the reader to conceptualize the results on the electrostatic lysis of alkoxyamine **1**.

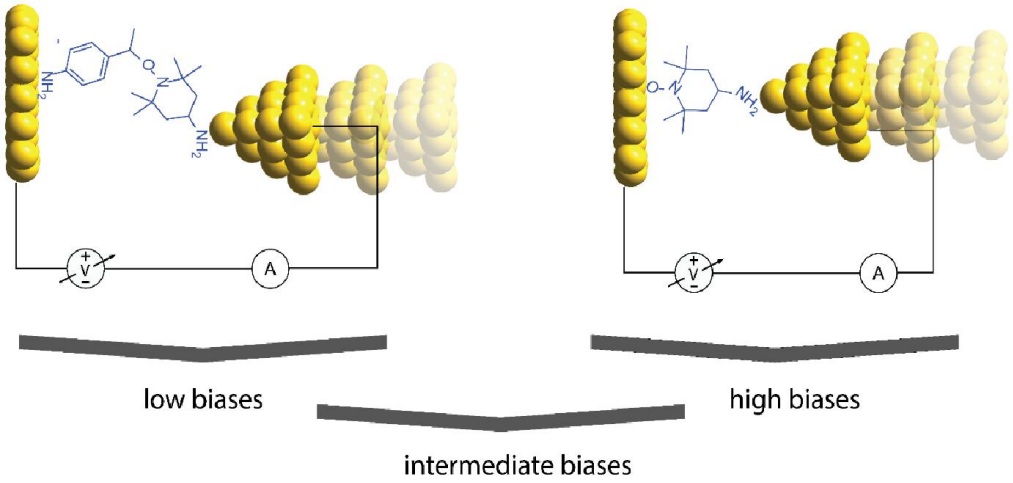

Figure 5.2 An external oriented electric field prompt the lysis of alkoxyamines. Schematics of a STM-BJ setup on alkoxyamines in low dielectric solvents. Detailed results and experimental procedures are in the Figures 5.3 and 5.4. The fate of the parent alkoxyamine **1** (left panel) is probed by measuring the single-molecule conductivity at different magnitudes of electric field. Molecules have very distinct electrical finger-prints in STM-BJ and. For instance, the 4-amino TEMPO molecule (right panel) is less electrically conducting than the parent alkoxyamine by one order of magnitude.

This work investigates the role of electric fields on the lysis of alkoxyamines by bridging a molecule (alkoxyamine **1**, Figure 5.3a) between a gold STM tip and an Au(111) substrate under a bias stimuli of variable magnitude. Alkoxyamine **1** is symmetrically substituted with primary amino groups at opposite ends of the molecule (see Figure 5.1). These two primary amine pendants have affinity towards gold, allowing electrical contacts to be made with the reactant, i.e., molecules of **1**, by both the STM Au tip and the Au(111) surface. The single molecule conductance is measured by repeatedly forming and breaking the molecular junction by "tapping" the STM tip in and out of contact with the Au(111) surface while this is covered by a diluted sample of **1** (in mesitylene/DCM, 10:1, v/v solvent). Current plateaus appear in the pulling curves reflecting the formation of a single-molecule junction. By means of accumulating thousands of individual current-distance traces, (Figure 5.3d-f), conductance histograms (Figure 5.3g-i) have been built showing peak maxima that reflect the most probable conductance value of the molecule(s) in the junction at a given tip–surface bias.

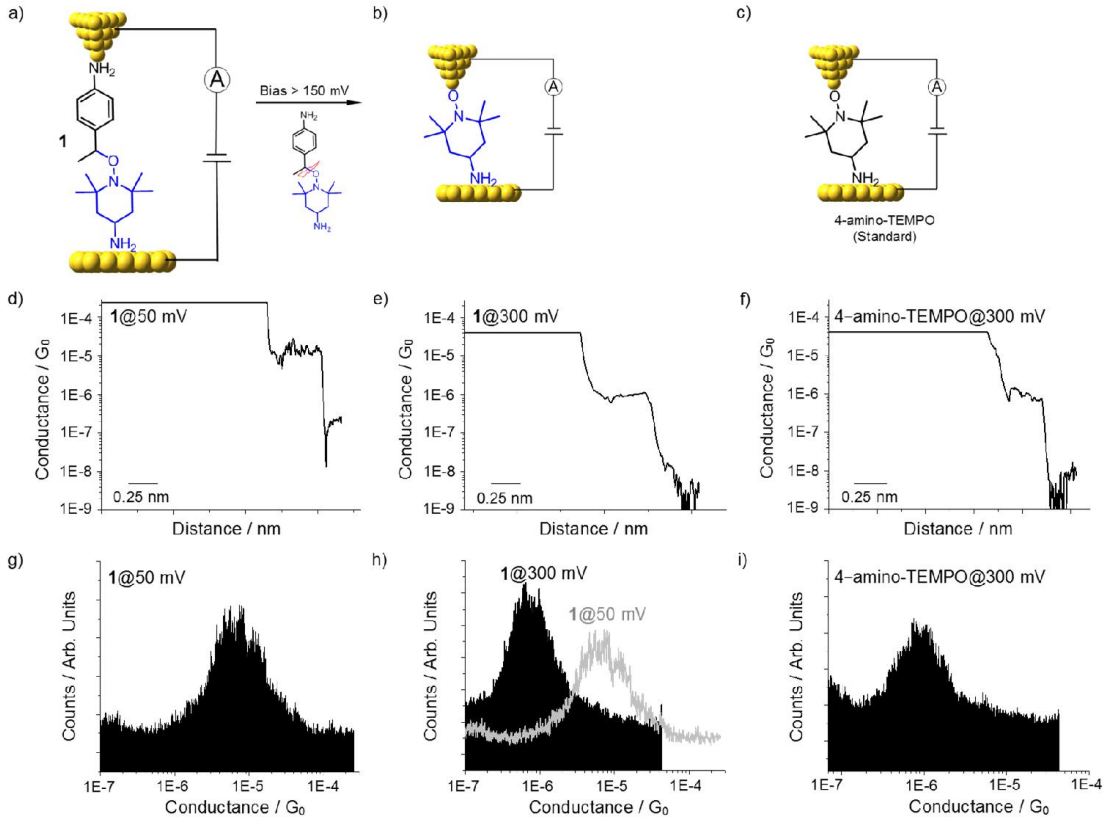

Figure 5.3 Electrostatic catalysis in the homolysis of alkoxyamines. (a-c) Schematic depiction of the STM-BJ setup for a single-molecule junction experiment used to

investigate the effect of an external electrical field on the breaking of a C–ON bond. Single-molecule STM-BJ conductance measurements were used to probe the fate of the alkoxyamine molecule **1** under a variable electric field stimulus in a low dielectric solvent. The experiments capture discrete electrical signals from either the intact parent molecule **1** or from the putative 4-amino-TEMPO fragment that is produced upon the homolysis of **1**. A STM tip is brought into and out of contact with an Au(111) surface while this is covered with a diluted solution of the molecule of interest (either **1** or a 4-amino-TEMPO standard in mesitylene/DCM, 10:1, v/v). The surface is biased against the tip and the current versus distance signal is collected as the tip is moved away from the surface. (d-f) Typical current versus distance traces with conductance plateaus indicative of a single-molecular junction. The current drops from the current-saturation value to the current-amplifier detection limit, passing through breakage steps, "plateaus", each of a specific conductance value. (g-i) Conductance histograms showing the electrical "fingerprints" of either the intact alkoxyamine **1** (i.e. before splitting, tip-surface bias < 150 mV) at 1E-5 G_0 ($G_0 = (2e^2/h = 77.5$ μS, quantum of conductance) or the free nitroxide that is unmasked after splitting (bias > 150 mV) at 1E-6 G_0. The molecular conductance obtained upon homolysis of **1**, as shown in (h, **1**@300 mV), is a perfect match of the results from control experiments where the two electrodes are forming junctions in a standard sample of commercial 4-amino-TEMPO (c,f,i).

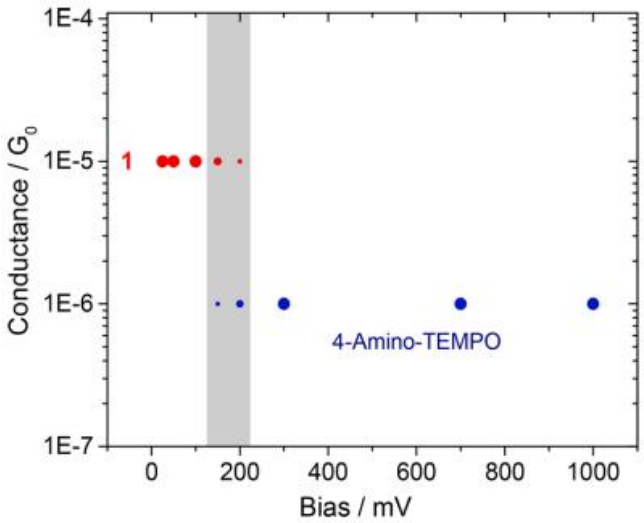

Figure 5.4 Electric fields and breaking probability of single-molecules. The plot shows the effect of the bias between the STM tip and the Au(111) surface over the fate of several thousand molecular junctions (ca. 4000 for each data point) each obtained by electrically "wiring" molecules of alkoxyamine **1** in a STM-BJ experiment. At biases in the range between 150 and 200 mV, discrete conductance plateaus at both 1E-5 G_0 and 1E-6 G_0 appear, reflecting the co-existence of both the parent molecule **1** and its homolysis product (4-amino-TEMPO). The area of each data point reflects the relative bias-dependent abundance of the species.

Figure 5.4 summarizes visually the outcome of STM-BJ experiments on alkoxyamine **1**. In brief, below a threshold bias of 150 mV, the statistical analysis of individual plateaus in the current versus distance curves leads to a single prominent peak in the conductance histogram at ca. 1E-5 G_0 (where G_0 = 77.5 μS). This peak is unambiguously assigned to the parent alkoxyamine, indicating the presence exclusively of intact molecules of **1** in the electrified gap (left column in Figure 5.3). Between 100 mV and 200 mV, however, a second plateau appears at 1E-6 G_0. Finally, above 300 mV, the 1E-5 G_0 peak disappears completely to be replaced by a 1E-6 G_0 electrical signature (Figure 5.4 and panels e and h in Figure 5.3). This conductance signature at 1E-6 G_0 is assigned to nitroxide species that are generated from the electric field-induced splitting of **1** by a bias > 150 mV. Nitroxides have a known affinity for gold surfaces,[31, 32] and the same 1E-6 G_0 conductivity signature is observed in control STM-BJ experiments that are performed using a standard 4-amino-TEMPO solution (right column in Figure 5.3). Moreover, unlike for the alkoxyamine **1**, STM-BJ experiments performed only in the presence of 4-amino-TEMPO molecules do not show a dependency of molecular conductance on bias, and for instance the conductance/G_0 ratio of these controls is unchanged between 50 mV and 300 mV (see panels c-d in Figure 5.5). It appears therefore extremely unlikely that the 1E-6 G_0 signature in this field-assisted lysis of **1** is arising from chemical entities other than a free nitroxide fragment. For example, STM-BJ control experiments of 4-vinylaniline (i.e., a putative end product of the homolysis[33, 34]) are shown in panels e-f of Figure 5.5 and carry no evidence of any sizable peak in conductance histogram. The STM tip-to-substrate bias appears therefore to guide the redistribution between an alkoxyamine-only population (up to ca 100 mV of dc bias between STM tip and substrate) to a mixed alkoxyamine/nitroxide population (between 150 and 200 mV) and ultimately to a nitroxide-only presence (bias over 300 mV).

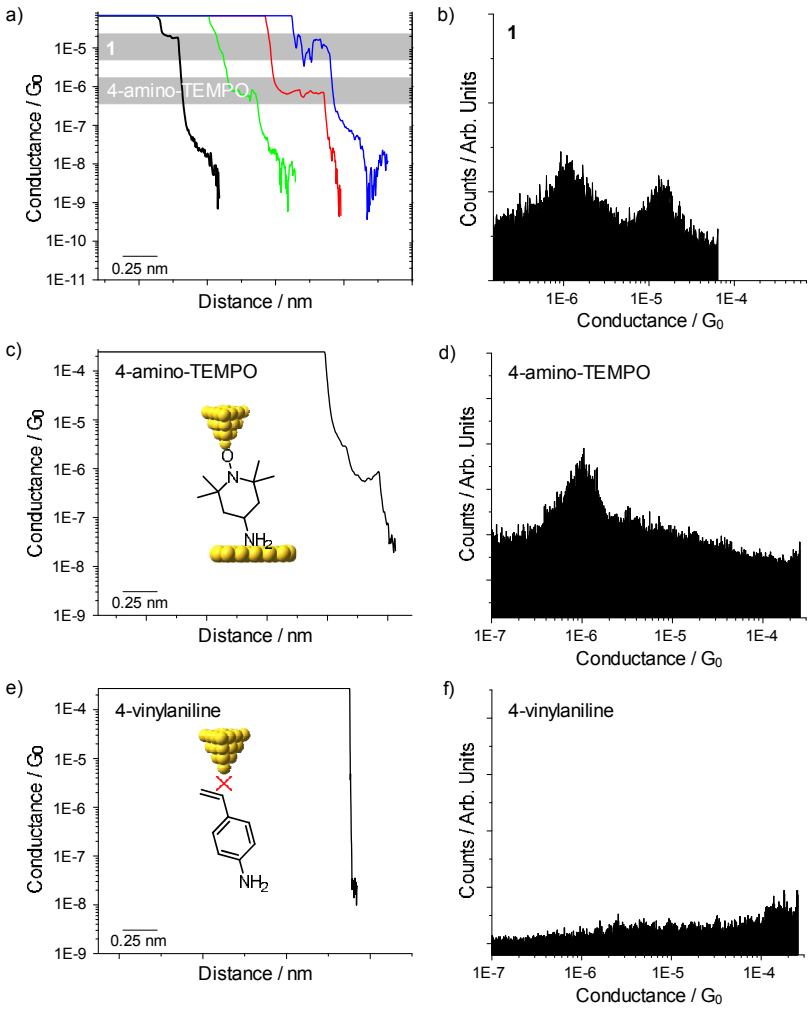

Figure 5.5 Electrostatic catalysis in the homolysis of alkoxyamines. (a,b) Representative single-molecule STM-BJ conductance "pull" trace and statistical conductance histograms for samples of alkoxyamine **1** in mesitylene/DCM biased at 200 mV (gold STM tip-to-Au(111) substrate bias). The histograms that are built from the analysis of ca. 4000 pulling traces show the coexistence of the 1E-5 Go "signature" which is assigned to the parent molecule (**1**) with the 1E-6 G_0 population which is assigned to one of the lysis product (4-amino-TEMPO molecules, i.e. the putative nitroxide fragment originated from the C–O lysis in **1**). (c,d) STM-BJ control experiments of the molecule 4-amino-TEMPO held at 50 mV showing a representative conductance-distance trace alongside conductance histograms revealing a major contributor of electrical conductance centred at 1E-6 G_0. The conductance does not change between 50 mV and 300 mV (Figure 5.3) for the 4-amino-TEMPO control, indicating that this molecule is not affected by the electric field in this bias range and remains intact during the measurement. (e,f) STM-BJ experiments on samples of 4-vinylaniline molecule, one of the putative product of the lysis of **1**. Plateaus are absent from the STM-BJ curves and this is statistically evident as no "peak" can be observed in conductance histograms built from the data. It can be inferred that the original alkoxyamine molecule **1** breaks in response to an electric field (threshold of about 200

mV bias between the gold STM tip and the Au(111) substrate) to release a 4-amino-TEMPO fragment (electrical "fingerprinting" of 1E-6 G_0) and possibly a vinylaniline that however is not forming a top & bottom junction with the gold electrodes.

The above STM-BJ data give statistically significant and clear insights on the role of electrostatic in the lysis of the C-O bond of the alkoxyamine **1**. The exact magnitude of the field (V/nm) delivered between the Au(111) substrate and the approaching/retracting STM tip in the STM-BJ technique can probably reach very large values,[35] therefore, to suggest number and not just insights, one can compare the experiments against a quantum model of the system (vide infra). Quantum-chemical calculations of the reaction profile in the presence of a field of varying strength that is aligned along the N–O bond axis suggest that the homolysis of **1** is possibly promoted by as much as 35 kJ mol^{-1} (Theoretically, the barrier of the alkoxyamine (**1**) → TEMPO + R• reaction is lowered by up to 35 kJ/mol going from a zero external-field scenario to a 4 V/nm field). This barrier-lowering effect is consistent with the expected stabilization of the charge-separated resonance contributor to the nitroxide radical (N–$O^{\bullet}$ ↔ $N^{+\bullet}$–O^{-})[19, 23] and is enough to account for the radical formation. Electrostatic effects can thus promote homolysis of alkoxyamines and can explain the observed STM results. However, it is difficult to extract truly quantitative theoretical data on the field/barrier relationship. This is because, while clearly it is possible to control in STM-BJ the alkoxyamine/nitroxide population, the upper limit of the experimental electric field (V/nm) in the STM experiment is nonetheless relatively difficult to quantify as the distance between the tip and the Au(111) plate varies during the tapping experiments. Therefore, as a conservative measure, the range of field strengths considered in the theoretical model are probably a lower estimate (vide infra).

At this point, to examine the effect of EEFs on the bond cleavage reaction of alkoxyamines, the reaction energy of the C-O bond cleavage reaction in Figure 5.6 is calculated as a function of field strength. This model includes the tethers which would attach to the gold surfaces in the STM experiment, however the gold itself is not included due to the large increase in computational cost and complexity associated with dealing with modelling a surface. Moreover, previous studies suggest that the gold

cluster in that case underestimated the effect of EEFs by more than a third, so they will not be considered for this study.[6] In addition to the preferred homolytic cleavage reaction, two alternative heterolytic cleavage reactions are also studied as a function of field strength. These calculations confirmed that homolytic cleavage remained the preferred process across all field strengths studied. Calculations were performed in both the gas phase and in mesitylene solvent, using the SMD solvent model, to mimic experimental conditions.

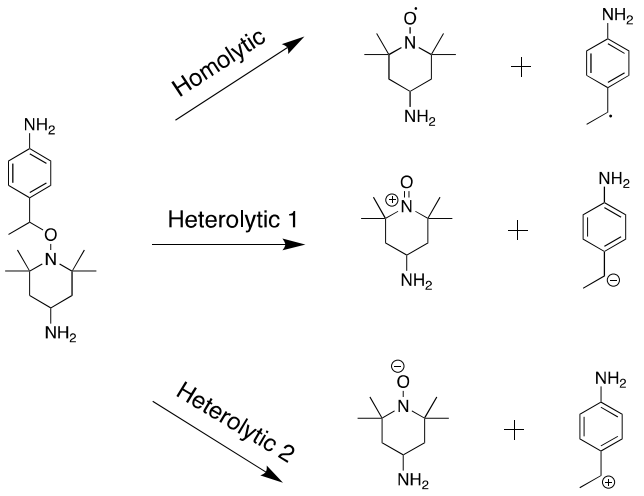

Figure 5.6 Alkoxyamine homolytic and heterolytic bond cleavage.

In assessing the effects of EEFs, the field strength and direction needs to be chosen so as to mimic the experimental conditions. This is more complex than in our previous study of Diels-Alder reactions[6] in EEFs for two reasons: (1) the alkoxyamine is tethered but not as held rigidly in the STM as the norbornene derivatives of the previous work; (2) the present experiments are STM tapping experiments rather than blinking. In the latter, the tip is held a fixed distance above the plate and this distance, together with the applied voltage, can be used to calculate the field strength experienced by the reagents. In tapping experiments, the tip is repeatedly driven into the plate and in principle the field at any applied voltage is variable can reach levels as the distance between the tip and the plate diminish. Given these problems, it is decided to assess EEFs along a wide range of field strengths, +0.0125 au to -0.0125 au, a range chosen for consistency with previous theoretical studies of the effects of EEFs[1, 36, 37] on chemical reactions. It is presumed that if the molecule is free to move to some extent in the field then it should,

within the constraints of tethering, adopt the orientation most likely to minimize its energy, both in the reactant and product. Thus, the field is initially aligned along the reaction axis (the z-axis in Figure 5.7), but additional sensitivity analysis was also undertaken using moderate strengths of +0.0010 au (approximately 0.5 V nm^{-1}). In performing these calculations, rotation of the coordinate axis was prevented using the Nosymm keyword and the field itself was applied using the Field = Read keyword. At every field strength, the geometries were allowed to relax in order to obtain the lowest energy of each species at every field strength tested.

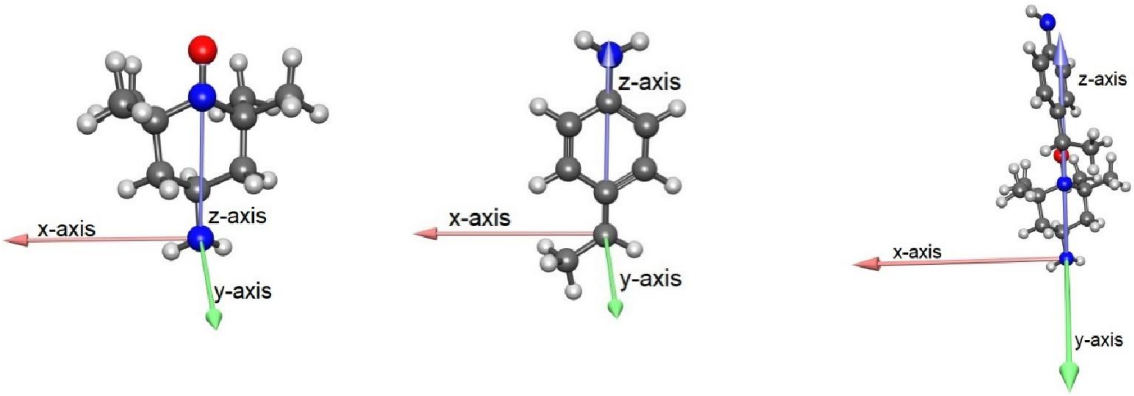

Figure 5.7 Selection of the x-, y- and z-directions (axes) for the reactant and product molecules of the homolytic cleavage reaction.

5.5 Conclusions

The STM-BJ experiments provide proof-of-concept that electric fields can trigger alkoxyamines homolysis to nitroxides and carbon-centred radicals under conditions where they would otherwise be stable. It can be noted that this is the first time a measurement of a single-molecule "circuitry" that uses electrostatics as the "switch" between two discrete molecules (parent alkoxyamine **1** and its splitting product of 4-amino-TEMPO), both able to form junctions, is demonstrated. It opens a new platform in the field of molecular electronics. In brief, the STM-BJ experiments demonstrate that "field-assisted" lysis of alkoxyamines can directly translate into "electrostatic switches" of molecular conductance in single-molecule electronic devices. This could conceptually lead to a new type of "field-effect transistor". This is possible as both the parent molecule **1** as well as the product of the "field-driven" lysis (4-amino-TEMPO)

have affinity for gold surfaces with binding occurring either via an amino group or a nitroxide radical.

5.6 References

(1) Shaik, S.; Mandal, D.; Ramanan, R. Oriented electric fields as future smart reagents in chemistry. *Nat. Chem.* **2016,** *8*, 1091-1098.

(2) Warshel, A. Electrostatic origin of the catalytic power of enzymes and the role of preorganized active sites. *J. Biol. Chem.* **1998,** *273*, 27035-27038.

(3) Shaik, S.; Shurki, A. Valence bond diagrams and chemical reactivity. *Angew. Chem. Int. Ed.* **1999,** *38*, 586-625.

(4) Sola, M.; Lledos, A.; Duran, M.; Bertran, J.; Abboud, J. L. M. Analysis of solvent effects on the Menshutkin reaction. *J. Am. Chem. Soc.* **1991,** *113*, 2873-2879.

(5) Fried, S. D.; Bagchi, S.; Boxer, S. G. Extreme electric fields power catalysis in the active site of ketosteroid isomerase. *Science* **2014,** *346*, 1510-1514.

(6) Aragonès, A. C.; Haworth, N. L.; Darwish, N.; Ciampi, S.; Bloomfield, N. J.; Wallace, G. G.; Diez-Perez, I.; Coote, M. L. Electrostatic catalysis of a Diels–Alder reaction. *Nature* **2016,** *531*, 88-91.

(7) Geng, C.; Li, J.; Weiske, T.; Schlangen, M.; Shaik, S.; Schwarz, H. Electrostatic and charge-induced methane activation by a concerted double C-H bond insertion. *J. Am. Chem. Soc.* **2017,** *139*, 1684-1689.

(8) Parsegian, A. Energy of an ion crossing a low dielectric membrane: solutions to four relevant electrostatic problems. *Nature* **1969,** *221*, 844-846.

(9) Warshel, A.; Levitt, M. Theoretical studies of enzymic reactions: dielectric, electrostatic and steric stabilization of the carbonium ion in the reaction of lysozyme. *J. Mol. Biol.* **1976,** *103*, 227-249.

(10) Novotny, J.; Sharp, K. Electrostatic fields in antibodies and antibody/antigen complexes. *Prog. Biophys. Mol. Biol.* **1992,** *58*, 203-224.

(11) Fried, S. D.; Bagchi, S.; Boxer, S. G. Measuring electrostatic fields in both hydrogen-bonding and non-hydrogen-bonding environments using carbonyl vibrational probes. *J. Am. Chem. Soc.* **2013,** *135*, 11181-11192.

(12) Simon, M. L. A.; Platre, M. P.; Marquèsbueno, M. M.; Armengot, L.; Stanislas, T.; Bayle, V.; Caillaud, M.; Jaillais, Y. A PI4P-driven electrostatic field controls cell membrane identity and signaling in plants. *Nat. Plants* **2016,** *2*, 16089-16123.

(13) Stein, D.; Kruithof, M.; Dekker, C. Surface-charge-governed ion transport in nanofluidic channels. *Phys. Rev. Lett.* **2004,** *93*, 035901-035904.

(14) Feng, J.; Graf, M.; Liu, K.; Ovchinnikov, D.; Dumcenco, D.; Heiranian, M.; Nandigana, V.; Aluru, N. R.; Kis, A.; Radenovic, A. Single-layer MoS_2 nanopores as nanopower generators. *Nature* **2016,** *536*, 197.

(15) Pocker, Y.; Buchholz, R. F. Electrostatic catalysis of ionic aggregates. I. Ionization and dissociation of trityl chloride and hydrogen chloride in lithium perchlorate-diethyl ether solutions. *J. Am. Chem. Soc.* **1970,** *92*, 2075-2084.

(16) Warshel, A. Electrostatic basis of structure-function correlation in proteins. *Acc. Chem. Res.* **1981,** *14*, 284-290.

(17) Shaik, S. What happens to molecules as they react? A valence bond approach to reactivity. *J. Am. Chem. Soc.* **1981,** *103*, 3692-3701.

(18) Shaik, S.; Danovich, D.; Wu, W.; Hiberty, P. C. Charge-shift bonding and its manifestations in chemistry. *Nat. Chem.* **2009,** *1*, 443.

(19) Gryn'ova, G.; Marshall, D. L.; Blanksby, S. J.; Coote, M. L. Switching radical stability by pH-induced orbital conversion. *Nat. Chem.* **2013,** *5*, 474-481.

(20) Gorin, C. F.; Beh, E. S.; Kanan, M. W. An electric field–induced change in the selectivity of a metal oxide–catalyzed epoxide rearrangement. *J. Am. Chem. Soc.* **2011,** *134*, 186-189.

(21) Akamatsu, M.; Sakai, N.; Matile, S. Electric-field-assisted anion-π catalysis. *J. Am. Chem. Soc.* **2017,** *139*, 6558-6561.

(22) Klinska, M.; Smith, L. M.; Gryn'ova, G.; Banwell, M. G.; Coote, M. L. Experimental demonstration of pH-dependent electrostatic catalysis of radical reactions. *Chem. Sci.* **2015,** *6*, 5623-5627.

(23) Gryn'ova, G.; Coote, M. L. Origin and scope of long-range stabilizing interactions and associated SOMO–HOMO conversion in distonic radical anions. *J. Am. Chem. Soc.* **2013,** *135*, 15392-15403.

(24) Gryn'ova, G.; Smith, L. M.; Coote, M. L. Computational design of pH-switchable control agents for nitroxide mediated polymerization. *Phys. Chem. Chem. Phys.* **2017,** *19*, 22678-22683.

(25) Zhang, L.; Laborda, E.; Darwish, N.; Noble, B. B.; Tyrell, J. H.; Pluczyk, S.; Le Brun, A. P.; Wallace, G. G.; Gonzalez, J.; Coote, M. L. Electrochemical and electrostatic cleavage of alkoxyamines. *J. Am. Chem. Soc.* **2017,** *140*, 766-744.

(26) Danko, M.; Szabo, E.; Hrdlovic, P. Synthesis and spectral characteristics of fluorescent dyes based on coumarin fluorophore and hindered amine stabilizer in solution and polymer matrices. *Dyes Pigments* **2011,** *90*, 129-138.

(27) Frisch, M. J.; Trucks, G. W.; Schegel, H. B.; Scuseria, G. E.; Robb, M. A.; Cheeseman, J. R.; Scalmani, G.; Barone, V.; Mennucci, B.; Petersson, G. A.; Nakatsuji, H.; Caricato, M.; Li, X.; Hratchian, H. P.; Izmaylov, A. F.; Bloino, J.; Zheng, G.; Sonnenberg, J. L.; Hada, M.; Ehara, M.; Toyota, K.; Fukuda, R.; Hasegawa, J.; Ishida, M.; Nakajima, T.; Honda, Y.; Kitao, O.; Nakai, H.; Vreven, T.; Montgomery, J. A.; Jr. Peralta, J. E.; Ogliaro, F.; Bearpark, M.; Heyd, J. J.; Brothers, E.; Kudin, K. N.; Staroverov, V. N.; Keith, T.; Kobayashi, R.; Normand, J.; Raghavachari, K.; Rendell, A.; Burant, J. C.; Iyengar, S. S.; Tomasi, J.; Cossi, M.; Rega, N.; Millam, J. M.; Klene, M.; Knox, J. E.; Cross, J. B.; Bakken, V.; Adamo, C.; Jaramillo, J.; Gomperts, R.; Stratmann, R. E.; Yazyev, O.; Austin, A. J.; Cammi, R.; Pomelli, C.; Ochterski, J. W.; Martin, R. L.; Morokuma, K.; Zakrzewski, V. G.; Voth, G. A.; Salvador, P.; Dannenberg, J. J.; Dapprich, S.; Daniels, A. D.; Farkas, O.; Foresman, J. B.; Ortiz, J. V.; Cioslowski, J.; Fox, D. J. *Gaussian 09, revision E.01* **2009**, Gaussian, Inc., Wallingford CT.

(28) Xu, B.; Tao, N. J. Measurement of single-molecule resistance by repeated formation of molecular junctions. *Science* **2003,** *301*, 1221-1223.

(29) Chen, F.; Hihath, J.; Huang, Z.; Li, X.; Tao, N. Measurement of single-molecule conductance. *Annu. Rev. Phys. Chem.* **2007,** *58*, 535-564.

(30) Tao, N. J. Electron transport in molecular junctions. *Nat. Nanotechnol.* **2006,** *1*, 173-181.

(31) Krukowski, P.; Kowalczyk, P. J.; Krzyczmonik, P.; Olejniczak, W.; Klusek, Z.; Puchalski, M.; Gwozdzinski, K. Electrochemical behaviour of gold modified with

contaminated TMP amine adlayers studied by STM, CV, EPR. *Appl. Surf. Sci.* **2009,** *255*, 3946-3952.

(32) Swiech, O.; Hrynkiewicz-Sudnik, N.; Palys, B.; Kaim, A.; Bilewicz, R. Gold nanoparticles tethered to gold surfaces using nitroxyl radicals. *J. Phys, Chem. C* **2011,** *115*, 7347-7354.

(33) Tsuchimoto, T.; Tobita, K.; Hiyama, T.; Fukuzawa, S.-i. Scandium (III) triflate-catalyzed Friedel-Crafts alkylation reactions. *J. Org. Chem.* **1997,** *62*, 6997-7005.

(34) Noji, M.; Ohno, T.; Fuji, K.; Futaba, N.; Tajima, H.; Ishii, K. Secondary benzylation using benzyl alcohols catalyzed by lanthanoid, scandium, and hafnium triflate. *J. Org. Chem.* **2003,** *68*, 9340-9347.

(35) Xiang, L.; Tao, N. Organic chemistry: reactions triggered electrically. *Nature* **2016,** *531*, 38.

(36) Lai, W.; Chen, H.; Cho, K. B.; Shaik, S. External electric field can control the catalytic cycle of Cytochrome P450cam: A QM/MM study. *J. Phys, Chem. Lett.* **2010,** *1*, 2082-2087.

(37) Meir, R.; Chen, H.; Lai, W.; Shaik, S. Oriented electric fields accelerate Diels−Alder reactions and control the endo/exo selectivity. *ChemPhysChem* **2010,** *11*, 301-310.

Chapter 6 Switchable Interfaces: Redox Monolayers on Si(100) by Electrochemical Trapping of Alcohol Nucleophiles

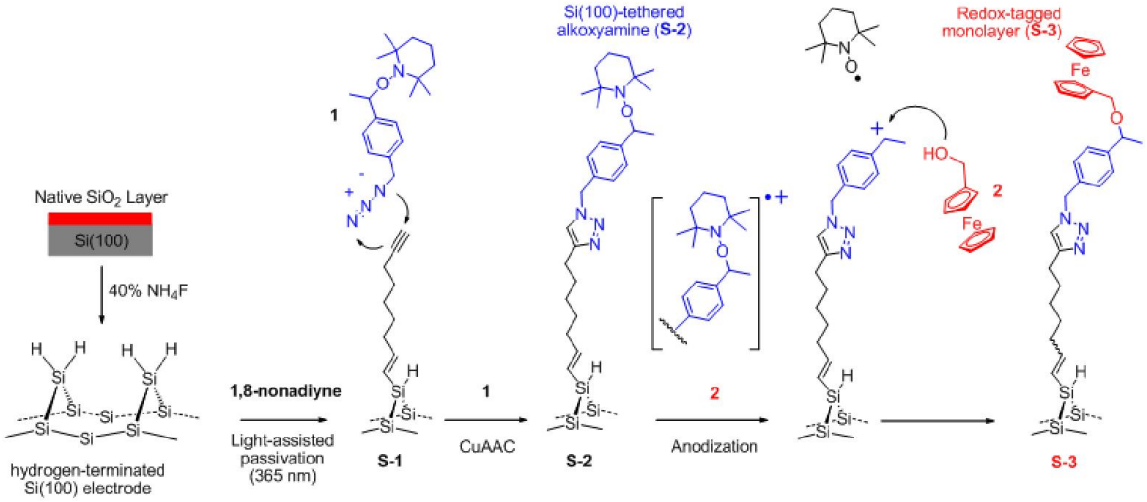

6.1 Abstract

Organic electrosynthesis is going through its renaissance but its scope in surface science as a tool to introduce specific molecular signatures at an electrode/electrolyte interface is under explored. Here we have investigated an electrochemical approach to generate *in situ* surface-tethered and highly-reactive carbocations. We have covalently attached an alkoxyamine derivative on a Si(100) electrode and used an anodic bias stimulus to trigger its fragmentation into a diffusive nitroxide (TEMPO) and a surface-confined carbocation. As a proof-of-principle we have used this reactive intermediate to trap a nucleophile dissolved in the electrolyte. The nucleophile was ferrocenemethanol and its presence and surface concentration after its reaction with the carbocation were assessed by cyclic voltammetry. The work expands the repertoire of available electrosynthetic methods and could in principle lay the foundation to a new form of electrochemical lithography.

6.2 Introduction

Synthetic organic electrochemistry traces its origin back to the work of Faraday and Kolbe and its green credentials are currently prompting a renaissance.[1-3] Chemical reactions that are coupled to the flow of electricity allow, for instance, chemists to generate unstable intermediates *in situ*, to control very precisely and accurately the supply of reactants, and to monitor reaction processes in real-time.[4] While the large majority of the work on synthetic electrochemistry has focused on bulk synthesis,[5, 6] there are also a strong motivation to expand electrochemical synthetic methods toward the chemical modification of interfaces.[7-10] Addressing the molecular details of a surface,[11] especially those of semiconductors, has been central to the development of fields such as molecular electronics[12], sensing[13], energy conversion[14] and cell biology[15]. Semiconductor electrodes, and in particular silicon electrodes, have the advantage of being readily available in a crystalline form, they have unique photo-electrochemical properties and can form strong covalently-bound monolayers.[16] Silicon like all non-oxide semiconductors is thermodynamically unstable and especially under anodic polarization in aqueous environments tends to grow an electrically-insulating silica

layer.[17-18] A common laboratory approach to attach covalently organic molecules on silicon substrates is a three-step wet chemical process. Removal of the native silica layer with fluoride-containing solutions is followed by chemical passivation[19] of the hydrogen-terminated silicon surface by means of hydrosilylation of terminal alkenes or alkynes[20-22] and finally chemical derivatization of the aliphatic monolayer[16]. In this work we seek to expand the chemical repertoires of this last step and explore the synthetic scope of reactive carbocations in the context of surface chemistry. There are several methods to generate carbocations in solution[23] but few examples are available for electrochemical generation of carbocations at electrodes. We have recently reported on the putative generation of carbocations at metallic electrodes after the fragmentation of anodic intermediates of alkoxyamines. Alkoxyamines are heat-labile molecules, widely used as an *in situ* source of nitroxides in polymer and materials sciences. We have shown that the one-electron oxidation of an alkoxyamine leads to an anodic intermediate that rapidly fragments releasing a nitroxide species at room temperature.[24]

In the current work we have developed a surface model system to explore the feasibility of using surface-tethered carbocations to trap solution nucleophiles. The carbocation is electro-generated *in situ* from an alkoxyamine molecule that is exposed at the distal end of an organic monolayer grown on a Si(100) electrode. By means of applying a positive bias to the Si(100) electrode the alkoxyamine is anodically cleaved to release a 2,2,6,6-tetramethylpiperidine-1-oxyl (TEMPO) molecule and generate a surface-confined carbocation species. The latter is attacked by electron donors via nucleophilic substitutions. As proof-of-principle we have prepared redox-active monolayers by generating the surface carbocations in the presence of ferrocene methanol (**2**) molecules. This study shows how an electric potential can be used to manipulate geometry of surface bound molecules, that is, one is able to switch a surface from thermal/light-liable (*i.e.*, alkoxyamine monolayers) to ferrocene (Fc) terminated monolayers.

6.3 Materials and methods

6.3.1 Chemicals

All chemicals, unless specified otherwise, were of analytical grade and used as received.

Milli-Q™ water (> 18 MΩ cm) was used to prepare solutions and to clean all glassware. Anhydrous solvents used in chemical reactions were purified under nitrogen by a solvent drying system from LC Technology Solutions Inc. Dichloromethane (DCM), methanol (MeOH) and 2-propanol were redistilled prior to use. Hydrogen peroxide (30 wt.% in water), ammonium fluoride (Puranal^{TM}, 40 wt.% in water) and sulfuric acid (Puranal^{TM}, 95-97%) were used to clean the wafers and were of semiconductor grade. 1,8-nonadiyne (Sigma-Aldrich, 98%) was redistilled from sodium borohydride (Sigma-Aldrich, 99+%) under reduced pressure (80 °C, 10−12 Torr) and stored under a high purity argon atmosphere prior to use. Tetrabutylammonium hexafluorophosphate salt (Bu_4NPF_6, Sigma-Aldrich, ≥98%) was used as supporting electrolyte. 4-Vinylbenzyl chloride (90%), ammonium sulfite, ferrocene (98%), ferrocenemethanol (**2**, 97%) and 2,2,6,6-tetramethylpiperidine-1-oxyl (TEMPO hereafter, 98%) were purchased from Sigma-Aldrich. The surface reactive (azide-tagged) alkoxyamine 1-(1-(4-azidomethyl)phenyl)ethoxy-2,2,6,6-tetramethylpiperidine (**1**) was synthesized according to minor modification of previously reported procedure (see Scheme 1).[25] Prime grade, single-side polished silicon wafers of 100-orientation (<100> ± 0.5°), p-type (boron-doped) of 100 mm diameter, 500-550 μm thickness, and of a nominal resistivity of 0.001–0.003 Ω cm were obtained from Siltronix, S.A.S. (Archamps, France).

6.3.2 Synthetic methods

Thin-layer chromatography (TLC) was performed on silica gel Merck aluminum sheets (60 F_{254}). Merck 60 Å silica gel (220−400 mesh particle size) was used for column chromatography. Nuclear magnetic resonance (NMR) spectra were recorded on a Bruker Avance 400 spectrometer in deuterated dimethyl sulfoxide (d-DMSO) using the residual solvent signal as internal reference. High-resolution mass spectral data (HRMS, mass accuracy 2-4 ppm) of alkoxyamine **1** were obtained using a Waters Xevo QTof MS via ESI experiments and infusing the sample at 8 μL/min.

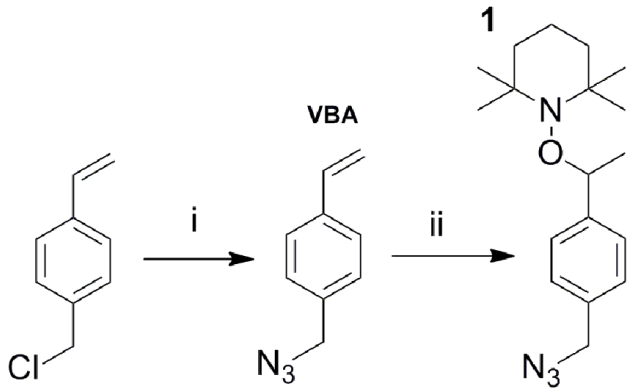

Scheme 6.1 Synthesis of the azide-tagged alkoxyamine **1**. i. NaN_3, DMF, 82%. ii. $Mn(OAc)_3•2H_2O$, $NaBH_4$, Toluene/EtOH, 50%.

*Synthesis of 4-Vinylbenzyl azide (**VBA**)*. Sodium azide (1.30 g, 20 mmol) was added in one-portion to a stirred solution of 4-vinylbenzyl chloride (1.53 g, 10 mmol) in *N*,*N*-dimethylformamide (DMF, 20 mL). The reaction mixture was stirred at room temperature for 12 h under argon then poured into a large excess water (100 mL). The mixture was extracted with DCM (3 × 50 mL). The combined organic layers were then washed with brine (2 × 100 mL), dried over $MgSO_4$, filtered and dried under vacuum to afford the crude title compound as a brown oily residue. The crude material was purified by silica gel column chromatography (hexane) to give **VBA** as a light yellow oil (1.31 g, 82%). ^{1}H NMR (400 MHz, d-DMSO): δ 7.50 p.p.m. (d, Ar-H, J = 8.12 Hz, 2H), 7.35 (d, Ar-H, J = 8.04 Hz, 2H), 6.74 (dd, Ar-CH=CH_2, J = 17.66 Hz, 1H), 5.85 (dd, Ar-CH=CH_2, J = 17.68 Hz, 0.96 Hz, 1H), 5.28 (dd, Ar-CH=CH_2, J = 11.84 Hz, 0.92 Hz, 1H), 4.43 (s, Ar-CH_2-N_3, 2H); ^{13}C NMR (100 MHz, d-DMSO): δ 136.96, 136.11, 135.13, 128.69, 126.39, 114.64, 53.32.

*Synthesis of 1-(1-(4-Azidomethyl) phenyl)ethoxy-2,2,6,6-tetramethylpiperidine (**1**)*. Alkoxyamine **1** was synthesized from **VBA** via the following procedure. To an ice-cold solution of TEMPO (0.31g, 2 mmol) in toluene/ethanol (60 mL, 1:1, v/v) **VBA** (3.20g, 20 mmol) and $Mn(OAc)_3•2H_2O$ (5.36 g, 20 mmol) were added in one portion while stirring in air. Stirring was continued for one min and then a 15-fold molar excess (with respect to TEMPO) of $NaBH_4$ was added in portions over 15 min. After stirring overnight under nitrogen atmosphere, the residue was isolated by filtration, the filtrate was suspended in water and the aqueous solution was then extracted three times with

DCM. The combined organic layers were evaporated under vaccum and the crude material was purified by silica gel column chromatography (ethyl acetate/hexane, 1:40, v/v) to yield alkoxyamine **1** as a colorless oil liquid (0.32 g, 50%).

^{1}H NMR (400 MHz, d-DMSO): δ 7.36-7.29 p.p.m. (m, Ar-H, 4H), 4.75 (q, NO-CH-Ar, J = 13.50 Hz, 1H), 4.42 (s, N_3-CH_2-Ar, 2H), 1.54-1.38 (m, 6H), 1.37-1.19 (m, 6H), 1.12 (s, 3H), 0.97 (s, 3H), 0.57 (s, 3H); ^{13}C NMR (100 MHz, d-DMSO): δ 145.08, 134.08, 128.21, 126.76, 82.09, 59.22, 58.98, 53.40, 33.99, 33.76, 23.00, 20.04, 16.66; HRMS (1, m/z): $[M+H]^+$ calcd for $C_{18}H_{29}N_4O$ 317.2336, found 317.2335.

6.3.3 Surface modification

6.3.3.1 Light-assisted hydrosilylation of 1,8-nonadiyne on Si(100)

The assembly of the acetylenylated Si(100) surface by covalent attachment of 1,8-nonadiyne on hydrogen-terminated silicon is based on a photochemical hydrosilylation method.[26] In brief, silicon wafers were mechanically cut into pieces (approximately 10 × 10 mm in size), rinsed several times with small portions of DCM, MeOH and Milli-Q™ water. The samples were then immersed in hot Piranha solution (100 °C, a 3:1 (v/v) mixture of concentrated sulfuric acid to 30% hydrogen peroxide, **Caution: piranha solution reacts violently with organic substances**) for 20 min. The samples were then rinsed with water and immediately etched with a deoxygenated 40% aqueous ammonium fluoride solution for 5 min under a stream of argon. A small amount (*ca*. 5 mg) of ammonium sulfite was added to the etching bath for building an anaerobic environment and hence avoiding the *in situ* oxidation of the hydrogen-terminated silicon. The freshly etched samples were washed sequentially with Milli-Q™ water and DCM and blown dry with argon before dropping a small deoxygenated sample of 1,8-nonadiyne (approximate 50 μL) on the hydrogen-terminated wafer and covering it with a quartz slide to minimize evaporation. The wafer was then rapidly transferred to an air-tight UV reaction chamber and kept under positive argon pressure. A collimated LED source (λ = 365 nm, nominal power output > 190 mW, Thorlabs part M365L2 coupled to a SM1P25-A collimator adapter) was fixed over the sample at a distance of about 10 cm. After illumination for a 2 h period, the resulting acetylene-functionalized

sample (**S-1**, Scheme 2) was removed from the reaction chamber, rinsed several times with DCM and rested for 12 h in a sealed vial at +4 °C under DCM before being further reacted with alkoxyamine **1**.

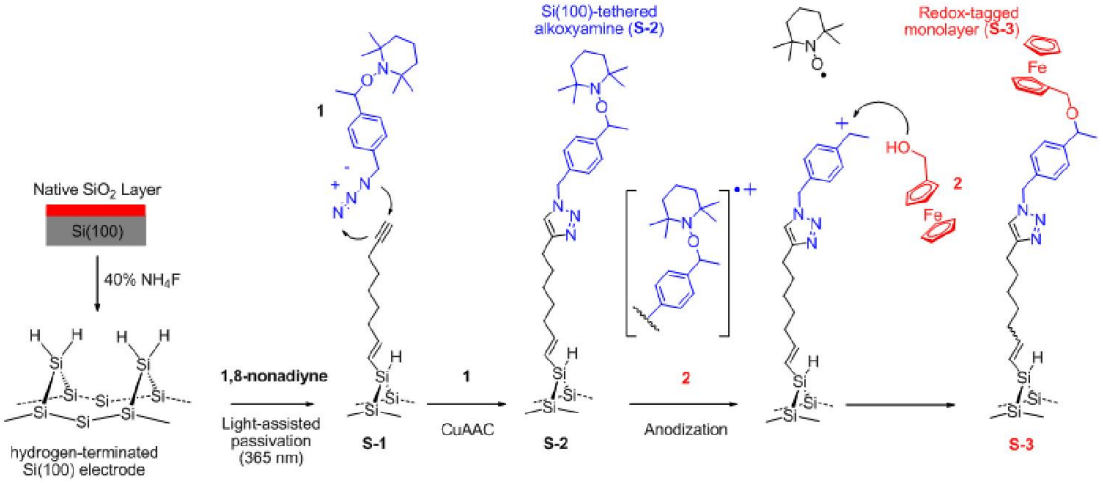

Scheme 6.2 Light-assisted (365 nm) hydrosilylation of 1,8-nonadiyne to passivate an hydrogen-terminated Si(100) surface (**S-1**) and covalent attachment of alkoxyamine **1** via CuAAC "click" reactions to yield an alkoxyamine monolayer (**S-2**). Anodization of **S-2** in the presence of the alcohol nucleophile **2** leads to release of TEMPO in the electrolyte with formation of a redox-active monolayer (**S-3**) by reaction of **2** with the putative surface-tethered carbocation intermediate.

6.3.3.2 Click immobilization of alkoxyamine 1

Surface **S-1** was reacted with molecule **1** to yield the alkoxyamine monolayers (**S-2**) via a copper(I)-catalyzed "click" alkyne-azide cycloaddition (CuAAC) reaction. In brief, to a reaction vial containing the alkyne-functionalized silicon surface (**S-1**) was added (i) the azide (alkoxyamine **1**, 0.5×10^{-3} M, 2-propanol/water, 1:1, v/v), (ii) copper(II) sulfate pentahydrate (1.0×10^{-4} M) and (iii) sodium ascorbate (5 mg/mL). The reaction was carried out without excluding air from the reaction environment, at room temperature and under ambient light. The samples were removed from the reaction vessel after a reaction time of 2 h and were rinsed thoroughly with copious amounts of 2-propanol, water, 2-propanol and DCM and blown dry with argon before being analyzed or further reacted (Scheme 2).

6.3.4 Surface characterization

6.3.4.1 X-ray photoelectron spectroscopy

X-ray photoelectron spectroscopy (XPS) characterization was performed on an ESCALab 250 Xi (Thermo Scientific) spectrometer with a monochromated Al Kα source to characterize the formation of an alkoxyamine **1** monolayer on silicon. The pressure in the analysis chamber during measurement was $<10^{-8}$ mbar. The pass energy and step size for narrow scans were 20 eV and 0.1 eV respectively, with a take-off angle normal to the sample surface. Spectral analysis was performed using Avantage 4.73 software and curve fitting was carried out with a mixture of Gaussian–Lorentzian functions after background subtraction. Peaks were calibrated to C–C at 284.8 eV.

6.3.4.2 Electrochemical measurements

Electrochemical experiments were performed in a single-compartment, three-electrode PTFE cell with the modified silicon surface as the working electrode, a platinum mesh (*ca*. 200 mm^2) as the counter electrode, and silver/silver chloride "leakless" electrode in 3 M sodium chloride as the reference electrode. A rectilinear cross-section gasket defined the geometric area of the working electrode to 28 mm^2. Electrical contact between the silicon substrate and a copper plate was ensured by rapidly rubbing a gallium indium eutectic onto the back of the silicon electrode. Cyclic voltammetry (CV) measurements were performed using a CHI 910B electrochemical analyzer. All potentials are reported versus the reference electrode. Tetrabutylammonium hexafluorophosphate (Bu_4NPF_6, Sigma-Aldrich, ≥98%) was recrystallized twice from 2-propanol and used at the concentration of 1.0×10^{-1} M as the supporting electrolyte in DCM solutions. The reaction between the anodically-cleaved **S-2** samples and ferrocenemethanol (**2**), as well as control experiments were **2** is replaced by ferrocene, were performed under argon and at room temperature. **S-3** samples (Scheme 2) were thoroughly washed with DCM prior to analysis. Cyclic voltammetry of **S-3** samples was performed under ambient conditions in aqueous 1.0 M $HClO_4$ electrolytes.

6.4 Results and discussions

As a proof-of-principle, we have devised "trapping" experiments on an electrode surface modified by alkoxyamine **1** (**S-2**, Scheme 2). The anodization of the **S-2** monolayers is expected to generate benzylic cations tethered on the electrode surface while the nitroxide fragment is released into the electrolyte. The covalent attachment of alkoxyamine **1** to the silicon surface was first verified by the XPS (Figure 6.1). Peaks at 99.3 and 100.0 eV for **S-2** samples were respectively ascribed to the Si $2p_{3/2}$ and Si $2p_{1/2}$ emissions (Figure 6.1b). The presence of a band at 101.1–104.3 eV is due to SiO_x formed during the hydrosilylation and/or CuAAC processes. Two signals in the carbon envelope that are centered at 284.6 and 286.3 eV indicates the formation of C–C and C–O/–N, respectively,[27] as expected for the putative structure of **S-2** samples (Figure 6.1c). As shown in Figure 6.1d, refinement of the N 1s emission gives two fitted peaks with binding energies of 400.5 and 401.7 eV in an approximate 3:1 ratio. The position of the low binding energy line in the **S-2** samples is in agreement with the 400.6 eV previously assigned to nitroxide nitrogen atoms in thin films.[22] Electrons from the triazole heterocycle also contributed to the 400.5 and 401.7 emissions with an expected 2:1 ratio.

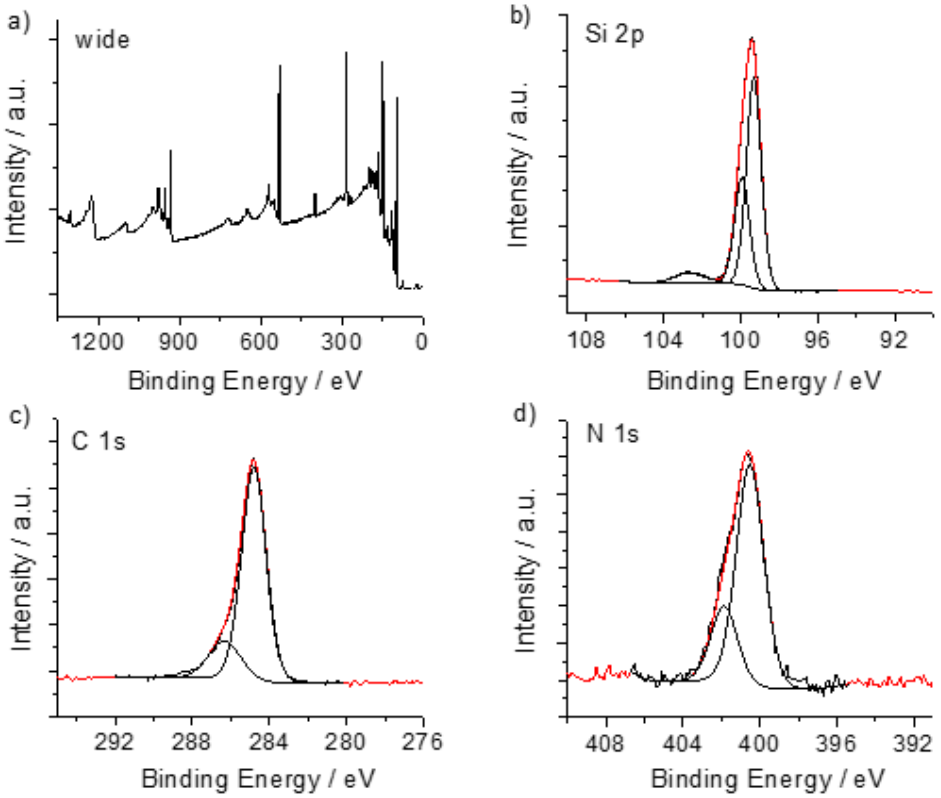

Figure 6.1 XPS survey spectra and high-resolution Si 2p, C 1s, and N 1s scans of **S-2** samples assembled on high-doped p-type Si(100) surface by CuAAC reactions between alkoxyamine **1** and alkyne-terminated monolayers (**S-1**)

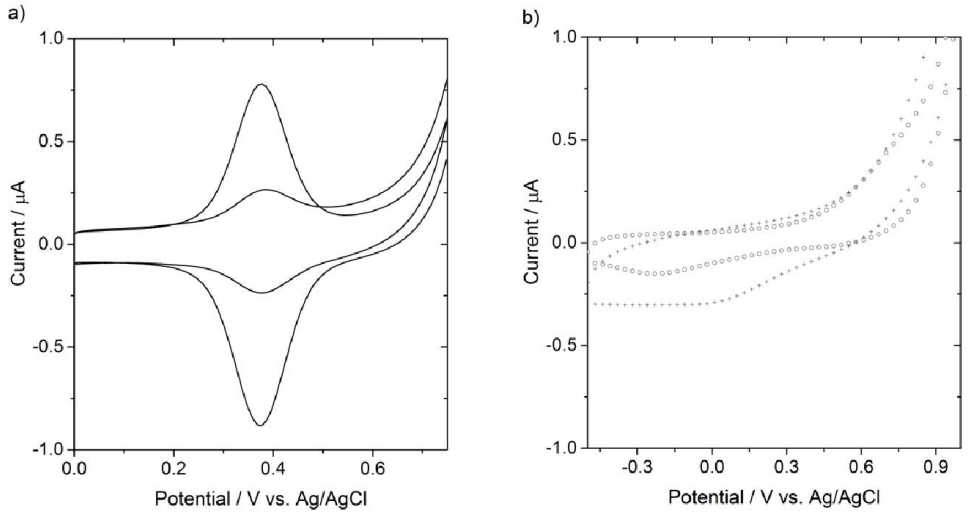

Figure 6.2 Cyclic voltammograms (CVs) of redox nucleophiles reacted with the anodized alkoxyamines monolayer (conversion of **S-2** into **S-3**). CVs were acquired at a voltage sweep rate of 100 mV s^{-1}. (a) CVs analysis of the Si(100) electrode in 1.0 M $HClO_4$ after the anodization of **S-2** monolayers in the presence of ferrocene methanol (**2**) with the surface coverage of ferrocene units ranging from 5.5×10^{-12} mol cm^{-2}, as the low end, up to the value of 3.1×10^{-11} mol cm^{-2}. (b) Control experiments for prolonged standing of **S-2** electrodes at open circuit potential in the presence of **2** at (○) or CVs for the experiments as in (a) but with ferrocene replacing **2** (+).

As shown Figure 2, the anodization of the alkoxyamine monolayer (**S-2**) via a potentiostatic experiment (electrode held at 1.0 V vs reference for 30 s) in 1.0×10^{-1} M DCM/Bu_4NPF_6 in the presence of an excess of **2** is effective in trapping the alcohol at the distal end of the monolayer. The newly-formed redox-active surface (**S-3**) is washed with copious DCM and then analyzed by cyclic voltammetry in an electrolyte that does not contain a redox-active species. Figure 2a shows the well-defined pair of redox waves (solid red lines) which are ascribed to the surface-confined redox tag (**S-3**). The surface coverage of ferrocenyl units, derived from integration of the anodic wave, ranges over almost on order of magnitude from 5.5×10^{-12} mol cm^{-2}, as the low end, up to the value of 3.1×10^{-11} mol cm^{-2} for our highest current yield. Our best result is still only about 10% of close-packed packed layer of redox ferrocenes; defining the exact nature of any competitive side-reactions is beyond the scope of this work. Two control experiments were carried out as follows. We used ferrocene, which lacks the hydroxyl function, to rule out non-specific adsorption of the redox probe as well as trying to remove the anodic step. That is, the working electrode modified bearing the alkoxyamine **1** is rested at open circuit potential (OCP) conditions in the presence of the nucleophile (**2)**. In both controls (Figure 2b) we found no evidence of redox peaks when either the nucleophile is removed from the system (+, Figure 2b) or when the **S-2** surface is not anodized to trigger the switch masked alkoxyamine/reactive carbocation (○, Figure 2b).

6.5 Conclusions

We have demonstrated a method to achieve a switchable interface – from unreactive to electrophilic – and used it to attach alcohol species as monolayers on Si(100) electrodes. Unlike conventional esterification approaches on surfaces (e.g. DCC/DMAP), here we show an electrochemical alternative that involves a surface carbocation. This reactive intermediate is generated *in situ* under an external potential stimulus that switches a stable alkoxyamine into a reactive surface trap for nucleophiles. This proof-of-principle expands to the realm of surfaces some of the recent advances made in synthetic organic electrochemistry. This knowledge may aid the development of cationic polymerization

on surfaces and this surface chemistry platform can in principle be coupled to photo-electrochemical reactions on semiconductors and photoconductors[26] in order to control electron transfer, hence chemical reactivity, in two dimensions.[28, 29]

6.5 References

(1) Horn, E. J.; Rosen, B. R.; Baran, P. S., Synthetic organic electrochemistry: an enabling and innately sustainable method. *ACS Cent. Sci.* **2016**, *2*, 302-308.

(2) Yan, M.; Kawamata, Y.; Baran, P. S., Synthetic organic electrochemical methods since 2000: on the verge of a renaissance. *Chem. Rev.* **2017**, *117*, 13230-13319.

(3) Yan, M.; Kawamata, Y.; Baran, P. S., Synthetic organic electrochemistry: calling all engineers. *Angew. Chem., Int. Ed.* **2018**, *57*, 4149-4155.

(4) Frontana-Uribe, B. A.; Little, R. D.; Ibanez, J. G.; Palma, A.; Vasquez-Medrano, R., Organic electrosynthesis: a promising green methodology in organic chemistry. *Green Chem.* **2010**, *12*, 2099-2119.

(5) Gütz, C.; Selt, M.; Bänziger, M.; Bucher, C.; Römelt, C.; Hecken, N.; Gallou, F.; Galvão, T. R.; Waldvogel, S. R., A novel cathode material for cathodic dehalogenation of 1, 1-dibromo cyclopropane derivatives. *Chem. - Eur. J.* **2015**, *21*, 13878-13882.

(6) Gütz, C.; Bänziger, M.; Bucher, C.; Galvão, T. s. R.; Waldvogel, S. R., Development and scale-up of the electrochemical dehalogenation for the synthesis of a key intermediate for NS5A inhibitors. *Org. Process Res. Dev.* **2015**, *19*, 1428-1433.

(7) Andrieux, C. P.; Gonzalez, F.; Savéant, J.-M., Derivatization of carbon surfaces by anodic oxidation of arylacetates. Electrochemical manipulation of the grafted films. *J. Am. Chem. Soc.* **1997**, *119*, 4292-4300.

(8) Robins, E.; Stewart, M.; Buriak, J., Anodic and cathodic electrografting of alkynes on porous silicon. *Chem. Commun.* **1999**, 2479-2480.

(9) Hurley, P. T.; Ribbe, A. E.; Buriak, J. M., Nanopatterning of alkynes on hydrogen-terminated silicon surfaces by scanning probe-induced cathodic electrografting. *J. Am. Chem. Soc.* **2003**, *125*, 11334-11339.

(10) Belanger, D.; Pinson, J., Electrografting: a powerful method for surface modification. *Chem. Soc. Rev.* **2011**, *40*, 3995-4048.

(11) Gooding, J. J.; Ciampi, S., The molecular level modification of surfaces: from self-assembled monolayers to complex molecular assemblies. *Chem. Soc. Rev.* **2011**, *40*, 2704-2718.

(12) Aragonès, A. C.; Darwish, N.; Ciampi, S.; Sanz, F.; Gooding, J. J.; Díez-Pérez, I., Single-molecule electrical contacts on silicon electrodes under ambient conditions. *Nat. Commun.* **2017**, *8*, 15056-15063.

(13) Scheres, L.; ter Maat, J.; Giesbers, M.; Zuilhof, H., Microcontact printing onto oxide-free silicon via highly reactive acid fluoride-functionalized monolayers. *Small* **2010**, *6*, 642-650.

(14) Bard, A. J.; Bocarsly, A. B.; Fan, F. R. F.; Walton, E. G.; Wrighton, M. S., The concept of Fermi level pinning at semiconductor/liquid junctions. Consequences for energy conversion efficiency and selection of useful solution redox couples in solar devices. *J. Am. Chem. Soc.* **1980**, *102*, 3671-3677.

(15) Ciampi, S.; James, M.; Le Saux, G.; Gaus, K.; Justin Gooding, J., Electrochemical "switching" of Si(100) modular assemblies. *J. Am. Chem. Soc.* **2012**, *134*, 844-847.

(16) Ciampi, S.; Harper, J. B.; Gooding, J. J., Wet chemical routes to the assembly of organic monolayers on silicon surfaces via the formation of Si−C bonds: surface preparation, passivation and functionalization. *Chem. Soc. Rev.* **2010**, *39*, 2158-2183.

(17) Ciampi, S.; Eggers, P. K.; Le Saux, G.; James, M.; Harper, J. B.; Gooding, J. J., Silicon (100) Electrodes resistant to oxidation in aqueous solutions: an unexpected benefit of surface acetylene moieties. *Langmuir* **2009**, *25*, 2530-2539.

(18) Noufi, R.; Frank, A. J.; Nozik, A. J., Stabilization of n-type silicon photoelectrodes to surface oxidation in aqueous electrolyte solution and mediation of oxidation reaction by surface-attached organic conducting polymer. *J. Am. Chem. Soc.* **1981**, *103*, 1849-1850.

(19) Nemanick, E. J.; Hurley, P. T.; Webb, L. J.; Knapp, D. W.; Michalak, D. J.; Brunschwig, B. S.; Lewis, N. S., Chemical and electrical passivation of single-crystal silicon(100) surfaces through a two-step chlorination/alkylation process. *J. Phys. Chem. B* **2006**, *110*, 14770-14778.

(20) Linford, M. R.; Chidsey, C. E. D., Alkyl monolayers covalently bonded to silicon

surfaces. *J. Am. Chem. Soc.* **1993**, *115*, 12631-12632.

(21) Sun, Q.-Y.; de Smet, L. C. P. M.; van Lagen, B.; Wright, A.; Zuilhof, H.; Sudhöelter, E. J. R., Covalently attached monolayers on hydrogen-terminated Si(100): extremely mild attachment by visible light. *Angew. Chem., Int. Ed.* **2004**, *43*, 1352-1355.

(22) Zhang, L.; Vogel, Y. B.; Noble, B. B.; Gonçales, V. R.; Darwish, N.; Brun, A. L.; Gooding, J. J.; Wallace, G. G.; Coote, M. L.; Ciampi, S., TEMPO monolayers on Si(100) electrodes: electrostatic effects by the electrolyte and semiconductor space-charge on the electroactivity of a persistent radical. *J. Am. Chem. Soc.* **2016**, *138*, 9611-9619.

(23) Yoshida, J.-i.; Kataoka, K.; Horcajada, R.; Aiichiro Nagaki, Modern strategies in electroorganic synthesis. *Chem. Rev.* **2008**, *108*, 2265-2299.

(24) Zhang, L.; Laborda, E.; Darwish, N.; Noble, B. B.; Tyrell, J. H.; Pluczyk, S.; Le Brun, A. P.; Wallace, G. G.; Gonzalez, J.; Coote, M. L., Electrochemical and electrostatic cleavage of alkoxyamines. *J. Am. Chem. Soc.* **2018**, *140*, 766-774.

(25) Danko, M.; Szabo, E.; Hrdlovic, P., Synthesis and spectral characteristics of fluorescent dyes based on coumarin fluorophore and hindered amine stabilizer in solution and polymer matrices. *Dyes Pigm.* **2011**, *90*, 129-138.

(26) Vogel, Y. B.; Zhang, L.; Darwish, N.; Gonçales, V. R.; Le Brun, A.; Gooding, J. J.; Molina, A.; Wallace, G. G.; Coote, M. L.; Gonzalez, J., Reproducible flaws unveil electrostatic aspects of semiconductor electrochemistry. *Nat. Commun.* **2017**, *8*, 2066.

(27) Ciampi, S.; Böcking, T.; Kilian, K. A.; James, M.; Harper, J. B.; Gooding, J. J., Functionalization of acetylene-terminated monolayers on Si(100) surfaces: a click chemistry approach. *Langmuir* **2007**, *23*, 9320-9329.

(28) Choudhury, M. H.; Ciampi, S.; Yang, Y.; Tavallaie, R.; Zhu, Y.; Zarei, L.; Gonçales, V. R.; Gooding, J. J., Connecting electrodes with light: one wire, many electrodes. *Chem. Sci.* **2015**, *6*, 6769-6776.

(29) Vogel, Y. B.; Gonçales, V. R.; Gooding, J. J.; Ciampi, S., Electrochemical microscopy based on spatial light modulators: A projection system to spatially address electrochemical reactions at semiconductors. *J. Electrochem. Soc.* **2018**, *165*, H3085-H3092.

Chapter 7 Conclusions and Future Works

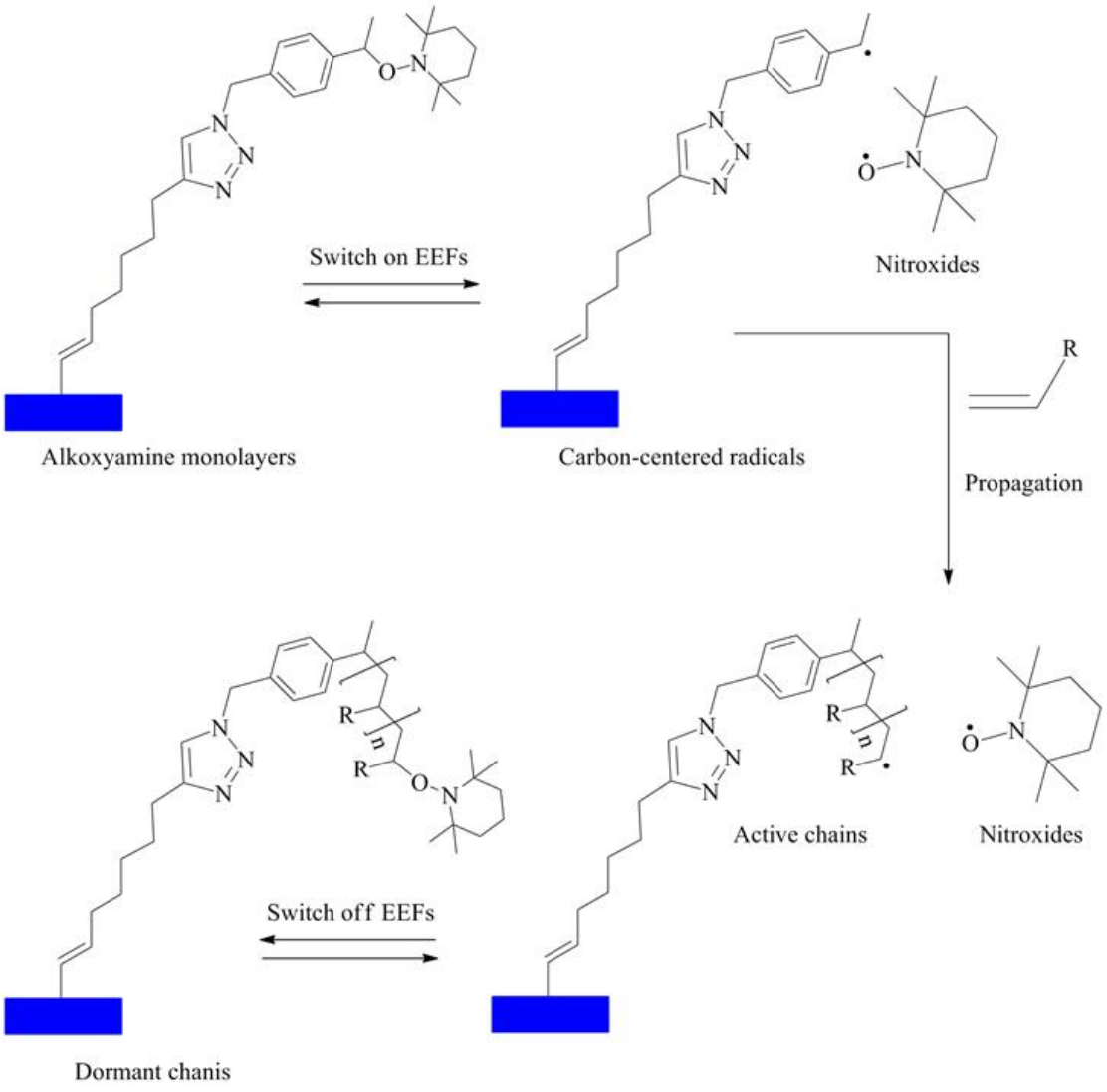

7.1 General conclusions

This doctoral work has demonstrated experimentally that electrostatic forces can affect chemical bonding and reactivity. It has laid solid foundations in terms of proof-of-principle and platforms to move from single reactions to a molecular assembly and eventually towards diffusive (i.e. scalable) systems. Most of the experimental work was based on nitroxides and alkoxyamines and analyzed either in diffusive system or on surface models. Specifically, emphasis was placed on electrostatic interactions formed within electric double layers. In addition, all experimental results show good agreement with simulations and theoretical calculations.

In Chapter 3, the hydrogen-terminated silicon surfaces is converted into structurally well-defined acetylenyl-terminated organic monolayers by the thermal hydrosilylation with commercial 1,8-nonadiyne, followed by the preparation and functionalization of persistent nitroxide monolayers on Si(100) surfaces using the 'click' cycloaddition of 4-azido-TEMPO with surface-bound acetylenes based on a two-step wet-chemical route. Importantly, the unpaired electrons of nitroxides are preserved upon the modification procedures. Subsequently, validation was achieved to show that the electroactivity of the prepared nitroxide monolayers on highly-doped silicon electrodes can be predictably manipulated by altering the electrolyte anions. Namely, the magnitude of electrostatic interactions between the oxidized oxoammonium molecules and electrolyte anions, on the other hand, while tethering the nitroxide molecules to the poorly doped silicon surfaces, electrostatic interactions between nitroxide units and space charges in the semiconductors are favorable, resulting in dramatically kinetic changes to the redox performance of radical monolayers as well as the appearance of reproducibly electrochemical nonidealities of both peak-inversion phenomena and FWHM < 90.6 mV. In addition, the electrode reactions in this chapter are further analyzed with the aid of digital simulations and quantum chemical calculations by emulating a similar nitroxide monolayer model, defining the kinetic and thermodynamic parameters during the electrochemical processes.

Chapter 4 presented the analysis of the electrostatic factor on non-redox steps that

are coupled to a redox event. The case study was the ECE mechanism for electrochemical oxidation of alkoxyamine molecules; that alkoxyamines in diffusive systems would lose an electrode to produce alkoxyamine radical cations upon a positive bias, followed by a rapid fragmentation of these intermediates into carbocations and nitroxides, and nitroxides were then oxidized to oxoammoniums. Digital simulations and *in-situ* EPR-electrochemistry experiments were employed to confirm the assumed ECE mechanism and also used to gauge the thermodynamic and kinetic parameters of electrode reaction processes and chemical fragmentation step. Similarly, a surfaced-tethered alkoxyamine monolayer showed a nitroxide signature (compared with TEMPO monolayer modified with commercial nitroxides) upon positive biases, opening a new route to synthetic organic electrochemistry. High-level *ab initio* calculations were carried out to reproduce the parameters obtained in simulation work; the lysis of oxidized alkoxyamines however was energetically unfavorable if not considering an explicit environment within electric double layers. That is to say, the decomposition step of alkoxyamine radical cations can be promoted while including either an explicit ion or an explicit solvent in the calculations. Unfortunately, it was not possible to quantify the strength of the electrostatic force due to the fact that considering both ions and solvents in a high level of computation is impractical and the exact measurement of an electric field within an electric double layer in electrolyte solution is beyond current knowledge.

A surface model developed for quantifying the electric field used to decompose the alkoxyamine molecules is described in Chapter 5. Use was made of the STM-BJ setup to track the fate of an alkoxyamine molecule (di-amino-TEMPO-PE) when this molecule was positioned in the electrified gap between a gold STM tip and an Au(111) substrate. The homolysis of alkoxyamine molecules was successfully accomplished while imposing a bias stimulus of variable magnitude to form a molecular circuit. Two discrete molecular junctions were formed during the homolysis process of C-O bonds of alkoxyamine **1** because both the amino groups on parent alkoxyamines and nitroxide radicals on homolytic products have affinity towards gold electrodes. The single molecule conductance was obtained from the analysis of ca. 4000 individual

measurements by repeatedly forming and breaking the molecular junctions at each fixed bias and, by repeating the procedure for 8 biases in steps of 50-100 mV, it was possible to construct conductance histograms that reveal the homolysis of alkoxyamine **1** to release the TEMPO fragment at biases greater than 150 mV. A quantum model of this system detailed the homolysis mechanism and optimized the strength and orientation of field aligned along the reaction axis, suggesting that the barrier of this homolysis reaction was lowered by up to 35 kJ/mol by going from a zero external-field stimulus to a 4 V/nm field. Although these results backed the theoretical calculations in Chapter 4 and provided concrete values of an electric field on lysis of alkoxyamine molecules, it was clearly not practical to process workable quantities of materials in STM-BJ technique but do lead to proof-of-concept data in an experimental scenario.

The ECE mechanism of alkoxyamine decomposition under an anodic bias evokes the renaissance of organic electroynthesis on surfaces. Generation of a surface-tethered and highly-reactive carbocation by an electrochemical approach was described in Chapter 6. An alkoxyamine derivative was first covalently attached to silicon surface, an anodic bias stimulus triggers the immediate fragmentation of alkoxyamine monolayers into diffusive nitroxides and surface-confined carbocations. As a proof-of-principle we have used this reactive intermediate to trap a nucleophile dissolved in the electrolyte. The nucleophile was ferrocenemethanol and its presence and surface concentration after its reaction with the carbocation were assessed by cyclic voltammetry. The work expands the repertoire of available electrosynthetic methods and could in principle lay the foundation to a new form of electrochemical lithography.

All in all, considerable experimental progress has been achieved on confirming that oriented EEFs are potent effectors of chemical change and control based on lab benchwork; especially in developing self-assembly monolayers on semiconductor surfaces and molecular circuitry in the STM-BJ surface setup. The intended purposes of this research were potential studies of two new chemical areas in synthetic organic electrochemistry[1, 2] (the use of electrochemical reaction in organic synthesis) and electrostatic catalysis[3-7] (the use of static electric fields to catalyze non-electrochemical reactions), and the present work indeed sits at the intersection of these fields.

7.2 Future works

The aim of this project is to establish static electricity as a "smart" reagent - a catalyst or inhibitor in a broad range of chemical reactions - this will bring the concept of electrostatic catalysis into the realm of chemical methods that are available to process workable quantities of materials.

7.2.1 Electrocatalysis of heterogeneous systems

As discussed in Chapter 3, the oxidizing power of nitroxide monolayers can predictably be tuned by simply changing either the electrolyte anions or electrode types. This knowledge may aid the development of electrocatalytic heterogeneous systems where the redox reactions of interest can be coupled to homogeneous reactions of surface-tethered monolayers. For example, the heterogeneous oxidation potential of bromide to bromine is driven contra-thermodynamically by up to 0.5 V under illumination while tethering the redox mediator of TEMPO monolayers to poorly-doped silicon electrodes, compared with that of grafting TEMPO molecules on highly-doped (metallic) surfaces.

7.2.2 Surface polymerization

The development of grafting strategies is of great current importance in industrial application of confined polymers. Grafting can be accomplished in a number of ways, including by growth of polymer chains from a solid surface using immobilized initiators ("grafting-from" technique)[8], or covalent attachment of preformed polymers to reactive sites on an inorganic surface ("grafting-to" technique)[9]. In parallel, the growing demand for well-defined functionalized materials has led to the development of robust methodologies to precisely control the physical structure of the grafted polymer layer. Among the different methods (e.g. anionic, cationic, and anionic-coordinated ring-opening polymerizations), controlled free radical polymerization has attracted considerable attention due to its simplicity and versatility compared with ionic processes[10].

The STM-BJ experiments in Chapter 5 were initially designed as an attempt to harness electrostatic catalysis in nitroxide-mediated polymerization, in other words, using alkoxyamine molecules on a surface that dissociate to tether carbon-centered

radicals and free nitroxides in the presence of an electric field and adds more monomers which then recombines to form tethered alkoxyamine when the field is switched off, which can be investigated (Figure 7.1). One point needs to be noted that the generated carbon-centered radicals may eject hydrogens and become olefins due to short lifetime and active reactivity. This protocol presents a new perspective for surface grafting methodology controlled by the EEFs under mild and non-reducing conditions, which is much less hazardous than traditional thermal- and irradiation- induced polymerizations, leading to the development of new materials with innovative self-healing or photoelectronic properties. In addition, single-molecule STM-BJ experiments also allow one to develop EEFs-effect 'mono-molecular' electronic devices where a single molecule will integrate the fundamental functions and interconnections required for computation.

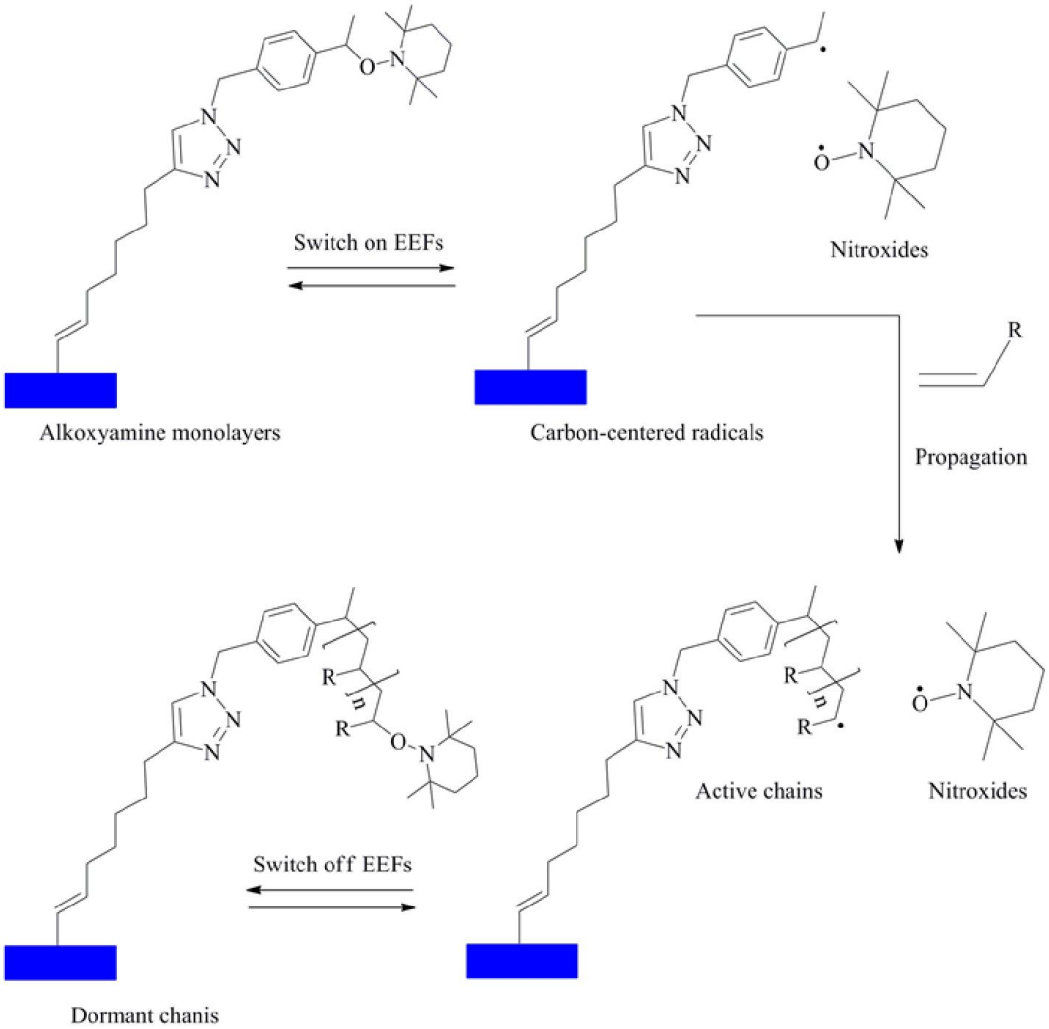

Figure 7.1 Electric fields triggered living radical polymerization on the surface.

7.3 References

(1) Yan, M.; Kawamata, Y.; Baran, P. S. Synthetic organic electrochemistry: calling all engineers. *Angew. Chem. Int. Ed. Engl.* **2017**.

(2) Yan, M.; Kawamata, Y.; Baran, P. S. Synthetic organic electrochemical methods since 2000: on the verge of a renaissance. *Chem. Rev.* **2017,** *117*, 13230-13319.

(3) Shaik, S.; Mandal, D.; Ramanan, R. Oriented electric fields as future smart reagents in chemistry. *Nat. Chem.* **2016,** *8*, 1091-1098.

(4) Fried, S. D.; Bagchi, S.; Boxer, S. G. Extreme electric fields power catalysis in the active site of ketosteroid isomerase. *Science* **2014,** *346*, 1510-1514.

(5) Aragonès, A. C.; Haworth, N. L.; Darwish, N.; Ciampi, S.; Bloomfield, N. J.; Wallace, G. G.; Diez-Perez, I.; Coote, M. L. Electrostatic catalysis of a Diels–Alder reaction. *Nature* **2016,** *531*, 88-91.

(6) Geng, C.; Li, J.; Weiske, T.; Schlangen, M.; Shaik, S.; Schwarz, H. Electrostatic and charge-induced methane activation by a concerted double C-H bond insertion. *J. Am. Chem. Soc.* **2017,** *139*, 1684-1689.

(7) Ramanan, R.; Danovich, D.; Mandal, D.; Shaik, S. Catalysis of methyl transfer reactions by oriented external electric fields: are gold-thiolate linkers innocent? *J. Am. Chem. Soc.* **2018**.

(8) Prucker, O.; Rühe, J. Synthesis of poly(styrene) monolayers attached to high surface area silica gels through self-assembled monolayers of azo initiators. *Macromolecules* **1998,** *31*, 592-601.

(9) Krenkler, K. P.; Laible, R.; Hamann, K. Polyreaktionen an pigmentoberflächen. VII. Mitteilung: reaktionen von polymeren mit endständigen chlorsilangruppen an siliciumdioxidoberflächen. *Macromol. Mater. Eng.* **1976,** *53*, 101-123.

(10) Bartholome, C.; Beyou, E.; Bourgeat-Lami, E.; Chaumont, P.; Lefebvre, F.; Zydowicz, N. Nitroxide-mediated polymerization of styrene initiated from the surface of silica nanoparticles. In situ generation and grafting of alkoxyamine initiators. *Macromolecules* **2005,** *38*, 1099-1106.